ISSN 0911-5730
UVSOR-52
August 2025

UVSOR ACTIVITY REPORT 2024

UVSOR Synchrotron Facility
Institute for Molecular Science
National Institutes of Natural Sciences

Preface

This Activity Report reviews the scientific and technological work carried out using the UVSOR-III Synchrotron in FY2024 (April 2024 – March 2025). We present examples of research conducted by users at the UVSOR Synchrotron Facility. The selection policy for the important results in each field has changed. A new chapter "Highlight" has been created, and the reports have been brought together with the aim of increasing their visibility beyond the research field.

The UVSOR-III Synchrotron is one of the world's leading third-generation, low-energy SR facilities and serves as a critical resource for advancing molecular science. Although its electron storage ring is compact, it supports six undulator beamlines (three VUV and three in-vacuum soft X-ray) alongside seven dipole beamlines. Through our strategic international collaboration program, we continue to enhance micro- and nano-scale photoabsorption and photoemission techniques—as well as in situ/operando measurements—in the IR, VUV, and soft X-ray regions. A feasibility study is also under way to develop instrumentation tailored to complex, inhomogeneous samples, including biology and life science systems. The issue of low beam current during 200 mA operation is expected to be resolved by maintenance at the end of FY2024.

UVSOR operates 40 weeks per year (approximately 2,200 h of user time over 36 weeks), accepts around 230 proposals annually, and supports about 500 individual researchers—totaling roughly 5,000 user-days per year. Most users conduct experiments over one- or two-week visits. To sustain high-level achievements, our in-house staff remains dedicated to maintaining and improving high-performance accelerators and beamlines.

On the experimental front, technological development never pauses. We are advancing operando and imaging-related techniques to drive breakthroughs in molecular science. Since 2020, we have been constructing a new end-station at the undulator-based soft X-ray beamline BL6U, featuring a photoelectron momentum microscope (PMM) equipped with a double-hemispherical analyzer and a 2D spin detector. This article summarizes the current status of that instrumentation. At beamline BL1U, we have been developing novel light sources—most notably twin-undulator configurations for attosecond interference experiments. These advanced SR-related instruments will expand opportunities to characterize the electronic structure of surface atomic sites, thin films, molecular adsorbates, bulk crystals, and more.

Since 2019, we have also been planning Post-UVSOR-III as a long-term strategy for sustainable development (see our dedicated website for UVSOR-IV*). Several workshops have been held to discuss future perspectives, and we welcome your feedback and suggestions on the facility's continued evolution. We look forward to the many excellent studies users will carry out at UVSOR-III, and to its role as a unique international hub for advanced molecular-science research.

*"Website"

May 2025
Satoshi Kera
Director of the UVSOR Synchrotron Facility

Staff

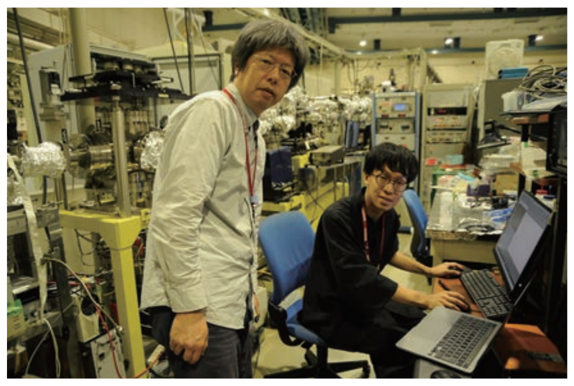

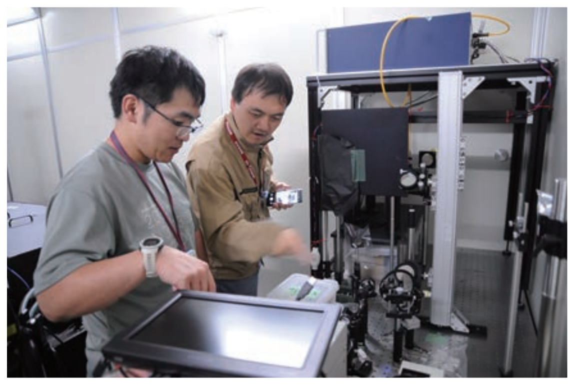

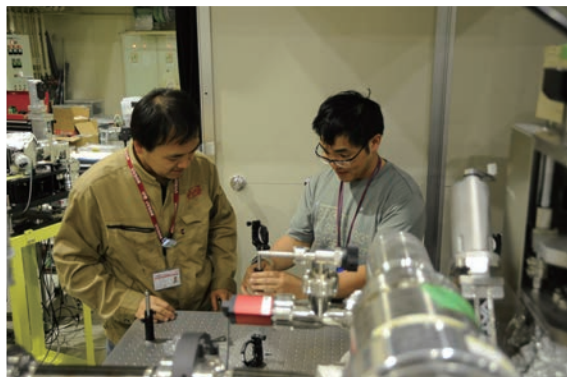

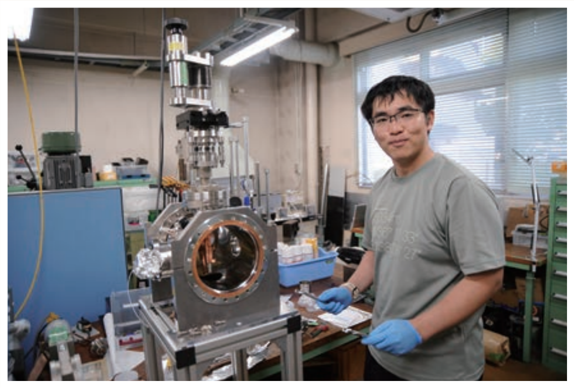

UVSOR User 1

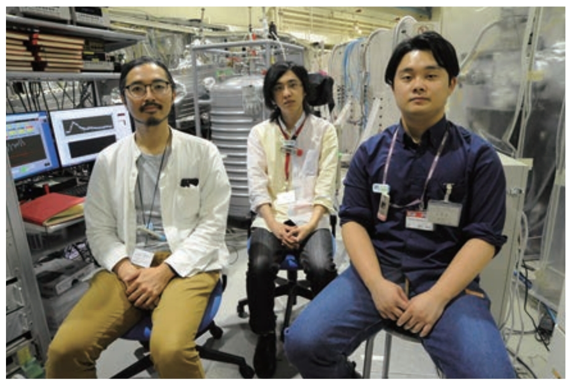

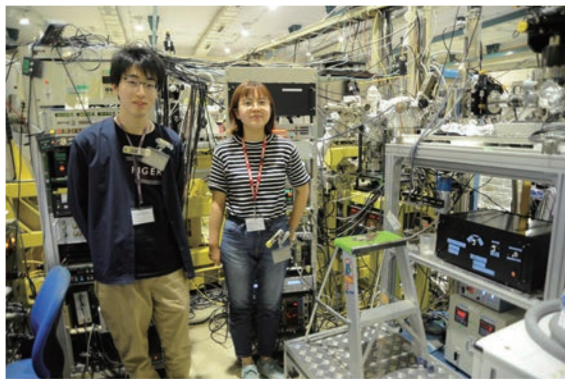

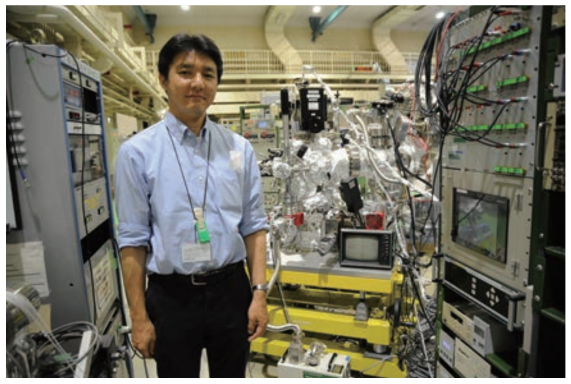

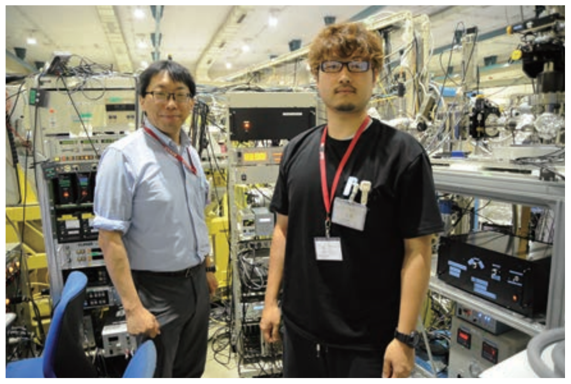

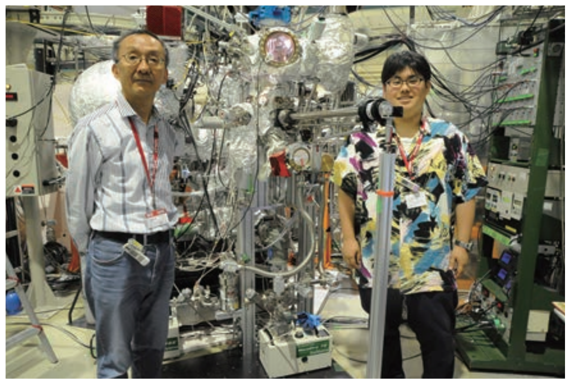

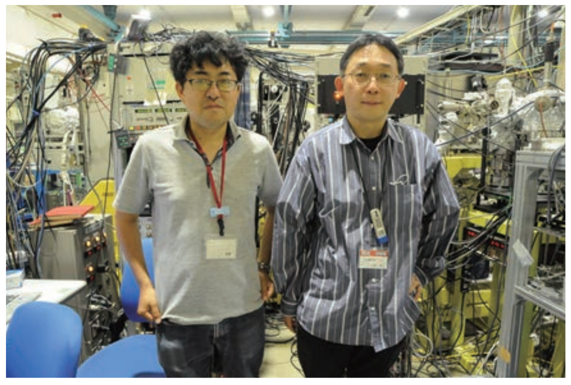

UVSOR User 2

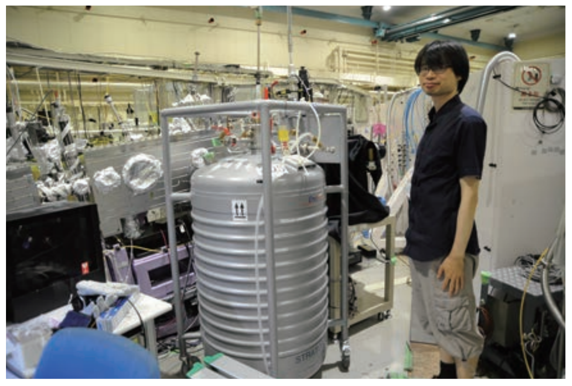

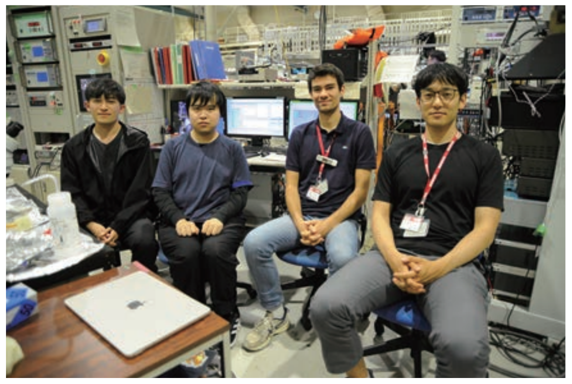

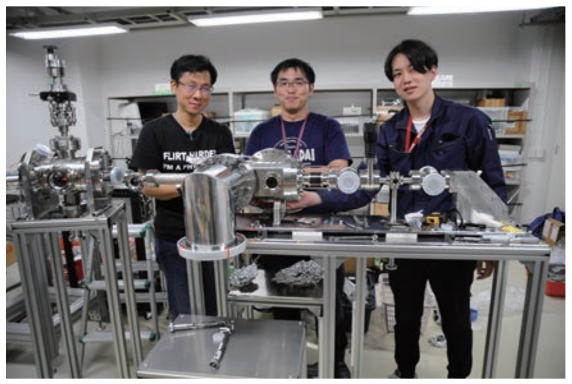

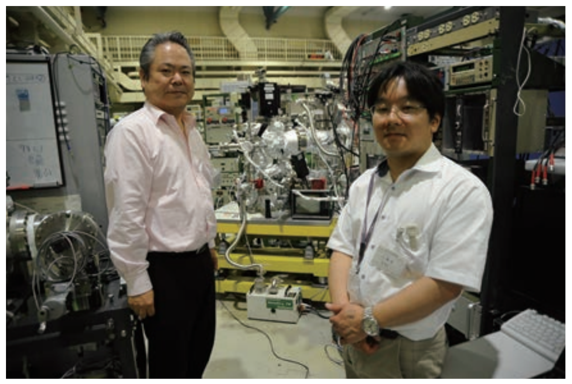

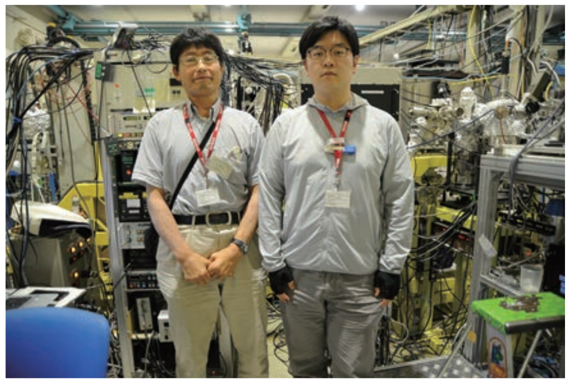

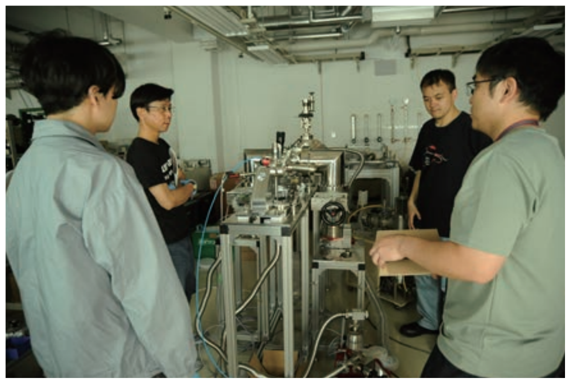

UVSOR ACTIVITY REPORT 2024

Preface

III Research Activities

III-3 Chemistry 111

UVSOR User 3

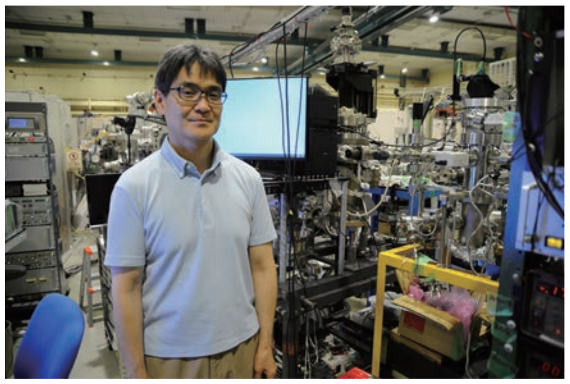

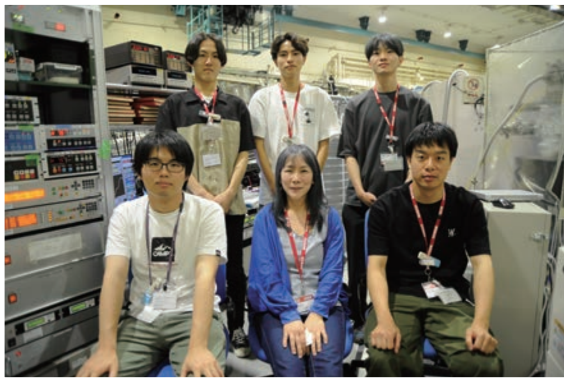

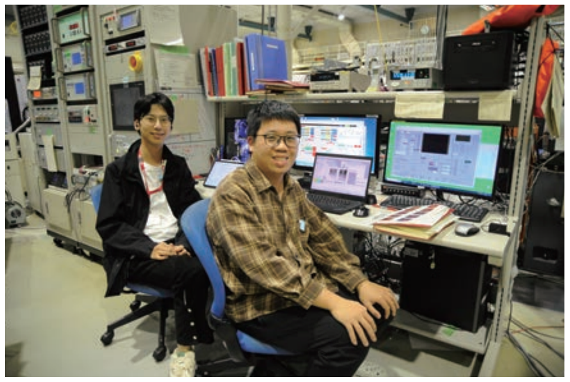

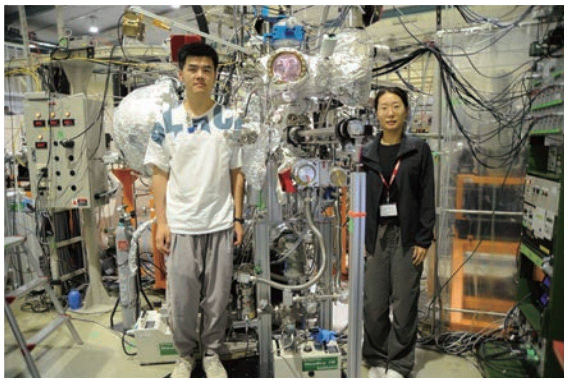

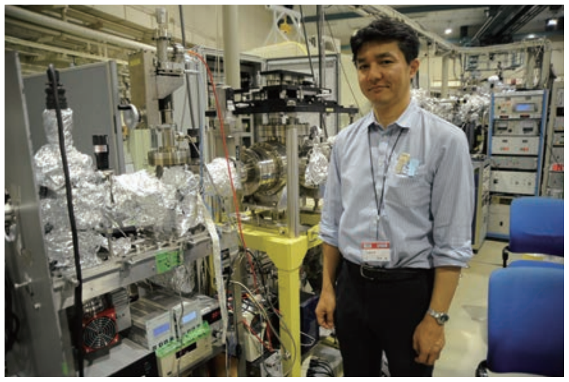

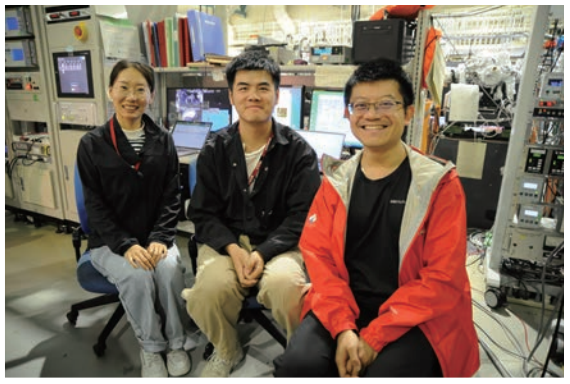

I

Organization and Staff List

UVSOR Synchrotron Facility Organization

Mar. 2025

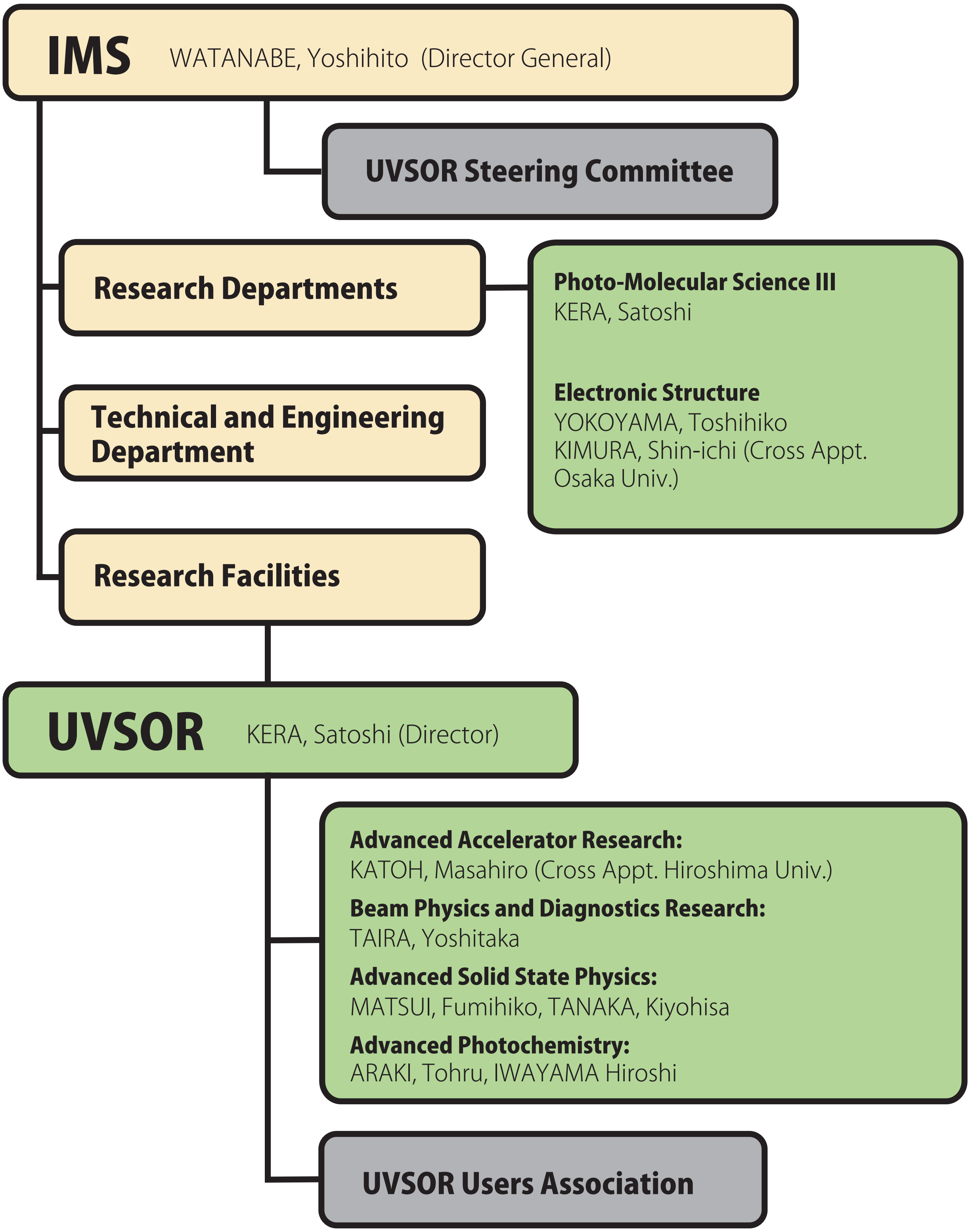

IMS WATANABE, Yoshihito (Director General)

UVSOR Steering Committee

Research Departments

Photo-Molecular Science III
KERA, Satoshi

Electronic Structure
YOKOYAMA, Toshihiko
KIMURA, Shin-ichi (Cross Appt. Osaka Univ.)

Technical and Engineering Department

Research Facilities

UVSOR KERA, Satoshi (Director)

Advanced Accelerator Research:
KATOH, Masahiro (Cross Appt. Hiroshima Univ.)

Beam Physics and Diagnostics Research:
TAIRA, Yoshitaka

Advanced Solid State Physics:
MATSUI, Fumihiko, TANAKA, Kiyohisa

Advanced Photochemistry:
ARAKI, Tohru, IWAYAMA Hiroshi

UVSOR Users Association

Staff List

Mar. 2025

UVSOR Staff

Director

KERA, Satoshi	Professor	kera@ims.ac.jp	

Division of Advanced Accelerator Research

KATOH, Masahiro	Project Professor (Cross Appt. Hiroshima Univ.)	mkatoh@ims.ac.jp	

Division of Beam Physics and Diagnostics Research

TAIRA, Yoshitaka	Associate Professor	yostaira@ims.ac.jp	
MATSUDA, Hiroyuki	Project Research Staff	hmatsuda@ims.ac.jp	

Division of Advanced Solid State Physics

MATSUI, Fumihiko	Professor	matui@ims.ac.jp	
TANAKA, Kiyohisa	Associate Professor	k-tanaka@ims.ac.jp	
HAGIWARA, Kenta	Project Research Staff		(until Mar. 2025)

Division of Advanced Photochemistry

ARAKI, Tohru	Senior Researcher	araki@ims.ac.jp	
IWAYAMA, Hiroshi	Senior Researcher	iwayama@ims.ac.jp	

Research Staff

KANEYASU, Tatsuo	Associate Professor (Concurrent Appt. SAGA-LS)		(until Mar. 2025)
IZUMI, Yudai	Research Lecturer	izumi@ims.ac.jp	(since Sep. 2024)
KATAYANAGI, Hideki	Research Associate	kata@ims.ac.jp	
SUGIMOTO, Yasunobu	Specially Appointed Senior Specialist		(until Sep. 2024)

Technical Staff

HAYASHI, Kenji	Engineer (Unit Leader)
NAKAMURA, Eiken	Chief Engineer
MAKITA, Seiji	Engineer
OKANO, Yasuaki	Engineer
SAKAI, Masahiro	Chief Technician
YANO, Takayuki	Chief Technician
TESHIMA, Fumitsuna	Chief Technician
KONDO, Naonori	Chief Technician
YUZAWA, Hayato	Chief Technician
OTA, Hiroshi	Technician (Concurrent Appt. SPring-8)
SHIMIZU, Kohei	Technician

YAMAZAKI, Jun-ichiro	Technical Fellow
MIZUKAWA, Tetsunori	Technical Fellow
MINAKUCHI, Aki	Technical Fellow

Secretary

ISHIHARA, Mayumi
KAMO, Kyoko
YOKOTA, Mitsuyo

Departments in IMS (*Group Leader)

Division of Photo-Molecular Science III

KERA, Satoshi*	Professor
NAGASAKA, Masanori	Assistant Professor
FUKUTANI, Keisuke	Assistant Professor
SAGEHASHI, Ryunosuke	Research Assistant Professor

Division of Electronic Structure

YOKOYAMA, Toshihiko*	Professor
KIMURA, Shin-ichi	Professor (Cross Appt. Osaka Univ.)
KURAHASHI, Naoya	Assistant Professor
MAEJIMA, Naoyuki	Research Assistant Professor

Graduate Students

KAWANO, Kento	Nagoya University	(until Sep. 2024)
MASUDA, Keisuke	Nagoya University	(until Sep. 2024)
SASABA, Ryohei	The University of Osaka	(until Jun. 2024)
ZHU, Yupeng	Southern University of Science and Technology	(since May. 2024)
YANG, Yuxuan	Zhengzhou University	(since Oct. 2024)
ZHOU, Weixin	Tsinghua University	(since Oct. 2024)
HATAE, Yuta	Nagoya University	(since Nov. 2024)
YODA, Yasuto	Nagoya University	(since Nov. 2024)

UVSOR Steering Committee (*Chair)

KERA, Satoshi*	UVSOR, IMS	Chair
MATSUI, Fumihiko	UVSOR, IMS	
KATOH, Masahiro	UVSOR, IMS	
TANAKA, Kiyohisa	UVSOR, IMS	
TAIRA, Yoshitaka	UVSOR, IMS	
ARAKI, Tohru	UVSOR, IMS	
IWAYAMA, Hiroshi	UVSOR, IMS	

KITAURA, Mamoru	Yamagata University
KURODA, Kenta	Hiroshima University
AMEMIYA, Kenta	KEK PF
MISAWA, Kazuhiko	Tokyo University of Agriculture and Technology
NAKAMURA, Tetsuya	Tohoku University
YABASHI, Makina	RIKEN
ITO, Takahiro	Nagoya University
WATANABE, Yoshihito	IMS, Director General
YOKOYAMA, Toshihiko	IMS
KATO, Koichi	IMS
AKIYAMA, Shuji	IMS
KUMAGAI, Takashi	IMS
SHIGEMASA, Eiji	IMS
HAYASHI, Kenji	IMS
NAKAMURA, Toshikazu	IMS

UVSOR Users Association (*Chair)

ITO, Takahiro*	Nagoya University	(since Apr. 2024)
KIMURA, Shin-ichi	Osaka University	(since Apr. 2024)
HIRAHARA, Toru	Tokyo Insititute of Technology	
YOSHIDA, Tomoko	Osaka Metropolitan University	(since Apr. 2024)
MIYAMACHI, Toshio	Nagoya University	

Visiting Scientists

SFORNA, Marie Catherine	Center for Biochemical physics- University of Orleans	May 2024, Oct. 2024
MILOJEVIC, Tetyana	Center for Biochemical physics- University of Orleans	May. 2024, Jun. 2024
ZENG, Meng	Southern University of Science and Technology	Jun. 2024
LUO, Ronghao	Southern University of Science and Technology	Jun. 2024
LIU, Chang	Southern University of Science and Technology	Jun. 2024
WANG, Jian	City university of Hong Kong	July 2024
ZHANG, Yunze	City university of Hong Kong	Jul. 2024, Aug. 2024
LEI, Jia	City university of Hong Kong	Jul. 2024, Aug. 2024
CHUANG, Cheng-Hao	Tamkang University	Aug. 2024
MARIANO, Carl Osby Marcelo	Tamkang University	Aug. 2024
HSIEH, Zong-Jhe	Tamkang University	Aug. 2024
LU, Hsin-Chan	Tamkang University	Aug. 2024
HE, Ruihua	Westlake University	Aug. 2024, Jan. 2025
HONG, Caiyun	Westlake University	Aug. 2024
HUANG, Chaozhi	Westlake University	Aug. 2024, Jan. 2025
JIANG, Congying	Westlake University	Aug. 2024, Jan. 2025

ZHENG, Xiaonan	Westlake University	Aug. 2024, Jan. 2025
KONG, Xiangrui	University of Gothenburg	Aug. 2024, Mar. 2025
ZHU, Mingyuan	Southern University of Sceince and Technology	Spt. 2024
MA, Xiaoming	Southern University of Sceince and Technology	Spt. 2024, Feb. 2025, Mar. 2025
YANG, Cheng-Chieh	National Taiwan University of Science and Technology	Spt. 2024, Mar. 2025
KUMARAVELU, Thanigai Arul	Tamkang University	Spt. 2024, Mar. 2025
TA, Thi Thuy Nga	National Yang Ming Chiao Tung University	Spt. 2024, Mar. 2025
DONG, Chung-Li	Tamkang University	Spt. 2024, Mar. 2025
KIM, Hongjoo	Kyungpook National University	Spt. 2024, Jan 2025, Mar. 2025
CHO, Jaeyoung	Kyungpook National University	Spt. 2024, Jan. 2025, Mar. 2025
JEONG, Dongwoo	Kyungpook National University	Spt. 2024, Jan. 2025, Mar. 2025
LEE, Doohyeok	Kyungpook National University	Spt. 2024
SUBACH, Sergey	Forschungszentrum Jülich	Oct. 2024
TAN, Xin Liang	Norwegian University of Science and Technology	Oct. 2024
BRINKMAN, Stefanie	Norwegian University of Science and Technology	Oct. 2024
WATTS, Benjamin	Paul Scherrer Institute	Oct. 2024, 'Nov. 2024
KIM, Younsik	Seoul National University	Nov. 2024
KIM, Sehoon	Seoul National University	Nov. 2024
YOO, Junseo	Seoul National University	Nov. 2024
YANG, Jinpeng	Yangzhou University	Nov. 2024'Dec. 2024
LIU, Xianjie	Linköping University	Nov. 2024, 'Dec. 2024
SPÄTH, Andreas	Friedrich-Alexander University Erlangen-Nuremberg	Nov. 2024, 'Dec. 2024
JEONG, Dongjoon	Pohang University of Science and Technology	Dec. 2024
LEE, Siwon	Pohang University of Science and Technology	Dec. 2024
PARK, Sangjun	Institute for Basic Science	Dec. 2024
KIM, Jaeyoung	Institute for Basic Science	Dec. 2024
KO, Kyung-Tae	Korea Basic Science Institute	Dec. 2024
KIM, Wondong	Korea Research Institute of Standards and Science	Dec. 2024
LIANG, Xin	City University of Hong Kong	Dec. 2024
LIN, Zihan	City University of Hong Kong	Dec. 2024
QIAN, Chengyang	Westlake University	Jan. 2025
ZHANG, Yue	Shanghai Advanced Research Institute	Jan. 2025
XU, Hanghua	Shanghai Advanced Research Institute	Jan. 2025
CHOI, Eunjin	Kyungpook National University	Jan. 2025, Mar. 2025
CHO, Soohyun	Sunchon National University	Feb. 2025
JING, Wenchuan	Shanghai Institute of Microsystem and Information Technology	Feb. 2025
LUO, Qiben	University of Science and Technology of China	Feb. 2025
DAI, Yue	Southern University of Science and Technology	Feb. 2025, 'Mar. 2025
SHAO, Tianhao	Southern University of Science and Technology	Feb. 2025, 'Mar. 2025
FAURÉ, Nicolas	University of Gothenburg	Mar. 2025
THOMSON, Erik	University of Gothenburg	Mar. 2025
TRINH, Hai Binh	National Yang Ming Chiao Tung University	Mar. 2025

UVSOR User 4

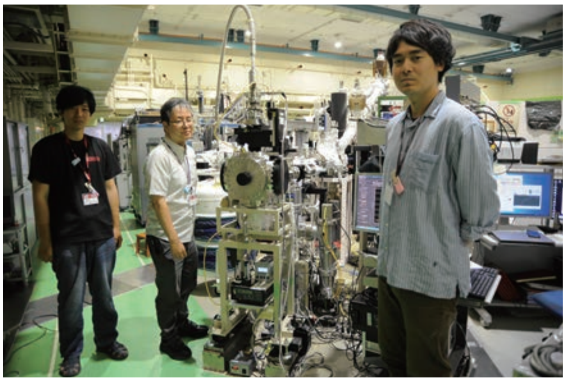

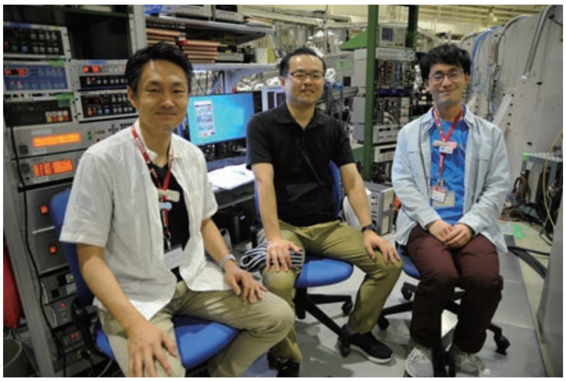

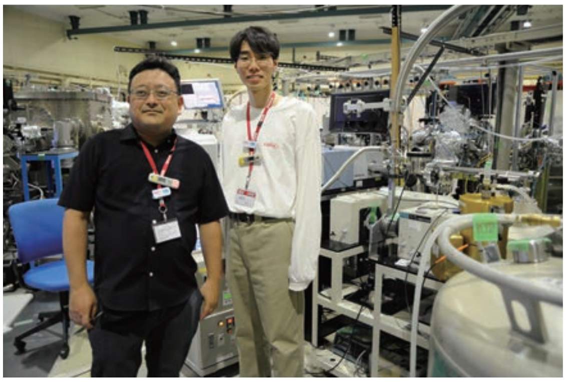

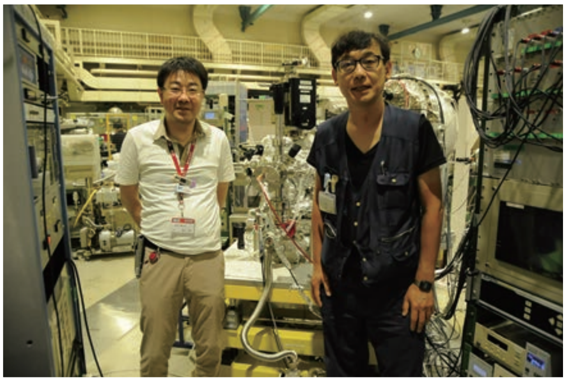

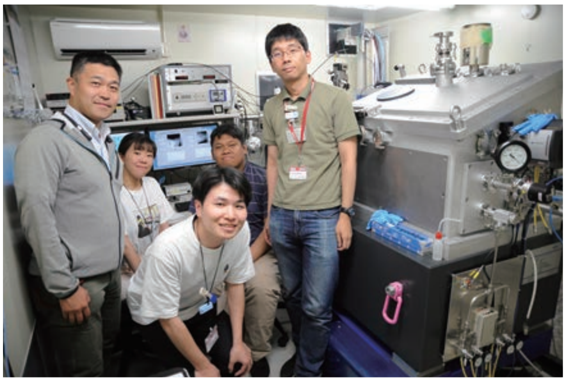

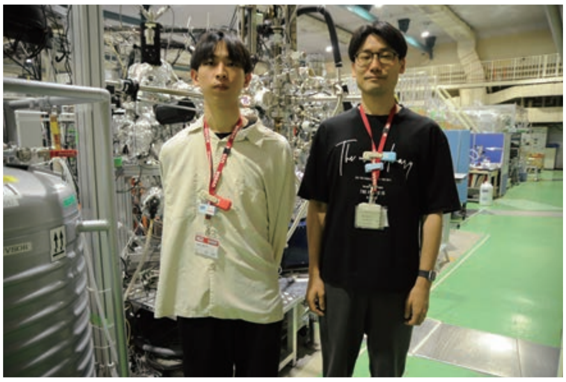

II

Current Status of Light Sources and Beamlines

Light Source in 2024

Yoshitaka Taira
UVSOR Synchrotron Facility, Institute for Molecular Science, Okazaki 444-8585, Japan

In FY2024, UVSOR-III was operated for users as scheduled for 36 weeks from end of May 2024 to March 2025. Monthly statistics of operation time and integrated beam current are shown in Fig. 1. From the beginning of April to early May, during which periodic inspections were conducted. The two weeks following the shutdown were allocated to the adjustment of the accelerator and beamlines.

The weekly operation schedule is as follows. Mondays are assigned to machine studies from 9:00 AM to 9:00 PM. User operation is assigned Tuesday through Friday, with Tuesday and Wednesday operating from 9:00 AM to 9:00 PM, and Thursday from 9:00 AM to 9:00 PM on Friday for 36 continuous hours. Thus, the user's beam time per week is 60 hours.

A few mA loss in stored beam current has been occurring since FY2023 when the gap of a particular undulator is changed during user operation. As it has been observed that the electron beam size circulating the storage ring increases during loss, instantaneous beam instability is thought to occur. No significant change in betatron tune before and after the loss was observed, and the cause of the beam instability has not been identified. However, by changing the current value of sextupole electromagnets in March 2024, the loss of stored beam current almost did not occur thereafter.

Injection efficiency of the electron beam into the storage ring started to decrease around January 2023. The injection efficiency is calculated as the ratio of the increase in the stored current value, δI, to the current value passing through the transport line between the booster synchrotron and the storage ring. Under normal conditions, the injection efficiency was 60~70% and δI was 0.4~0.6 mA/shot, but after January 2023, the efficiency dropped to 20~30% and δI 0.1~0.3 mA/shot. The limited number of electrons that can be injected into the storage ring per week makes it difficult to continue 300 mA operation. Therefore, user operation has been conducted with the stored current value reduced to 200 mA since May 2023. Various investigations are continuing to determine the cause, but so far no clear cause has been identified. However, the betatron function and emittance of the booster synchrotron were found to deviate significantly from the design values. The vacuum ducts in the bending magnet section of the booster synchrotron have experienced multiple vacuum leaks, and there is concern that opening the ducts to the atmosphere may induce serious vacuum leaks, so it is currently impossible to visually check inside the ducts. All vacuum ducts in the bending magnet section are scheduled to be replaced with new ones in April 2025. At that time, we will check the inside of the vacuum ducts of the booster synchrotron.

We started a design study for the future plan of UVSOR-IV. As a first step, we have analyzed the present magnetic lattice, seeking a possibility to reduce the emittance more [1]. Although, we did not find a solution to drastically reduce emittance, we have found a few interesting solutions that achieved lower emittance than the current situation. As the second step, we have started designing a totally new storage ring, which is close to the diffraction limit in the VUV range [2].

The light source development and utilization beamline BL1U, constructed under the support of Quantum Beam Technology Program by MEXT/JST, continue to develop new light source technologies and their applications such as free electron laser, coherent harmonic generation, coherent synchrotron radiation, coherent control [3], laser Compton scattered gamma rays [4, 5], and optical vortices [6].

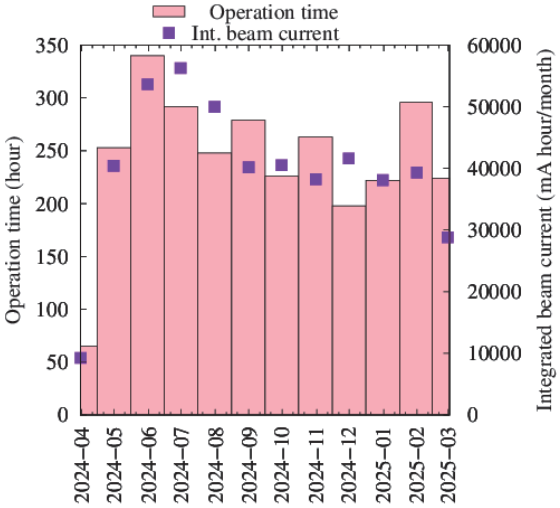

Fig. 1. Monthly statistics in FY2024.

[1] E. Salehi and M. Katoh, Proceedings of IPAC2021 (2021) 3970.
[2] E Salehi *et al.*, Phys.: Conf. Ser. **2420** (2023) 012062.
[3] Y. Hikoska *et al.*, Sci. Rep. **13** (2023) 10292.
[4] Y. Taira, Phys. Rev. A **110** (2024) 043525.
[5] S. Endo *et al.*, Eur. Phys. J. A **60** (2024) 166.
[6] S. Wada *et al.*, Sci. Rep. **13** (2023) 22962.

UVSOR Accelerator Complex

Injection Linear Accelerator	
Energy	15 MeV
Length	2.5 m
RF Frequency	2856 MHz
Accelerating RF Field	2π/3 Traveling Wave
Klystron Power	1.8 MW
Energy Spread	~1.6 MeV
Repetition Rate	1 Hz (Max. 3 Hz)

UVSOR-III Storage Ring	
Energy	750 MeV
Injection Energy	750 MeV
Normal Operation	300 mA (multi bunch)
Current (Top-up)	40 mA (single bunch)
Natural Emittance	17.5 nm rad
Circumference	53.2 m
RF Frequency	90.1 MHz
RF Voltage	120 kV
Harmonic Number	16
Bending Radius	2.2 m
Lattice	Extended DB×4
Straight Section	(4 m×4)+(1.5 m×4)
Betatron Tune	
Horizontal	3.75
Vertical	3.20
Momentum Compaction	0.030
Natural Chromaticity	
Horizontal	-8.1
Vertical	-7.3
Energy Spread	5.26×10^{-4}
Coupling Ratio	1%
Natural Bunch Length	128 ps

Booster Synchrotron	
Energy	750 MeV
Injection Energy	15 MeV
Beam Current	15 mA (uniform filling)
Circumference	26.6 m
RF Frequency	90.1 MHz
Harmonic Number	8
Bending Radius	1.8 m
Lattice	FODO×6
Betatron Tune	
Horizontal	2.25
Vertical	1.25
Momentum Compaction	0.138
Repetition Rate	1 Hz (Max. 3 Hz)

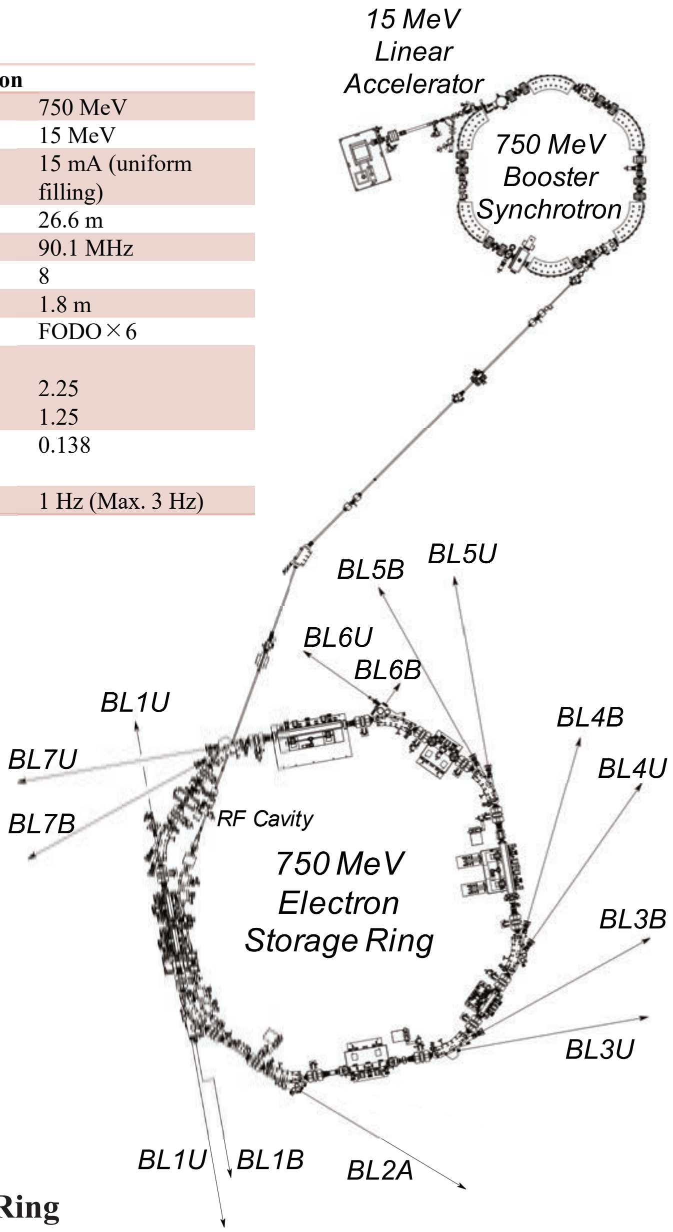

Electron Beam Optics of UVSOR-III Storage Ring

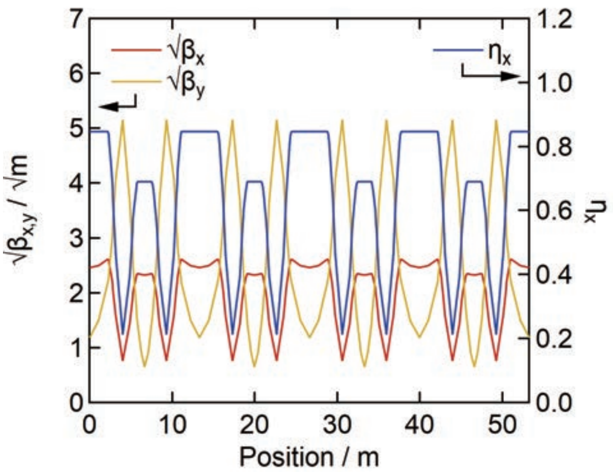

Horizontal / vertical betatron functions and dispersion functions

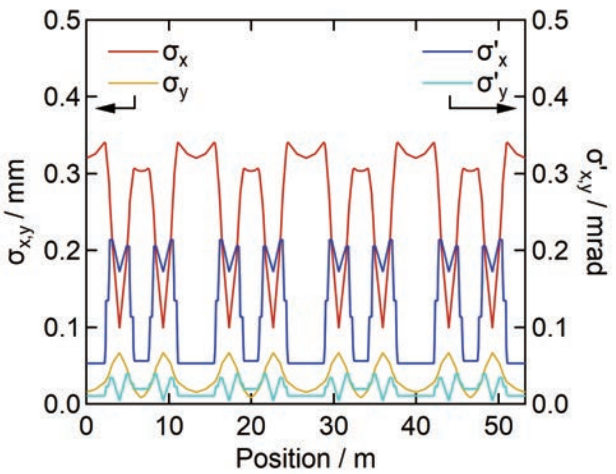

Horizontal / vertical electron beam size and beam divergences

Insertion Devices

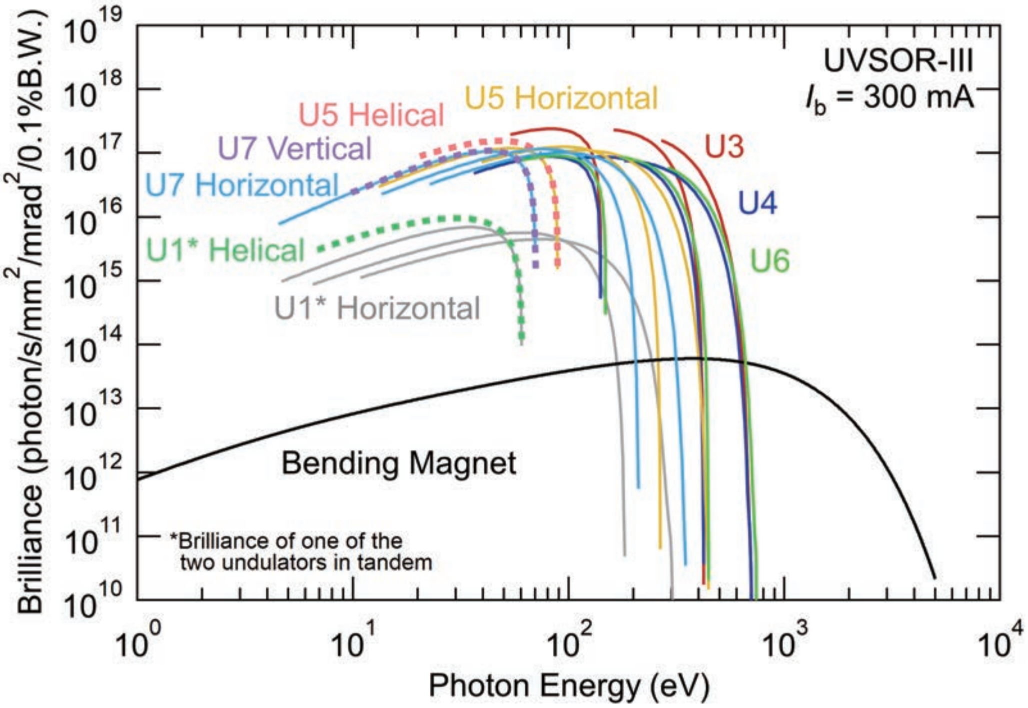

Brilliance of radiation from the insertion devices (U3, U4, U5, U6 and U7) and a bending magnet of UVSOR-III

U1 Apple-II Undulator / Optical Klystron

Number of Periods	10 + 10
Period Length	88 mm
Pole Length	0.968 m + 0.968 m
Pole Gap	24–200 mm
Deflection Parameter	7.36 (Max. Horizontal) 4.93 (Max. Vertical) 4.06 (Max. Helical)

U3 In-Vacuum Undulator

Number of Periods	50
Period Length	38 mm
Pole Length	1.9 m
Pole Gap	16.5–40 mm
Deflection Parameter	1.8–0.24

U4 In-Vacuum Undulator

Number of Periods	26
Period Length	38 mm
Pole Length	0.99 m
Pole Gap	13–40 mm
Deflection Parameter	2.4–0.19

Bending Magnets

Type	Combined ×8
Magnetic Length	1.728 m
Bending Radius	2.2 m
Bending Angle	45 deg.
Pole Gap	55.2 mm
Pole Width	140 mm
Critical Energy	425 eV

U5 Apple-II Variable Polarization Undulator

Number of Periods	38
Period Length	60 mm
Pole Length	2.28 m
Pole Gap	24–190 mm
Deflection Parameter	3.4 (Max. Horizontal) 2.1 (Max. Vertical) 1.8 (Max. Helical)

U6 In-Vacuum Undulator

Number of Periods	26
Period Length	38 mm
Pole Length	0.94 m
Pole Gap	13–40 mm
Deflection Parameter	2.1–0.19

U7 Apple-II Variable Polarization Undulator

Number of Periods	40
Period Length	76 mm
Pole Length	3.04 m
Pole Gap	24–200 mm
Deflection Parameter	5.4 (Max. Horizontal) 3.6 (Max. Vertical) 3.0 (Max. Helical)

(Last updated, August, 2025)

Beamlines in 2024

Fumihiko Matsui
UVSOR Synchrotron Facility, Institute for Molecular Science, Okazaki 444-8585, Japan

The UVSOR facility stands as a premier synchrotron radiation source, offering exceptional brilliance in the extreme-ultraviolet (EUV) region, particularly among facilities with electron energies below 1 GeV. A significant milestone was achieved in 2012 with the successful completion of the UVSOR-III storage ring upgrade project, which dramatically reduced the natural emittance to a low 17.5 nm-rad.

UVSOR currently provides synchrotron light from eight bending magnets and six insertion devices. The facility houses a total of thirteen operational beamlines. Among these, eleven are designated as “Public beamlines”, accessible to scientists from universities, government research institutes, private enterprises, and international collaborators. Beamline BL6U is an “In-house beamline”, exclusively dedicated to research groups within the Institute for Molecular Science and their collaborators. Beamline BL1U operates as a hybrid, serving both “Public” and “In-house” research.

As of 2024, the beamlines at UVSOR are configured as follows (details are also provided in the appended table on the next page):

- One tender X-ray (TX) station equipped with a double-crystal monochromator [**BL2A**].
- Six extreme ultraviolet (EUV) and soft X-ray (SX) stations equipped with grazing incidence monochromators [**3U**, **4U**, **4B**, **5U**, **5B**, **6U**].
- Three vacuum ultraviolet (VUV) stations equipped with normal incidence monochromators [**3B**, **7U**, **7B**].
- Two infrared (IR) stations equipped with Fourier Transform interferometers [**1B**, **6B**].
- One direct radiation station positioned after two tandem undulators [**1U**].

The latest information on the undulator beamline is detailed below.

BL1U: A Unique Beamline for VUV and Gamma Rays

At the **BL1U** beamline, novel light source development and gamma-ray utilization are actively being pursued. This beamline is uniquely equipped with tandem undulators featuring a buncher section. This sophisticated setup enables a range of advanced capabilities:

- Free electron laser operation spanning from the visible to deep UV regions.
- VUV coherent harmonic generation.
- The creation of spatiotemporal structured light, including optical vortex beams, vector beams, and double-pulsed wave packets.

Furthermore, BL1U boasts a femtosecond laser system precisely synchronized with the accelerator. This system is crucial for the generation of Compton scattered gamma-rays. UVSOR provides users with gamma-ray induced positron annihilation spectroscopy, a powerful technique for analyzing nanometer-scale defects within bulk materials. To significantly boost the counting rate of annihilation gamma rays, an array detector with eight BaF_2 scintillators has been developed. This advancement enables the completion of measurements on metal samples within just a few hours.

Since fiscal year 2022, a modification to the storage ring electron beam’s orbit has enabled continuous undulator light irradiation experiments at BL1U, significantly improving the efficiency of user operations.

BL3U: Advanced Soft X-ray Spectro-scopy for Soft-Matter Samples

At **BL3U**, significant progress has been made in low-energy X-ray absorption spectroscopy (XAS) with the development of an ultrathin-liquid cell. This innovation has enabled detailed studies of:

- The local structures of various aqueous solutions.
- Diverse chemical processes in solution, including catalytic and electrochemical reactions.
- Laminar flows in microfluidics, all demonstrated using operando XAS at the C, N, and O K-edges.

Furthermore, an argon gas window has been established, proving effective from 60 to 240 eV. This window, which also removes higher-order X-rays, is expected to significantly advance chemical research. It encompasses the K-edges of elements like Li and B, as well as the L-edges of Si, P, S, and Cl, opening new avenues for investigation.

Resonant soft X-ray scattering (RSoXS) for soft materials is also applicable at BL3U. Similar to small-angle X-ray scattering (SAXS), RSoXS provides valuable information on the mesoscopic structure (1-100 nm) of samples. This method offers crucial selectivity based on elements, functional groups, and molecular orientation. Given that the soft X-ray region includes the K-edge energies of light elements (C, N, O), RSoXS stands as a powerful tool for investigating soft matter.

During the first half of fiscal year 2024, a vacuum accident occurred due to a water leak from the cooling mechanism of the entrance slit. However, repairs have been completed, and we’ve confirmed that the performance, including soft X-ray intensity and resolution, has been restored to its previous levels. User beamtime that was canceled in the first half of fiscal year 2024 has been reallocated to the second half.

BL4U: STXM for Elemental and Chemical State Mapping

BL4U, equipped with a scanning transmission soft X-ray microscope (STXM), is a beamline that has been extensively utilized by both academic and industrial researchers. The STXM's versatility allows for its application across a wide range of scientific disciplines, including polymer science, materials science, cell biology, and environmental science.

We are currently investigating the potential of UVSOR to contribute to advancements in the life sciences through the exploitation of low photon energy techniques, particularly within the framework of the BL4U, leveraging soft X-ray spectromicroscopy.

BL5U: Enhancing Spin-Resolved ARPES Capabilities

At **BL5U**, high energy resolution angle-resolved photoemission spectroscopy (ARPES) is available to users. The latest version of the ARPES analyzer now allows for "deflector mapping" across all kinetic energies and lens modes, significantly enhancing experimental flexibility. Researchers can also investigate the spatial-dependence of electronic structures on solid surfaces using a micro-focused beam, which has a spot size of 50 µm.

To facilitate a wider range of experiments, an alkali-metal deposition system has been installed. This enables the deposition of materials like potassium onto samples while they remain mounted on the manipulator at low temperatures. As part of ongoing development in spin-resolved ARPES, two-dimensional images of the spin-resolved spectrum showing the Rashba splitting of the Au(111) surface have been successfully obtained.

In the latter half of fiscal year 2024, an automated spin target magnetization system was developed and implemented to enhance user access for spin-resolved Angle-Resolved Photoemission Spectroscopy (ARPES). This new system allows for free magnetization of the target via PC control.

While we currently offer spin-resolved ARPES measurements in two in-plane directions, the precise control afforded by the automated magnetization system has opened up the prospect of obtaining out-of-plane spin information from samples. Moving forward, we will be fine-tuning the final electron lens to achieve all-directional spin-resolved ARPES.

BL6U: Unveiling Electronic States with Momentum Microscopy

BL6U, one of UVSOR's in-house beamlines, now features and operates a photoelectron momentum microscope (PMM). This new-concept, multi-modal system offers high resolution in both real and momentum space for electronic structure analysis. A key advantage of the PMM is its ability to significantly reduce radiation-induced damage. It achieves this by directly projecting a single photoelectron constant energy contour in reciprocal space (with a radius of a few Å^{-1}) or real space (with a radius of a few hundred µm) onto a 2D detector.

Current experiments at BL6U include valence band photoelectron spectroscopy on the micrometer scale and resonant photoelectron diffraction using soft X-ray excitation. In FY2023, the PMM's capabilities were further expanded with the introduction of an additional 2D spin filter. This enhancement allowed for the successful acquisition of 2D images of the spin-resolved spectrum of the Rashba splitting on the Au(111) surface.

Beyond grazing-incidence soft X-ray excitation, a normal-incidence vacuum ultraviolet (VUV) beam with variable polarizations (horizontal/ vertical) has also become available at the PMM's focal position. The beamline was configured to use both BL6U and BL7U (branch) as light sources, allowing us to irradiate the same sample position with both beams. Performing full solid-angle photoelectron spectroscopy measurements using direct incidence linear polarization from 6 to 26 eV is now capable. This highly symmetrical measurement geometry completely eliminates the p-polarized linear dichroism effect in circular dichroism measurements of the valence band, significantly simplifying and increasing the reliability of transition matrix element analysis. However, since it is necessary to ensure sufficient activity at BL7U, advanced use of this configuration is currently only possible during limited hours and under coordination within the facility.

BL7U: A World-Class Beamline for High-Resolution ARPES

BL7U offers high-energy resolution angle-resolved photoemission spectroscopy (ARPES), allowing for experiments with exceptionally low photon energies, starting from 6 eV. This is facilitated by a low-temperature 6-axis manipulator, which maintains sample temperatures between 4.5 K and 350 K.

In FY2021, a deflector-type detector was installed for the hemispherical analyzer. This upgrade, combined with automated manipulator control, enables effective 2D measurements. Users can now conduct highly sensitive investigations into the bulk electronic structure of solids. Furthermore, the ability to utilize low-excitation photon energies with high photoionization cross-sections allows for high-throughput measurements of molecular materials.

For those interested in utilizing UVSOR's open or in-house beamlines, it's recommended to first contact the appropriate beamline contact persons, whose details can be found on the next page. Applications for beamtime can be submitted through the **NOUS system** at https://nous.nins.jp/user/signin. All users are required to consult the beamline manuals and the UVSOR guidebook prior to conducting any experimental procedures. For the most up-to-date information on UVSOR, please visit the official website: http://www.uvsor.ims.ac.jp.

Beamlines at UVSOR

Beamline	Monochromator / Spectrometer	Energy Range	Targets	Techniques	Contact
BL1U	Light Source Development Gamma-ray FEL	2.5 - 82 eV		Irradiation (UV and Gamma-rays)	Y. Taira yostaira@ims.ac.jp
BL1B	Martin-Puplett FT-FIR	0.5 – 30 meV	Solid	Reflection Absorption	K. Tanaka k-tanaka@ims.ac.jp
BL2A	Double crystal	800 – 4 keV	Solid	Reflection Absorption	F. Matsui matui@ims.ac.jp
BL3U	Varied-line-spacing plane grating (Monk-Gillieson)	60 – 800 eV	Gas Liquid Solid	Absorption Photoemission Photon-emission	H. Iwayama iwayama@ims.ac.jp
BL3B	2.5-m off-plane Eagle	1.7 – 31 eV	Solid	Reflection Absorption Photon-emission	F. Matsui matui@ims.ac.jp
BL4U	Varied-line-spacing plane grating (Monk-Gillieson)	55 – 770 eV	Gas Liquid Solid	Absorption (Microscopy)	T. Araki araki@ims.ac.jp
BL4B	Varied-line-spacing plane grating (Monk-Gillieson)	25 eV – 1 keV	Gas Solid	Photoionization Photodissociation Photoemission	H. Iwayama iwayama@ims.ac.jp
BL5U	Varied-line-spacing plane grating (Monk-Gillieson)	20 – 220 eV	Solid	Photoemission	K. Tanaka k-tanaka@ims.ac.jp
BL5B	Plane grating	6 – 600 eV	Solid	Calibration Absorption	K. Tanaka k-tanaka@ims.ac.jp
BL6U*	Variable-included-angle varied-line-spacing plane grating	40 – 700 eV	Solid	Photoelectron Momentum Microscopy	F. Matsui matui@ims.ac.jp
BL6B	Michelson FT-IR	4 meV – 2.5 eV	Solid	Reflection Absorption IR microscope	K. Tanaka k-tanaka@ims.ac.jp
BL7U	10-m normal incidence (modified Wadsworth)	6 – 40 eV	Solid	Photoemission	K. Tanaka k-tanaka@ims.ac.jp
BL7B	3-m normal incidence	1.2 – 25 eV	Solid	Reflection Absorption Photon-emission	F. Matsui matui@ims.ac.jp

Yellow columns represent undulator beamlines.

***In-house beamlines**

BL1U

Light Source Development Station

▼Description

BL1U is dedicated for developments and applications of novel light sources. This beamline is equipped with a dedicated tandem undulator for variable polarization with a buncher section, which can be used for free electron laser in the range from visible to deep UV, VUV coherent harmonic generation (CHG), and generation of spatiotemporal structured light such as an optical vortex beam, a vector beam and double-pulse wave packets. It is also equipped with a femto-second laser system synchronized with the accelerator, which is used for the generation of CHG, laser Compton scattered gamma-rays, and coherent THz radiation. Nowadays, material analysis by positron annihilation spectroscopy using laser Compton scattered gamma rays is actively used.

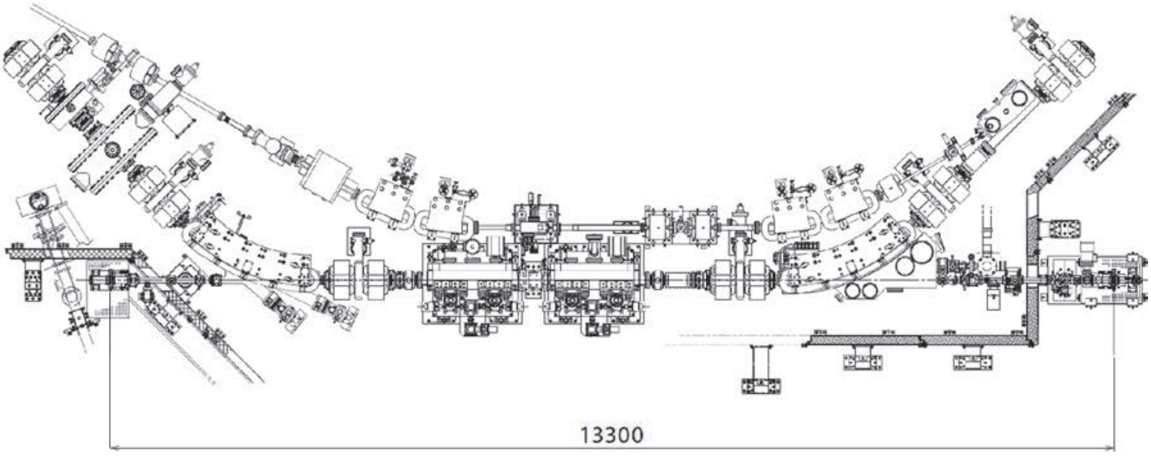

Fig. 1. Configuration of the free electron laser.

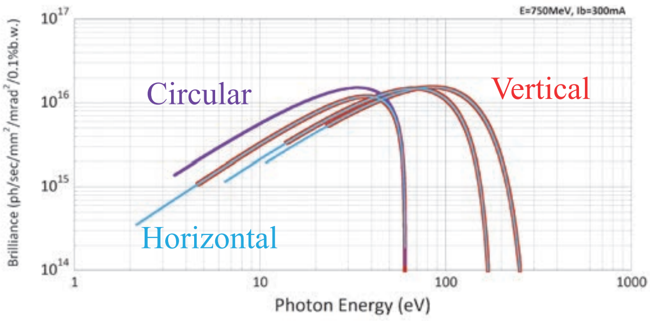

Fig. 2. Brilliance of BL1U Apple-II Undulator.

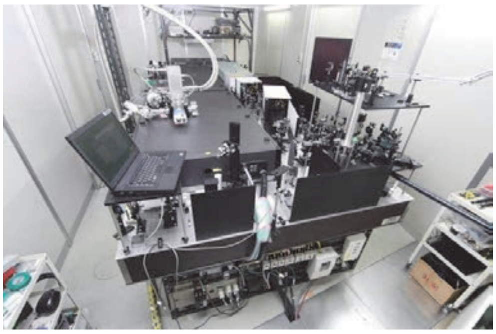

Fig. 3. Accelerator synchronized Laser System.

▼Technical Data of FEL

Wave Length	199-800 nm
Spectral Band Width	~10^{-4}
Polarization	Circular/Linear
Pulse Rate	11.26 MHz
Max. Ave. Power	~1 W

▼Technical Data of Ti:Sa Laser

Wave Length	800 nm		
Pulse Length	130 fsec		
Oscillator	90.1 MHz		
Pulse Energy	2.5 mJ	10 mJ	50 mJ
Repetition Rate	1 kHz	1 kHz	10 Hz

BL1B

Terahertz Spectroscopy Using Coherent Synchrotron Radiation

▼Description

Coherent synchrotron radiation (CSR) is a powerful light source in the terahertz (THz) region. This beamline has been constructed for basic studies on the properties of THz-CSR. However, it can be also used for measurements of reflectivity and transmission spectra of solids using conventional synchrotron radiation.

The emitted THz light is collected by a three-dimensional magic mirror (3D-MM, M0) of the same type as those already successfully installed at BL43IR in SPring-8 and BL6B in UVSOR-II. The 3D-MM was installed in bending-magnet chamber #1 and is controlled by a 5-axis pulse motor stage (x, z translation; θ_x, θ_y, θ_z rotation). The acceptance angle was set at 17.5-34 degrees (total 288 mrad) in the horizontal direction. The vertical angle was set at ±40 mrad to collect the widely expanded THz-CSR.

The beamline is equipped with a Martin-Puplett type interferometer (JASCO FARIS-1) to cover the THz spectral region from 4 to 240 cm^{-1} ($h\nu$ = 500 μeV-30 meV). There is a reflection/absorption spectroscopy (RAS) end-station for large samples (~ several mm). At the RAS end-station, a liquid-helium-flow type cryostat with a minimum temperature of 4 K is installed.

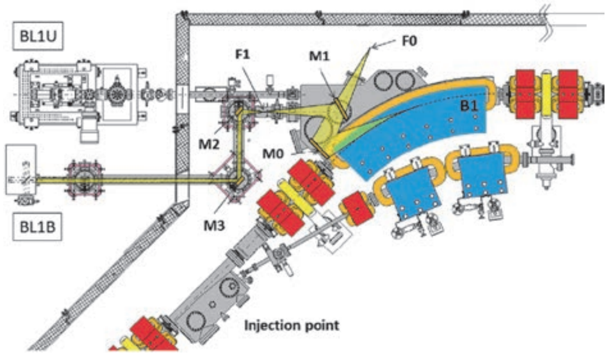

Fig. 1. Schematic top view of the beam extraction part of the THz-CSR beamline, BL1B. The three-dimensional magic mirror (3D-MM, M0) and a plane mirror (M1) are located in the bending-magnet chamber. A parabolic mirror (M2) is installed to form a parallel beam. The straight section (BL1U) is used for coherent harmonic generation (CHG) in the VUV region.

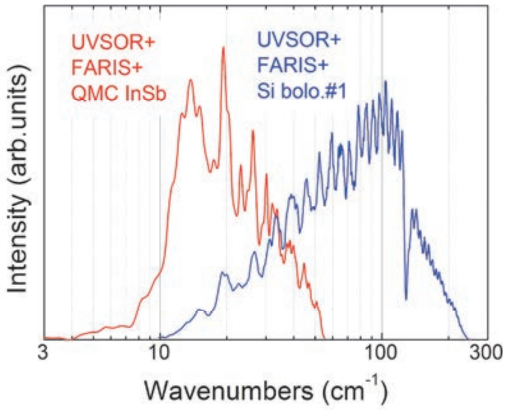

Fig. 2. Obtained intensity spectra with the combination of a light source (UVSOR), interferometer (FARIS-1), and detectors (Si bolometer and InSb hot-electron bolometer).

▼Technical Data

Interferometer	Martin-Puplett (JASCO FARIS-1)
Wavenumber range (Energy range)	4-240 cm^{-1} (500 μeV-30 meV)
Resolution in cm^{-1}	0.25 cm^{-1}
Experiments	Reflection/transmission spectroscopy
Miscellaneous	Users can use their experimental system in this beamline.

BL2A

Soft X-Ray Beamline for Photoabsorption Spectroscopy

▼Description

BL2A is a soft X-ray beamline for photoabsorption spectroscopy. The beamline is equipped with a pre-focusing mirror and a double-crystal monochromator [1]. The monochromator serves soft X-rays in the energy region from 585 to 4000 eV using several types of single crystals, such as beryl, KTP ($KTiOPO_4$), and InSb. The throughput spectra measured using a Si photodiode (AXUV-100, IRD Inc.) are shown in Fig. 1. The typical energy resolution (E / ΔE) of the monochromator is approximately 1500 for beryl and InSb.

There is a small vacuum chamber equipped with an electron multiplier (EM) detector. Photoabsorption spectra for powdery samples are usually measured in total electron yield mode, with the use of the EM detector. In addition, a hemispherical electron analyzer for photoelectron spectroscopy is equipped.

Recently, a new omnidirectional photoelectron acceptance lens (OPAL) has been developed aiming to realize 2π-steradian photoelectron spectroscopy and photoelectron holography [2]. By combining OPAL and the existing hemispherical electron analyzer, a photoelectron spectrometer with high energy resolution can be realized, and a full range (±90°) 1D angular distribution can be measured at once. This upgrade is currently in the commissioning phase.

[1] Hiraya *et al.*, Rev. Sci. Instrum. **63** (1992) 1264.
[2] H. Matsuda and F. Matsui, Jpn. J. Appl. Phys. **59** (2020) 046503.

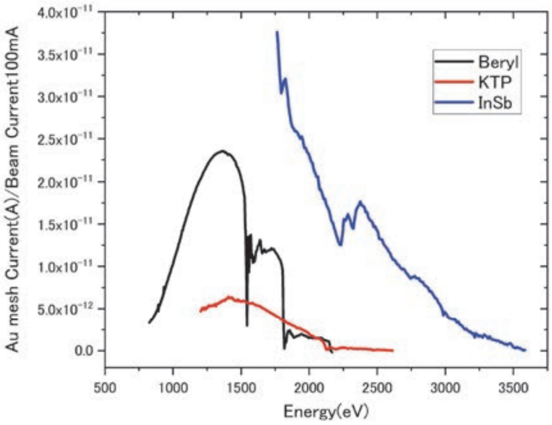

Fig. 1. Throughput spectra of the double-crystal monochromator at BL2A.

▼Technical Data

Monochromator	Double crystal monochromator
Monochromator crystals: (2d value, energy range)	beryl (15.965 Å, 826–2271 eV), KTP (10.95 Å, 1205–3310 eV), InSb (7.481 Å, 1764–4000 eV), Ge (6.532 Å, 2094–4000 eV)
Resolution	$E/\Delta E$ = 1500 for beryl and InSb
Experiments	Photoabsorption spectroscopy (total electron yield using EM and partial fluorescence yield using SDD)

BL3U

Varied-Line-Spacing Plane Grating Monochromator for Molecular Soft X-Ray Spectroscopy

▼Description

The beamline BL3U is equipped with an in-vacuum undulator composed of 50 periods of 3.8 cm period length. The emitted photons are monochromatized by the varied-line-spacing plane grating monochromator (VLS-PGM) designed for various spectroscopic investigations in the soft X-ray range. Three holographically ruled laminar profile plane gratings are designed to cover the photon energy range from 40 to 800 eV. The beamline has liquid cells for soft X-ray absorption spectroscopy (XAS) in transmission mode as shown in Fig. 1. The liquid cell is in the atmospheric helium condition, which is separated by a 100 nm thick Si_3N_4 membrane with the window size of 0.2 × 0.2 mm^2 from the beamline in an ultrahigh vacuum condition. The thin liquid layer is assembled by using two 100 nm thick Si_3N_4 membranes. The thickness of the liquid layer is controllable from 20 to 2000 nm by adjusting the helium pressures around the liquid cell in order to transmit soft X-rays. Liquid samples are exchangeable *in situ* by using a tubing pump. The liquid cell has two types of windows: one is the liquid part to obtain the soft X-ray transmission of liquid (I), and the other is the blank part to obtain the transmission without liquid (I_0). We can obtain the reliable XAS spectra based on the Lambert-Beer law $\ln(I_0/I)$. Since the liquid cell is in the atmospheric condition, we can measure XAS of liquid samples in the real environment. *Operando* XAS observation of several chemical reactions such as catalytic, electrochemical reactions are also possible by using our liquid cells developed for these purposes.

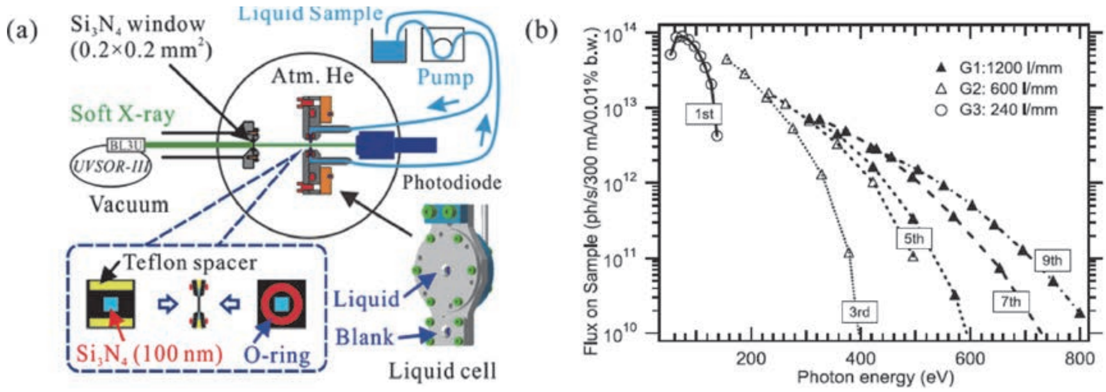

Fig. 1. (a) Schematics of a liquid cell for XAS in transmission mode settled in BL3U. The blowup shows a thin liquid layer assembled by two Si_3N_4 membranes with the thickness of 100 nm. (b) Flux at the sample position with the resolving power of $\lambda/\Delta\lambda=10^4$.

▼Technical Data

Monochromator	Varied-line-spacing plane grating monochromator
Energy Range	40-800 eV
Resolution	$E / \Delta E > 10\ 000$
Experiments	Soft X-ray absorption spectroscopy of liquid in transmission mode

BL3B (HOTRLU)

VIS-VUV Photoluminescence and Reflection/Absorption Spectroscopy

▼Description

BL3B has been constructed to study photoluminescence (PL) in the visible (VIS) to vacuum ultraviolet (VUV) region. This beamline consists of a 2.5 m off-plane Eagle type normal-incidence monochromator, which covers the VUV, UV, and VIS regions, i.e., the energy (wavelength) region of 1.7-31 eV (40-730 nm), with three spherical gratings having constant grooving densities of 1200, 600, and 300 l/mm optimized at the photon energies of ~20, ~16, and ~6 eV, respectively. The schematic side view and top view layouts are shown in Figs. 1(a) and 1(b), respectively. The FWHM of the beam spot at the sample position is 0.25 mm (V) × 0.75 mm (H). Low energy pass filters (LiF, quartz, WG32, OG53) can be inserted automatically to maintain the optical purity in the G3 (300 l/mm) grating region (1.7~11.8 eV). Figure 2 shows the throughput spectra (photon numbers at a beam current of 300 mA) for each grating with entrance and exit slit openings of 0.1 mm (resolving power E / ΔE of ~2000 (G3, ~6.8 eV)). Since both slits can be opened up to 0.5 mm, a monochromatized photon flux of 10^{10} photons/s or higher is available for PL measurements in the whole energy region.

The end station is equipped with a liquid-helium-flow type cryostat for sample cooling and two detectors; one of which is a photomultiplier with sodium salicylate and the other a Si photodiode for reflection/absorption measurement. For the PL measurements in the wide energy region from VIS to VUV, two PL monochromators, comprising not only a conventional VIS monochromator but also a VUV monochromator with a CCD detector, are installed at the end station.

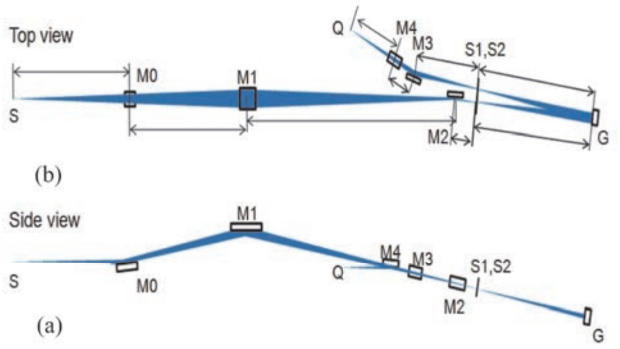

Fig. 1. Schematic layout of the BL3B (a) side view and (b) top view.

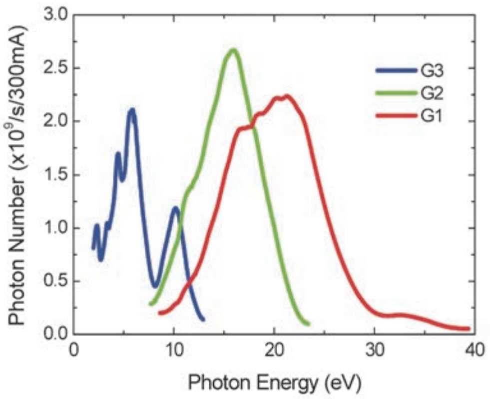

Fig. 2. Throughput spectra for each grating (G1:1200 l/mm, G2:600 l/mm and G3:300 l/mm) with S1 = S2 = 0.1 mm.

▼Technical Data

Monochromator	2.5 m normal-incidence monochromator
Energy range	1.7-31 eV (40~730 nm)
Resolution ($\Delta h\nu / h\nu$)	≥12000 (at ~ 6.9 eV, 0.02 mm slits, G1 (1200 l/mm)
Experiments	Photoluminescence, reflection, and absorption spectroscopy, mainly for solids

BL4U

Scanning Transmission X-ray Microscopy in the Soft X-ray Region

▼Description

In the soft x-ray region, there are several absorption edges of light elements and transition metals. The near edge X-ray absorption fine structure (NEXAFS) brings detailed information about the chemical state of target elements. A scanning transmission X-ray microscope (STXM) in the soft X-ray region is a kind of extended technique of the NEXAFS with high spatial resolution. The STXM has a capability of several additional options, for example, *in-situ* observations, 3-dimensional observation by computed tomography and ptychography, by utilizing the characteristics of the X-rays. The STXM can be applied to several sciences, such as polymer science, material science, cell biology, environmental science, and so on.

This beamline equips an in-vacuum undulator, a varied-line-spacing plane grating monochromator and a fixed exit slit. The soft X-ray energy range from 50 to 770 eV with the resolving power ($E/\Delta E$) of 6,000 is available. The aperture size of the fixed exit slit determines not only the resolving power but also the size of a microprobe. A Fresnel zone plate is used as a focusing optical device through an order select aperture and its focal spot size of ~30 nm is available at minimum. An image is acquired by detecting intensities of the transmitted X-rays by a photomultiplier tube with scintillator with scanning a sample 2-dimensionally. By changing the energy of the incident beam, each 2-dimensional NEXAFS image is stacked. A main chamber of STXM is separated from the beamline optics by a silicon nitride membrane of 50-nm thickness; therefore, sample folders can be handled in vacuum or in helium.

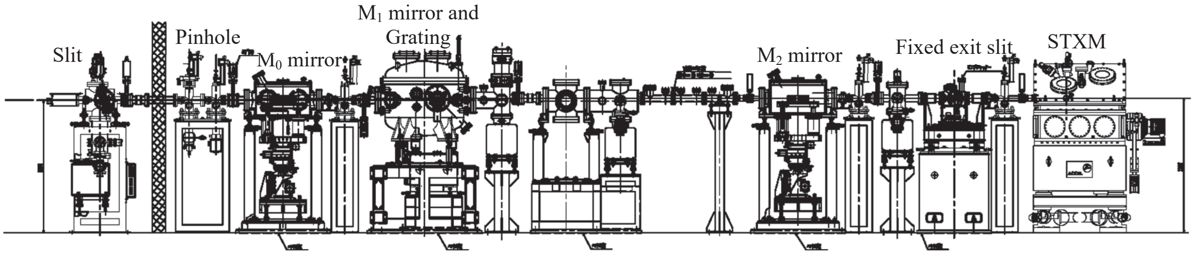

Fig. 1. Schematic image of BL4U.

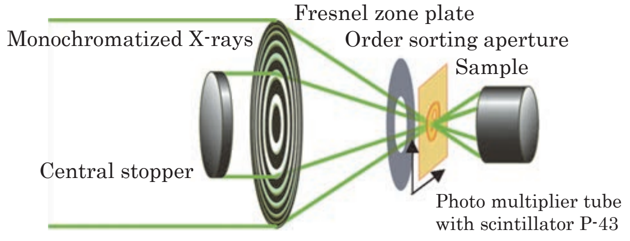

Fig. 2. Schematic image of STXM.

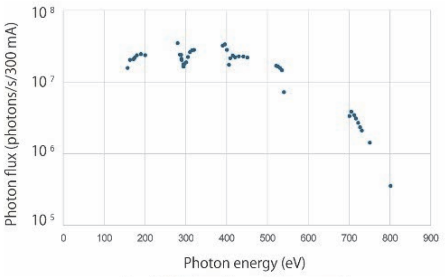

Fig. 3. Photon flux at the sample.

▼Technical Data

Energy range (E)	50 -770 eV
Resolving power ($E/\Delta E$)	~6,000
Photon flux on a sample (photons/s)	~2×10^7 @400 eV
Focusing optical element	Fresnel zone plate
Spatial resolution	~30 nm
Experiments	2-dimensional absorption spectroscopy
Measurement environment	Standard sample folder in vacuum or in helium, specially designed sample cell in ambient condition

BL4B

Varied-Line-Spacing Plane Grating Monochromator for Molecular Soft X-Ray Spectroscopy

▼Description

The beamline BL4B equipped with a varied-line-spacing plane grating monochromator (VLS-PGM) was constructed for various spectroscopic investigations in a gas phase and/or on solids in the soft X-ray range. Three holographically ruled laminar profile plane gratings with SiO_2 substrates are designed to cover the photon energy range from 25 to 1000 eV. The gratings with groove densities of 100, 267, and 800 l/mm cover the spectral ranges of 25–100, 60–300, and 200-1000 eV, respectively, and are interchangeable without breaking the vacuum. Figure 1 shows the absolute photon flux for each grating measured using a Si photodiode (IRD Inc.), with the entrance- and exit-slit openings set at 50 and 50 µm, respectively. The maximum resolving power (E/ΔE) achieved for each grating exceeds 5000.

By switching spectrometers at the end station, XAFS, XMCD and ARPES measurements are mainly carried out. Taking advantage of the low photon flux and low electric noise environment, XAFS and ARPES measurements are performed for fragile materials such as organic molecules and polymers.

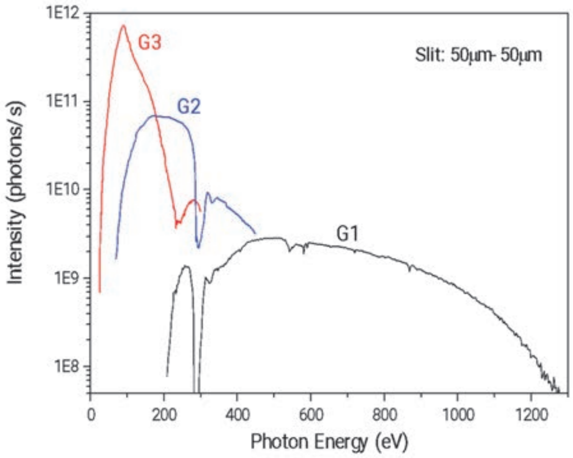

Fig. 1. Throughput from the VLS-PGM monochromator on BL4B.

Fig. 2. Photo of BL4B.

▼Technical Data

Monochromator	Varied-line-spacing Plane Grating Monochromator
Energy range	25-1000 eV
Resolution	$E / \Delta E > 5000$ (at maximum)
Experiments	X-ray absorption fine structure spectroscopy (XAFS) X-ray magnetic circular dichroism spectroscopy (XMCD) Angle-resolved photoemission spectroscopy (ARPES)

BL5U

Photoemission Spectroscopy of Solids and Surfaces

▼Description

Since the monochromator of BL5U was an old-style spherical grating type SGMTRAIN constructed in 1990s and the throughput intensity and energy resolution were poor, the whole beamline has been replaced to state-of-the-art monochromator and end station. The new beamline has been opened to users from FY2016 as high-energy resolution ARPES beamline. Samples can be cooled down to 3.8 K with newly developed 5-axis manipulator to perform high energy resolution measurements. Users can also obtain spatial-dependence of the electronic structure of solids using micro-focused beam (~ 50 µm). The new electron lens system makes it possible to obtain ARPES spectra without moving samples. This beamline will also have new capability to perform high-efficient spin-resolved ARPES in the future.

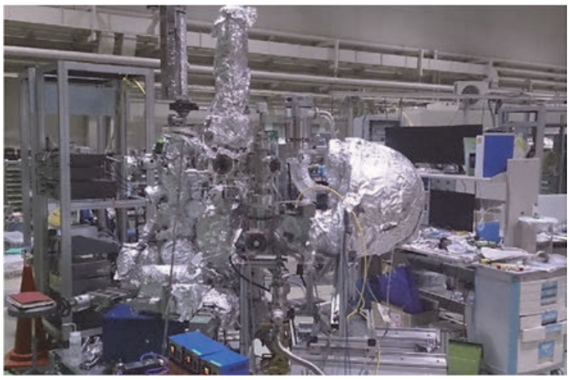

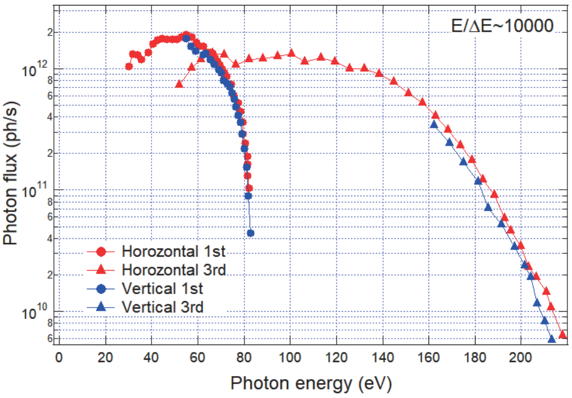

Fig. 1. Picture and photon flux of BL5U.

▼Technical Data (Expected Performance)

Light source	APPLE-II type undulator (λ_u = 60 mm, N = 38) vertical/horizontal, right/left circular (depending on *hv*)
Monochromator	Monk-Gillieson VLS-PGM
Energy Range	20-200 eV
Resolution	*hv*/ *ΔE* > 10,000 for < 10 µm slits
Experiment	ARPES, Space-resolved ARPES, Spin-resolved ARPES
Flux	$<10^{12}$ photons/s for <10 µm slits (at the sample position)
Beam spot size	23 (H) x 40 (V) µm
Main Instruments	Hemispherical photoelectron analyzer with deflector scan (MBS A-1 Lens#4), Liq-He flow cryostat with 5-axis manipulator (3.8 K-350 K)

BL5B

Calibration Apparatus for Optical Elements and Detectors

▼Description

BL5B has been constructed to perform calibration measurements for optical elements and detectors. This beamline is composed of a plane grating monochromator (PGM) and three endstations in tandem. The most upstream station is used for the calibration measurements of optical elements, the middle one for optical measurements for solids, and the last for photo-stimulated desorption experiments. The experimental chamber at the most downstream station is sometimes changed to a chamber for photoemission spectroscopy. The calibration chamber shown in Fig. 2 is equipped with a goniometer for the characterization of optical elements, which has six degrees of freedom, X-Y translation of a sample, and interchanging of samples and filters. These are driven by pulse motors in vacuum. Because the polarization of synchrotron radiation is essential for such measurements, the rotation axis can be made in either the horizontal or vertical direction (s- or p-polarization).

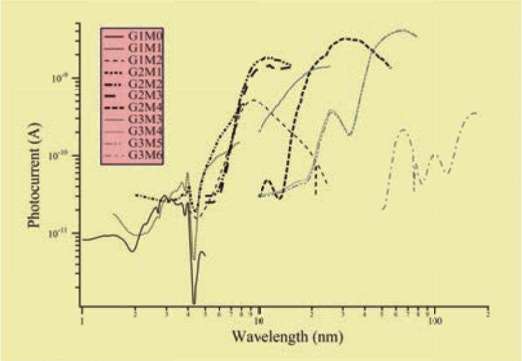

Fig. 1. Throughput spectra for possible combinations of gratings and mirrors at BL5B measured by a gold mesh.

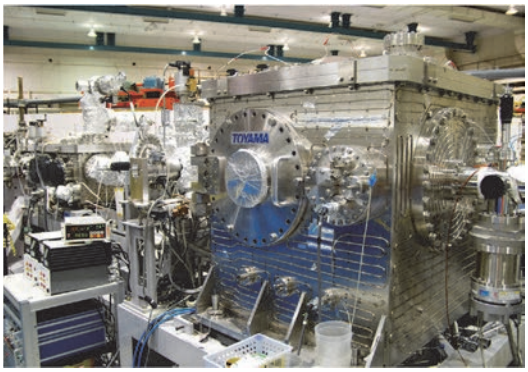

Fig. 2. A side view of the experimental chamber for calibration measurements.

▼Technical Data

Monochromator	Plane Grating Monochromator
Energy range	6-600 eV (2-200 nm)
Resolution	$E / \Delta E$ ~500
Experiments	Calibration of optical elements, reflection and absorption spectroscopy mainly for solids

BL6U

Variable-Included-Angle / Variable-Line-Spacing Plane Grating Monochromator for Soft X-Ray photoelectron Spectroscopy

▼Description

The beamline BL6U equipped with a variable-included-angle Monk-Gillieson mounting monochromator with a varied-line-spacing plane grating was constructed for various spectroscopic investigations requiring high-brilliance soft X-rays on solid surfaces. Through a combination of undulator radiation and sophisticated monochromator design (entrance slit-less configuration and variable-included-angle mechanism), using a single grating, the monochromator can cover the photon energy ranging from 40 to 500 eV, with resolving power of greater than 10000 and photon flux of more than 10^{10} photons/s. Figure 1 shows an example of the monochromator throughput spectra measured using a Si photodiode, with the exit-slit opening set at 30 µm, which corresponds to the theoretical resolving power of 10000 at 80 eV.

A new Momentum Microscope experimental station for photoelectron spectroscopy resolved in 3D momentum space with a microscopic field of view has been built at BL6U (SPECS KREIOS 150 MM). A momentum resolution of 0.01 Å^{-1} in $\boldsymbol{k}_x/\boldsymbol{k}_y$ as well as $\boldsymbol{k}_z$ is achieved. A spatial resolution of 50 nm, an energy resolution of 20 meV at 9 K, and a field of view of 2 µm for ARPES are successfully demonstrated. This experimental station specializes in characterizing the electronic structure of surface atomic sites, thin films, molecular adsorbates, and bulk crystals. This method opens the door to direct observation of the Fermi surface of µm-sized crystals, which was difficult with conventional ARPES-type hemispherical analyzers.

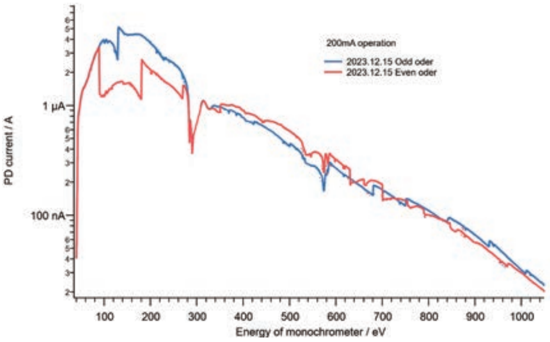

Fig. 1. Photodiode current after the BL6U monochromator versus photon energy.

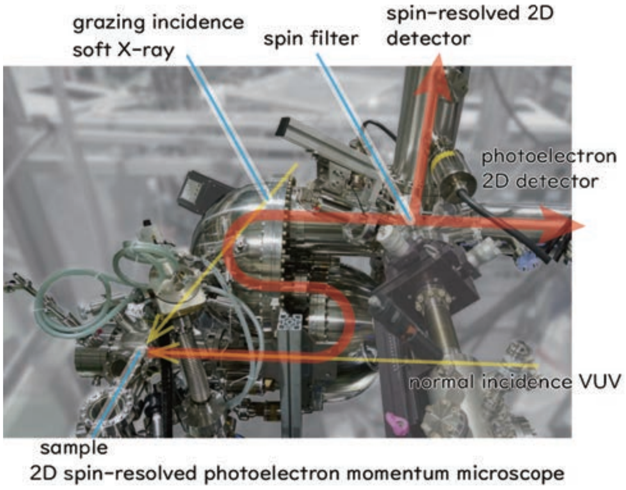

Fig. 2. Photograph of BL6U end station.

▼Technical Data

Monochromator	Variable-included-angle Varied-line-spacing Plane Grating Monochromator
Energy range	40-500 eV(practical)
Resolution	$E / \Delta E > 10000$ (at maximum)
Experiments	High-resolution soft X-ray spectroscopy (photoelectron spectroscopy for solid surfaces)

BL6B

Infrared and Terahertz Spectroscopy of Solids

▼Description

Synchrotron radiation (SR) has good performance (high brilliance and high flux) not only in the VUV and soft X-ray (SX) regions but also in the infrared (IR) and THz regions. BL6B covers the IR and THz regions. The previous beamline, BL6A1, which was constructed in 1985, was the pioneer in IRSR research. The beamline was deactivated at the end of FY2003 and a new IR/THz beamline, BL6B (IR), was constructed in FY2004. The front-end part including bending duct #6 was replaced with a new part having a higher acceptance angle (215 (H) × 80 (V) mrad^2) using a magic mirror, as shown in Fig. 1.

There are two Michelson type interferometers in this endstation; with first one (Bruker Vertex70v), which covers a wide spectral region from 30 to 20,000 cm^{-1} ($h\nu = 4$ meV-2.5 eV), reflection/absorption spectroscopy measurements of large samples (up to several mm) and IR/THz microscopy measurements of tiny samples (up to several tens of μm) can be performed. For reflection/absorption spectroscopy measurements, a liquid-helium- flow type cryostat with a minimum temperature of 4 K is installed. The other interferometer (Jasco FT/IR-6100), which covers 350 to 15,000 cm^{-1} ($h\nu = 45$ meV-1.8 eV), has been available for IR microscopy imaging measurements from FY2014. One can also perform ATR measurements using diamond ATR prism.

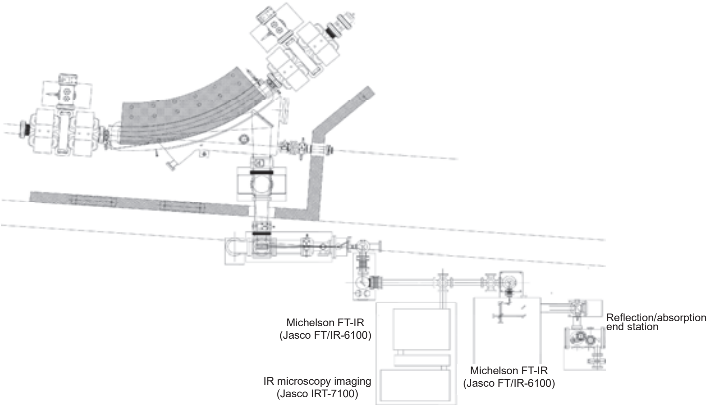

Fig. 1. Schematic top view of BL6B.

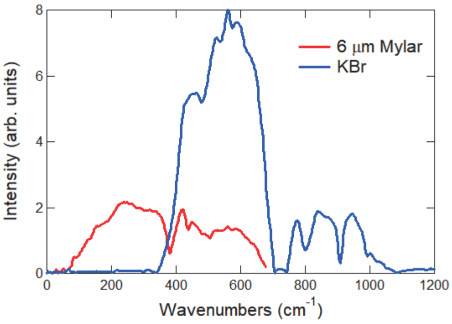

Fig. 2. Obtained intensity spectra with the combination of a light source (UVSOR), detector (Si bolometer), and interferometer (Bruker Vertex70v) with different beamsplitters (6 μm Mylar and KBr) . (Only low energy side is shown).

▼Technical Data

Interferometer	Michelson (Bruker Vertex70v)	Michelson (Jasco FT/IR-6100)
Wavenumber Range (Energy range)	30-20,000 cm^{-1} (4 meV-2.5 eV)	350-15,000 cm^{-1} (45 meV-1.8 eV)
Resolution in cm^{-1}	0.1 cm^{-1}	0.5 cm^{-1}
Experiments	Reflectivity and transmission spectroscopy THz Microspectroscopy	IR microscopy imaging (JASCO IRT-7000) ATR spectroscopy

BL7U (SAMRAI)

Angle-Resolved Photoemission of Solids in the VUV Region

▼Description

Beamline 7U, named the Symmetry- And Momentum-Resolved electronic structure Analysis Instrument (SAMRAI) for functional materials, was constructed to provide a photon flux with high energy resolution and high flux mainly for high-resolution angle-resolved photoemission spectroscopy, so-called “ARPES”, of solids [1]. An APPLE-II-type variable-polarization undulator is installed as the light source. The undulator can produce intense VUV light with horizontal/vertical linear and right/left circular polarization. The undulator light is monochromatized by a modified Wadsworth type monochromator with three gratings (10 m radius; 1200, 2400, and 3600 lines/mm optimized at $h\nu = 10$, 20, and 33 eV). The energy resolution of the light ($h\nu/\Delta h\nu$) is more than 10^4 with a photon flux of 10^{11}-10^{12} ph/s or higher on samples in the entire energy region. The beamline has a photoemission end-station equipped with a 200 mm-radius hemispherical photoelectron analyzer (MB Scientific AB, A-l analyzer) with a wide-angle electron lens and a liquid-helium-cooled cryostat with 6-axis pulse motor control. The main function of the beamline is to determine the electronic structure of solids and its temperature dependence in order to reveal the origin of their physical properties.

[1] S. Kimura *et al*., Rev. Sci. Instrum. **81** (2010) 053104.

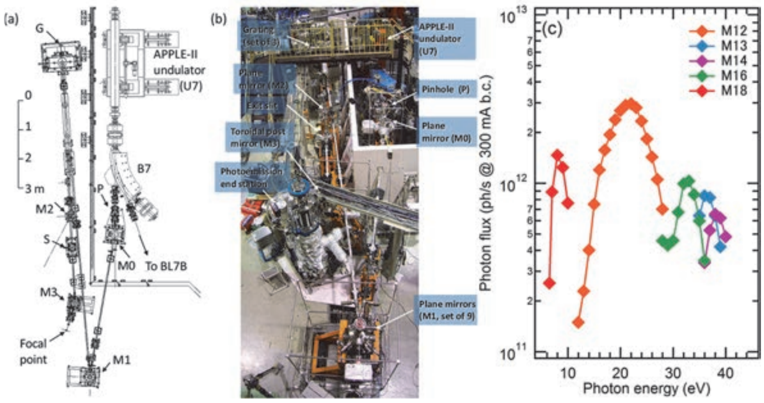

Fig. 1. SAMRAI beamline [(a), (b)] consisting of an APPLE-II type undulator (U7), a modified Wadsworth type monochromator (M0-S), and a high-resolution photoemission analyzer at the focal point. The monochromator has five major optical components: two plane mirrors (M0 and M1) with water cooling, one set of three spherical gratings (G), an exit slit (S), and one toroidal refocusing mirror (M3). (c) Example of flux intensity *versus* photon energy [1].

▼Technical Data

Light source	APPLE-II type undulator ($\lambda_u = 76$ mm, N = 36) vertical/horizontal, right/left circular (depending on $h\nu$)
Monochromator	10 m normal-incidence monochromator (modified Wadsworth type)
Photon energy range	6 – 40 eV ($\lambda = 30 – 200$ nm)
Resolution ($h\nu/\Delta h\nu$)	$E / \Delta E > 10000$-50000
Photon flux on sample	$\geq 10^{11}$-10^{12} ph/s (depending on $h\nu$)
Beam size on sample	200 (H) × 50 (V) μm^2
Experiments	Angle-resolved photoemission of solids (MV Scientific A-1 analyzer, acceptance angle: ± 18 deg)

BL7B

3 m Normal-Incidence Monochromator for Solid-State Spectroscopy

▼Description

BL7B has been constructed to provide sufficiently high resolution for conventional solid-state spectroscopy, sufficient intensity for luminescence measurements, wide wavelength coverage for Kramers–Kronig analyses, and minimum deformation to the polarization characteristic of incident synchrotron radiation. This beamline consists of a 3-m normal incidence monochromator, which covers the vacuum ultraviolet, ultraviolet, visible, and infrared, i.e., the wavelength region of 50–1000 nm, with three gratings (1200, 600, and 300 l/mm). Two interchangeable refocusing mirrors provide two different focusing positions. For the mirror with the longer focal length, an LiF or a MgF_2 window valve can be installed between the end valve of the beamline and the focusing position. Figure 1 shows the absolute photon intensity for each grating with the entrance and exit slit openings of 0.5 mm. A silicon photodiode (AXUV-100, IRD Inc.) was utilized to measure the photon intensity and the absolute photon flux was estimated, taking the quantum efficiency of the photodiode into account.

The cooling system for the pre-focusing mirror has been removed, resulting in longer beam settling times. Currently, BL7B is opened during single bunch mode, but limited use is possible during multi bunch mode.

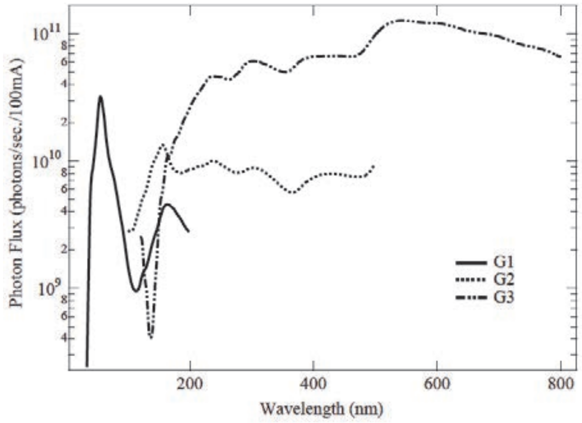

Fig. 1. Throughput spectra of BL7B measured using a silicon photodiode.

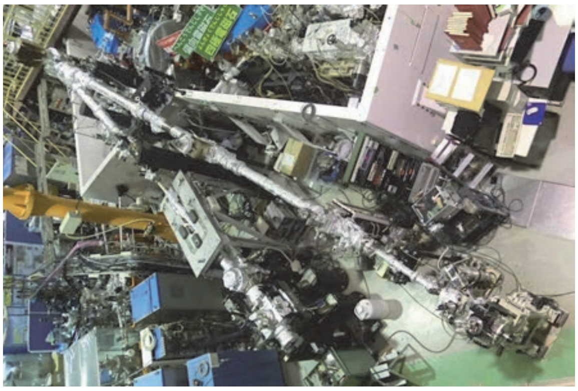

Fig. 2. Photo of BL7B.

▼Technical Data

Monochromator	3 m Normal-Incidence Monochromator
Wavelength Range	50-1000 nm (1.2-25 eV)
Resolution	$E / \Delta E$ = 4000-8000 for 0.01 mm slits
Experiments	Absorption, reflection, and fluorescence spectroscopy, mainly for solids

UVSOR User 5

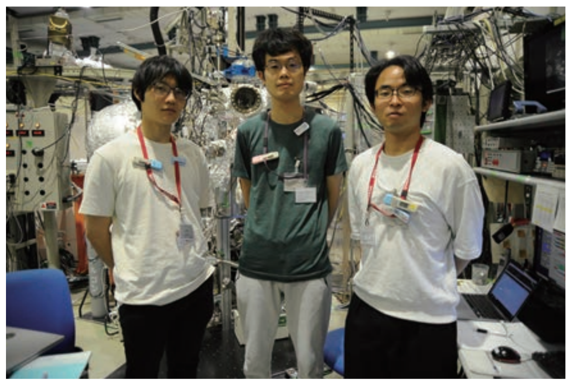
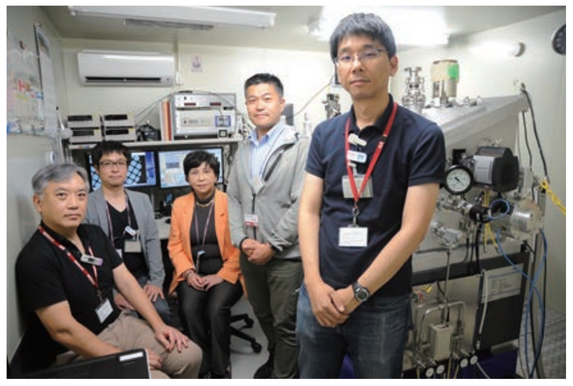
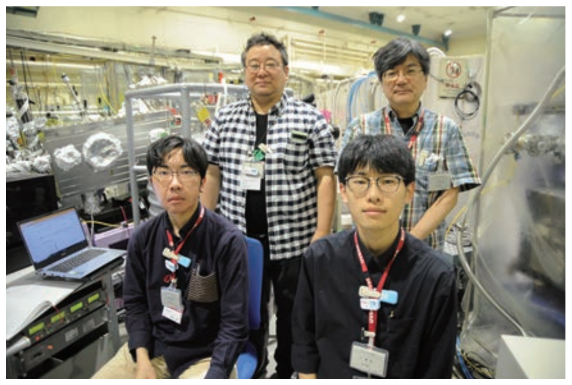
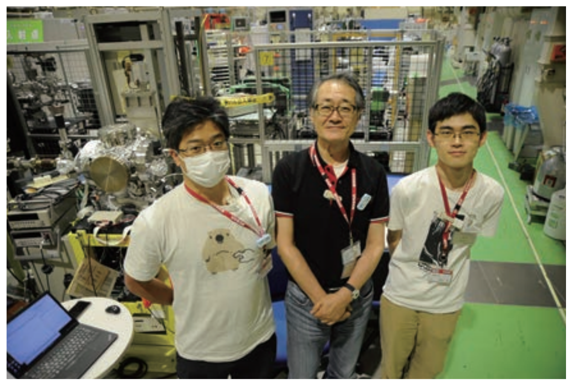
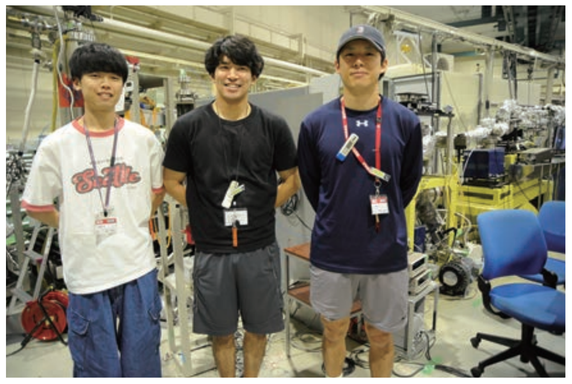

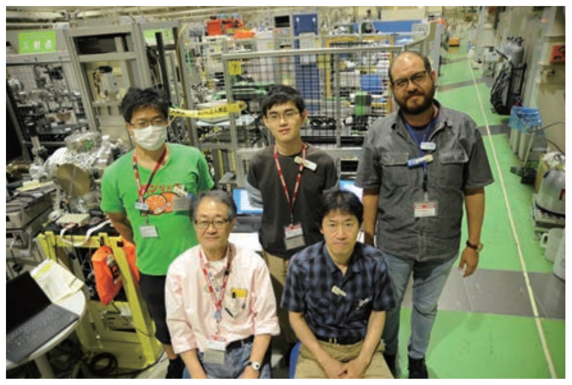
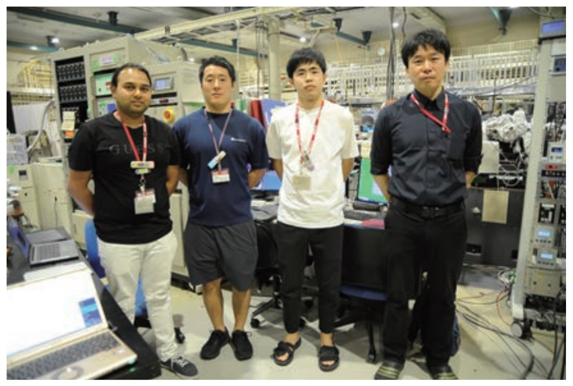

III

High light

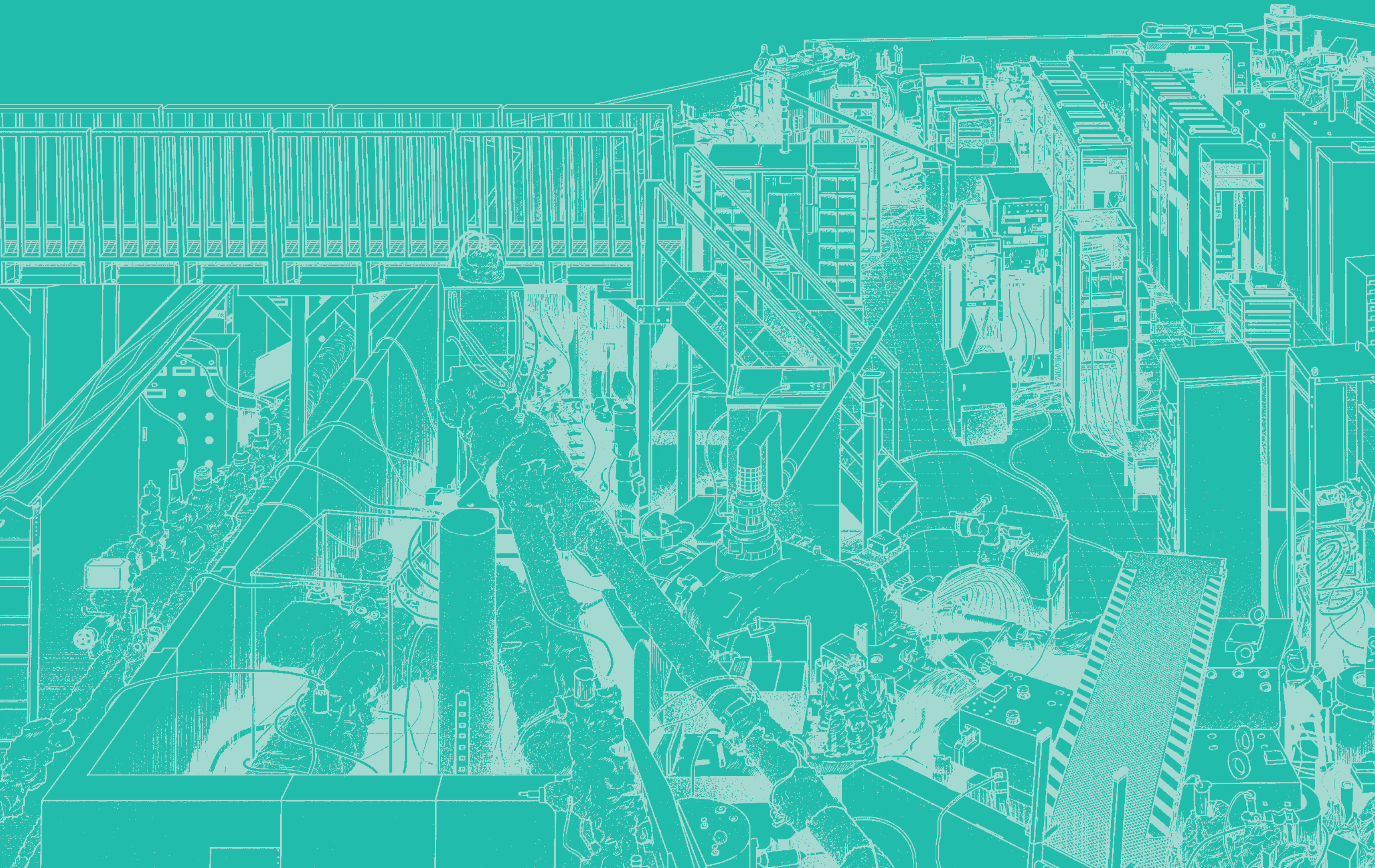

BL1U

Change in Positron Lifetime of Tensile-Deformed Pure Iron after Stress Release and Room-Temperature Aging

M. Fujinami[1], R. Awaji[1], H. Abe[1], A. Yabuuchi[2], T. Hirade[3], N. Oshima[4] and Y. Taira[5]
[1]Department of Applied Chemistry and Biotechnology, Chiba University, Chiba 263-8522, Japan
[2]Institute for Integrated Radiation and Nuclear Science, Kyoto University, Kumatori 590-0494, Japan
[3]Nuclear Science and Engineering Center, Japan Atomic Energy Agency, Tokai 319-1195, Japan
[4]National Institute of Advanced Industrial Science and Technology, Tsukuba 305-8568, Japan
[5]UVSOR Synchrotron Facility, Institute for Molecular Science, Okazaki 444-8585, Japan

Understanding the formation of lattice defects in metals not only while applying deformation stress but also after releasing stress and subsequent aging is essential for accurately assessing the durability of structural materials. Positron annihilation lifetime spectroscopy (PALS) is an effective technique for examining vacancy-type defects within crystalline materials [1]. Nevertheless, measuring the positron lifetime in metals while applying deformation stress presents significant challenges when using conventional PALS techniques. As a result, most previous studies have conducted positron lifetime measurements on deformed metals only after the deformation stress has been released. It should be noted that the properties of defects within metals may undergo alterations when the deformation stress is released. This study applied PALS to a pure iron specimen subjected to tensile deformation, using the gamma-ray-induced PALS (GiPALS) technique [2].

A well-annealed pure iron specimen (99.99% purity) was elongated to ~7% nominal strain using a small tensile tester installed at the BL1U beamline (Fig. 1). The thickness and gauge width of the test piece were 3 mm and 6 mm, respectively. Positron lifetime measurements were conducted at three different stages following the deformation: (1) under applied stress after elongation, (2) after releasing the tensile stress, and (3) after 3 days at room temperature following the stress release. The results revealed significant changes in the longer positron lifetime component (associated with defect species) across the three conditions. In addition, the intensity of the defect component (I_2) changed from approximately 45% under stress to 60% immediately after unloading, and then decreased to 28% after 3 days of room-temperature aging (Fig. 2).

These findings suggest that tensile stress release leads to additional defect formation, while subsequent room temperature aging facilitates partial defect recovery. Therefore, it is essential to consider both stress release effects and room-temperature aging when characterizing defect structures in deformed metals. This highlights the importance of in situ characterization in studies of deformed structural materials.

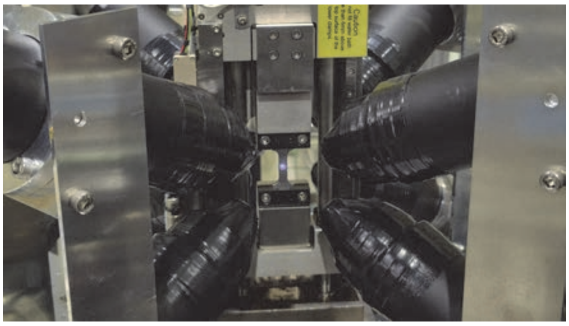

Fig. 1. A view of a small tensile tester installed at the BL1U beamline with a tensile test piece attached.

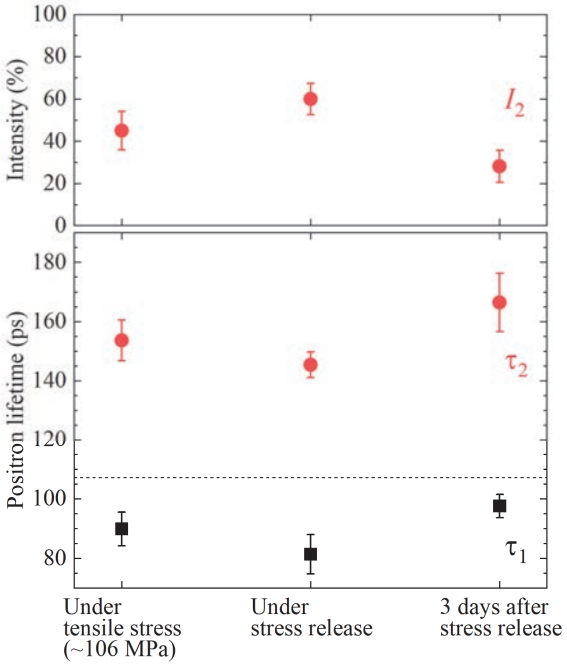

Fig. 2. Positron lifetimes and their intensities of elongated pure iron. The results are shown for the same specimen while applying stress, after releasing the stress, and after aging at room temperature for 3 days. The positron lifetime of the specimen before elongation is also depicted by the dashed line.

[1] R. W. Siegel, Annu. Rev. Mater. Sci. **10** (1980) 393.
[2] Y. Taira *et al.*, Rev. Sci. Instrum. **93** (2022) 113304.

BL3U

X-ray Absorption Spectra of Lipid Bilayer Membranes in Electrolyte Solutions and Its Dependence on Cation Species

R. Tero [1], Yu Kinjo[1] and M. Nagasaka[2]
[1]*Toyohashi University of Technology, Toyohashi 441-8580, Japan*
[2]*Institute for Molecular Science, Okazaki 444-8585, Japan*

The lipid bilayer is a self-assembled structure of amphiphilic lipid molecules. It is the fundamental structure of biomembranes such as cell membranes, which are the fields for the transportation of materials, information, and energy into and out of cells. All these physiological reactions proceed in the presence of electrolytes. Ions in the aqueous solution significantly influence physical properties and structures of lipid bilayers. Phosphatidylcholine (PC) is the most abundant lipid of eukaryotic cell membranes. Cations bind to the phosphate and carbonyl groups of PC. However, the affinity of cations to PC and effects of cations to molecular orientation are still controversy especially in the fields of theoretical simulations. We aim to determine the binding affinity of cations to lipids in aqueous solutions experimentally, by means of X-ray absorption spectroscopy (XAS) [1]. Recently, we measured the dependence of O-K edge XAS spectra of DOPC bilayer on Na^+ concentration in the aqueous solution [2, 3].

Supported lipid bilayers (SLBs) of dioleoyl-PC (DOPC) were formed on the Si_3N_4 membranes of the XAS flow cell [1] by the vesicle fusion method in a buffer solution (KCl 100 mM, HEPES 25 mM/ pH 7.4 KOH). The K^+ concentration ($[K^+]$) was varied by exchanging the buffer solution in the flow cell in in the range of $[K^+] = 2.1 – 510.4$ mM. The O-K edge XAS spectra of SLB were obtained at the energy range of 527 – 535 eV. The X-ray incident angle of 35º. The XAS spectrum of the Si_3N_4 membrane without SLB was subtracted from that with SLB.

The O-K-edge spectrum of DOPC appeared at 531 - 533 eV [2, 3]. It consists of 1s→π* transitions of double-bond oxygens in the phosphate and carbonyl groups on the PC headgroup: two components attributed to the P=O in the former, and one component attributed to the latter. We measured XAS spectra at the X-ray incident angle (T) of 35º. We obtained a specific dependence of the P=O peak at the lower energy on $[K^+]$: its position was little affected by $[Na^+]$ in the range of 2.1 – 10.4 mM and shifted to higher energy by ~0.4 eV at $[K^+] = 20.4$ mM, while the position showed slight change at $[K^+] \geq 50.4$ mM. The former tendency at was similar to that of Na^+ at $[Na^+] \leq 20.4$ mM, but latter was different from the peak shift and broadening observed at $[Na^+] \geq 50.4$ mM [2, 3].

The inner-shell quantum chemical calculation [4] of O K-edge spectrum of P=O indicated that coordination of K^+ to the phosphate group causes higher-energy shift of P=O peaks. The XAS spectra shows the difference in the coordination affinity between K^+ and Na^+. The effects of the cation species on the XAS components will be evaluated by the theoretical calculations.

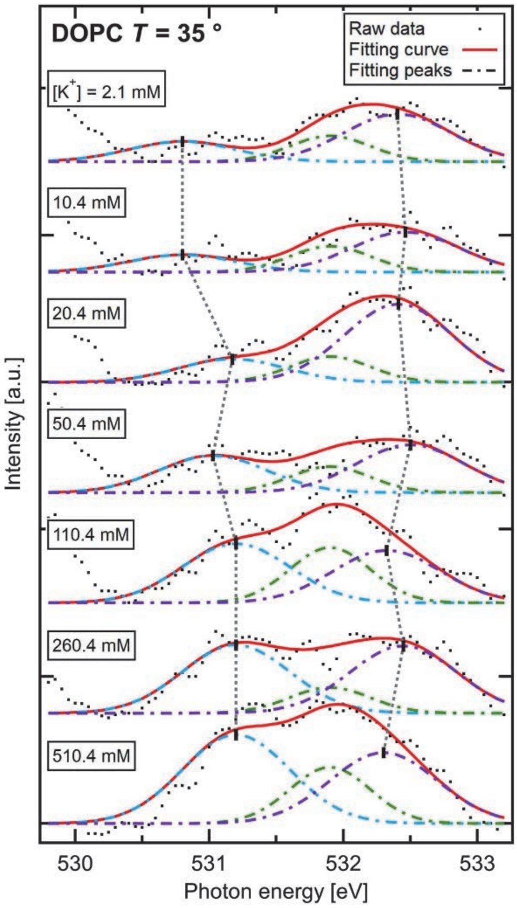

Fig. 1. O K-edge XAS spectra of DOPC-SLB at $[K^+] = 2.1 – 510.4$ mM obtained at the X-ray incident angle of 35°. Black dotted curves represent raw data. Dashed curves and red solid curves show deconvoluted components and their summation, respectively.

[1] M. Nagasaka *et al.* , J. Electron Spectros. Relat. Phenomena **224** (2018) 93.
[2] R. Tero, Y. Kinjo and M. Nagasaka, UVSOR Activity Report **50** (2022) 165.
[3] R. Tero, W.-Z. Goh and M. Nagasaka, UVSOR Activity Report **51** (2023) 174.

BL3B, 6B

Temperature-Dependent Electronic Structure Modification on an Altermagnet Candidate MnTe

S. Kimura[1,2,3], H. Watanabe[1,2], K. Yuan[2], Y. Pan[2], H. Ishida[2] and M.-H. Jung[4]
[1]Graduate School of Frontier Biosciences, The University of Osaka, Suita 565-0871, Japan
[2]Department of Physics, Graduate School of Science, The University of Osaka, Toyonaka 560-0043, Japan
[3]Institute for Molecular Science, Okazaki 444-8585, Japan
[4]Department of Physics, Sogang University, Seoul 04107, Republic of Korea

Recently, materials with antiferromagnetic and ferromagnetic characters, namely altermagnet, have attracted attention and are classified as the third magnetic material group [1]. The materials have no net magnetism, but owing to the crystal symmetry combined with the antiferromagnetic structure, there are two novel characteristics: a strong time-reversal symmetry-breaking response and the other spin-polarization phenomena typical of ferromagnets [2]. Thanks to their physical properties, the materials are considered helpful for spintronics devices [3].

One candidate for altermagnets is MnTe. The material has a Neel temperature of 307 K. The Spin-split band structure of the material has been observed with angle-resolved photoelectron spectroscopy (ARPES) [4, 5]. The experimental result is considered to be evidence of the altermagnet.

ARPES can detect the occupied electronic structure below the Fermi level (E_F), but it is impossible to observe the unoccupied state. Thus, the whole band picture cannot be probed by ARPES. On the other hand, optical conductivity (σ_1) spectra have information on the joint density of states between the occupied and unoccupied states. By the experimental characters, the combination of ARPES and σ_1 spectra provides information on the unoccupied states. Additionally, in-gap states with very low density can be observed with σ_1 spectra. Then, we measured σ_1 spectra of MnTe.

Reflection spectroscopy has been performed at BL3B from the visible to the VUV regions and at BL6B from the IR to the THz regions. The measurements were combined with the reflection spectra in the IR – visible region taken at the laboratory, and finally, whole reflectivity spectra in the photon energy of 8 meV – 40 eV were obtained. σ_1 spectra were obtained with the Kramers-Kronig analysis of the wide-range reflectivity spectra.

Figure 1 shows the temperature dependence of the σ_1 spectrum of MnTe near the energy gap at 1 eV. At 370 K, higher than T_N, a broad peak is visible at about 2.25 eV. As the temperature decreases, the peak shifts to the low energy side and narrows. The temperature dependence is almost consistent with a valence band peak observed in ARPES results [5]. However, the energy shift is about 0.2 eV, much smaller than the peak shift of 0.4 eV appearing in ARPES. To clarify the inconsistency, further band structure calculations are needed.

As shown in the inset of Fig. 1, the structural temperature change within the energy gap appearing at the low energy side is remarkable. With decreasing temperature, the intensity at around 0.5 eV decreases, while that below 0.2 eV increases. The former corresponds to the onset of the absorption edge shifting to the high energy side, which is the opposite behavior of the peak energy. This suggests that the band structure at the gap edge is modulated with decreasing temperature. The newly appeared peak below 0.2 eV suggests another localized electronic state emerges in the energy gap below T_N.

The observed characteristic temperature dependence in the σ_1 spectrum does not correspond to conventional antiferromagnetic materials; the spectral change can be regarded as originating from the band modification of altermagnetic character.

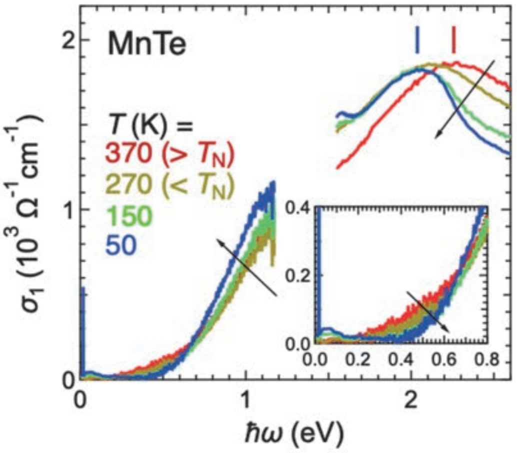

Fig. 1. Temperature-dependent optical conductivity [σ_1] spectra of MnTe near the energy gap. (Inset) The enlarged figure of the in-gap states.

[1] I. Mazin, Phys. Rev. X **12** (2022) 040002.
[2] L. Šmejkal, J. Sinova and T. Jungwirth, Phys. Rev. X **12** (2022) 040501.
[3] C. Sun and J. Linder, Phys. Rev. B **108** (2023) L140408.
[4] S. Lee *et al.*, Phys. Rev. Lett. **132** (2024) 036702.
[5] T. Osumi *et al.*, Phys. Rev. B **109** (2024) 115102.

BL4U

Carbon K-Edge NEXAFS and Sulfur L-Edge NEXAFS Measurements of Samples from Asteroid Ryugu

T. Matsumoto[1]

[1]*The Hakubi Center for Advanced Research, Kyoto University Kitashirakawa-Oiwakecho, Sakyo, Kyoto 606-8502, Japan*

The *Hayabusa2* spacecraft from the Japan Aerospace Exploration Agency (JAXA) explored the asteroid Ryugu and returned surface grains to Earth. It was anticipated that the grains brought back directly from the asteroid might contain previously undiscovered substances not found in meteorites. Among these could be highly water-soluble materials, which readily react with moisture in Earth's atmosphere and are therefore difficult to detect unless examined in their pristine state as preserved in space.

In this study, Ryugu grains were analyzed using FE-SEM and (scanning) transmission electron microscopy ((S)TEM), and synchrotron radiation-based Scanning transmission X-ray microscopy (STXM). Thin sections for STXM and TEM analysis were prepared using a focused ion beam system (FIB). Near edge X- ray absorption fine structure (NEXAFS) spectra at carbon K-edge and sulfur L-edge of FIB sections of Ryugu grain C0071 were measured using the STXM beamline, BL4U. The custom-built sample transfer vessel and a nitrogen-filled glove box were used to prevent sample exposure to the air. The date analysis was performed using the aXis 2000 software.

Using a transmission electron microscope (TEM), which allows observation of structures at the nanometer scale, I identified sodium carbonates (Na_2CO_3 and a hydrate phase), halite crystals (NaCl: sodium chloride) in Ryugu grains. These mineral phases have not been reported in Ryugu samples. The STXM analyses were performed to identify chemical features of these sodium carbonates.

The C K-edge NEXAFS spectrum from the sodium carbonates exhibits a sharp peak at 290.2 eV, which is assigned to the $1s \rightarrow \pi$ transition of carbonate (Fig. 1). Sulfur L-edge in the sodium carbonates of the grain C0071 corresponds to sodium sulfate (Fig. 1). STEM-energy dispersive X-ray spectrometer (EDX) analysis showed that the major elements within the sodium carbonates are sodium (Na), carbon (C), oxygen (O), with minor amounts of sulfur (S) (<6 atomic %) and fluorine (F) (<4 atomic %). STXM analysis suggests that sulfur component detected by STEM-EDS analysis is derived from sodium sulfate included in the sodium carbonate minerals.

The sodium salt minerals are all highly water-soluble. The fact that they dissolve easily in water suggests that their crystallization could only occur if the liquid was extremely limited and had a very high salt concentration. The salt minerals were hypothesized to be formed during the disappearance of the liquid water after the major aqueous minerals found in the Ryugu samples precipitated in the parent body. One possible explanation for the loss of liquid is the evaporation of saltwater. If large-scale fractures formed and connected the interior of the parent body to the outer vacuum environment, the liquid body could have undergone depressurization and evaporation. On Earth, when lakes dry up, highly concentrated saltwater forms, leading to the precipitation of minerals such as sodium carbonate and halite. The remnants of the vaporization are referred to as "evaporites". Similar processes may have occurred in Ryugu's parent body. Another possibility is the freezing of liquid water. After the Ryugu's parent body reached its peak temperature, it cooled due to the exhaustion of the radioactive heat. The remaining alkaline brines probably concentrated as H_2O ices formed. As a result, the sodium salts would have formed at subzero Celsius temperatures. The frozen ice could have sublimated into space over time. Currently, Ryugu shows no signs of large amounts of liquid, nor do its surface grains appear wet. Until now, it was unclear how the liquid water in the parent body was lost. This study has revealed that the loss of liquid water in Ryugu's parent body occurred through evaporation or freezing.

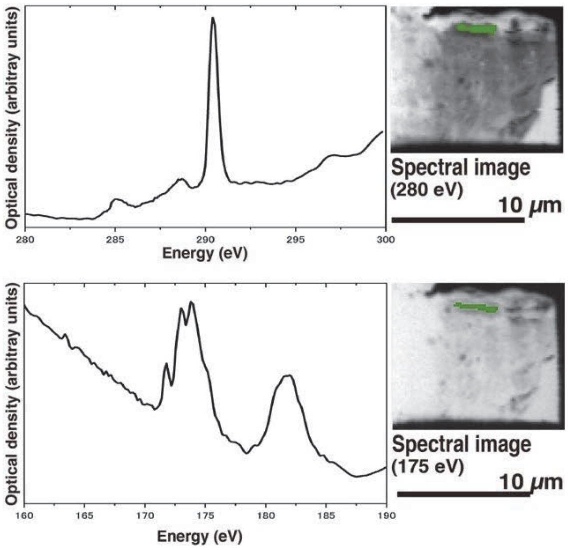

Fig. 1. The C K-edge NEXAFS spectrum (upper figure) and S L-edge NEXAFS spectrum of Ryugu sample(C0071).

[1] T. Mastsumoto *et al.*, *Nature Astronomy*, 8:12, 1536-1543. (2024)

BL4B

Collective Auger Decay of Double Inner-Shell Vacancies in Xe Studied by Multielectron–Ion Coincidence Spectroscopy

Y. Hikosaka[1]

[1]*Institute of Liberal Arts and Sciences, University of Toyama, Toyama 930-0194, Japan*

Auger decay of atomic and molecular core holes generally involves two-electron transitions, where an electron fills an inner-shell vacancy, causing another electron to be emitted into the continuum. An uncommon Auger process, called cascade Auger decay (CAD), can occur when double inner-shell vacancies form in atoms and molecules. Here, two outer electrons simultaneously fill the double vacancies while releasing a single high-energy Auger electron. This study investigates the CAD of Xe^{2+} $4d^{-2}$ double core-hole states using multielectron–ion coincidence spectroscopy with a magnetic bottle electron spectrometer [1,2]. Its high coincidence efficiency allows a detailed spectroscopic analysis of the very rare decay path of double core-hole states.

Figure 1(a) presents an Auger spectrum coincident with a $3d_{5/2}$ photoelectron, measured at a photon energy of 921.2 eV. The formation of $4d^{-2}$ double core-hole states is most prominent among the first-step Auger transitions from the $3d_{5/2}^{-1}$ state. The yields recorded in further coincidence with Xe^{3+} and Xe^{4+} are shown in red and blue, respectively, with ion detection efficiency being compensated. The decay of the double core-hole states mainly results in the production of Xe^{4+} due to cascade double Auger decay. Meanwhile, the red spectrum manifests that the decay of the $4d^{-2}$ states weakly produces Xe^{3+} through the emission of a single Auger electron, indicating a CAD path.

The Xe^{3+} levels populated by the CAD are distinctly observable in the single Auger electron spectrum emitted from the $4d^{-2}$ states. The Auger electron should be detected in a four-fold coincidence with a 3d photoelectron, an $M_{4,5}N_{4,5}N_{4,5}$ Auger electron, and a Xe^{3+} ion. The single Auger electron spectrum extracted is shown in Fig. 1(b), where the Auger transition energies from Xe^{2+} $4d^{-2}$ to Xe^{3+} $5l^{-3}$ levels and the energy position of the Xe^{4+} threshold relative to Xe^{2+} $4d^{-2}$ are indicated. The spectrum exhibits a broad structure in the kinetic energy range of 45–100 eV, suggesting that excited Xe^{3+} levels up to the Xe^{4+} threshold are predominantly produced by the CAD. This spectral feature differs significantly from the CAD observation for Ar^{2+} $2p^{-2}$, where Ar^{3+} $3p^{-3}$ ground states are mainly produced [3].

Peculiar behavior in the CAD of Xe^{2+} $4d^{-2}$ levels is observed also in the branching ratio relative to the total decay of the double core-hole states. The branching ratio is estimated from the coincidence yields to be as large as $2 \times 10^{-2} \pm 1 \times 10^{-2}$. The CAD branching ratio for Ar^{2+} $2p^{-2}$ states was reported to be $1.9 \times 10^{-3} \pm 1.0 \times 10^{-3}$ experimentally and approximately 1.0×10^{-3} theoretically [3]. Thus, the CAD branching ratio for Xe^{2+} $4d^{-2}$ double core-hole states is an order of magnitude greater than that for Ar^{2+} $2p^{-2}$. This amplified CAD for Xe^{2+} $4d^{-2}$, along with the favorable formation of excited Xe^{3+} levels, can be explained by analyzing the number and locations of intermediate configurations needed to promote CAD in second-order perturbation theory [4].

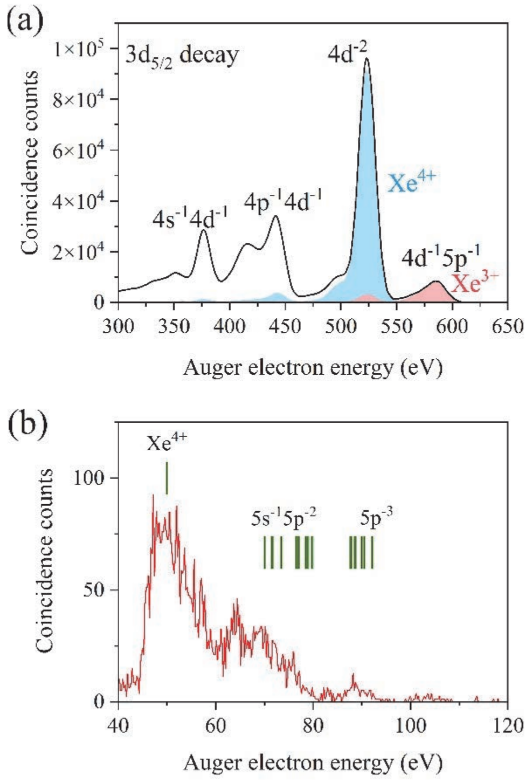

Fig. 1. (a) Coincident Auger spectrum (black) associated with the $3d_{5/2}$ core-hole state of Xe. The yield of Auger electrons, filtered further in coincidence with the Xe^{3+} and Xe^{4+} product ions, are shown in red and blue shading, respectively. (b) Spectrum of single Auger electrons emitted from the Xe^{2+} $4d^{-2}$ states populated via the decay of the $3d_{5/2}$ single vacancy levels, obtained through four-fold coincidence with a 3d photoelectron, an $M_{4,5}N_{4,5}N_{4,5}$ Auger electron, and a Xe^{3+} ion.

[1] Y. Hikosaka and E. Shigemasa, Int. J. Mass Spectrom. **439** (2019) 13.
[2] Y, Hikosaka, J. Electron Spectrosc. Relat. Phenom. **255** (2022) 147158.
[3] M. Mailhiot *et al.*, Phys. Rev. A **107** (2023) 063108.
[4] Y. Hikosaka and S. Fritzsche, Phys. Rev. Lett. **134** (2025) 103001.

BL6B

Performance Evaluation of Infrared Microspectroscopy Station Using Human Hair

Y. Ikemoto[1] and T. Moriwaki[1]
[1]*Spectroscopy Divison, Japan Synchrotron Radiation Research Institute, Sayo, Hyogo 679-5198, Japan*

At infrared beamline BL43IR in SPring-8, microspectroscopy experiments under various sample environments have been conducted and many results have been published. Currently, SPring-8 upgrade plan is ongoing. After the upgrade, it will be difficult to obtain infrared beam due to a ring design. Therefore, it has been decided that BL43IR will be shut down in FY2025.

On the other hand, there is a high demand for research using infrared synchrotron radiation. On September 20, 2023, we held the UVSOR/SPring-8 Infrared Beamline Joint Users' Meeting, where we introduced the UVSOR infrared beamline BL6B to users of BL43IR/SPring-8. BL6B has maintained high performance of light source through facility upgrades. It was decided to start preparations for the transfer of SPring-8/BL43IR activities to BL6B at UVSOR. For the transfer, we must identify the necessary equipment to conduct experiments equivalent to those being conducted at BL43IR. In this proposal, human hair samples were measured, which have been measured at BL43IR as test samples to evaluate the spatial resolution and signal-to-noise ratio.

The sliced hair sample was put on a BaF_2 substrate (10 mm diameter, 1mm thickness) and placed on a sample stage of an infrared microscope (JASCO FT/IR-6100, IRT-7000) installed at BL6B. The absorption spectrum and its imaging were measured in the transmission configuration. The hair should be thin enough to prevent saturation of the absorption peak, which is known to be around 10 μm based on our experience, and we bring samples prepared to the appropriate thickness. The magnification of the objective mirror was x32. All measurements were performed at room temperature. Wavenumber resolution was 4 cm^{-1} and the wavenumber range is 8000-700 cm^{-1}, and a Ge/KBr beam splitter is used.

The following parameters will be varied to obtain a comparison data.

- Light source: standard light source inside the instrument, synchrotron radiation (SR)
- Measurement mode: imaging measurement using linear array detector, multi-point measurement using single element detector

In addition, a sliced hair sample were measured at the micorospectoroscopy station (BRUKER VERTEX70 and HYPERION2000) in BL43IR/SPring-8 for comparison. Wavenumber resolution, wavenumber range and beam splitter were the same as those in BL6B. Result are shown in Fig. 1. All data are mapping image, in which integrated C-H stretching band (2805 – 3141 cm^{-1}) intensity is plotted. The white bars in the figure correspond 20 μm. The samples are not exactly same but prepared at same condition and the thickness is almost same. Figure 1 (a) was measured at BL6B with standard light and 125 μm x 15 μm aperture. The detector was a linear array MCT detector. Figure 1 (b) was a result of BL6B with SR and 4 μm x 4 μm aperture. The detector was a single MCT element detector. Figure 1 (c) was measured at BL6B with SR and 125 μm x 15 μm aperture. The detector was a linear array MCT detector. Figure 1 (d) was measured at BL43IR/SPring-8 using SR with an aperture 5 μm x 5 μm. The detector was a single MCT element detector. Measurement times were 140 min, 220 min, 13min and 13 min for Fig. 1. (a) to (d), respectively. All image has lipid area called cortices are observed in the center. The size of the cortex is about 5 μm, and spatial resolutions are found to be smaller than that. In Fig. 1. (c), un-uniformity is observed, which is caused by non-uniform exposure of light to the array elements. It means that the SR spot is too small to the array detector. Measurement time is very short when array detectors are used. We propose a method at BL6B to measure a large number of samples with an array detector + standard light source, and to measure important samples over time with a single detector + SR. We will examine devices to control the sample environment such as humidification and temperature, and make preparations so that many users can continue their research at BL6B.

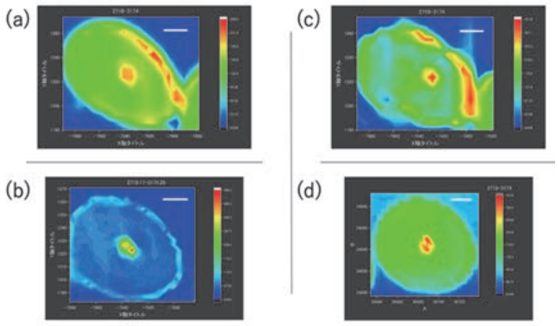

Fig. 1. CH absorption band intensity map of slice hair sample.

BL7U

Direct Measurements of Metallic Property of Organic Materials upon Temperature-Dependent Photoelectron Spectroscopy

X. Liu[1], J. P. Yang[2], K. Tanaka[3], H. Tang[4], F. Huang[4], S. Kera[3] and M. Fahlman[1]
[1]*Laboratory of Organic Electronics, ITN, Linköping University, Norrköping SE-60174, Sweden*
[2]*College of Physical Science and Technology, Yangzhou University, Jiangsu 225009, China*
[3]*UVSOR Synchrotron Facility, Institute for Molecular Science, Okazaki 444-8585, Japan*
[4]*Institute of Polymer Optoelectronic Materials and Devices, State Key Laboratory of Luminescent Materials and Devices, South China University of Technology (SCUT), Guangzhou, China*

Engineering electronic properties of pi-conjugated polymers upon functional groups from material synthesis to post-treatment with external dopants is of vital importance for the development of air stable, soluble, effective charge transport materials on organic devices [1]. Doping induced delocalization of (bi) polarons and their intra-chain carrier transport in pi-conjugated polymers is the basis of the field of “organic synthetic metals”, as well as the foundation of modern organic electronic devices. For instance, PEDOT:PSS, are commercially available hole-dominant (p-type doping) materials with conductivity up to several thousand S/cm, which can be labelled as semi-metallic polymer [2] with no energy gap and very low density of states (like tail states) at the Fermi level due to the contribution of high (bi)polaron density. The information related to the high-conducting n-type (electron-dominant) ones is rather less, e.g., there is still controversy about the new states near the Fermi level of K-doped picene [3], related to the semiconductor-metal transition. Recently, the successful synthesis of air-stable, soluble, and high conducting n-type polymer PBFDO ($(C_{10}O_4H_4)_n$, shown in the inset of Fig. 1(b)) shows the electron conductivity up to 2000 S/cm and very deep LUMO (lowest unoccupied molecular orbitals) [4]. It is believed that the PBFDO is at the critical regime of Mott transition by n-type self-doping with 0.9 electron per unit during polymerization process while the presence of protons in the solvent was used to balance the negative charge. We carried out a UPS study of our-synthesized PBFDO film, a clear Fermi edge feature on free-standing PBFDO films was obviously visible with a work function of up to 5.4 eV, like clean Pt or Au metals.

Any information related to clear Fermi edge feature in high-conducting organic synthetic metals from photoelectron spectroscopy will offer solid evidence of their metallic properties, but it is missing yet for PBFDO. The temperature-dependent Fermi edge features can provide a test about applying Tomonaga–Luttinger liquid or Fermi liquid/glass theory to electronic transport properties of organic synthetic metals.

In this study, we examined the valence band feature of PBFDO close to the Fermi edge regions using high-resolution photoelectron spectroscopy at UVSOR-III BL7U. We used variable excitation photon energy from 7 to 40 eV and the photoelectron spectra were collected by an electron analyzer (A-1, MB-Scientific) with PBFDO sample at temperature from 10 to 298 K.

Figure 1 (a) and (b) show the valence band feature of PBFDO at 298 and 10 K compared to that of Au. It clearly demonstrates the metallic properties of PBFDO with metal-like Fermi edge. The valence feature at around 0.25 eV of PBFDO might be related to the filled LUMO, which results in a broad spectral feature crossing the Fermi edge as the lower part can be deconvoluted with metallic Fermi-Dirac function. Since there is short of theoretical analysis of the metallic properties of PBFDO, we may tentatively analyze the feature with the convolution of a gaussian valence peak at 0. 25 eV and metallic Fermi edge at 0 eV. Furthermore, Figure 1 (c) and (d) show the temperature dependent feature at 0 eV in PBDFO is very similar to that of Au metal. The broadening of the feature above the 0 eV monotonically increases with temperature. Based on our knowledge, the result is the first direct observation of the metallic Fermi feature in organic materials.

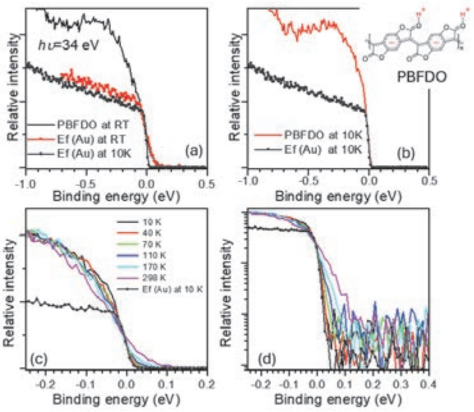

Fig. 1. Valence band feature of PBFDO at photon energy of 34 eV. (a,b) Comparison of Fermi edge feature of PBFDO and Au at 298 and 10 K. (c,d) Fermi edge feature of PBFDO as a function of temperature with linear (c) and logarithmic (d) intensity plots.

[1] A. Heeger, Angew. Chem. Int. Ed. **40** (2001) 2591.
[2] O. Bubnova *et al.,* Nat. Mater. **13** (2014) 190.
[3] A. Ruff *et al.,* Phys. Rev. Lett. **110** (2013) 216403.
[4] H. Tang *et al*., Nature **611** (2022) 271.

BL7U

Coexistence of Ferromagnetism and Altermagnetism in MnTe Thin Films

R. Akiyama[1], T. T. Sasaki[2], M. Valvidares[3], T. Okauchi[4], K. Tanaka[5], S. Ichinokura[1,2],
S. V. Ereemev[6], M. M. Otrokov[7], E. V. Chulkov[8], A. Hariki[4] and T. Hirahara[1]
[1]*Department of Physics, Institute of Science Tokyo, Tokyo 152-8551, Japan*
[2]*National Institute for Materials Science, Tsukuba 305-0047, Japan*
[3]*ALBA Synchrotron Light Source, E-08290 Cerdanyola del Valles, Spain*
[4]*Department of Physics and Electronics, Osaka Metropolitan University, Osaka 599-8531, Japan*
[5]*UVSOR III Synchrotron, Institute for Molecular Science, Okazaki 444-8585, Japan*
[6]*Institute of Strength Physics and Materials Science, Tomsk 634055, Russia*
[7]*Instituto de Nanociencia y Materiales de Aragón (INMA), Zaragoza 50009, Spain*
[8]*Donostia International Physics Center (DIPC), Basque Country, Spain*

Altermagnetic materials exhibit spin-compensated magnetic order like antiferromagnets while breaking time-reversal symmetry like ferromagnets [1]. MnTe, which has a NiAs-type structure, has been identified as an altermagnet with in-plane magnetic moments, as evidenced by nodal spin splitting observed in angle-resolved photoemission spectroscopy (ARPES) [2] and oscillatory x-ray magnetic circular dichroism (XMCD) signals [3]. In our previous study, we demonstrated that embedding 4 layers of MnTe into a topological insulator Bi_2Te_3 (BT) results in the formation of a $Mn_4Bi_2Te_7$/BT heterostructure, where the MnTe layers adjacent to the BT interface adopt a NaCl-type structure and the system exhibits out-of-plane ferromagnetism [4]. Building up on these findings, we consider embedding multilayer MnTe into the minimal unit of BT, a single quintuple layer (1QL- BT), which should allow the growth of MnTe thin films with surfaces and substrate interfaces terminated by Bi and Te atomic layers. However, the influence of such termination modifications on the altermagnetic properties of MnTe thin films remains unclear and requires investigation. Therefore in this study, we fabricated MnTe thin films terminated with Bi and Te atomic layers both at the surface and the interface to the Si substrate and compared their electronic structure with that of pure MnTe films directly grown on Si. Temperature and photon energy dependent *in situ* ARPES measurements were conducted at UVSOR BL-7U with p-polarized photons on and off the nodal plane. The energy and angular resolutions were 15 meV and 0.25°, respectively.

Scanning transmission electron microscopy (STEM) revealed that while these MnTe films terminated with Bi and Te predominantly exhibit the NiAs-type structure, NaCl-type stacking appears near the Si interface, resembling our previously reported $Mn_4Bi_2T_7$/BT heterostructure. XMCD measurements performed at BL29 BOREAS at ALBA confirmed the coexistence of altermagnetic and out-of-plane ferromagnetic signals, reproduced by ab initio calculations. This was also confirmed from ARPES measurements, as shown in Fig. 1. Upon cooling, the nodal splitting emerges in association with the altermagnetic transition (red arrow) at the nodal plane. Furthermore, an exchange splitting at the Γ point, likely induced by ferromagnetism, was also observed by further cooling as shown by the yellow arrow. In contrast, although the nodal splitting was observed for the pure MnTe film grown on Si, the exchange splitting was absent. This was consistent with the XMCD measurement. These findings indicate that the structural change at the interface cants the magnetic moment to the out-of-plane direction, resulting in the coexistence of altermagnetism and ferromagnetism in the MnTe films with Bi and Te termination.

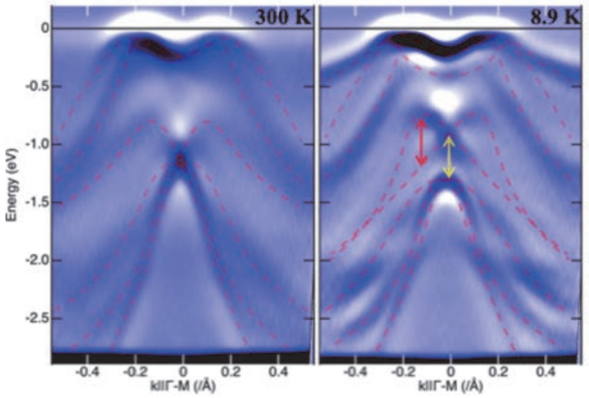

Fig. 1. Band structure of MnTe terminated with Bi and Te, measured along the Γ-M direction measured with hν = 19 eV. The left panel shows the paramagnetic state measured at T = 300 K and the right one shows the coexistence of altermagnetic and ferromagnetic states measured at T = 8.9 K. Red and yellow arrows indicate altermagnetic and ferromagnetic band splitting, respectively.

[1] L. Šmejkal *et al.*, Phys. Rev. X **12** (2022) 031042.
[2] S. Lee *et al.*, Phys. Rev. Lett. **132** (2024) 036702.
[3] A. Hariki *et al.*, Phys. Rev. Lett. **132** (2024) 176701.
[4] T. Hirahara *et al.*, Nat Commun. **11** (2020) 4821.

UVSOR User 6

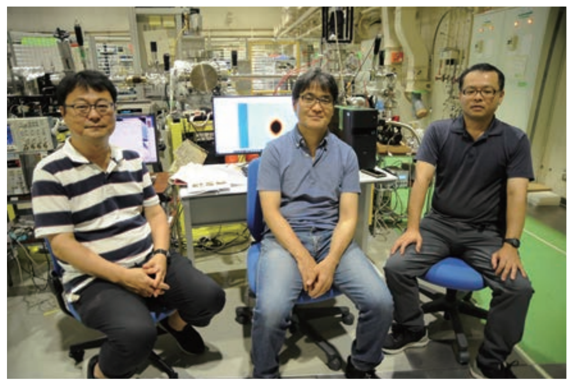
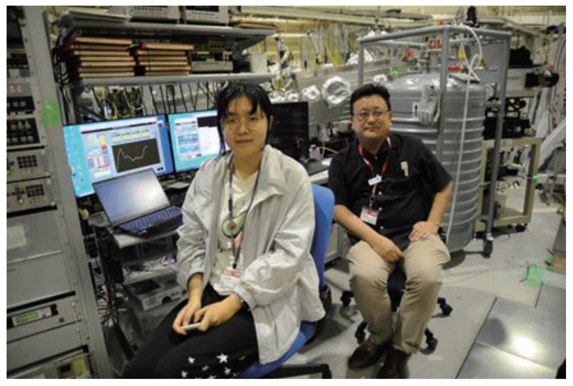
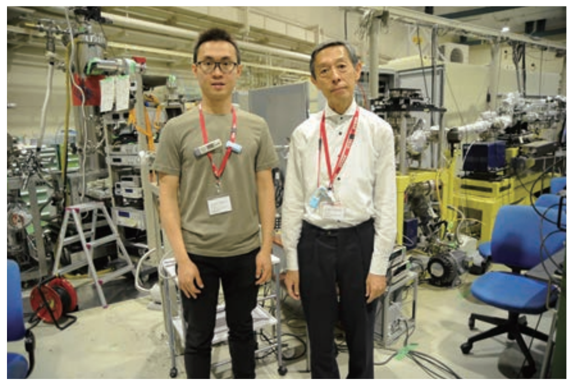
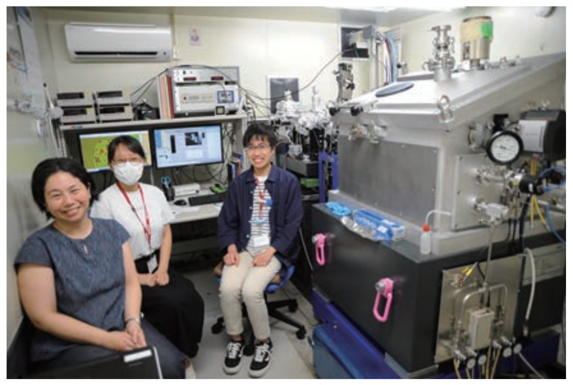
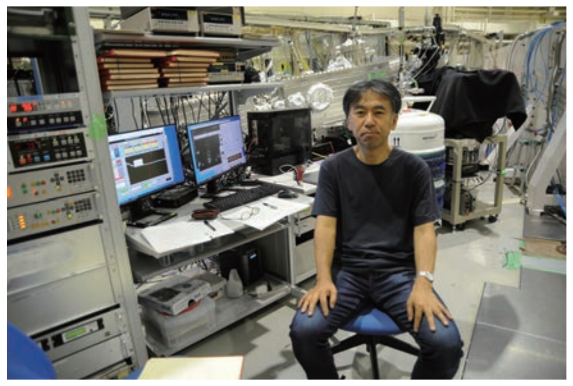
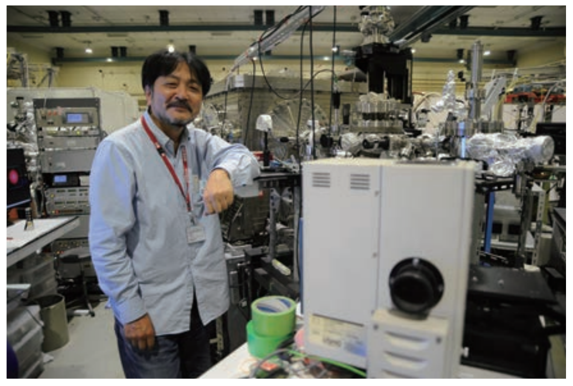

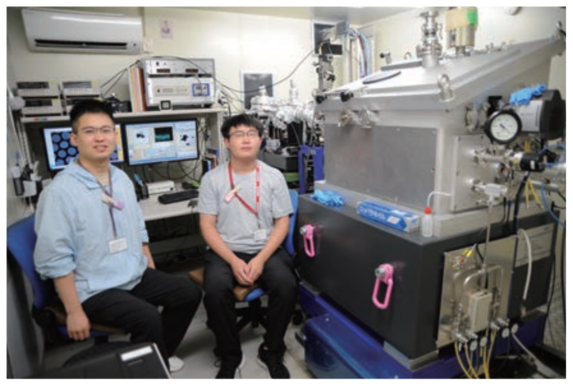

UVSOR User 7

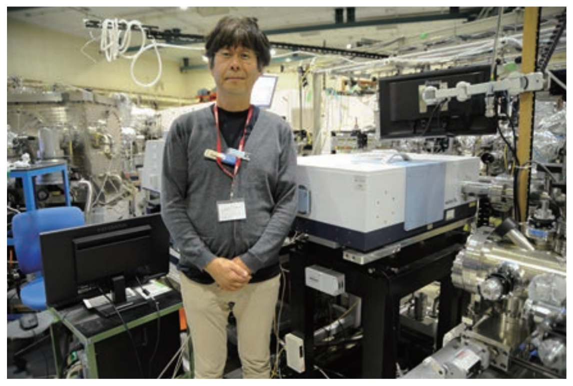

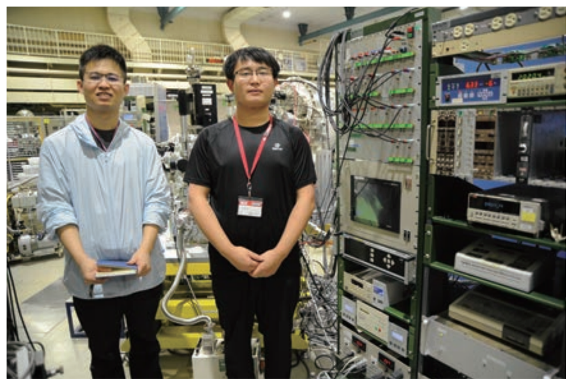

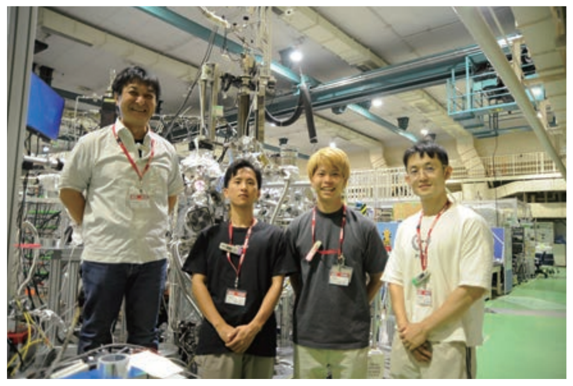

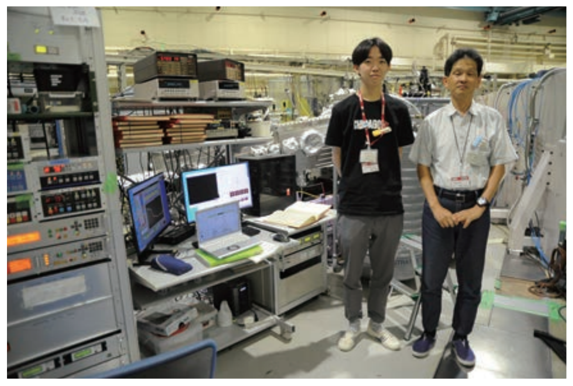

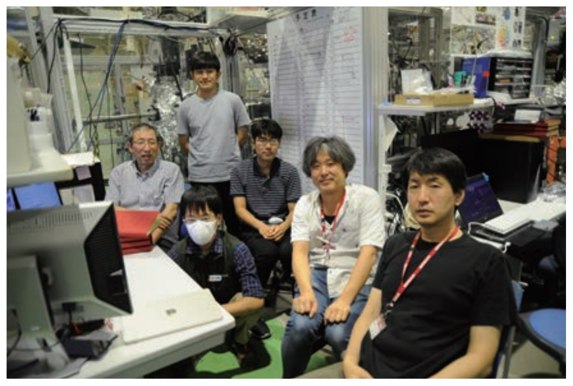

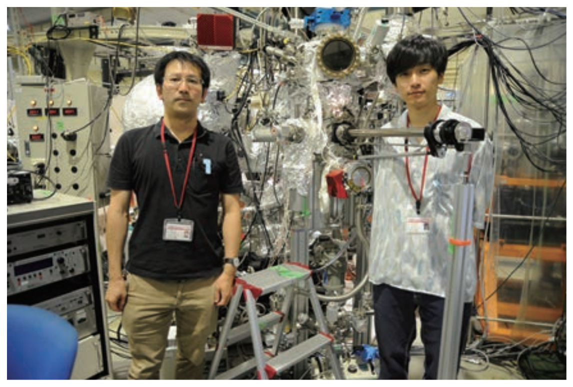

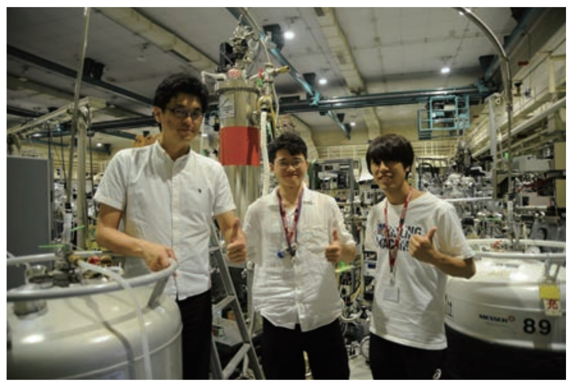

III-1

Accelerators and Instruments

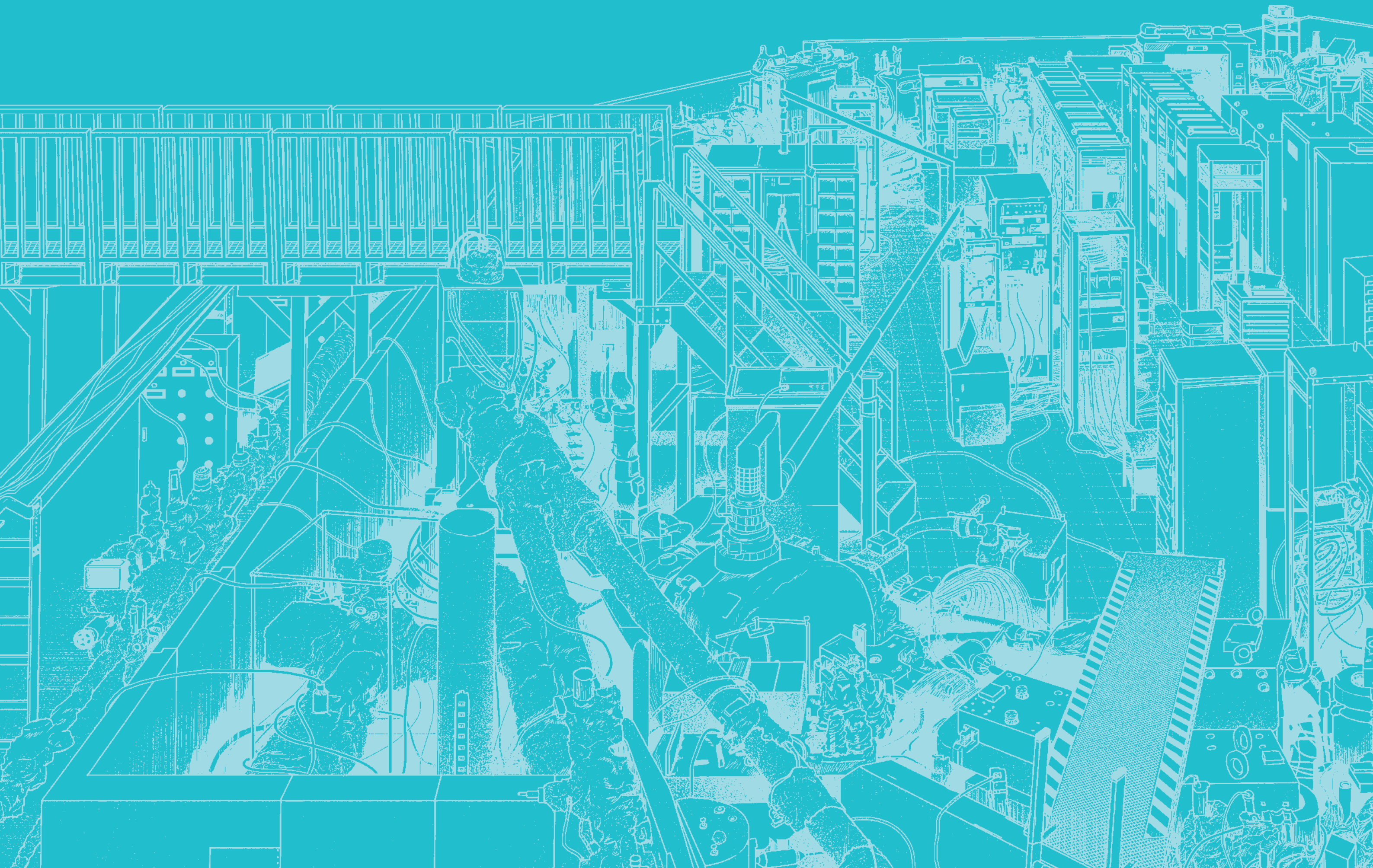

BL1U

Measurements of Temperature-Dependent Absorption Ratios in Transmission Nuclear Resonance Fluorescence

T. Shizuma[1,2], M. Omer[2], R. Hajima[1], M. Koizumi[2], H. Zen[3], H. Ohgaki[3] and Y. Taira[4]
[1]*National Institutes for Quantum Science and Technology, Kizugawa 619-0215, Japan*
[2]*Japan Atomic Energy Agency, Tokai 319-1195, Japan*
[3]*Institute of Advanced energy, Kyoto University, Uji 611-0011, Japan*
[4]*UVSOR Synchrotron Facility, Institute for Molecular Science, Okazaki 444-8585, Japan*

Nuclear Resonance Fluorescence (NRF) is a phenomenon where atomic nuclei absorb and emit γ-rays of specific energies unique to each nuclide. Therefore, by measuring these emitted γ-ray energies, it is possible to identify the nuclide. Additionally, because a γ-ray beam in the MeV energy range is highly penetrating, non-destructive measurement is achievable even when the sample is enclosed in heavy shielding.

In transmission NRF, a γ-ray beam that passes through an absorption target is directed onto another target, called a witness plate (WP), made of the same nuclide as the absorption target. The NRF γ-rays emitted from the WP are then measured. This method is advantageous over scattering NRF as it helps reduce the effects of background radiation [1].

The absorption of γ rays in transmission NRF depends on the temperatures of the absorption and/or WP targets due to variations in the Doppler broadening of the resonant width. As a result, the temperature of the absorption and/or WP targets can affect the measurement's duration and sensitivity. To investigate the temperature dependence of absorption ratios which is defined as R=1-C/C_0 where C and C_0 are NRF γ-ray counts with and without the absorption target [2], we irradiated ^{206}Pb samples (both absorption and WP target) at liquid nitrogen (LN_2) temperature using a laser Compton scattering (LCS) γ-ray beam. The LCS γ-rays, with a maximum energy of 5.54 MeV, were produced by the collision of 746-MeV electrons with laser photons of a 1.895 μm wavelength. A 20-cm thick lead collimator with a 3-mm aperture was employed to confine the LCS γ rays, forming the energy width to approximately 8% (FWHM). Two high-purity Ge detectors positioned horizontally at a scattering angle of 90° relative to the incident γ-ray direction were used to measure scattered γ rays from the WP target. The transmitted LCS γ-rays were monitored by a large volume $LaBr_3$ detector placed downstream of the WP target. The experimental setup used for the present measurement is shown in Fig. 1.

Figure 2 shows γ-ray energy spectra measured with (black) and without (red) the absorption target, respectively. Six NRF peaks of ^{206}Pb [3] are observed at 4971, 5037, 5127, 5377, 5470, and 5524 keV. The differences between the intensities at each peak are associated with nuclear resonant absorption (so called self-absorption). The larger the absorption cross section, the greater the difference becomes. The largest self-absorption occurs for the resonance at 5037 keV which has the integrated cross section of 1150 eV b [3]. The measured absorption ratio for this resonance is R=0.68(11) which can be compared with the expected value of 0.58 within the experimental uncertainties. Further analysis is in progress.

This work is in part a contribution of JAEA to IAEA coordinated research program, J02015.

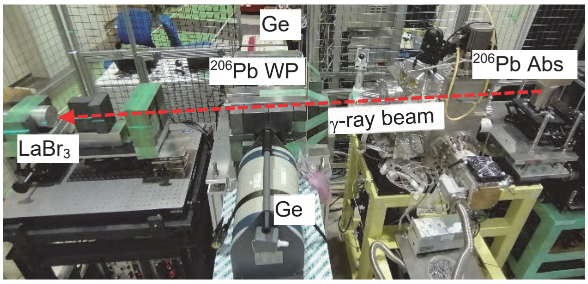

Fig. 1. Photo of the experimental setup used for the present measurement.

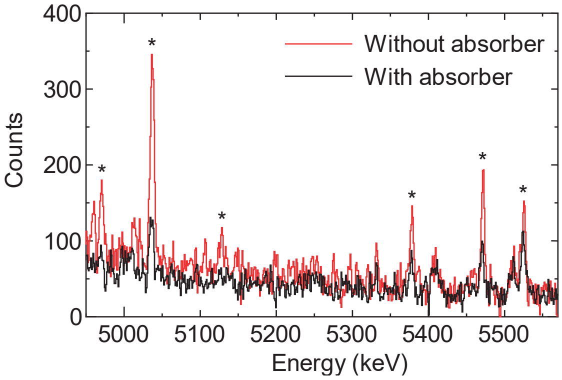

Fig. 2. Energy spectra obtained in transmission NRF experiments. The red (black) spectrum corresponds to the measurement without (with) the absorption target at LN_2 temperature. Asterisks indicate NRF peaks of ^{206}Pb.

[1] C.T. Angell *et al.*, Nucl. Instrum. Methods Phys. Res. B **347** (2006) 11.
[2] F. Metzger, in *Progress in Nuclear Physics*, edited by O. Frisch (Pergamon, New York, 1959), Vol. 7, pp. 53-58.
[3] T. Shizuma *et al.*, Phys. Rev. C **98** (2018) 064317.

BL1U

Study on 2D Isotope Imaging Using UVSOR-BL1U Undulator

H. Ohgaki[1], K. Nishimoto[1], H. Zen[1], T. Hayakawa[2,3], T. Shizuma[2] and M. Omer[4]
[1]*Institute of Advanced Energy, Kyoto University, Kyoto 611-0011, Japan*
[2]*Kansai Photon Science Institute, National Institutes for Quantum Science and Technology,*
Kizugawa, Kyoto 619-0215, Japan
[3]*Institute of Laser Engineering, Osaka University, Suita 565-0871, Japan*
[4]*Integrated Support Center for Nuclear Nonproliferation and Nuclear Security, Japan Atomic Energy Agency,*
Tokai, Ibaraki 319-1195, Japan

A flat laser Compton scattering gamma-ray (F-LCS) beam, which has a flat distribution in the energy spectrum and a spatial distribution with a few mm diameter beam size, has been developed to study an isotope selective CT Imaging application at the beamline BL1U in UVSOR[1]. We generate an F-LCS beam by scattering an intense laser beam with a circular-motion electron beam excited by a helical undulator installed at the BL1U beam line. We carried out a proof of principle experiment at the BL1U in UVSOR in 2022 machine time and we obtained a 1D multi-isotope ($^{207,\,208}$Pb) imaging using LCS and F-LCS beams in 2023[2].

In 2024, we started evaluation of quantitative information on measured isotopes using an absorption method. We used an absorption target whose composition was one of natural Pb, enriched ^{207}Pb, and ^{208}Pb and three enriched isotope witness targets placed behind the absorption target as shown in Fig.1. The F-LCS beam was generated by using the helical undulator with a K-value of 0.2 as well as normal LCS beam. Most other experimental conditions were the same as the 2023 experiment [2]. To reduce the atomic scattering from the witness targets, the Ge detector angles were changed from 90-deg. in 2023 to 135-deg. We also added the 2nd collimator behind the absorption target to reduce the atomic scattering from the absorption target. The improvement of the background rejection was factor 2 as shown in Fig. 2. Clear NRF peaks from the three witness targets from 5037 keV (^{206}Pb, J^{π}=1^{-}) to 5525 keV (^{206}Pb, J^{π}=1^{-}) were observed. The abundances of ^{207}Pb and ^{208}Pb in the natural Pb target were evaluated by comparison with the NRF yields by the enriched ^{207}Pb and ^{208}Pb targets as the absorption target. The three absorption targets of natural Pb, enriched ^{207}Pb, and ^{208}Pb have the sizes of 5-mm thickness plate, 6.2-mm × 6-mmϕ cylinder, and 15-mm × 8.1-mmϕ (perpendicularly placed). Because the gamma-rays are absorbed by all targets located upstream of the witness target, the thickness correction must be considered for the abundance evaluation. We take into account the atomic absorption in the NRF absorption method, and the result is listed in Table 1[3]. Although the thickness correction to the NRF absorption has not been applied, the evaluated abundances with LCS beams are far beyond the margin of errors. We noticed that the measured LaBr$_3$(Ce) data, which gave the thickness information of the absorption targets, were not reasonable. We are trying to improve the analysis method and figure out the reason for the funny LaBr$_3$(Ce) data.

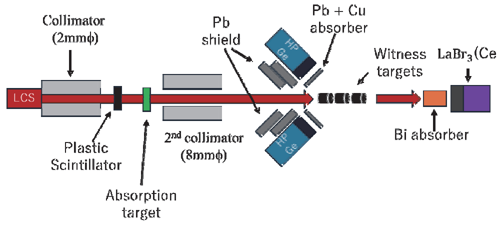

Fig. 1. Schematic drawing of the experiment.

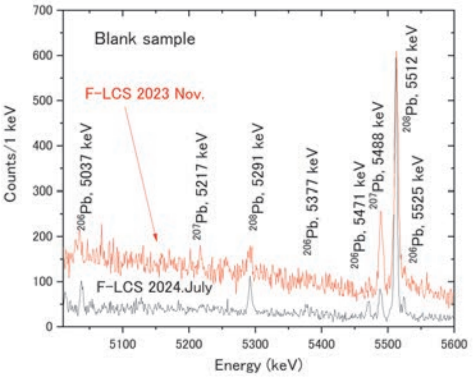

Fig. 2. Measured NRF spectra with the F-LCS beams (red line:2023 Nov., black line: 2024 July).

Table 1. Abundance Evaluation

	Gamma ray beam	^{207}Pb 5488 keV (%)	^{208}Pb 5512 keV (%)
No correction	LCS	−2.9±6.9	46.1±4.2
	F-LCS	11.9±6.2	52.7±5.3
With atomic absorption	LCS	−2.9±6.8	45.7±4.1
	F-LCS	10.6±6.3	52.0±5.3
Established abundance		22.1	52.4

[1] H. Ohgaki *et al.*, Phys. Rev. Accel. Beams **26** (2023) 093402.

[2] H. Ohgaki *et al.*, UVSOR Activity Report **51** (2023) 44.

[3] K. Nishimoto *et al.*, ”Quantitative Evaluation of NRF Yield by Using F-LCS beam in UVSOR”, AESJ Spring Meeting, online, 2025/03/14.

BL1U

Initial Study of Positron Lifetime Imaging Technique Using Gamma-Ray Beam at UVSOR

S. Takyu[1], Y. Taira[2], T. Hirade[3], F. Nishikido[1], H.G. Kang[1],
H. Tashima[1], F. Obata[1], K. Matsumoto[1], M. Takahashi[1] and T. Yamaya[1]
[1]National Institutes for Quantum Science and Technology (QST), 4-9-1 Anagawa, Inage-ku, Chiba-shi, Chiba 263-8555, Japan
[2]National Institutes of Natural Sciences (NINS), 38 NishigoNaka, Myodaiji, Okazaki-shi, Aichi 444-8585, Japan
[3]Japan Atomic Energy Agency (JAEA), 2-4 Shirakata, Tokai-mura, Naka-gun, Ibaraki 319-1195, Japan

Positron emission tomography (PET) is used to diagnose cancer and heart disease, and so on. Unlike CT and MRI, PET can image the internal functions in the living body, and therefore allow us to get closer to the root of internal abnormalities and diseases.

In PET, a positron-emitting drug is administered into the body, and the positrons annihilate with electrons and emit 511 keV photon pairs in the opposite direction, which are detected by a ring-shaped radiation detector. 10^6-10^9 lines of response (LOR) connecting these detection positions are collected, and the drug distribution (radioactivity distribution) is imaged by image reconstruction.

Recently, it has been pointed out that it may be possible to extract new information from the time it takes for positrons to annihilate (lifetime) and use it for diagnosis, because the positron lifetime varies with the surrounding electron density [1]. Therefore, we are currently aiming at the research and development of "quantum PET (Q-PET)" which diagnose by the positron lifetime (Fig. 1.) [2]. To date, we have demonstrated two-dimensional imaging of positron lifetime using a pair of PET detectors [2], and have reported the possibility of imaging hypoxic regions of tumors, which were previously difficult to get quantitative images [3].

However, in living organisms, there are many factors other than oxygen partial pressure that may affect electron density, but there are few basic data that correlates positron lifetime values with diseases. Therefore, the objective of this study is to develop a positron lifetime imaging analysis system that enables three-dimensional analysis of deep inside samples, including living organisms, using 6.6 MeV gamma-ray beam at the UVSOR (Fig. 2. (a)) [4]. Specifically, the beam is irradiated onto the sample, and positrons produced by pair production at the sample depth (to 10 cm) are imaged using the PET principle. The positron lifetime is imaged in three dimensions, with the beam generation as the start and the detection of annihilation photon pairs as the stop. This technique provides accurate information about the start time compared to the technique that accumulates radioisotopes (RIs). This technique also enables three-dimensional analysis of voids in metals and free volume in polymers. This year, we carried out an experiment at UVSOR aimed at the initial demonstration of this technique.

We used one pair of detectors consisting of a 3.2 mm square 8×8 LGSO scintillator array coupled to a 3.2 mm pitch 8×8 MPPC array module. This detector pair was placed opposite each other at a distance of 10 cm, inclined at 15 degrees to the direction of the beam (Fig. 2. (b)). A stainless-steel plate (lifetime value: 106 ps) and a polycarbonate plate (lifetime value: 2.1 ns) were placed separately, and we confirmed the difference in positron lifetime spectra during beam irradiation. We also placed two samples within the field of view of the detector pair and performed simple 2D PET imaging. Details of these achievements will be reported in the conference presentations [5, 6].

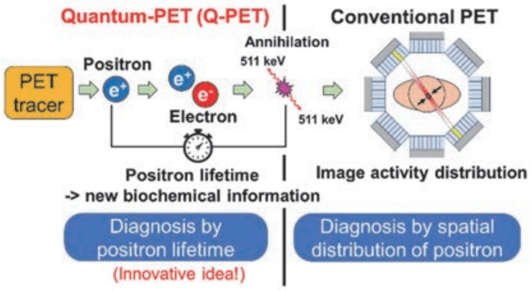

Fig. 1. A difference between quantum PET (Q-PET) and conventional PET.

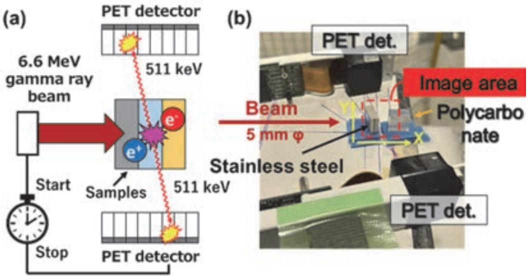

Fig. 2. (a) The principle of the proposed method. (b) The experimental setup.

[1] P. Moskal *et al.,* PET Clin. **15** (2020) 439.
[2] S. Takyu *et al.,* Appl. Phys. Express. **15** (2022) 106001.
[3] S. Takyu *et al.,* Nucl. Instr. Meth. Phys. Res. A. **1065** (2024) 169514.
[4] Y. Taira *et al.,* Rev. Sci. Instrum. **93** (2022) 113304.
[5] S. Takyu *et al.,* Abstract of the 72nd JSAP Spring Meeting 2025, 14p-K502-3, (14, Mach, 2025)
[6] S. Takyu *et al.,* Abstract of the ICPA20, 2025, (submitted)

BL1U

Investigation of Electron Acceleration Location and Condition for Thunderstorm Gamma-ray Flashes

K. Nakazawa[1], A. Tanaka[1], M. Baba[1], Y. Nishimura[1], M. Saito[1], M. Oguchi[1] and K. Okuma[1]
[1]*Graduate school of Sciences, Nagoya University, Nagoya 464-8602, Japan*

Thunderstorm activity is known to produce gamma rays with energies exceeding 30 MeV, which are direct evidence of electron acceleration in the dense atmosphere [1]. Winter thunderstorms along the Sea of Japan is famous for their low-altitude cloud bases (~0.2–0.8 km), which enables ground detection of thunderstorm gamma rays, and we are operating gamma-ray detectors there to understand the location of the acceleration region and its geometry [2-3]. Among them, there are a phenomena called "downward TGFs" which are short duration (< 1 ms), and intense gamma-ray flashes reaching up to 30 MeV [2]. To identify the "origin" of the TGF, we are developing a new detector system, using Cherenkov emission from Compton recoil electron emerged in small acrylic rods, as shown in Fig.1. Our aim is to obtain azimuth and elevation information from the data, and identify the 3D location of the electron acceleration regions, as shown in the right panel of Fig.1.

The detector is made of four acrylic rods, with photo sensors (SiPM) attached to individual ends. As the Cherenkov emission retains some information of the direction of incoming gamma-rays, we can observe the left-right identification of the photon incoming direction by comparing the count rate of the two SiPMs. Although overall performance of the "Cherenkov-rods detectors" have been calibrated using the ~8 MeV gamma-rays from a neutron beam facility KUANS at Kyoto University, the detailed position and angular response of the detector was yet to be understood. We used UVSOR BL1U 6.6 MeV gamma-ray pencil beam and scanned the acrylic rod detector.

We used one acrylic rod for the calibration test in UVSOR. The set up is shown in the left-top panel of Fig.1. Obtained count rates and its ratio as a function of incident angle are summarized in Fig.2. We found that, directed gamma-ray hit to SiPM is non-negligible in side-illumination, while in angled illumination the Cherenkov photon induced events are dominant. The overall angular response is shown in the bottom panel of Fig.2. It reproduced the average profile obtained in the KUANS experiment.

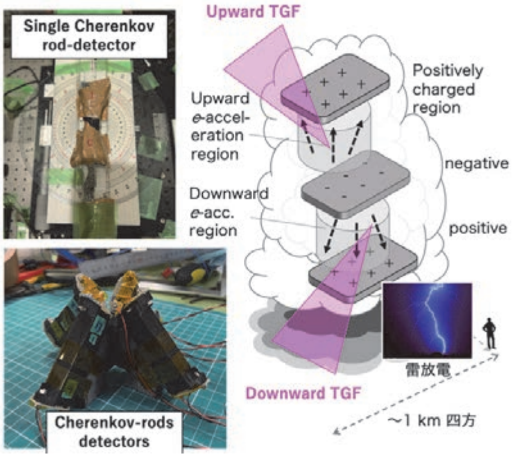

Fig. 1. (right) Concept of our experiment. (left) Our detectors.

Our experiment in December 2024 was the first time we irradiated a narrow (1 mm) pencil beam to the rod, and found many unexpected, but reasonable phenomena. Based on this result, we are planning more comprehensive experiment to understand the angular response in more detail.

We thank the UVSOR and Dr. Taira for enabling these measurements.

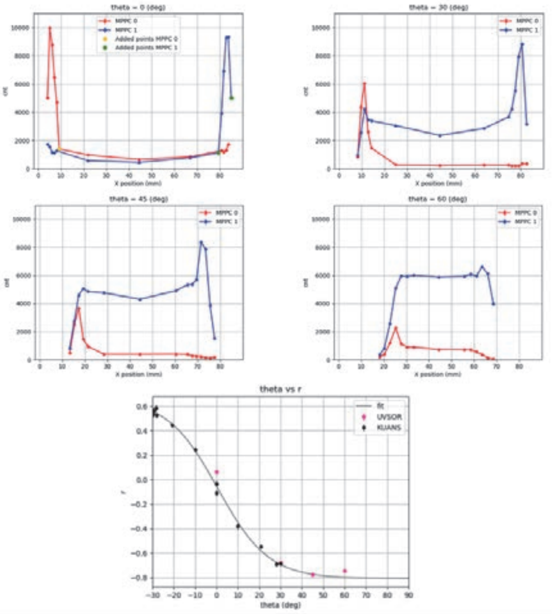

Fig. 2. (top four) Plot of photon count rate vs incident angle. Red is the signals from "right" SiPM and blue is those from "left". (bottom) Angular response as a count-rate ratio as a function of incident angle. UVSOR/BL1U 6.6 MeV result is compared with those obtained in KUANS.

[1] J. R. Dwyer *et al.*, Space Sci. Rev. **173** (2012) 133.
[2] T. Enoto *et al.*, Nature **551** (2017) 481.
[3] K. Nakazawa *et al.*, J. Geophys. Res.:Atmos. **130** (2025) 2024JD042303.

BL1U

Progress in Experimental Study on Single Electron Storage

Y. Asai[1], H. Miyauchi[2, 3], M. Shimada[2, 3] and M. Katoh[2, 4]
[1]*Graduate School of Advanced Science and Engineering, Hiroshima University,*
Higashi-Hiroshima 739-8526, Japan
[2]*Research Institute for Synchrotron Radiation Science, Hiroshima University, Higashi-Hiroshima 739-0046, Japan*
[3]*High Energy Accelerator Research Organization (KEK), Tsukuba 305-0801, Japan*
[4]*UVSOR Synchrotron Facility, Institute for Molecular Science, Okazaki 444-8585, Japan*

We have been continuing experimental studies on the single-electron storage at UVSOR-III since 2021 with the aim of conducting fundamental research on the accelerator physics and the electromagnetic radiation from relativistic electrons [1-8]. At BL1U of UVSOR-III, we extracted undulator light in the UV region at a wavelength of 355 nm into the atmosphere through a sapphire window and observed its intensity using a photomultiplier tube with an appropriate band-pass filter to reduce background light. After injecting a small amount of electrons which corresponds to 0.1 mA, the beam current is reduced by using the beam scraper. When the number of the electrons comes to be smaller than a few tens, we observe a step-function-like intensity change with a good SN ratio, that allows us to confirm the number of the stored electrons. When the number of the electrons comes to be unity, we pull out the beam scraper, then the last electron is stored in the ring for longer than several hours.

After establishing the operation technique for the single electron storage described above, we have conducted several experiments, which have been reported elsewhere [3-8]. In this report, we shortly describe a few results from the recent progresses.

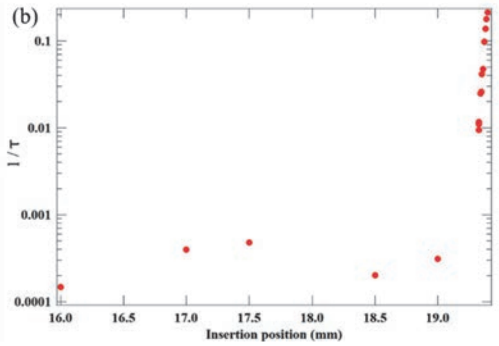

Fig. 1. Beam loss rate vs. Scraper position.

To achieve the single electron storage, we have been using the beam scraper, which is a copper rod installed on the beam pipe. It is inserted to the beam pipe to limit the transverse aperture in the vertical direction. Figure 1 shows the relationship between the insertion position, which is the distance from the pipe wall to the head of the rod, and the beam loss rate. The beam loss rate shows steep increase toward the scraper position around 19.5 mm. The vertical aperture of the beam pipe is 38 mm, which means that the position 19 mm corresponds to the beam center. From the data, the beam center seems to exist at around 19.5 mm. This small discrepancy may arise from the misalignment between the beam and the pipe and also from the mechanical error of the scraper position. When the scraper position is smaller than 19 mm, the beam loss does not show strong dependence on the scraper position. This suggests that, in this range, the beam loss is dominantly caused by the gas scattering or Touschek effect. On the other hand, the beam loss beyond 19 mm is considered to be due to so-called quantum lifetime. Quantitative analysis will be made in near future.

To investigate the properties of radiation from a single electron, we are planning to construct measurement system based on optical fibers, which is expected to make the measurement system more flexible, robust and hard against the background light. We have tested a fiber coupler and a new photomultiplier tube, which is capable of directly producing a photon counting signal without amplifier nor signal processor. The new detector system gave an excellent result in the photon counting measurement.

[1] R. Shinomiya *et al.*, UVSOR Activity Report 2021, **40** (2022) 40.
[2] R. Shinomiya *et al.*, presented at JSR2022, 9PS01S (Jan., 2022).
[3] Y. Asai *et al.*, presented at JSR2023, 1F03S (Jan., 2023).
[4] Y. Asai *et al.*, UVSOR Activity Report 2022, **42** (2023) 42.
[5] Y. Asai *et al.*, presented at PASJ2023, WEP26 (Aug. 2023).
[6] Y. Asai *et al.*, presented at 2023 Annual meeting of JPS, 19aRD11, 3 (Sep., 2023).
[7] Y. Asai *et al.*, presented at 2023 HiSOR Symp., P02S (Mar., 2023).
[8] Y. Asai *et al.*, presented at 2024 Annual meeting of JPS, 18pB111-11 (Sep., 2024).

BL1U

Spatial Polarization Distribution Measurements of Gamma Rays Produced by Inverse Compton Scattering

Y. Yang[1,3,4], Y. Taira[1,2], T. Shizuma[5] and M. Omer[6]
[1]*Institute for Molecular Science, National Institutes of Natural Sciences, Okazaki 444-8585, Japan*
[2]*School of Physical Sciences, The Graduate University for Advanced Studies (SOKENDAI),*
Okazaki 444-8585, Japan
[3]*School of Physics, Zhengzhou university, Zhengzhou 450001, China*
[4]*Shanghai Institute of Applied Physics, Chinese Academy of Sciences, Shanghai 201800, China*
[5]*National Institutes for Quantum Science and Technology, Kizugawa 619-0215, Japan*
[6]*Integrated Support Center for Nuclear Nonproliferation and Nuclear Security, Japan Atomic Energy Agency,*
Tokai 319-1195, Japan
Email:yangyuxuan@ims.ac.jp

Polarization measurements of MeV gamma-rays are essential in astrophysics and nuclear physics, offering profound insights into fundamental physical processes [1]. Highly polarized MeV gamma rays can be generated in the laboratory by inverse Compton scattering (ICS) of a polarized laser with a relativistic electron beam. ICS gamma rays possess characteristics such as energy tunable, quasi-monochromatic, and a low divergence angle (<1 mrad). At the UVSOR synchrotron facility, 6.6 MeV gamma rays can be generated by a 90° collisional ICS between a 750 MeV electron beam and an 800 nm laser. The gamma rays are used for user applications such as positron annihilation spectroscopy and detector evaluation of polarized gamma-ray detectors.

By shifting the position of the lead collimator, which is placed on the gamma-ray beam axis, the gamma-ray energy can be changed in the range of 3 ~ 6.6 MeV [2]. However, since the polarization of ICS gamma rays also varies with the position of the beam cross-section, it is necessary to measure the two-dimensional polarization distribution of the gamma rays. We have developed a new polarimeter that can measure the linear polarization of gamma rays in the MeV region. The measurement setup is shown in Fig. 1. The system enables asymmetry analysis of Compton scattering cross-sections using a 50-mm-thick iron target and seven NaI detectors arranged at the scattering angle of 45° with the azimuthal angles spanning 0°~180° in 30° increments. Figure 2 shows the azimuthal distribution of Compton scattered gamma rays when vertically polarized gamma rays are measured, allowing us to measure the asymmetry due to polarization.

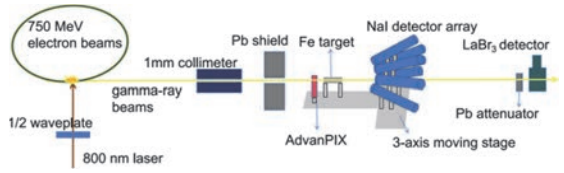

Fig. 1. The Schematic illustration of the spatial polarization distribution measurement.

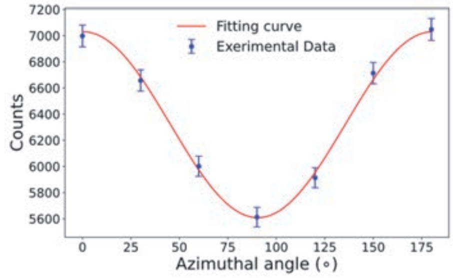

Fig. 2. Azimuthal scattering distribution of vertically polarized gamma-rays when collimator position is horizontal $x = 0$ mm and vertical $y = 4$ mm.

The ICS gamma-ray beam was collimated by a 1-mm lead collimator and then irradiated to the iron target. Two dimensional spatial polarization distribution of ICS gamma rays can be obtained by measuring the azimuthal distribution of Compton scattered gamma rays while shifiting the collimator, target, and detectors in two dimensions. Simultaneously, the gamma-ray beam profile injecting into the target was monitored using an AdvanPIX CdTe image sensor, and the ICS gamma energy spectrum was recorded by a LaBr$_3$ detector. The range of the two dimensional scan was $0 \leq \gamma\theta \leq 1$ and $0 \leq \phi \leq 2\pi$, which sufficiently covers the cross section of the ICS gamma-ray beam, where γ is the Lorentz factor of the electron beam, θ is the scattering angle of gamma rays, and ϕ is the azimuthal angle.

We measured the two-dimensional spatial polarization distribution of horizontally and vertically linearly polarized gamma rays. Building on this methodology, the two-dimensional polarization distributions of ICS gamma rays generated by using a radially and azimuthally polarized laser [3] will be evaluated.

[1] J. Speth *et.al.*, Rep. Prog. Phys. **44** (1981) 719.
[2] Y. Taira *et.al.*, Phys. Rev. A **107** (2023) 063503.
[3] Y. Taira, Phys. Rev. A **110** (2024) 043525.

BL2A

Success of the World's First Solar Flare X-ray Focusing Imaging Spectroscopic Observation by the Sounding Rocket Experiment FOXSI-4 and Post-Flight Calibration of Its CMOS Sensors

N. Narukage[1,2], T. Hirose[1,2], Y. Sato[2,1] and R. Shimizu[2,3]
[1]*National Astronomical Observatory of Japan (NAOJ), Mitaka 181-8588, Japan*
[2]*The Graduate University for Advanced Studies, SOKENDAI, Hayama 240-0193, Japan*
[3]*Institute of Space and Astronautical Science (ISAS), Japan Aerospace Exploration Agency (JAXA), Sagamihara 252-5210, Japan*

The solar corona is full of dynamic phenomena such as solar flares. The understanding of these phenomena has progressed step-by-step with the evolution of observation technology in EUV and X-rays from space. But fundamental questions remain unanswered or have not been addressed so far. Our scientific objective is to understand the underlying physics of the dynamic phenomena in the solar corona, covering some of the long-standing questions in solar physics, such as particle acceleration in flares and coronal heating. To achieve this objective, we identify imaging spectroscopy (the observations with spatial, temporal, and energy resolutions) in the soft X-ray range (from ~0.5 keV to ~10 keV) as a powerful approach for the detection and analysis of energetic events [1]. This energy range contains many lines emitted below 1 MK to beyond 10 MK plasmas and a continuum component reflecting the electron temperature.

The soft X-ray imaging spectroscopy is realized with the following method. We take images with a short enough exposure to detect only single X-ray photon in an isolated pixel area with a fine pixel Silicon sensor. So, we can measure the energy of the X-ray photons one by one with spatial and temporal resolutions. When we use a high-speed soft X-ray camera that can perform the continuous exposure with a rate of more than several hundred times per second, we can count the photon energy with a rate of several 10 photons/pixel/second. This high-speed exposure is enough to track the time evolution of spectra generated by dynamic phenomena in the solar corona including solar flares, whose lifetimes are about from several ten seconds to several ten minutes.

For the world's first focusing imaging-spectroscopic observation of a solar flare in X-ray range, we launched a NASA's sounding rocket as the fourth flight of FOXSI sounding rocket series (called "FOXSI-4") on April 17th, 2024 (Fig. 1) and successfully obtained the unprecedented solar flare data using a combination of high-precision X-ray mirrors and high-speed X-ray cameras (Fig. 2). For the soft X-ray cameras, we use fully depleted CMOS sensors with a silicon thickness of 25 μm [2,3], which provide high sensitivity to high-energy X-rays.

FOXSI-4 detected more than 10^{7} X-ray photons during an observation period of about 5 minutes. Using these photons, we can make spatially and temporally resolved X-ray spectra from a solar flare (see Fig. 3) and then investigate the physics of the high-energy plasmas generated by the solar flare.

For the precise scientific analysis of FOXSI-4 data, post-flight calibration of the CMOS sensors is indispensable. In FY2024, this was done for the energy range from 0.85 keV to 4.5 keV at UVSOR BL2A.

Fig. 1. Photo of FOXSI-4 launch at Poker Flat Research Range in Alaska.

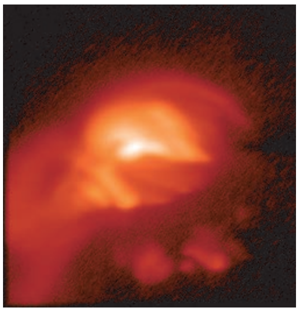

Fig. 2. A solar flare image in soft X-rays observed by the CMOS camera aboard FOXSI-4 sounding rocket.

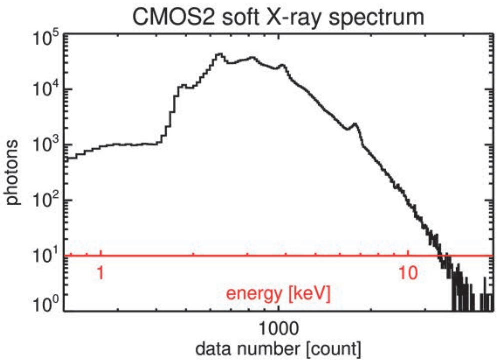

Fig. 3. A soft X-ray spectrum of a solar flare obtained with the CMOS camera aboard FOXSI-4.

[1] N. Narukage *et al.*, White paper of the "soft X-ray imaging spectroscopy", arXiv:1706.04536 (2017).
[2] N. Narukage *et al.*, UVSOR Activity Report **51** (2023) 48.
[3] R. Shimizu *et al.*, Proc. SPIE Int. Soc. Opt. Eng. **13103** (2024) 1310308.

BL2A

Operando Analysis of Battery Materials Using NEXAFS Spectroscopy with a Transportable Potential-Applying Manipulator

E. Kobayashi[1] and A. Inoishi[2]
[1]*Kyushu Synchrotron Light Research Center, 8-7 Yayoigaoka, Tosu, Saga 841-0005, Japan*
[2]*Institute for Materials Chemistry and Engineering, Kyushu University*
6-1 Kasuga-koen, Kasuga-Shi 816-8580, Japan

Research on battery materials is actively being conducted from the perspective of resource and energy issues, as well as global environmental concerns. In the development of new battery materials, information on changes in the valence of each element before and after the application of potential to the fabricated battery is essential for analyzing the reaction mechanism. Moreover, operando measurements during analysis enable more accurate reaction analysis. Additionally, in the analysis of battery materials, non-exposure measurements to atmospheric components are indispensable due to the materials' reactivity to atmospheric substances. From this perspective, we developed a manipulator for soft X-ray absorption spectroscopy that allows samples to be transported without exposure to the atmosphere [1].

The elements contained in battery materials exhibit a wide range of absorption edge energies, from lithium to sulfur, chlorine, and even metals. Consequently, depending on the synchrotron radiation facility, it may not be possible to measure all elements on a same beamline, or the facility itself might not be able to accommodate the measurements. Furthermore, due to differences in sample holders across facilities and beamlines, challenges arise when handling rare samples, such as difficulty in making adjustments and reproducing surface conditions. To enable analysis of the surface state of the same sample, we developed a transportable manipulator [1]. This device allows the sample to be directly attached to the sample-fixing part and transported under vacuum or gas atmospheres. The sample-fixing part is connected to a coaxial feedthrough Bayonet Neill-Concelman (BNC) at the top of the device, enabling the measurement of sample current. Furthermore, since the device can be installed on the conflat flange with an outer diameter of 70 mm (ICF70) port, it facilitates cross-beamline or cross-facility measurements. Additionally, to more accurately evaluate the reactions occurring in batteries, we developed a device capable of applying voltage to the battery, allowing for measurements of the actual reaction state under operational conditions [2].

Previously, the soft X-ray absorption spectra of electrodes and solid electrolytes were measured after disassembling batteries that had undergone charge and discharge cycles without exposure to the atmosphere. However, since the samples used were different, the changes due to charge and discharge were not fully reflected. On the other hand, operando observation allows for the monitoring of changes at the same location, which is expected to enable a more accurate evaluation of electrochemical changes. In this study, we analyze battery materials using a manipulator capable of applying voltage.

The sample was attached to the transfer vessel in a glove box under an argon atmosphere and transported to the analyzer. Soft X-ray absorption spectrum of the sample was measured at the BL2A of the UVSOR in the Institute for Molecular Science. The XAFS spectra was obtained using the partial fluorescence yield (PFY) mode at room temperature. Fluorescence detector used was a silicon drift detector (SDD).

Figure 1 shows the time dependence results of the Mg K-edge NEXAFS of MgI_2 under applied voltage. The peak near 1305 eV, which corresponds to metallic Mg, was not observed. This is because the battery had high resistance and not enough electricity flowed, so the electrode reaction did not progress to a detectable range. However, as discharge progressed, the spectrum shifted slightly to the lower energy side. This indicates that the slight changes associated with the reduction reaction at the electrode could be observed using this device.

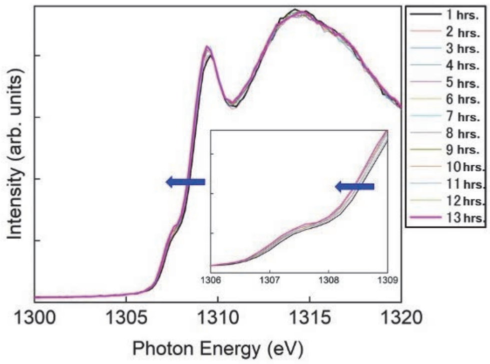

Fig. 1. Mg K-edge NEXAFS of MgI_2 under applied voltage.

[1] E. Kobayashi and A. Inoishi, UVSOR Activity Report **50** (2022) 44.
[2] E. Kobayashi and A. Inoishi, UVSOR Activity Report **51** (2023) 49.

BL3B

Low Temperature Measurements to Understand Luminescence Characteristics of Synthetic Diamond

Atsuhiro Umemoto[1]

[1]*International Center for Quantum-field Measurement Systems for Studies of the Universe and Particles (QUP),*
High Energy Accelerator Research Organization (KEK), Tsukuba 305-0801, Japan

Diamond is a wide-bandgap semiconductor with unique physical properties, such as the highest Debye temperature among crystals and easy formation of optical color centers by impurity doping. Owing to these characteristics, diamond is expected to be used as a scintillating bolometer in the field of particle physics, detecting both luminescence and heat generated by charged particles. Scintillating bolometers exhibit excellent energy resolution and particle identification capabilities, which are important for rare event searches, such as dark matter search. We have been conducting research and development on both diamond scintillators and bolometers for dark matter detection. Recently, we have shown the basic characteristics of diamond scintillators by using nitrogen-doped, commercially available synthetic crystals [1]. At present, with the cooperation of Prof. Taniguchi and Miyakawa at the Research Center for Materials Nano-Architectonics, National Institute for Materials Science, synthetic diamonds with controlled dopants for optical color centers can be manufactured and used to study their luminescence properties.

During the beam time in FY2024, photoluminescence measurements were conducted on synthetic diamonds with nitrogen concentrations ranging from 1 to 200 ppm. Since scintillating bolometers operate at low temperatures, understanding their luminescence characteristics at these temperatures is very important. Figure 1 shows a comparison of the photoluminescence spectra of diamond with a nitrogen concentration of 1 ppm, measured at different temperatures. The excitation wavelength was set to λ=220 nm, which is a similar energy as the bandgap of diamond. The peak wavelength shifted from 516 nm to 569 nm when the temperature was lowered from room temperature to 7 K. While a detailed analysis has not yet been conducted, this suggests that lowering the temperature may have induced changes in the crystal structure. In any case, luminescence was observed at low temperatures, and although it was not easy to quantify the light yield, it was shown to be comparable to that at room temperature. As an interesting point from physical properties perspective, we observed that the change in the peak wavelength between low and room temperatures depends on the nitrogen concentration. The linear line shown in Fig. 2 represents predictions, but the peak wavelength might shift to shorter wavelengths at lower temperatures when the nitrogen impurity concentration exceeds 150 ppm.

The decay time constants of luminescence and other parameters show different behavior in samples with nitrogen impurity concentrations exceeding 150 ppm. Further investigations are needed to understand the luminescence characteristics at low temperatures and to determine the optimal nitrogen concentration for dark matter search.

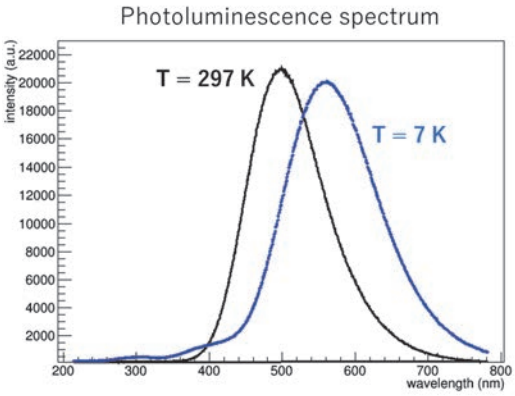

Fig. 1. Photoluminescence spectra of nitrogen-doped synthetic diamond with a nitrogen concentration of 1 ppm, measured at different sample temperatures.

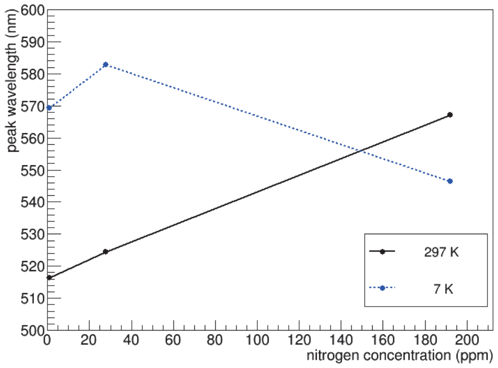

Fig. 2. The shift of the photoluminescence peak wavelength depended on the temperature. It was performed on three samples with different nitrogen concentrations.

[1] A. Umemoto *et al.*, Nucl. Instrum. Methods A **1057** (2023) 168789.

BL7B

Development of a Lyman-α Detector

T. Kaneyasu[1,2] and M. Kobayashi[3]
[1]*SAGA Light Source, Tosu 841-0005, Japan*
[2]*UVSOR Synchrotron Facility, Institute for Molecular Science, Okazaki 444-8585, Japan*
[3]*National Institute for Fusion Science, Toki 509-5292, Japan*

The attosecond phase-control of electromagnetic radiation from an ultra-relativistic electron is a new capability of synchrotron radiation that allows the control of quantum wave packet interference in the short wavelength regime [1,2]. This unmarked capability of synchrotron radiation has been successfully applied to quantum control and ultrafast spectroscopy of atoms in the extreme ultraviolet wavelength. As a next step of the quantum control by synchrotron radiation, we plan to observe the quantum interference between the vibrational wave packets in the hydrogen molecule excited by vacuum ultraviolet (VUV) pulses.

In the designed experiment, the hydrogen molecule interacts with a pair of VUV pulses. The quantum interference between the vibrational wave packets is monitored by detecting the fluorescence in the ultraviolet wavelength. In particular, the Lyman-α emission from a fragment can be used to probe the vibrational excitation in a particular state [3].

Figure 1 shows the developed detector. The Lyman-α detector consists of a gas cell and a micro-channel plate (MCP). The gas cell is equipped with a MgF_2 window which allows selective detection of fluorescence larger than 120 nm wavelength. The MCP is coated with CsI to increase the quantum efficiency in the VUV wavelength.

As a performance test of the detector system, we have measured the fluorescence yield spectrum of hydrogen molecules in the VUV wavelength at BL7B. The detection angle was set to be 55 degrees with respect to the polarization vector of the synchrotron radiation. A Nb filter of 160 nm thickness was inserted in front of the experimental chamber to filter out the second harmonic and to maintain the ultrahigh vacuum condition in the beamline.

Figure 2 shows the fluorescence yield spectrum where we have assigned three vibrational progressions belonging to the B $^1\Sigma_u^+$, C $^1\Pi_u$, and D $^1\Pi_u$ electronic states according to the EELS study [4]. The Lyman-α from the D state is attributed to the production of H(2*l*) atoms generated by the predissociation of the vibrationally excited states. In contrast to the spectrum measured with a detector equipped with a ceratron [3], the fluorescence yield from the B and C states is enhanced in the observed spectrum. They are most likely a consequence of the molecular fluorescence of more than 150 nm wavelength emitted from these states [5]. Given that the relative quantum efficiency of the CsI-coated MCP for the 150 nm wavelength is about one order of magnitude higher than that for the Lyman-α wavelength [6], the fluorescence intensity is enhanced in the region of the B and C states. The performance of the detector is satisfactory, and its application to the quantum interference experiment is planned.

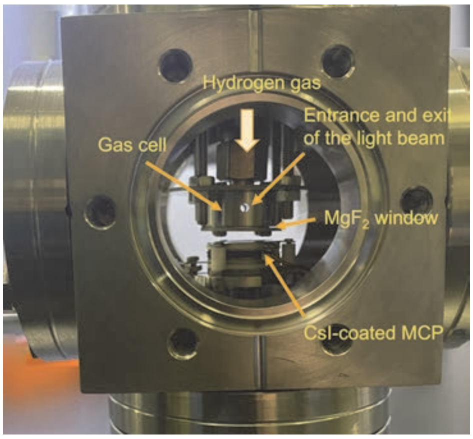

Fig. 1. Photo of the Lyman-α detector. The detector components were assembled inside the ICF-70 cube-type chamber.

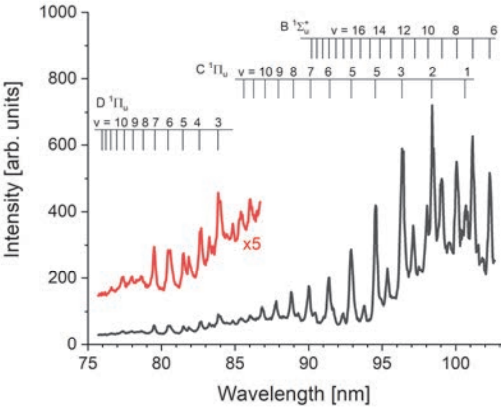

Fig. 2. VUV fluorescence yield spectrum measured by the Lyman-α detector.

[1] Y. Hikosaka *et al*., Nat. Commun. **10** (2019) 4988.
[2] T. Kaneyasu *et al*., Phys. Rev. Lett. **126** (2021) 113202.
[3] S. Arai *et al*., Z. Phys. D **4** (1986) 65.
[4] W. F. Chan *et al*., Chem. Phys. **168** (1992) 375.
[5] P. Schmidt *et al*., J. Phys. Conf. Ser. **635** (2015) 112130.
[6] Kuwabara *et al*., JAXA-RR-16-011 (2017).

Others

Development of Nuclear Emulsion Focusing on Gelatin Composition for Suppression of Latent Image Fading

A. Yoshihara[1], K. Morishima[1], N. Kitagawa[1] and T. Yoshida[1]
[1]*Graduate School of Science, Nagoya University, Nagoya 464-8602, Japan*

Nuclear emulsion is three-dimensional radiation detector consisting of emulsion in which AgBr crystals are dispersed in gelatin and coated onto a support. When a charged particle passes through the emulsion layer, ionization generates electrons. These electrons combine with silver ions to form latent image (Ag_n) consisting of multiple silver atoms. In development process, only latent image with $n \geq 4$ is developed and recorded as tracks.

Nuclear emulsion is being used in various fields, one notable example being Cosmic ray imaging. Cosmic ray imaging is new non-destructive inspection technique of large-scale constructions with cosmic ray muon. We had ever applied this technique to the pyramid of khufu in Egypt and discovered a big void [1]. To further expand its application to diverse structures, improving detector’s temperature resistance is essential.

The issue of temperature resistance is latent image fading. Latent image fading refers to the gradual disappearance of tracks under high-temperature conditions. One possible cause is the oxidation of latent image by Br_2, which reduces their size and makes them undevelopable [2]. As shown in Fig 1, GD [counts/100μm] decreases over time in high-temperature conditions.

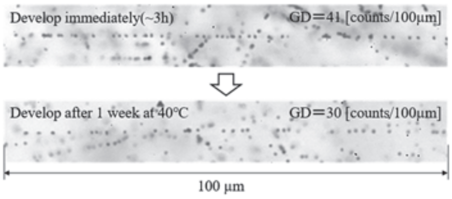

Fig.1. Latent image fading of electron tracks irradiated at UVSOR.

To suppress of latent image fading, we propose a method to prevent Br_2 from approaching the latent image. Specifically, we utilize halogen bonding with sulfur compounds in gelatin to capture and immobilize Br_2. Typically, bovine bone gelatin used in nuclear emulsions contains only methionine as sulfur compound, with approximately four functional groups per 10^3 Amino acids. To increase the amount of sulfur compounds in gelatin, we developed “thiol-introduced gelatin” by artificially incorporating sulfur compounds. Additionally, we used “fish gelatin” which naturally contains the highest amount of sulfur compounds among natural sources, to produce nuclear emulsions. Table 1 shows the sulfur compound content of each gelatin type. Since neither type of gelatin has been previously applied to nuclear emulsions, evaluation is essential.

Table 1. Amount of functional groups with sulfur in each gelatin [/10^3 Amino acids]

	Bovine bone gel	Thiol gel	Fish gel
Methionine	4	4	10
Thiol	-	4	-
Total	4	10	10

As a result of its application, thiol-introduced gelatin was confirmed to form a strong bond between Ag^+ on the AgBr surface and thiol groups, leading to the coagulation of the emulsion. We prevented coagulation by adding NaBr solution, making its application feasible. In case of fish gelatin, due to its low molecular weight and low viscosity, preventing it from adequately supporting AgBr, which resulted in sedimentation. We introduced thickening agents to crosslink gelatin molecules, increasing their molecular weight and enabling uniform dispersion of the emulsion, thereby making its application possible.

Next, for the sensitivity test, we prepared nuclear emulsion using each type of gelatin (crystal size of approximately 200 nm) and irradiated them with an electron beam at UVSOR. Figure 2 shows the micrographs of nuclear emulsions using each type of gelatin.

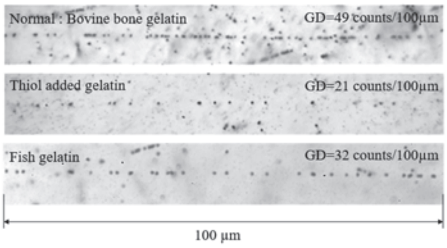

Fig.2. Micrographs of electron tracks recorded in nuclear emulsions with different gelatin compositions.

A sensitivity test was conducted as part of the development of nuclear emulsions with different types of gelatin. In the future, we plan to investigate the differences in sensitivity and the effects on latent image fading.

[1] K. Morishima *et al.*, Nature **552** (2017) 386.
[2] T. Tani *et al.*, Nucl. Instrum. Methods A **1006** (2021) 165427.

UVSOR User 8

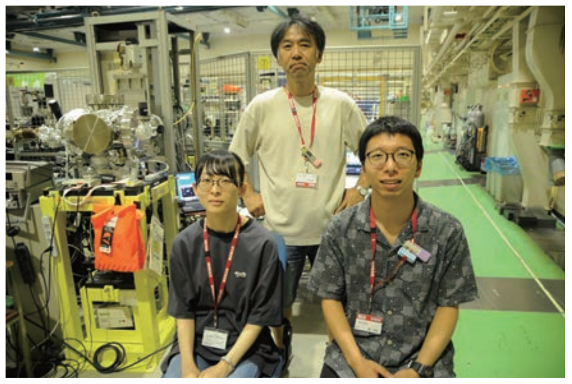

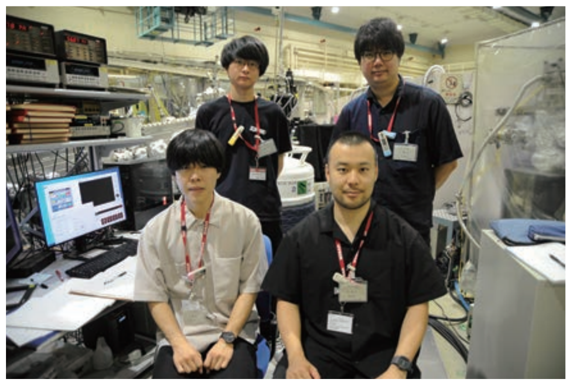

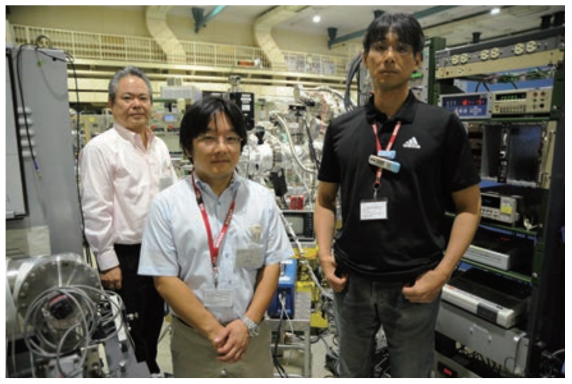

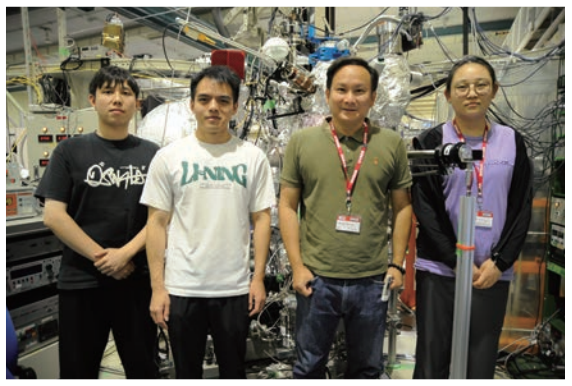

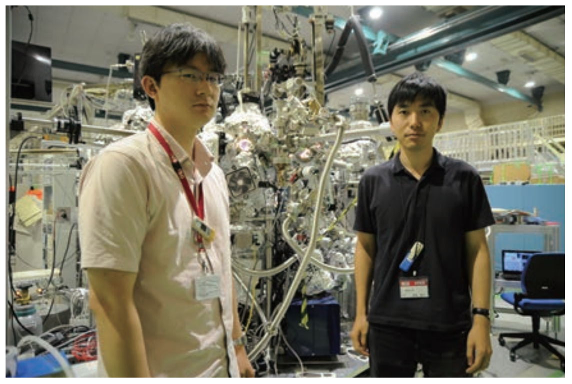

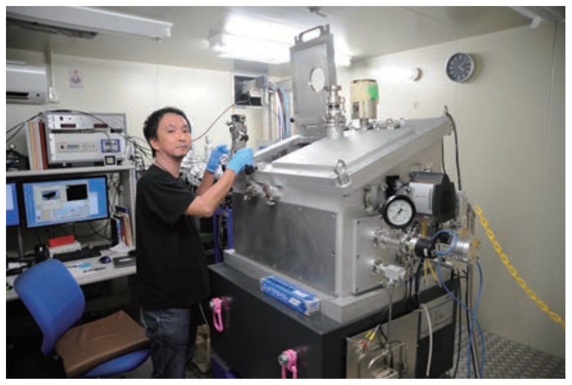

III-2

Material Sciences

BL1U

Gamma-Ray Induced Positron Annihilation Lifetime Spectroscopy of Undoped and Bi-Doped $SrTiO_3$ Ceramics

K. Kamoshida[1], M. Kitaura[1], M. Hagiwara[2], H. Masai[3], S. Watanabe[4] and Y. Taira[5,6]
[1] *Facalty of Science, Yamagata University, Yamagata 990-8560, Japan*
[2] *Department of Applied Chemistry, Keio University, Yokohama 223-8522, Japan*
[3] *Department of Materials and Chemistry, National Institute of Advanced Industrial Science and Technology (AIST), Ikeda 563-8577, Japan*
[4] *Innovative Technology Laboratories, AGC Inc., Yokohama 230-0045, Japan*
[5] *UVSOR Synchrotron Facility, Institute for Molecular Science, National Institutes of Natural Science, Okazaki 444-8585, Japan*
[6] *School of Physical Science, The Graduate University for Advanced Studies (SOKENDAI), Okazaki 444-8585, Japan*

Relaxors are dielectrics with substantial energy storage capacity. It is expected that these materials will contribute to the miniaturization and efficiency of diverse electrical systems. However, well-known lead-free ceramics exhibit challenges, including the generation of heat during voltage application, which can markedly reduce the capacitor's lifespan. To address this challenge, the focus has shifted to relaxor dielectrics such as (Sr,Bi)TiO_3 (SBT), which are obtained by Bi doping into $SrTiO_3$ (STO). This material has garnered significant attention due to its potential as a solution to the aforementioned issues [1]. The valence of the Bi atom occupying the A site (Sr site) is not equivalent to that of the Sr atom, suggesting the introduction of atomic vacancies to compensate for the charge of the Bi atom at the A site. In this study, we employed gamma-ray induced positron annihilation lifetime spectroscopy (GiPALS) and first-principles calculations based on density functional theory (DFT) to investigate whether atomic vacancies are introduced by Bi doping in STO.

Samples of STO and SBT were ceramics synthesized by the solid state reaction. The experimental details of the GiPALS analysis have been previously reported [2]. To identify the origin of atomic vacancies in SBT, positron annihilation lifetimes were determined by DFT calculation using the ABINIT code [3]. The GiPALS spectra of STO and SBT ceramics are shown in Fig. 1. The data were measured at room temperature. The GiPALS spectra of STO and SBT are characterized by a predominant exponential decay component. The positron annihilation lifetimes of STO and SBT were determined to be 187 ± 1 ps and 291 ± 1 ps, respectively. It is evident that the lifetime of the ceramics undergoes a substantial alteration upon the introduction of Bi doping. This substantial alteration in the lifetime of the ceramics suggests the introduction of atomic vacancies as a consequence of the Bi doping process. The calculated positron annihilation lifetime for the unit cell of STO (bulk lifetime) was 157 ps. The calculated bulk lifetime for STO was nearly equivalent to the experimental bulk lifetime of the STO single crystal (146 ± 2 ps). This outcome serves to substantiate the validity of the experimental approach employed in this study. Furthermore, the calculated lifetimes for the 2×2×2 supercells of STO containing cation vacancies at the A and Ti (B) sites were 277 ps ($q=-2$) and 195 ps ($q=-4$), respectively. It is noteworthy that these values exhibited slight variations depending on the valence of the supercell (q). In the STO ceramics, positrons can annihilate at either of dislocations or Ti vacancies at the B sites. The experimental lifetime for the SBT ceramics exhibited agreement with the calculated lifetime for the 2×2×2 supercells of STO containing a Sr vacancy at the A site. In the SBT ceramics, positrons most likely annihilate at Sr vacancies at the A sites. The analysis of the effect of Na and K codoping on vacancies at the A site is currently underway. This work was supported in part by JSPS Grants-in-Aid for Transformative Research Areas (A) Hyper-Ordered Structures Sciences (Nos. 23H04094, 23H04119, 20H05882).

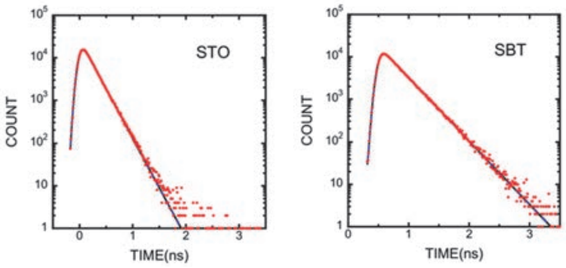

Fig. 1. GiPALS spectra of STO and SBT ceramics, measured at room temperature.

[1] D. Yuqin *et al*., Composites B **230** (2022) 109493.
[2] M. Kitaura *et al*., Opt. Mater.: X **14** (2022) 100156.
[3] X. Gonze *et al*., Comput. Phys. Commun. **248** (2020) 107042.

BL1U

Changes in Positron Annihilation Lifetimes for CeO_2 by Heat Treatment and Re-Adsorption of Oxygen

S. Dohshi[1], K. Maeda[1], Y. Taira[2] and T. Hirade[3]
[1]*Osaka Research Institute of Industrial Science and Technology*
2-7-1, Ayumino, Izumi, Osaka 594-1157, Japan
[2]*UVSOR Synchrotron Facility, Institute for Molecular Science, Okazaki 444-8585, Japan*
[3]*Japan Atomic Energy Agency, Ibaraki 319-1195, Japan*

In the previous study, the authors arranged a cerium oxide (CeO_2) catalyst within a quartz tube and performed gamma-ray induced positron annihilation lifetime spectroscopy (GiPALS) measurements at room temperature in air. The positron annihilation lifetimes of CeO_2 arranged within a quartz tube were nearly equivalent to those of CeO_2 measured without quartz tube. This result suggests that the positron annihilation lifetime measurements of CeO_2 can be performed, even though using quartz tube. Then, the GiPALS measurements were performed on CeO_2 that was arranged within a quartz tube and subjected to treat at 200 °C under argon (Ar) flow, resulting in changing the lifetime component attributed to the annihilation at CeO_2 surface. Additionally, the positron annihilation lifetime spectrum was observed to return to its original state when air containing water vapor was introduced, possibly due to the re-adsorption of oxygen and/or water molecules on the surface defect sites [1]. However, it was uncleared that which gas was re-adsorbed on the surface defect sites.

This study observed the changes in the positron annihilation lifetime spectra as the heating temperature was varied. Additionally, the changes in positron annihilation lifetime spectra were observed when only oxygen was re-adsorbed on CeO_2 treated at 200 °C under Ar flow.

The pellet sample with 20 mm in diameter and 10 mm in thickness were prepared using CeO_2 nanoparticles with a primary particle size of ca. 2 nm. In this experiment, the pellets were heated in a quartz tube at a rate of 10 °C/min using a jacket heater under Ar (purity: 99.999%) flow at pre-determined temperature (50 °C ~ 200 °C) and held for 2 h. After cooling under Ar flow, GiPALS measurements were performed. Finally, oxygen (purity: 99.999%) was flowed through at a rate of 200 mL/min for 1 h at room temperature, followed by another GiPALS measurement under oxygen flow.

We have set up a gamma-ray spectroscopy system at the laser-Compton scattering (LCS) beamline of BL1U at UVSOR-III [2], and measured the lifetime of the annihilation gamma-rays at room temperature using BaF_2 scintillation detector. We used the software Lifetime9 (LT9) to analyze the spectra.

The spectra were changed with the increase in the heating temperature. This is because the positron lifetime increases when heated under Ar flow. Adsorbed active oxygen species have been reported to desorb at temperatures above 150 °C. Consequently, the spectral change below 150 °C can be attributable to desorption of water molecules adsorbed on surface defect sites.

Figure 1 shows the positron annihilation lifetime spectra of CeO_2 at room temperature in air, treated at 200°C under Ar flow, and re-adsorbed oxygen. The positron annihilation lifetime becomes longer when CeO_2 was treated at 200 °C. This change was believed to result from the emergence of oxygen defects on the surface caused by the desorption of adsorption species such as active oxygen and water molecule, as above mentioned. Additionally, the positron annihilation lifetime spectrum was observed not to return to its original state when only oxygen was introduced. Considering the recovery of the spectrum to its original state upon the introduction of air containing water vapor, it can be assumed that there are multiple types of defect sites on CeO_2 surface. Details will be discussed in the future.

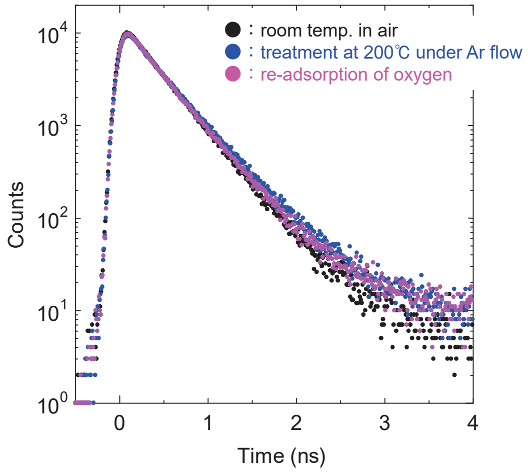

Fig. 1. Positron annihilation lifetime spectra of CeO_2 measured under different conditions.
(a) at room temperature in air, (b) after heating at 200 °C for 2h in Ar, (c) re-adsorption of oxygen.

[1] S. Dohshi *et al*., UVSOR Activity Report **51** (2023) 63.
[2] Y. Taira *et al*., Rev. Sci. Instrum. **84** (2013) 053305.

BL1U

Characterization of Defects in Ni Alloys Based on Gamma-ray-induced Positron Annihilation Spectroscopy

Z. Weixin[1,3], Y. Yuxuan[2,3], Y. Yigang[1] and Y. Taira[3]
[1]*Key Laboratory of Particle and Radiation Imaging (Ministry of Education) and Department of Engineering Physics, Tsinghua University, Beijing 100084, China*
[2]*School of Physics, Zhengzhou University, Science Avenue 100, Zhengzhou 450001, China*
[3]*UVSOR Synchrotron Facility, Institute for Molecular Science, Okazaki 444-8585, Japan*

Positron annihilation spectroscopy (PAS) serves as a powerful non-destructive probe for characterizing atomic-scale defects including vacancy and dislocation in bulk materials. In recent years, gamma-ray-induced positron annihilation spectroscopy (GiPAS) which can be used to study defects in crystals, metals, alloys, and polymers for thick samples (~cm) has developed rapidly [1]. This technology can be used to predict the fatigue and failure of the engineering materials by detecting the volumetric assay of defects at early stage.

The determination of the fatigue and failure level at the early stage before appearing obvious cracks of thick engineering materials is important to evaluate its service life. Inconel 718, a Ni-Fe-Cr austenite (γ) has attracted attention as its particular applications in a variety of applications like gas turbine blades, combustors. We systematically investigate defect evolution in industrial-grade Inconel 718 nickel-based superalloy subjected to incremental tensile deformation (0%, 0.2%, 1%, 2%, 5%, and 10%). GiPAS has been developed at UVSOR [2] and can be used to probe the detects of thick materials. The setup of positron annihilation lifetime spectroscopy (PALS) measurement is shown in Fig1.

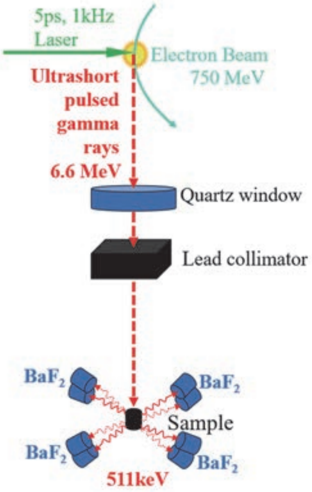

Fig. 1. Setup for PALS measurements.

We implemented PALS coupled with first-principles calculations based on density functional theory (DFT) to quantify defect characteristics. The experimental positron annihilation lifetimes (τ_1 and τ_2) and relative intensities (I_1 and I_2; $I_1 + I_2 = 1$) are analyzed using LT9 software. The results are shown in Fig2.

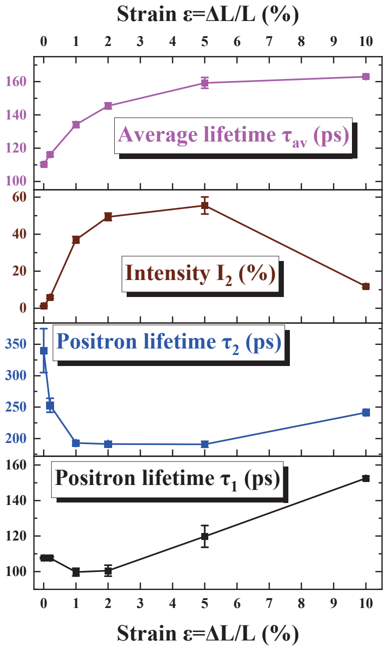

Fig. 2. Fitting results of the experimental positron lifetime spectra.

The calculated free-state positron lifetime of Ni alloy ($Ni_{19}Fe_6Cr_6Nb$) is approximately 106ps. As the positron lifetime τ_1 is larger than this value, it can be considered as a weighted sum of the free-state positron lifetime and the positron lifetime at the dislocation defects. The positron lifetime τ_2 has a range of 190-400ps, which corresponds to the positron lifetime at the vacancy-type defects according to the calculated results. The average positron lifetime tend to increase with increasing tensile strain and indicates that the densities of dislocation and vacancy defects in the sample increase with increasing tensile strain. When the tensile strain reached to 10%, the intensity I_2 has an obvious change which may mean that the defect structure in the sample has changed significantly.

[1] F. A. Selim *et al.*, Nucl. Instr. Meth. Phys. A **495** (2002) 154.
[2] Y. Taira *et al.*, Rev. Sci. Instrum. **84** (2013) 053305.

BL2A

Mo L_{III}-edge XANES Study of Formation of Catalytically Active Mo_2C Species on H-MFI Zeolites for Methane Aromatization

K. Kuramochi[1], Y. Mita[2], A. Kosuge[2] and H. Aritani[2]
[1]*Advanced Science Research Laboratory, Saitama Institute of Technology, Fukaya 369-0293, Japan*
[2]*Faculty of Engineering, Saitama Institute of Technology, Fukaya 369-0293, Japan*

Molybdenum-modified H-MFI zeolite (Mo/H-MFI) is a typical GTL (Gas To Liquid) catalyst for natural gas transformation. High catalytic activity over the Mo/H-MFI is shown for methane conversion to benzene although definite deactivation due to coke deposition has been a serious problem for durable MTB reactivity. It has been revealed that the reactions at high pressure (0.15 - 0.20 MPa) and the addition of H_2 to the CH_4 reactant were each effective in suppressing catalyst deactivation. On these reaction conditions, deactivation process over the catalysts is one of the important points. A cause of the deactivation is based on coke deposition on strong acid sites over H-MFI and structural deactivation on carbonized MoC_x species. Thus, clarification of Mo sites with high and durable activity for methane dehydrogenation is one of the most important subjects. In the present study, Mo L_{III}-edge XANES is applied to characterize the active Mo carbide species on Mo/H-MFI. In the present study, time course of the formation of active Mo_2C species on H-MFI has been investigated.

Mo(5wt%)/H-MFI (Si/Al_2 ratios in H-MFI supports are 23 and 50) catalysts were prepared by impregnation of H-MFI in $MoO_2(acac)_2$-$CHCl_3$ solution, and followed by drying overnight and calcination at 773 K. The methane aromatization reactivity was evaluated at 1023 K in a steady-state reaction by using CH_4(20%)-H_2(2%)-Ar(base) reactant as described in a previous report[1]. Mo L_{III}-edge XANES spectra were obtained in BL2A of UVSOR-IMS in a total-electron yield mode using InSb double-crystal monochromator. REX-2000 (Rigaku) software was used for normalization of each XANES spectra.

It has been summarized that the catalytic MTB activity over Mo/H-MFI with Si/Al_2=50 shows high activity at high pressure (0.15-0.20 MPa), and deactivation rate over reaction time is extremely small. In contract, Mo/H-MFI with Si/Al_2=23 exhibited high activity with significant deactivation over time[2]. For these catalysts, time course of the formation of Mo species during the reaction was investigated as follows. The L_{III}-edge XANES spectra over the Mo/H-MFI catalysts on time course of the MTB reaction in 0.15 MPa are shown in Fig. 1. In both catalysts before reaction, the spectra are almost similar to that of MoO_2, indicating the formation of Mo^{4+} by pre-reduction treatment with CO(2%)-Ar. For Mo/H-MFI in Si/Al_2=23, the XANES spectrum after the reaction for 30 minutes was very similar to that of α-type Mo carbide (α-MoC_{1-x}) with cubic structure, indicating that the Mo species were carbonized reductively at the early stage of the reaction. The XANES edge energy of the active Mo species shifted to the lower energy side with the progression of reaction time, suggesting that reduction by carbonization had further progressed. For Mo/H-MFI in Si/Al_2=50, the XANES spectrum after the reaction for 30 minutes was very similar to that of β-type Mo_2C with orthorhombic structure. It indicates the formation of easily reduced Mo sites to form more deeply carbonized species than that of Mo/H-MFI in Si/Al_2=23. Since the β-Mo_2C active species hardly changed with the progression of reaction time, it is suggested that they exist as stable carbide species. The result is likely to relate to a suppression effect of deactivation.

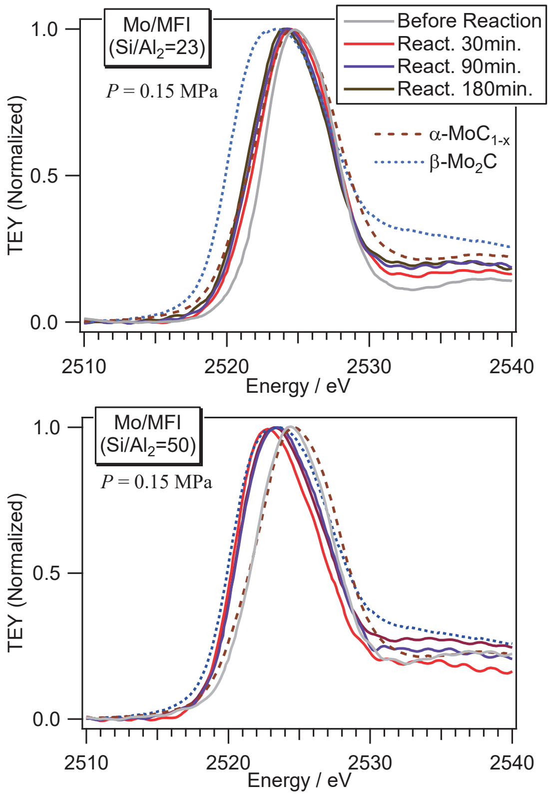

Fig. 1. Mo L_{III}-edge XANES spectra of Mo/H-MFI catalysts in Si/Al2=23 (top) and 50 (bottom) after the MTB reaction at 1023 K.

[1] H. Aritani *et al.*, J. Environm. Sci. **21** (2009) 736.
[2] K. Kuramochi *et al.*, UVSOR Activity Report **51** (2023) 69.

BL2A

Local Structure Investigation of Zn Dopant in Ga_2O_3

S. Yoshioka[1], K. Yasuda[1], C. Hsiao[2], C Hsu[2], W. Olovsson[2], J. Brick[2],
C. Hemmingsson[2] and G. Pozina[2]
[1]*Department of Applied Quantum Physics and Nuclear Engineering, Kyushu University,*
Fukuoka 819-0395, Japan
[2]*Department of Physics, Chemistry, and Biology, Linköping University, Linköping 58183, Sweden*

Gallium oxide (Ga_2O_3) is a promising ultrawide bandgap semiconductor for high-voltage and high-power applications. Monoclinic β-phase of Ga_2O_3, which has tetrahedral and octahedral gallium sites, is unintentionally *n*-type doped, and a good control of electron carrier concentrations in the range of 10^{16}–10^{19} cm^{-3} or even higher can be achieved using intentional doping by Si, Sn, Ge and Nb. However, the electrical conductivity of *p*-type in β-Ga_2O_3 is difficult to be realized. First-principles calculations showed that Zn can be a suitable acceptor forming two shallow levels at 0.05 eV and 0.07 eV above the valence band in β-Ga_2O_3 when Zn substitutes Ga in tetrahedral and octahedral coordination, respectively. We utilize halide vapor phase epitaxy growth to synthesize epitaxial layers of β-phase Ga_2O_3 doped with Zn, which can serve as a suitable acceptor. To determine the location of Zn ions within the β-Ga_2O_3 lattice, we employed X-ray absorption near edge structure (XANES) in conjunction with first principles density functional theory (DFT) calculations.

The Zn concentration of thin films, named as ZGO-L and ZGO-H, were 1.7×10^{19} and 2.5×10^{20} ions/cm^3, respectively. XANES measurements of the Zn L_3-edge and Ga L_3-edge were performed on the BL2A beamline of UVSOR Okazaki, Japan, using the partial fluorescence yield method (PFY). A $Be_3Al_2Si_6O_{18}$ (beryl) double-crystal monochromator gives the Zn L_3-edge and the Ga L_3-edge in the energy regions 1000 – 1070 eV and 1100 – 1170 eV, respectively. The samples were set with their surface perpendicular to the incident X-ray beam. Fluorescence X-rays of Zn L_α and Ga L_α were collected using an energy dispersible silicon drift detector (SDD).

The XRD pattern of the Zn doped samples appear to be similar to that of the undoped Ga_2O_3 samples. However, the information obtained from the XRD measurements was insufficient to conclude the exact position of the Zn atoms in the monoclinic Ga_2O_3 lattice. Moreover, it was also not clear whether Zn can build clusters or if it can include small numbers of ZnO or $ZnGa_2O_4$.

XANES spectra with the Zn L_3-edge (1020 eV) were shown in Fig. 1 for the Zn-doped Ga_2O_3 thin film sample and a reference ZnO powder sample. The intensity of each spectrum was normalized to a value of 1 at 1050 eV after the removal of the background intensity. The spectral signal-to-noise ratios of the thin films were slightly low because of the dilute concentration of zinc, however, fine structures such as peaks *A* to *G* were detected. In terms of such identical peaks, the spectrum shape of ZGO is clearly different from that of standard sample ZnO with a wurtzite type structure. The theoretical investigation using first principles calculation indicated that Zn ions occupied at cationic positions at the tetrahedral coordinated sites [1].

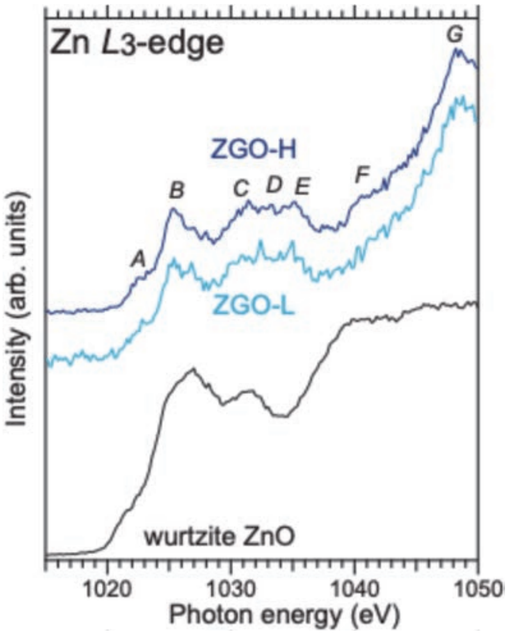

Fig. 1. Zn L_3-edge XANES spectra of the Zn-doped Ga_2O_3 thin films, together with the spectrum of wurtzite ZnO powder as a reference.

[1] S. Yoshioka *et al.*, J. Phys. Chem. C. **128** (2024) 18879.

BL2A

sXAS Study of the Fe-NiS OER Catalyst

Z. WANG[1], Y. ZHANG[1] and J. LEI[1]
[1]*City University of Hong Kong, Kowlong, Hong Kong*

Iron-doped nickel sulfide (Fe–NiS) catalysts are widely studied for the oxygen evolution reaction (OER) because adding Fe into NiS significantly enhances both activity and stability compared to pure NiS. Nickel sulfides possess high electrical conductivity and accessible redox chemistry but tend to reconstruct under anodic potentials: Ni^{2+} centers are oxidized to higher-valence states, and sulfide ligands transform into oxy- or sulfate species. Introducing Fe further adjusts the Ni–S electronic environment, accelerates redox kinetics, and helps suppress corrosion by promoting in situ formation of protective iron–oxygen clusters.

Soft X-ray absorption spectroscopy (sXAS) at the Ni L_3 and S K edges is particularly well suited to tracking these reconstruction events. At the Ni L_3 edge, 2p→3d transitions reveal changes in nickel oxidation state and local coordination—indicators of active Ni^{3+} (and Ni^{4+}) species forming under OER bias. At the S K edge, 1s→3p transitions distinguish sulfide (S^{2-}), intermediate oxy-sulfur species (e.g., sulfite), and final sulfate (SO_4^{2-}) states. Comparing spectra before and after OER clearly shows how the Ni–S framework evolves: the sulfide network converts into an oxyhydroxide-like shell enriched in Ni^{3+}/Ni^{4+} and surface sulfates, which directly influence catalytic kinetics and durability.

Understanding these electronic and chemical transformations is crucial for rational catalyst design. Ni^{3+} species on the surface are recognized as the true active sites for OER, while conversion of sulfur ligands to sulfate creates a passivating layer that repels corrosive ions (e.g., Cl^- in seawater), thereby improving long-term performance. Operando sXAS thus provides a microscopic picture of how Fe–NiS catalysts dynamically self-organize into their most active and stable configurations during water oxidation. These linsights guide strategies such as optimizing Fe/Ni ratios, controlling sulfide crystallinity, and adjusting electrolyte composition to develop highly efficient and durable OER catalyst

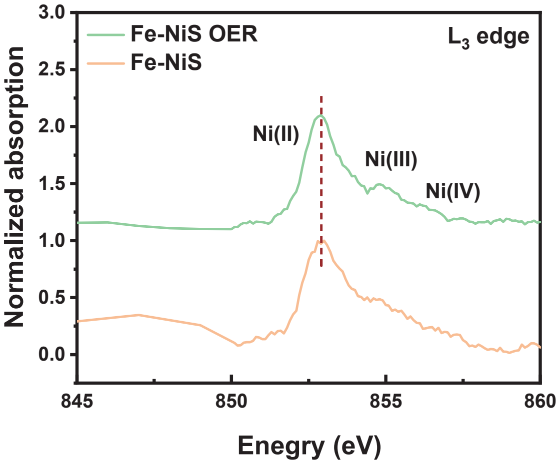

Fig. 1. Ni L-edge sXAS of Fe-NiS catalyst.

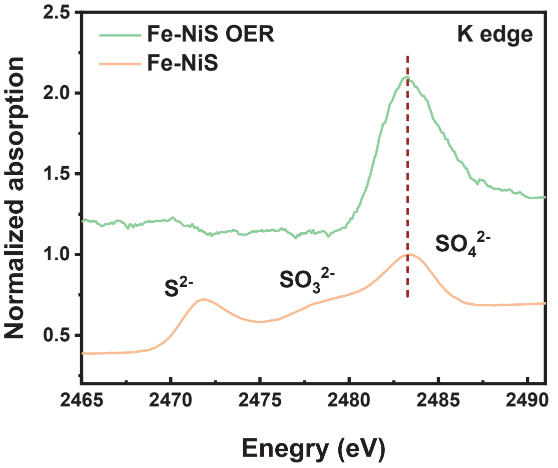

Fig. 2. S K-edge sXAS of Fe-NiS catalyst.

[1] Q. Dai *et al*., Nano Res. **17** (2024) 6820.
[2] X. Luo *et al*., Nat. Commun. **15** (2024) 8293.
[3] F. Jalilehvand, Chem. Soc. Rev. **35** (2006) 1256.

BL3U

Surface Effect on the Layer Structure in the Chiral SmC Variant Phase Delicate Balance of Ferroelectricity and Antiferroelectricity by Resonant Soft X-ray Scattering (RSoXS) at UVSOR

Y. Takanishi[1], F. Araoka[2] and H. Iwayama[3]

[1]*Department of Physics, Kyoto Prefectural University of Medicine,1-5, Shimogamohangi-cho,*
Sakyo, Kyoto 606-0823, Japan
[2]*RIKEN Center for Emergent Matter Science, Hirosawa 2-1, Wako, Saitama 351-0198, Japan*
[3]*UVSOR Synchrotron Facility, Institute for Molecular Science, Okazaki 444-8585, Japan*

The ferroelectricity and antiferroelectricity have been found in the tilted chiral smectic phases, called SmC* and SmC$_A$*, respectively. By competition of SmC* and SmC$_A$*, several phases with narrow temperature range were often found, called subphases. Subphases have are defined as the relative ratio of anticlinic and synclinic ordering, q$_T$. The structures of subphases becomes decisive using resonant X-ray scattering (RXS), and one of authors (YT) discovered new subphases with 6-, 7-, 8- and 10-layer periodicities[1,2].

In a certain chiral binary system, it was found that clear phase transition between subphases seems not to be seen[2]. The composed compounds do not have a specific atom, so that resonant soft x-ray scattering (RSoXS) has been applied to this study, and we directly observed the structure of continuous change between SmC* and SmC$_A$* using wide angle RSoXS.

The experiment was performed at BL3U of UVSOR. Used sample is a mixture of MC881 and MC452, as shown in Fig. 1. Figure 1(c) shows the phase diagram around the critical mixing ratios. In this study, two types of sample cells were prepared; a planar sub-micron thick sandwich cell whose substrates are 100 nm-thick Si_3N_4 membranes, and the liquid-crystal-filled grid mesh for electron transmission microscopy. The scattering was detected by CCD (ANDOR DO940P-BN). Incident X-ray beam was tuned between 270~300 eV, and carbon K-edge energy was 284.5 eV in the mixture.

RSoXS intensity profiles of the mixture of 55.7wt% MC452 at 24°C in the sandwich cell and the mesh are shown in Figs. 2(a) and (b), respectively. In Fig.2(a), a strong sharp peak was observed at Q ~ 1.1 nm^{-1} suggesting to the bilayer structure, while a splitted strong peak at Q ~ 0.55 nm^{-1} corresponding to the 4-layer periodicity was observed in Fig. 2 (b). (Peak splitting is caused by the helical structure.) This difference is considered to be caused by the surface effect. The gap of membrane sandwich cell was very thin. Hence the strong surface effect appears and molecular orientation is limited to the substrate surface plane. On the other hand, in the mesh cell, the surface effect is weak. As a result, the molecular orientation has the degree of freedom in the azimuthal angle as a bulk state. The difference in structure between these two cells is believed to be due to the surface effects mentioned above, and the small energy difference between the ferroelectric and antiferroelectric orders.

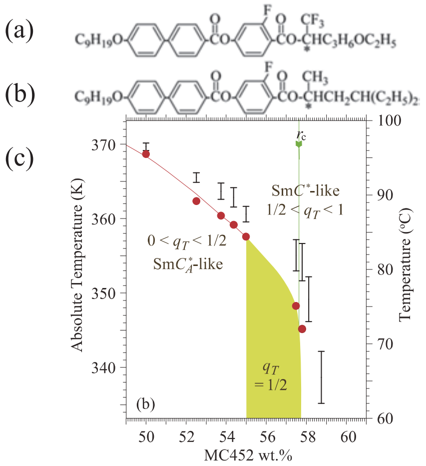

Fig. 1. Chemical structures of (a)MC452 and (b) MC881, and (c)the phase diagram referred from [3].

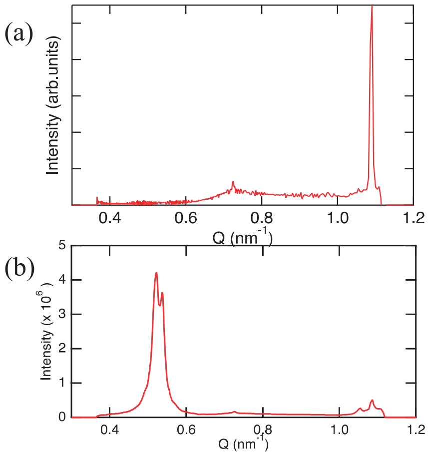

Fig. 2. RSoXS intensity profiles of the sandwich cell (a) and the grid mesh (b) of the mixture of 55.7wt% MC452 at 24°C.

[1] Y. Takanishi *et al.*, Phys. Rev. E **87** (2013) 050503 (R).
[2] Z. Feng *et al.*, Phys. Rev. E **96** (2017) 012701.
[3] Z. Feng *et al.*, Phys. Rev. E **102** (2020) 012703.

BL3B

Non-Proportional Response between Scintillation Light Yield and Energy of the Incident Gamma Rays

S. Kurosawa[1,2,3], Y. Urano[2,4], C. Fujiwara[2,4] and A. Yamaji[1,2]
[1]New Industry Creation Hatchery Center (NICHe), Tohoku University, Sendai 980-8579, Japan
[2]Institute for Materials Research (IMR), Tohoku University, Sendai 984-8577, Japan
[3]Institute of Laser Engineering, The University of Osaka, Suita, Osaka 565-0871, Japan
[4]Graduate School of Engineering, Tohoku University, Sendai 980-0845, Japan

Boron neutron capture therapy (BNCT) is one of the treatments to selectively destroy cancer cells using a nuclear reaction between ^{10}B and neutrons. Although evaluation of the treatment effect in real-time is required for patient safety, the monitoring system has not been realized. The use of prompt gamma rays (478 keV) emitted by the ^{10}B(n,α)^{7}Li reaction during BNCT therapy has been proposed as this monitoring system[1], and the 478-keV gamma-ray signal should be discriminated from the background (BG) events including 511-keV gamma rays from positron and electron annihilation. Thus, scintillators are required to have an energy resolution better than 4 % (FWHM) at 511 keV.

Tl-doped $Cs_3Cu_2I_5$ (Tl:CCI) scintillator has a high light output of over 90,000 photons/MeV and a high energy resolution of 3.3% at 662 keV (FWHM), which corresponds to 3.7% at 511 keV (FWHM) [2]. Moreover, the hygroscopic nature of this material is ignorable, as even typical iodide crystals have. Thus, this material is expected to be suitable for gamma-ray detection of the BNCT clearly, if the energy resolution is improved.

Here, energy resolution is related to light yield and non-proportionality between scintillation light yield and energy of the incident gamma rays. Tl:CCI has a non-proportional response (NPR) of over 3%, where NPR is defined in [3]. Recently, NPR and energy resolution for Sr^{2+}-co-doping Tl^{+}-doped NaI have been reported to be improved [3]. Therefore, we grew Tl^{+} and Sr^{2+} co-doped CCI (Tl,Sr:CCI) crystals and evaluated their luminescence and scintillation properties.

Tl,Sr:CCI, Sr:CCI, Tl:CCI and pure CCI crystals were grown by the vertical Bridgman-Stockburger method in our laboratory, and we verified the single crystal phase and composition using several X-ray devices. Also, we have measured several optical properties such as emission and excitation wavelength, light output and NPR. The results showed Sr-dopant effect was also observed for Tl,Sr:CCI; NPR and energy resolution were improved compared to Tl:CCI

In UVSOR, we investigated several properties, especially the role of the Sr. The temperature dependence of photoluminescence excitation and emission spectra from 10 to 350 K were evaluated at UVSOR BL3B beam line.

Here, we measured excitation and emission two-dimensinal map at each temperature, and over 150K the emission and excitation wavelengths were slightly shifted for the both samples. This result suggested CCI has different emission mechanisms in the lower and higher temperature regions.

Figure 1 shows the temperature dependence of emission intensities for pure CCI and Sr:CCI, and the both data were fitted by the Arrhenius equation blow 150 K. The fitting results showed the activation energy was shifted by Sr-co-doping. This result suggested Sr^{2+} or indirect effect by the Sr^{2+} co-doping affects some trap site which is related to the non-proportionality and energy resolution.

We also measured the thermoluminescence grow curve in the BL3B beam line for the Sr-doped and Sr-free CCI. Although the results are preliminary ones, the differences are not observed clearly. These results indicated the de-excited electrons from such trap sites to ground state are relaxed by non-radiative process, or these trap sites can be located at deep level, which means de-trapping energy is expected to be over room temperature.

To analyze the details, we grew different concentration of Sr to doped with Tl:CCI and also Ca-co-dopant effect is investigated.

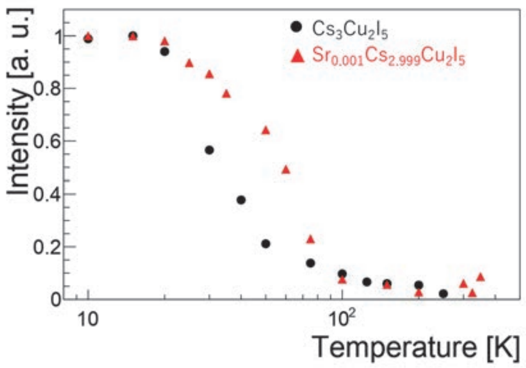

Fig. 1. Emission intensity as a function of temperature, where the intensities are normalized to 1 at 10 K.

[1] D.M. Minsky *et al.*, Appl. Radiat. Isot. **67** (2009) 179.
[2] L. Stand *et al.*, Instrum. Methods Phys. Res. A **991** (2021)164963.
[3] K. Yang *et al.,* J. Appl. Phys. **118** (2015) 213106.

BL3B

VUV Excitation Property of NIR Phosphor Eu:$CaSc_2O_4$

S. Kodama[1], T. Saito[1], I. Yanase[1] and H. Takeda[1]
[1]Graduate school of Science and Engineering, Saitama University,
255 Shimo-Okubo, Sakura-ku, Saitama 339-8570, Japan

Red or NIR emitting phosphors are widely used in white light-emitting diodes (LEDs) and as sensor materials such as scintillators or dosimeters. Most of the red or NIR phosphor was activated by the transition metals (particularly Cr^{3+} or Mn^{2+}) or rare earth metals exhibiting 4f-4f electron transition emission (particularly Pr^{3+}, Nd^{3+} or Yb^{3+}). Conventional red or NIR luminescence centers have several limitations, for instance, the luminescence decay is slow, and the range of excitation wavelength is narrow.

Recently, some phosphors activated by Eu^{2+} were reported to exhibited fast red or NIR emission. For example, the emission wavelengths of Eu:CaO and Eu:$Ca_3Sc_2Si_3O_{12}$ were 650 nm and 850 nm, respectively, with the faster luminescence decay than 1 µs [1,2]. Eu^{2+}-doped calcium-based materials are getting a attention as next-generational fast red or NIR phosphors. In this report, the VUV excitation property of noble NIR phosphor Eu:$CaSc_2O_4$ was investigated for the first time.

Eu:$CaSc_2O_4$ was synthesized via the high-temperature solid phase reaction from $CaCO_3$ (99.99%), Sc_2O_3 (99.99%) and Eu_2O_3 (99.99%). The starting powders are mixed in an agate mortar. The mixed powders were calcined at 1500 °C for 5 h in air. After calculating, the powders were annealed in a reducing atmosphere (N_2+H_2 gas) at 1000 °C for 5 h, and Eu^{2+}:$CaSc_2O_4$ was finally obtained [3].

The VUV-VIS-NIR photoluminescence excitation and emission spectra were measured in BL3B. The measurement temperature was 300 K. In order to cut the Eu^{3+} emission, the short-wavelength-filter (700 nm) was used in the measurement.

The photoluminescence excitation and emission spectra of Eu:$CaSc_2O_4$ is depicted in Fig. 1. The sample was excited using monochromatic photons ranging from 100 to 700 nm, and the photoluminescence emission spectra were recorded within the 550–1050 nm range. This measurement identified the Eu^{2+} emission wavelength of Eu:$CaSc_2O_4$ as 750 nm, situated in the red-NIR region. N_2+H_2 annealing at 1000 °C for 5 h should be insufficient to reduce Eu^{3+} completely into Eu^{2+}, and the Eu^{3+} 4f-4f emission was strongly observed in the same time.

The photoluminescence excitation spectra of Eu:$CaSc_2O_4$ were notably broad, spanning from 120 to 700 nm, indicating that Eu:$CaSc_2O_4$ can be excited by the entire range of VUV and visible photons. For practical applications, the excitation source for Eu:$CaSc_2O_4$ should be compatible with UV LEDs, blue LEDs, or green laser diode systems (LDSs).

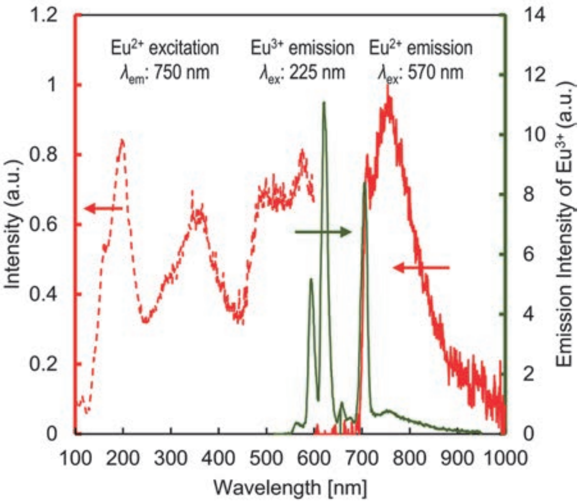

Fig. 1. Photoluminescence excitation and emission spectra of Eu:$CaSc_2O_4$.

[1] Q. Zhao *et al.*, J. Lumin. **253** (2023) 119457.
[2] I. V. Berezovskaya *et al.*, Chem. Phys. Lett. **585** (2013) 11.
[3] S. Kodama *et al.*, J. Soc. Inorg. Mater. Jpn *accepted.*

BL3B

Energy Transfer from I^- Centers to Ce^{3+} Centers in Co-Doped NaCl: I^-, Ce^{3+} Crystals

R. Oda[1] and T. Kawai[1]

[1]*Graduate School of Science, Osaka Metropolitan University, Sakai 599-8531, Japan*

Alkali halide crystals have the wide band-gap up to the vacuum ultraviolet energy region and are a suitable candidate host for doping of impurity ions. We have studied energy transfer between two kinds of impurity ions doped in alkali halide crystals from the measurements of their optical properties [1-3]. In this study, we focused on Ce^{3+} ions as acceptor ions and investigated the energy transfer from I^- Centers to Ce^{3+} Centers in co-doped NaCl:I^-, Ce^{3+} crystals.

The Ce^{3+} ions in crystals exhibit the luminescence due to the radiative transition from the lowest 5d excited level to the split 4f ground levels. The 5d -> 4f radiative transition in the Ce^{3+} ions is a dipole-allowed one with a typical decay time of about 20 ns [4]. The fast decay profiles allow us to measure a rise time due to energy transfer to the acceptor ions under single-bunch operation of UVSOR.

Figure 1 shows the luminescence and absorption spectra of co-doped NaCl:I^-, Ce^{3+} crystals at 10 K. The intense absorption and luminescence bands due to the I^- centers are observed at 6.9 eV and 5.7 eV, respectively. The luminescence band at 5.7 eV comes from one-center-type relaxed excitons, which consist of a hole localized on an iodine anion and a bound electron, that is to say, special type of bound excitons [5]. Two luminescence peaks due to the Ce^{3+} centers were observed at 3.37 eV and 3.64 eV.

Figure 2 shows decay profiles of the Ce^{3+} luminescence under the excitation on the I^- absorption band at various temperatures. Below 100 K, the Ce^{3+} luminescence exhibits the double exponential decay profiles, which have no rise time. Above 200 K, on the other hand, a rise time of a few tens of nanoseconds was observed in the decay profile of the Ce^{3+} luminescence. The rise time decreases with increasing temperature. It is difficult to believe that the slow rise time of a few tens of nanoseconds is attribute to energy transfer by the Förster-Dexter mechanism or the luminescence-reabsorption mechanism. In our previous paper [2], we have proposed the energy transfer processes through the migration of the V_K center generated from the excited I^- centers in NaCl crystals. The idea is supported by the slow rise time of a few tens of nanoseconds in the decay profile of the Ce^{3+} luminescence. The temperature dependence of the rise time indicates that the migration of the V_K center occurs by thermally activated hopping.

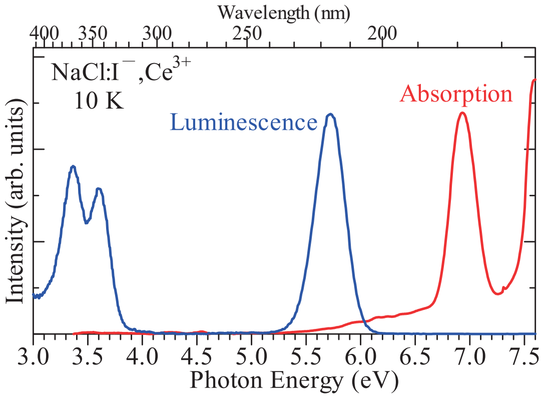

Fig. 1. Luminescence (blue) and absorption (red) spectra in co-doped NaCl:I^-, Ce^{3+} single crystals.

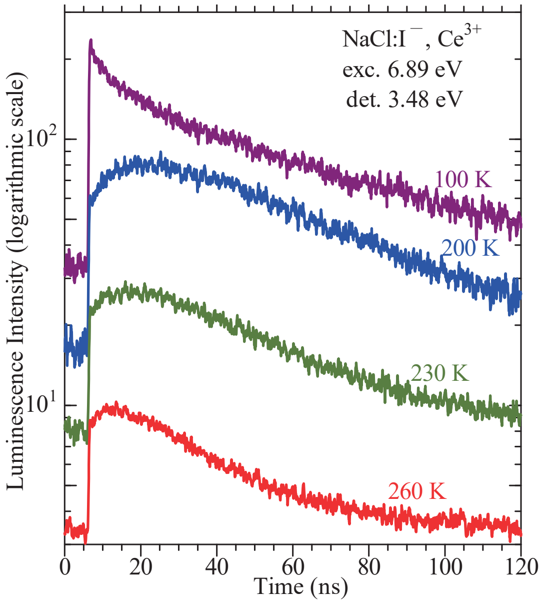

Fig. 2. Decay profiles of the Ce^{3+} luminescence under the excitation on the I^- absorption band at various temperatures.

[1] A. Iguchi, T. Kawai and K. Mizoguchi, Phys. Status Solidi C **13** (2015) 85.
[2] O. Yagi, T. Kawai and K. Mizoguchi, J. Lumin. **226** (2020) 117359.
[3] R. Oda and T. Kawai, UVSOR Activity Report **51** (2024) 80.
[4] Y. Yokota *et al.*, Radiat. Meas. **45** (2010) 472.
[5] I. Akimoto, M. Shimozato and K. Kan'no, Phys. Status Solidi C **6** (2009) 342.

BL3B

Investigation of Charge Transfer Energies in Eu^{3+}-Doped Layered Mixed-Anion Phosphor by VUV Spectroscopy

H. Miyata[1] and J. Ueda[1]

[1]*Japan Advanced Institute of Science and Technology, Nomi 923-1292, Japan*

Persistent phosphors are luminescent materials that emit light for a long duration after the excitation source is turned off. They are widely used in many applications such as luminous paints in the dark for hazard signboards and road markers and luminescent markers for in vivo imaging. Persistent luminescence originates from the temporary trapping of the electrons or holes, generated with light absorption, by crystalline defects. The trapped electrons or holes are thermally released and transferred back to the luminescent center.

So far, aluminate and silicate compounds such as $SrAl_2O_4:Eu^{2+}$-Dy^{3+} [1] and $Sr_2MgSi_2O_7:Eu^{2+}$-Dy^{3+} have been widely used as practical persistent phosphors. In contrast, oxides including other oxoanion (CO_3^{2-}, NO_3^- and etc.) and non-oxides are still an unexplored material group for persistent phosphors and have the potential to show excellent persistent luminescent properties. Existing persistent phosphors have mostly shown blue and green luminescence. Therefore, there is a need to develop high-performance red persistent phosphors. Eu^{3+} is a promising candidate as a red emitting central ion. In addition, long afterglow properties have been reported for Eu^{3+}-doped phosphors in $Y_2O_2S:Eu^{3+}$-Ti-Mg.

In Eu^{3+}-doped persistent phosphors, the (de)trapping carriers are holes. Thus, the holes migrate in the valence band (VB) after charge transfer excitation and are trapped by crystalline defects and metal ions.[2] Therefore, understanding charge transfer (CT) behavior in Eu^{3+}-doped phosphors is essential for the development of persistent phosphors. In this study, we focus on Eu^{3+}-doped $La_2O_2CO_3$ reported by Masui and Imanaka [3]. Here, we prepared another polymorph of Eu^{3+}-doped $La_2O_2CO_3$ and discussed its charge transfer behavior from VUV PLE spectra.

Photoluminescence excitation (PLE) spectra of Eu^{3+} doped $La_2O_2CO_3$ at 10 K are shown in Fig. 1. PLE spectra were measured with monitoring Eu^{3+} ${}^5D_0$–${}^7F_0$ emission. In the PLE spectra, two broad PLE bands are observed around 175 nm and 192 nm. The PLE band at 192 nm is attributed to the CT band of Eu^{3+}, and the PLE peak at 175 nm is attributed to the host-exciton formation. The E_g is calculated to be 6.98 eV using the obtained E_{ex} (192 nm). The CT bands were well-fitted by two Gaussian functions. Since $La_2O_2CO_3$ is a mixed anion compound, charge transfers derived from the two anions O^{2-} and CO_3^{2-} are possible. The CT energy (E_{CT}) of single anion compounds La_2O_3:Eu were reported to be 4.27 eV [4], and $Eu_2(CO_3)_3$ was estimated to be 5.30 eV from the PLE spectrum. Based on the obtained E_{CT}, a stacked vacuum referred binding energy (VRBE) diagram are prepared as shown in Fig. 2. According to the VRBE diagram, the low-energy CT band is attributed to O^{2-} and the high-energy CT band to CO_3^{2-}. By mixing with carbonate anion, the oxide can lower the valence band energy. Based on the valence band engineering by oxoanion doping, the hole-detrapping persistent phosphors will be developed in the future.

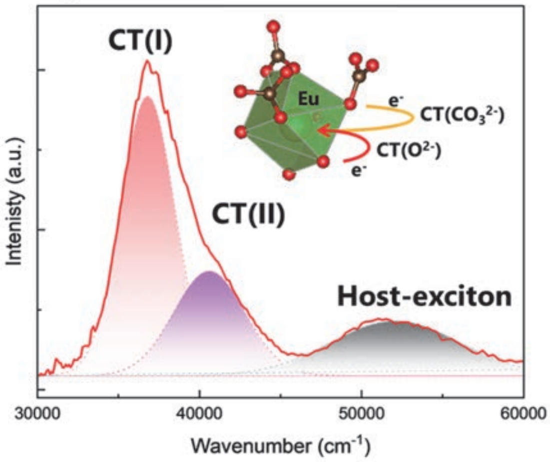

Fig. 1. PLE spectra of $La_2O_2CO_3$:Eu and crystal structure of $La_2O_2CO_3$ around La site.

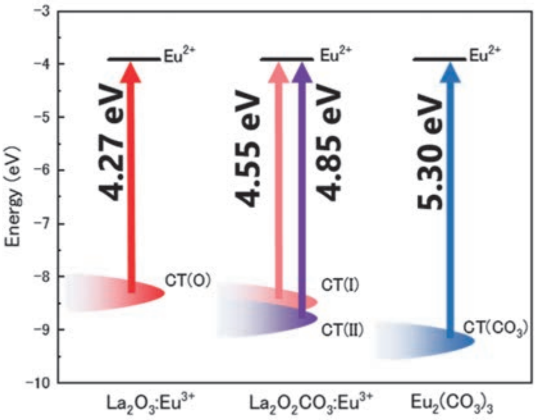

Fig. 2. Energy diagram of Eu3$^+$ charge transfer state and valence band top of La_2O_3, $La_2O_2CO_3$, $Eu_2(CO_3)_2$.

[1] T. Matsuzawa *et al.*, J. Electrochem. Soc. **143** (1996) 2670.

[2] J. Ueda, Bull. Chem. Soc. Japan **94** 2 (2021) 2807.

[3] K. Koyabu, N. Imanaka, *et al.*, J. Alloys Compd. **408–412** (2006) 867.

[4] Linkang Yu *et al.*, J. Lumin. **229** (2021) 117663.

BL3B

Effect of Ag-Doped Phosphate Glass for Radiophotoluminescence Dosimeter

J.Y. Cho[1], E.J. Choi[1], D.W. Jeong[1], N.D. Ton[1] and H.J. Kim[1]
[1]*Department of Physics, Kyungpook National University, Daegu 41566, Republic of Korea*

The release of large quantities of radioactive material during nuclear disasters such as Fukushima and Chernobyl has highlighted the critical importance of accurate radiation dosimetry. Reliable dose measurement is essential for ensuring radiation safety, assessing long-term health risks, and implementing appropriate protective measures. Traditional dosimeters such as Metal-Oxide-Semiconductor Field-Effect Transistor (MOSFET) dosimeters and thermoluminescence dosimeters (TLDs) are widely used due to their sensitivity and reusability. However, TLDs suffer from significant drawbacks, including high-temperature readouts, signal fading over time, and limited reproducibility. These limitations emphasize the need for alternative dosimetry technologies with improved performance and reliability. Radiophotoluminescence (RPL) glass dosimeters have emerged as a promising solution, offering excellent signal stability, dose linearity, and long-term reproducibility. In particular, the commercial GD-450 dosimeter, based on silver-doped phosphate glass, has demonstrated robust performance in both personal and environmental radiation monitoring.

Building on the strengths of existing RPL technologies, this study focuses on the development of enhanced RPL glass dosimeters through compositional engineering. Specifically, silver-doped phosphate glasses were synthesized using a variety of glass-modifying oxides to tailor their structural and luminescent properties. Glass modifiers play a crucial role in adjusting physical and optical characteristics by introducing non-bridging oxygens that alter the glass network. Drawing from previous research, including studies by Miyamoto *et al*. and Yoshida *et al*. [1, 2], which clarified the emission mechanisms and improved the thermal stability of silver-doped glasses, we aimed to further optimize RPL performance. By comparing the newly developed glasses with the commercial GD-450, this study investigates improvements in sensitivity and dose linearity, with the ultimate goal of advancing RPL dosimetry technologies for broader and more demanding applications.

The PLAN glasses were fabricated two way using conventional melting quenching method at atmospheric environment and induction melting quenching method at nitrogen enviroment in following composition: (75.6P_2O_5-18.2Li_2-2.6Al_2O_3-2.6NaBr-1.0Ag_3PO_4, PLAN). Fabricated glasses evaluated their photoluminescence (PL) at room temperature using BL3B beam line.

Fig. 1. PLAN:Ag glasses.

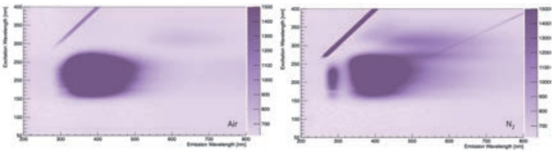

Fig. 2. The excitation and emission 2D scanning spectra.

Figure 1 shows fabricated glasses, and photoluminescence excitation and emission (2D scanning) spectra for these samples were displayed in Fig. 2. In the emission spectra, the emission around excitation wavelength between 150-275 nm is host emission of PLAN glasses and 300-350 nm is RPL emission. However, the RPL emission from nitrogen environment fabricated glasses slightly blue shift is observed. Also, emission from 275-300 nm is observed only nitrogen fabricated glasses.

This results indicated environment during fabrication is important to enhanced its luminescence and transparency.

[1] M. Yoshida *et al*., Radiat. Meas. **45** (2010) 890.
[2] Y. Miyamoto *et al*., Radiat. Meas. **45** (2010) 546.

BL4U

Correlation Between Electronic Structures and Supercapacitive Performance of NiCo/Pencil Lead Studied by X-ray Spectro-Microscopy

C. J. Yang[1,2], T. C. Huang[3], H. W. Chang[3], T. Araki[4], T. Ohigashi[4,5],
D. H. Wei[2] and C. L. Dong[1]
[1]*Department of Physics, Tamkang University, Tamsui 25137, Taiwan*
[2]*Graduate Institute of Manufacturing Technology, National Taipei University of Technology, Taipei 10608, Taiwan*
[3]*Department of Chemical Engineering, National United University, Miaoli 360302, Taiwan*
[4]*UVSOR Synchrotron Facility, Institute for Molecular Science, Okazaki 444-8585, Japan*
[5]*Photon Factory, High Energy Accelerator Research Organization, Tukuba 305-0801, Japan*

As the issue of energy shortage becomes increasingly serious, electrochemical energy storage is emerging as a highly active research area. Compared with other energy storage devices, supercapacitors have higher charge and discharge cycle life and better stability, while also enabling rapid charging and discharging reactions. The electrodes made of nanostructured nickel-cobalt oxides are not only facile to synthesize, but also offer the advantages such as low cost, high specific capacitances, low resistance, and environmental friendliness [1]. Carbon materials are also widely used as electrode materials due to their porous structure and high specific surface area, which could facilitate the electrothermal reactions and help improve overall performance [2]. In this study, NiCo-oxide nanostructures were prepared on pencil lead. The pencil lead was first activated using HNO_3 to form the activated pencil graphite electrode (APGE), and then treated hydrothermally with varying ratios of $Ni(NO_3)_2 \cdot 6H_2O$ and $Co(NO_3)_2 \cdot 6H_2O$ underwent hydrothermal treatment to obtain the nickel-cobalt oxides with different electrochemical activities.

The Scanning Transmission X-ray Microscopy (STXM) was used to investigate the electronic structure at the interface of different regions in the samples, which were prepared at different charge and discharge states based on Cyclic Voltammetry (CV). Among the samples with varying weight ratios, 1.6NiCo-20cy showed better electrochemical properties and charge storage capacity than the others. Therefore, this sample was subjected for *ex-situ* STXM to gain a deeper understanding of the electrochemical reaction mechanism.

Figure 1 displays the optical density images and corresponding stack-mapped STXM images for the O K-edge for the as-prepared 1.6NiCo-20cy sample (Fig. 1(a)), as well as those following full charging (Fig. 1(b)) and full discharging (Fig. 1(c)). Notably, two predominant regions, A and B, bisected at 535 eV are observed. In the region A, at around 532.8 eV is attributed to π^* transitions, which are strongly associated with the chemical environment of the oxygen bonds, and resulted from C=O and/or O-C–O π^* transitions. The region B mainly correspond to the σ^* transitions, attributed to a mixed O-H, C-O, or C=O states. A significant variation in the π^* state is clearly observed, indicating its critical role in charge storage performance.

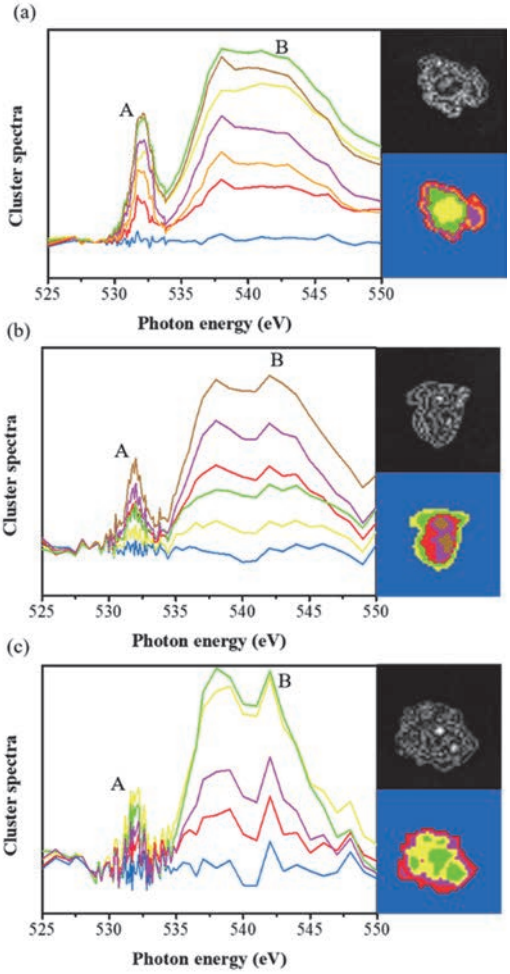

Fig. 1. Optical density images, stack-mapped STXM images, and the corresponding O K-edge XAS of (a) 1.6NiCo-20cy-Pristine, (b) fully charged-1.6NiCo-20cy and (c) fully discharged-1.6NiCo-20cy, focused at different sites of interest.

[1] T. Wang *et al.*, Nat. Commun. **14** (2023) 4607.
[2] M. Kuang *et al.*, Adv. Funct. Mater. **28** (2018) 1804886.

BL4U

Operando Nano-Scaled Identification to Carbon Dioxide and Water Gas Adsorption Coupling to Fe_3O_4 and Reduced Graphene Oxide

J. S. D. Rodriguez[1,2], H. Z. Lu[1], H. Yuzawa[3],
T. Araki[3] and C. H. Chuang[1]
[1]*Department of Physics, Tamkang University, Tamsui, New Taipei City 251301, Taiwan*
[2]*Institute of Chemistry, Leiden University, Leiden 2300 RA, The Netherlands*
[3]*Institute for Molecular Science, Okazaki 444-8585, Japan*

Graphene oxide (GO)-based membranes have shown excellent CO_2 gas separation performance due to the enlargement of the interlayer distance and chemical reactivity that provide a wiggle room on physical selectivity and chemical reactivity. On the other hand, Fe_3O_4 nanoparticles (NPs), aside from their apparent high surface area innate to their structure, have good reactivity towards CO_2 chemisorption due to their electron-donating nature. Hence, intercalating Fe_3O_4 NPs into GO membranes provides not only a straightforward combination but also a strategic method to enhance several factors: modulation of interlayer distance, increase in chemical reactivity to CO_2, and improvement of mechanical and thermal stability.

Our study aims to investigate the synergistic effects of Fe_3O_4 NP with GO in a membrane configuration, in particular the chemical change near the oxygen functional groups, via chemical mapping by scanning transmission X-ray microscopy (STXM) at C K-edge, O K-edge, and Fe L-edges. To identify the regions of interest, we select the high density/low density/absence of Fe_3O_4 NPs using the STXM obtained at the Fe 707.6 eV image, by the Fe-dependent optical density (OD) contrast. In Fig. 1 (d)-(g), the area selections in four samples marked by broken lines with labels “1”, “2”, and “3”, correspond to areas with high density, low density, and absence of Fe_3O_4 NPs, respectively. In this report, we will limit the discussion to the assessment of the high-density areas only, where the interaction between the Fe_3O_4 NPs and GO flakes is assumed to be at the greatest extent in four samples.

The oxygen functional groups (C-OH at 286.5 eV and C=O of COOH at 288.5 eV) are commonly found in DC GO-Fe_3O_4 with/without CO_2 in Fig. 1(c), assigned based on our previous pure DC GO[1]. Regarding F_3O_4 NP contribution, the high increases of C=O of COOH/C-OH at 289.7 eV and C-O of COOH/O-C(O)-O state at 290.1 eV are notable in Fig. 1(c) and our paper before[1]. The electrochemically-reduced GO (EC-rGO), when evaluated without CO_2, reveals a typical C=C bond at 285.2 eV and hexagonal C-C bond at 292.6 eV. Additionally, there has an emergence of C-OH bond at 286. 2 eV and C=O of COOH. However, the C-O-C bond at 287.4 eV is absent specifically in EC rGO[1] due to the involvement of additional Fe_3O_4 NPs. Adding CO_2 purging into the mixing solution, the apparent increases in C-OH, C-O-C, COOH, and O-C(O)-O state are observed in EC rGO-Fe_3O_4, hinting at strong oxidation between the GO flakes and the purged CO_2/further HCO_3 gases dissolved in the solution.

No significant change is observed between DC GO-Fe_3O_4 with and without CO_2, confirming that only Fe_3O_4 NPs has no function for carbon capture and storage. A notable CO_2 storage is achieved in EC GO-Fe_3O_4 w/ CO_2 compared to that w/o CO_2, in terms of EC-involved enhancement.

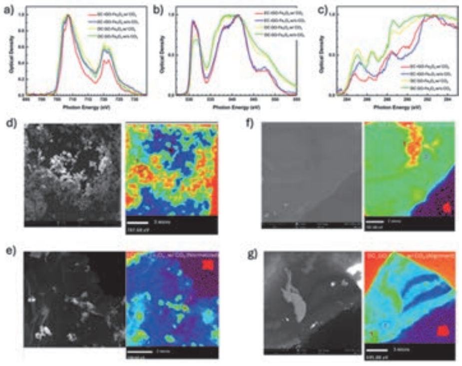

Fig. 1. (a) Fe L-edge, (b) O K-edge, and (c) C K-edge XAS spectra of EC rGO and DC GO, with and without CO_2 purging, all incorporated with Fe_3O_4 NPs. Corresponding STXM images outlining the Fe_3O_4 high-density areas of EC-rGO-Fe_3O_4 (d) w/o CO_2 and (e) w/ CO_2, and DC-GO-Fe_3O_4 (f) w/o and (g) w/ CO_2.

In the O *K*-edge (Fig. 1(b)), all samples show one π state (C=O) around 530-533.0 eV and σ state (C=O and O 2*p*-Fe 3*d*) around 537-545.0 eV, especially noted in the two DC GO-Fe_3O_4. Besides, the Fe_3O_4 characteres[2], typical of double Fe-t_{2g} and Fe-e_g states at 531.0 and 532.0 eV, are emerged in the first π peak. Through the EC method, the increase of reduced metallic states of Fe (i.e., Fe^0 and Fe^{2+}) and clear Fe 4s and 4p states become apparent at 531.0 and 545. 0 eV, respectively[2]. Compared to the only DC and EC rGO result[1], the oxygen absorption signal is dominant by the role of Fe_3O_4 NPs. No big difference is found between CO_2 purge or not. Figure 1(a) shows the Fe absorption spectra at the L_3 edge (~709.0 eV) and the L_2 edge (~722.0 eV), where they are split with the multiple crystal field and spin-orbit coupling. Two DC GO-Fe_3O_4 reveal the increasing shoulder at 707.5 eV, revealing the slight modulation of Fe_3O_4 NP after the EC method and CO_2 purge.

In summary, we exhibit the measurement of Fe_3O_4/GO composites in capturing CO_2 and the possible configurations when comparing EC rGO from DC solution, where the EC-rGO-Fe_3O_4 has shown the highest potential to capture CO_2.

[1] J. S. D. Rodriguez *et al.*, Carbon **185** (2021) 410.
[2] P.F. Teh *et al.*, J. Phys. Chem. *C* **117** (2013) 24213.

BL4U

STXM Analysis of Cathode Materials for Lithium-Ion Battery

E. Hosono[1,2], D. Asakura[1,2] and H. Yuzawa[3]
[1]Research Institute for Energy Efficient Technologies, National Institute of Advanced Industrial Science (AIST),
AIST Tsukuba Central 5, 1-1-1 Higashi, Tsukuba, Ibaraki 305-8565, Japan
[2]Global Zero Emission Research Center, AIST, AIST Tsukuba West,
16-1 Onogawa, Tsukuba, Ibaraki 305-8569, Japan
[3]UVSOR Synchrotron Facility, Institute for Molecular Science, Okazaki, Aichi 444-8585, Japan

Toward the realization of a sustainable low-carbon society, development of clean energy devices is actively underway. Secondary batteries, which can directly store renewable energy such as solar and wind power as electricity, are attracting significant attention. Lithium-ion batteries (LIBs) with high energy density are used in electric vehicles. Moreover, they are promising for large-scale stationary storage batteries. As such expanding the practical use of LIBs, it is essential to not only improve the energy density but also ensure high safety. Therefore, establishment of highly safe operation and elucidation of degradation mechanisms are of particular importance.

Among various analytical methods of LIBs, we have focused on synchrotron soft X-ray spectroscopy and conducted detailed analyses of the 3*d* transition metals and oxygen, which are the main elements of the cathode materials. Furthermore, we have also focused on microspectroscopy, which provides local spatial information and detail spatial distribution of target species. Thus, we have reported on synchrotron soft X-ray micro-electron spectroscopy using 3DnanoESCA [1-3] and synchrotron soft X-ray Scanning Transmission X-ray Microscopy (STXM) using UVSOR BL4U [4, 5].

In this study, we have applied the STXM to LIB cathode electrode sheet with active material ($LiNi_{0.5}Co_{0.2}Mn_{0.3}O_2$). The thin sample for STXM was prepared by Focused Ion Beam-Scanning Electron Microscope (FIB-SEM).

Figure 1 shows an image of a STXM sample; the LIB electrode sheets typically consist of active material, carbon as a conductive additive, and a binder. Additionally, it is known that a solid electrolyte interphase (SEI) forms on the surface of the active material in LIBs. It is anticipated that the degradation state differs between the interior and surface of the active material. In other words, the electronic/chemical states should not be uniform in each particle of the active material. Therefore, it is expected that STXM-based microspectroscopy will provide valuable knowledge.

Figure 2 shows Mn L_3-edge absorption spectrum in a region of interest for a cathode active material ($LiNi_{0.5}Co_{0.2}Mn_{0.3}O_2$). We have obtained enough quality of spectrum from this sample. We will conduct detailed analysis including mapping, and proceed toward elucidating the battery degradation mechanism.

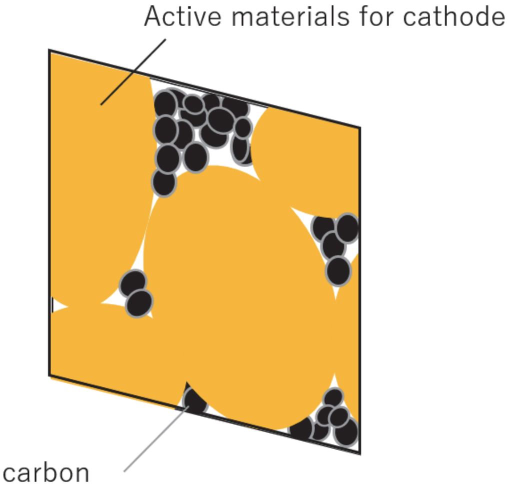

Fig. 1. Image of FIB thin section of LIB cathode electrode sheet with active material ($LiNi_{0.5}Co_{0.2}Mn_{0.3}O_2$) in STXM measurement. The structure of material is confidential until paper is published.

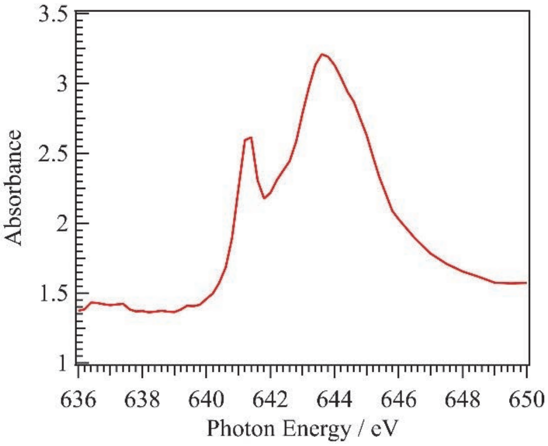

Fig. 2. Mn L_3-edge spectrum extracted from region of interest in FIB thin section of LIB cathode electrode sheet with active material ($LiNi_{0.5}Co_{0.2}Mn_{0.3}O_2$).

[1] K. Akada *et al.*, Sci. Rep. **9** (2019) 12452.
[2] K. Akada *et al.*, J. Electron Spectrsc. Relat. Phenom. **233** (2019) 64.
[3] W.X. Zhang *et al.*, CrystEngComm. **25** (2023) 183.
[4] W.X. Zhang *et al.*, Sci. Rep. **13** (2023) 4639.
[5] W.X. Zhang *et al.*, J. Electron Spectrsc. Relat. Phenom. **266** (2023) 147338.

Study of Localized Chemical State of Isoprene Rubber by STXM under Tensile-Stressed Condition

T. Ohigashi[1,2], F. Kaneko[3], H. Yuzawa[4] and H. Kishimoto[3]
[1]*Institute of Material Structure Science, High Energy Accelerator Research Organization, Tsukuba 305-0801, Japan*
[2]*Materials Structure Sciences, The Graduate University for Advanced Studies (SOKENDAI), Tsukuba 305-0801, Japan*
[3]*Sumitomo Rubber Industries Ltd., Kobe 651-0072, Japan*
[4]*UVSOR Synchrotron Facility, Institute for Molecular Science, Okazaki 444-8585, Japan*

In recent years, the Sustainable Development Goals (SDGs) have emerged as a framework guiding societal practices included in daily life. Among the various targets, the reduction of mass consumption represents a particularly critical challenge. Rubber, as a vital industrial material, is increasing its demand, especially driven by the expansion of the automobile society. In order to mitigate its consumption, it is necessary to establish a comprehensive Life Cycle Assessment (LCA) framework for rubber production, alongside the development of advanced rubber materials exhibiting enhanced functionalities, such as improved resistance to wear and mechanical failure.

A deeper understanding of the damage mechanisms in rubber materials is crucial for improving their properties. Damage in tire rubbers generally arises from a combination of chemical and mechanical factors. Recently, Mashita et al. investigated the mechanical degradation of rubber using four-dimensional X-ray tomography, revealing the creation of microvoids within deformed rubber pillars [1]. As a complementary approach aimed at elucidating the chemical aspects of mechanical damage, we have employed Scanning Transmission X-ray Microscopy (STXM). STXM enables the analysis of localized chemical states with a spatial resolution around 30 nm. Furthermore, STXM offers a relatively long working distance of ~300 µm, facilitating specialized experimental designs through the fabrication of customized sample cells. In the previous study, we developed a tensile-stress sample cell compatible with STXM and conducted *in-situ* measurements on rubber specimens [2].

An ultra-thin section (200 nm thick) of isoprene rubber was used as a sample and was attached on a tensile-stress sample grid. With changing tensile stress, 2-dimensioinal X-ray absorption spectroscopy (XAS) spectra around C K-edge (280~300 eV) were measured with 2 ms dwell time and 150 nm scanning step. Figure 1 shows the optical density images of the sample without (a, b) and with tensile stress (c, d) at 282 eV. In the tensile stress condition, the sample was stretched as 220% width for horizontal direction. Figure 1(b) and 1(d) were acquired from the same sample but at near different places to avoid radiation damage. Some bright spots in the images are considered as carbon black particles. XAS spectra under these conditions are shown in Fig. 2. Height of the spectra with tensile stress is ~52% of one without tensile stress because the sample was thinned by stretching. The main spectral change is ratio between intensity at π* (285.3 eV) and σ* (292.2 eV). The ratio (π*/σ*) changes from 0.97 to 1.12. This change is currently under discussion including formation of microvoids on the sample.

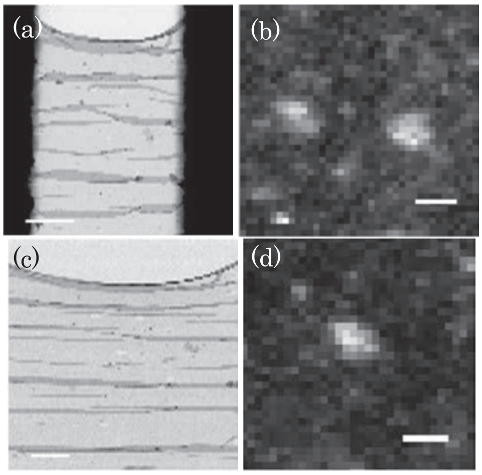

Fig. 1. Optical density images of the isoprene rubber (a, b) without and (c, d) with tensile stress at 282 eV. Scale bars are (a, c) 100 µm and (b,d) 1 µm, respectively.

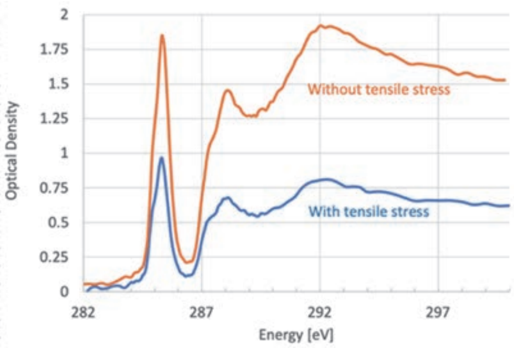

Fig. 2. C K-edge XAS spectra of the isoprene rubber without /with tensile stress.

[1] R. Mashita *et al.*, Sci. Rep. **13** (2023) 5805.
[2] T. Ohigashi *et al.*, UVSOR Activity Report **51** (2023) 84.

BL4U

Heterostructure of WO_3/V_2O_5 for Electrochromic and Energy Storage: A View by Spectro-Microscopy

K. T. Arul[1], P. C. Wang[2,1], T. Araki[3], T. Ohigashi[3,4],
D. H. Wei[2] and C. L. Dong[1]
[1]*Department of Physics, Tamkang University, Tamsui 25137, Taiwan*
[2]*Graduate Institute of Manufacturing Technology, National Taipei University of Technology, Taipei 10608, Taiwan*
[3]*UVSOR Synchrotron Facility, Institute for Molecular Science, Okazaki 444-8585, Japan*
[4]*Photon Factory, High Energy Accelerator Research Organization, Tukuba 305-0801, Japan*

To address high energy consumption and related energy issues, such as low energy and power densities and stability, a combination of electrochromism and energy storage has been explored to support both energy saving and charge storage, leading to the development of electrochromic supercapacitor (ECS) devices. ECS technology can control thermal radiation, and mitigate the need for artificial lighting in buildings, enhance energy efficiency, and even power electrical systems. These devices have been applied in energy harvesting, liquid crystal displays, wearable electronic devices, etc., [1]. Several metal oxides and their nanostructures, heterostructures, and composites have been extensively studied as ECS materials [2]. Among them, vanadium and tungsten oxides are particularly promising owing to their multi-oxidation states, high electronic conductivity, redox activity, structural stability, and high optical contrast.

The fundamental understanding of the electrochromic energy storage mechanism in the heterostructure is essential. In this study, the bifunctional WO_3/V_2O_5 thin films (~150-200 nm) were prepared using the sol-gel method. The XRD analysis revealed the presence of the (001) and (020) planes, indicating the crystalline phases of V_2O_5 and WO_3, respectively. The ultraviolet-visible spectroscopy revealed that the thin film exhibited the optical switching contrast of 17.4% between bleached and colored states, with a coloration efficiency of 10.78 cm^2/C. Moreover, the specific capacitance of WO_3/V_2O_5 was 8 F/g, which is higher than that of the individual V_2O_5 and WO_3 films, demonstrating its potential as a bifunctional material for smart film and charge storage. In this work, scanning transmission X-ray microscopy (STXM) is employed to investigate the active regions and/or elements responsible for the electrochromic energy storage performance.

Figure 1 shows the optical density and corresponding stack-mapped STXM images for the V L- and O K-edge XAS of the samples. The V L-edge originates from the V 2p-to-3d unoccupied state [3]. In the WO_3/V_2O_5 heterostructure, the intensity of the V L_3-edge peak is slightly higher at surface of the heterostructure. The O K-edge XAS, which arises from O 1s-to-2p transitions hybridized with V 3d and W 5d states, was also measured. The peaks a_1 and a_4 correspond to, respectively, the O 1s-to-2p states hybridized with W 5d-t_{2g} and 5d-e_g states. The peaks a_2 and a_3 are attributed to the O 1s-to-2p states hybridized with V 3d-t_{2g} and 3d-e_g states, respectively. The spectral evolutions indicate a higher concentration of oxygen vacancies at the surface than in the core, particularly around W sites, providing more active sites for electrochromic energy storage.

In contrast, the V L- and O K-edge XAS-STXM of WO_3/V_2O_5 heterostructure after cyclic voltammetry (CV) treatment shown in Fig.1b, revealed a stronger interaction between V and W through oxygen 2p states. Notably, the charge states of both V and W are more reduced at the surface of the particle compared to the core region, suggesting that both V and W in the heterostructure are electrochemistry active. The stability of such a defective heterostructure, the durability of these active sites, and whether both active sites are jointly (or separately) responsible for the electrochromic and charge storage functionalities remain to be explored.

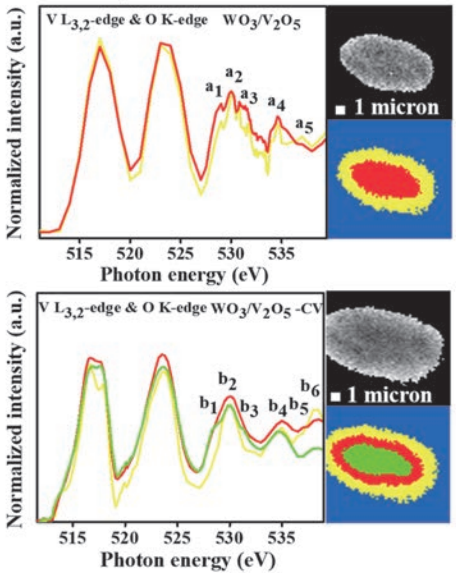

Fig. 1. Optical density and stack-mapped STXM images, and the corresponding V $L_{3,2}$- and O K-edge XAS of (a) WO_3/V_2O_5 and (b) WO_3/V_2O_5-CV.

[1] D. K. Pathak *et al.*, Mater. Horiz. **9** (2022) 2949.
[2] S. Zhang *et al.*, Energy Environ. Sci. **11** (2018) 2884,
[3] Q. Lu *et al.*, Adv. Funct. Mater. **28** (2018) 1803024.

BL4B

Soft X-ray Absorption Study of Semiconductor Photocatalysts Excited with Steady UV Light

Y. H. Chew[1], H. Onishi[1,2], N. Ichikuni[3] and T. Yoshida[4]
[1]School of Science, Kobe University, Kobe 657-8501, Japan
[2]Division of Advanced Molecular Science, Institute for Molecular Science, Okazaki 444-8585, Japan
[3]Graduate School of Engineering, Chiba University, Chiba 263-8522, Japan
[4]Graduate School of Engineering, Nagoya University, Nagoya 464-8603, Japan

Materials conversion on semiconductor photocatalysts has been intensively studied worldwide. Downhill reactions, in which the Gibbs free energy decreases during the conversion of reactants to products, have been successfully integrated into our society [1]. Artificial photosynthesis, a category of uphill reactions involving the oxidation of water, is being developed for societal implementation in the near future [2]. In addition, fundamental studies are being conducted to uncover new scientific discoveries related to light-driven, efficient materials conversion.

Here, in collaboration with Prof. Hiroshi Iwayama of UVSOR, we apply soft X-ray absorption to the characterization of semiconductor photocatalysts under UV light irradiation for band-gap excitation. A series of metal oxide photocatalysts including sodium tantalate ($NaTaO_3$), strontium titanate ($SrTiO_3$), titanium oxide (TiO_2), tin oxide (SnO_2), and zinc oxide (ZnO) were investigated in a beam time in FY2024.

The photocatalyst particles were formed into disks of 7 mm diameter. The disks were placed in a vacuum chamber, irradiated with incident X-rays, and the fluorescent X-rays were detected with a silicon drift detector (SDD). The detector was capped with a 150 nm thick aluminum film (LUXEL, TF110) to minimize the contribution of stray UV light to the detector response (Fig. 1). The capping device is deposited at UVSOR. Users are encouraged to use the device when operating the SDD under UV or visible light irradiation.

Figure 2 shows a set of fluorescence yield spectra at the oxygen K-edge observed on a $NaTaO_3$ photocatalyst doped with Sr^{2+} cations, in the presence and absence of UV light provided by a Hg–Xe lamp (200 W).

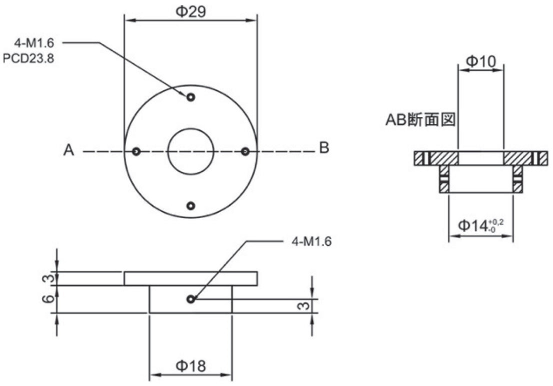

Fig. 1. A devise capping the SDD with the aluminum filter for fluorescence yield detection of oxygen K edge absorption spectrum under UV-light irradiation.

In the oxygen K-edge, electron transition from O1s to O2p orbitals of $NaTaO_3$ particles was detected. The O2p orbitals are hybridized with Ta5d orbitals to form the conduction band in perovskite-structured $NaTaO_3$. The hybridized O2p orbitals are thus split into t_{2g} and e_g levels, one at 532.6 eV and the other at 537.7 eV, according to the ligand field in TaO_6 octahedra.

The t_{2g} and e_g bands shifted to the low energy side under UV irradiation. The shifted bands induced differentiated forms in the difference spectrum. A possible reason for the band shifts is the conduction band partially filled with electrons excited across the band gap, where the oxidation state of some Ta cations decreased from 5+ to 4+.

The X-ray absorption of electronically excited metal oxides has been studied using ultrashort light pulses [3]. Here, we showed that the absorption spectrum was also sensitive to steady light irradiation. This study was supported by JSPS KAKENHI (grant number 22H00344).

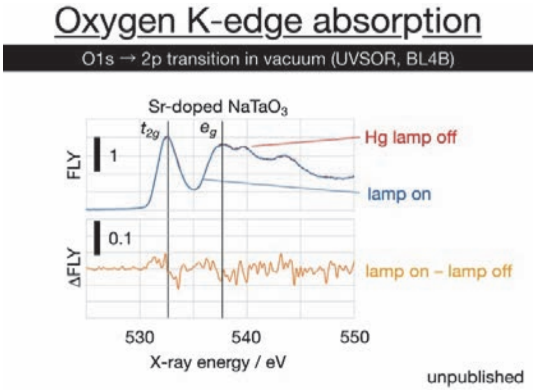

Fig. 2. Oxygen K edge absorption spectrum of a $NaTaO_3$ photocatalyst doped with Sr^{2+} cations in the absence (red spectrum) and presence (blue spectrum) of UV irradiation. The difference spectrum induced by the irradiation is shown in orange color at the bottom.

[1] A. Fujishima *et al.*, J. Photochem. Photobio. C **1** (2000) 1.
[2] H. Onishi, ChemSusChem **12** (2019) 1825.
[3] Y. Uemura *et al.*, J. Phys. Chem. Lett. **13** (2022) 4207.

BL4B

Oxygen K-Edge XAS Study of $Eu_2Zr_2O_7$

S. Yoshioka[1], E. Kobayashi[2] and K. Oudaira[3]
[1]*Department of Applied Quantum Physics and Nuclear Engineering, Kyushu University, Fukuoka 819-0395, Japan*
[2]*Kyushu Synchrotron Light Research Center, Saga 841-0005, Japan*
[3]*Graduate school of Advanced Integration Science, Chiba University, Chiba 263-8522, Japan*

Rare earth zirconates ($Re_2Zr_2O_7$) such as $Eu_2Zr_2O_7$ and $Gd_2Zr_2O_7$ exhibit attractive potential as functional materials for thermal barrier coatings and nuclear fuel inert matrixes. $Re_2Zr_2O_7$ displays two types of crystal structures depending on the ionic radius ratio between Re and Zr. There are the pyrochlore structure and the oxygen deficient fluorite structure, with the former being considered a cation and oxygen vacancy ordered form of the latter. The transformation between pyrochlore and defective fluorite structures can be described as cationic disordering. Regrading the local coordination on the disordering, Re ions partly move from eight-coordinated site (CN8) to a six-coordinated site (CN6), whereas Zr ions partly move from CN6 to CN8. The structure changes related to the cationic disorder of pyrochlore under swift heavy ion (SHI) irradiation have been reported using diffraction techniques and transmission electron microscopy observations. X-ray absorption near edge structure (XANES) spectroscopy is a powerful method for structure characterization, providing information on local atomic coordination and electronic structures. Moreover, XANES offers a significant advantage for the elemental selectivity of the multi-cation compounds such as pyrochlore. In this study, we investigated oxygen local structure change in $Eu_2Zr_2O_7$ induced by SHI using X-ray absorption spectra (XAS).

Polycrystalline Eu_2Zr_2O samples were synthesized via a solid-state reaction. Stoichiometric amounts of Eu_2O_3 and ZrO_2 oxides were intimately mixed and pressed into disc at 100 MPa. Finally, the discs were sintered under air at 1500 °C using an electric furnace.

The sintered Eu_2Zr_2O sample was confirmed to have pyrochlore structure by X-ray diffraction (XRD). SHI irradiation experiments with 200 MeV Xe ions at fluences ranging from 5×10^{11} up to 1×10^{13} cm^{-2} were performed at the H1 beamline of the tandem ion accelerator facility in the Japan Atomic Energy Agency (JAEA)-Tokai.

O K-edge XANES measurements were performed on the BL4B beamline of UVSOR Okazaki, Japan, using the partial fluorescence yield (PFY) method. A varied-line-spacing plane gratings monochromator provided the O K-edge in the energy regions 520–560 eV. The samples were positioned with their surface perpendicular to the incident X-ray beam. Fluorescence X-rays of O K_α was collected using an energy dispersible silicon drift detector (SDD).

The O K-edge XANES spectra (at 525 eV) are shown in Fig. 1 for the Eu_2Zr_2O powder sample and reference bixbyite Eu_2O_3 and monoclinic ZrO_2 powder samples. The intensity of each spectrum was normalized to a value of 1 at 555 eV after the removal of the background intensity.

The spectrum shape of $Eu_2Zr_2O_7$ is clearly different from those of standard samples Eu_2O_3 and ZrO_2. The peaks A – C in the spectrum of Eu_2O_3 were assigned to transitions from the O 1s orbitals to unoccupied bands derived from the Eu 5d-π, 6p, 5d-σ orbitals, respectively [1].

Detailed analysis on the local environment of O in $Eu_2Zr_2O_7$ is in progress, employing a combined approach of XANES and first principles band structure calculations.

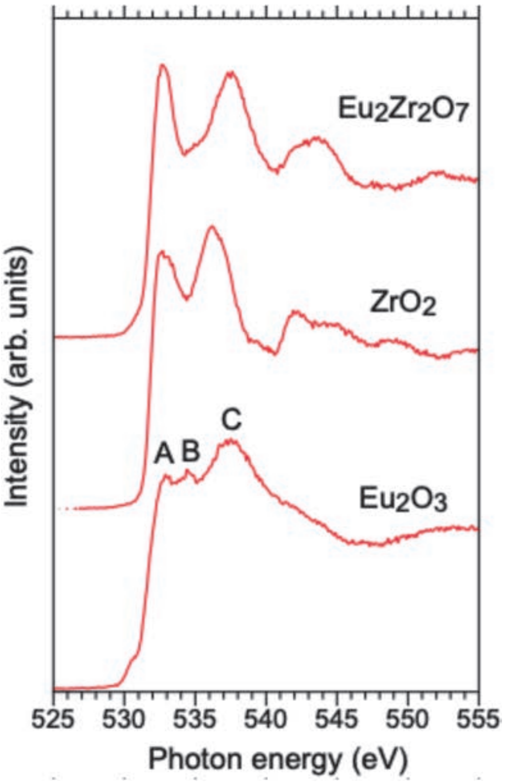

Fig. 1. O K-edge XANES spectra of pyrochlore Eu_2Zr_2O, including references spectra from bixbyite Eu_2O_3 and monoclinic ZrO_2 powder for comparison.

[1] A. B. Altman, *et al.*, Dalton Trans. **45** (2016) 9948.

BL5U

Micro-ARPES Study of the Electronic Structure in Kagome Superconductor $LaRh_3B_2$

T. Kato[1], K. Nakayama[2], T. Osumi[2], S. Souma[1,3], A. Honma[2], K. Tanaka[4,5],
T. Takahashi[2] and T. Sato[1,2,3,6,7]
[1]Advanced Institute for Materials Research (WPI-AIMR), Tohoku University, Sendai 980-8577, Japan
[2]Department of Physics, Tohoku University, Sendai 980-8578, Japan
[3]Center for Science and Innovation in Spintronics (CSIS), Tohoku University, Sendai 980-8577, Japan
[4]UVSOR Synchrotron Facility, Institute for Molecular Science, Okazaki 444-8585, Japan
[5]School of Physical Sciences, The Graduate University for Advanced Studies (SOKENDAI), Okazaki 444-8585, Japan
[6]International Center for Synchrotron Radiation Innov1ation Smart (SRIS), Tohoku University, Sendai 980-8577, Japan
[7]Mathematical Science Center for Co-creative Society (MathCCS), Tohoku University, Sendai 980-8578, Japan

Ternary rare-earth compounds RT_3X_2 (where R denotes a rare-earth element, T a transition metal, and X typically B, Si, or Ga) are an extensively studied class of intermetallic materials. This family has been attracted attention over the years primarily due to its rich and intriguing physical properties, including various types of magnetic ordering and superconductivity, depending on the specific elemental composition. More recently, stimulated by significant advances in the study of geometrically intriguing kagome lattices, there has been a marked revival of interest in RT_3X_2 compounds, as they feature an ideal kagome lattice formed by the T atoms. The kagome lattice, composed of corner sharing triangles, is known for its potential to host exotic electronic states, such as dispersionless flat bands, linearly dispersing Dirac points analogous to those in graphene, saddle-point van Hove singularity, and topologically non-trivial characters. There is growing interest in elucidating the relationship between the kagome lattice-derived electronic band structures and the physical properties of RT_3X_2 [1]. Nevertheless, despite this renewed focus, the application of experimental techniques capable of directly probing intrinsic electronic states, such as angle-resolved photoemission spectroscopy (ARPES), remains limited for RT_3X_2 [2].

In this work, we have focused on $LaRh_3B_2$, a rare material displaying superconductivity within the RT_3X_2 series. We performed detailed studies of its electronic structure utilizing high-resolution angle-resolved photoemission spectroscopy (ARPES). The experiments were conducted with micro-focused synchrotron radiation beam at beamline BL5U at UVSOR. Clean surfaces necessary for ARPES were obtained by cleaving the crystals *in-situ* in an ultrahigh vacuum better than 1×10^{-10} Torr.

Figure 1 shows representative ARPES data for $LaRh_3B_2$, displaying the second derivative intensity plot measured along the Γ-M high-symmetry line in the hexagonal Brillouin zone (inset) in the normal state (T = 40 K). Our data show multiple hole-like band dispersions centered near the Γ point, whose highest branch approaches the Fermi level (E_F), in agreement with previous work [2]. Our measurements also revealed a hole-like band topped 0.3 eV below E_F at the M point. Through comparing the observed band dispersions with those calculated by density functional theory as well as conducting photon energy dependent ARPES measurements, we found that some of the observed bands are attributed to two-dimensional electronic states at the surface. To clarify the origin of the surface states, we have carried out slab calculations, and found their intriguing electronic and structural properties.

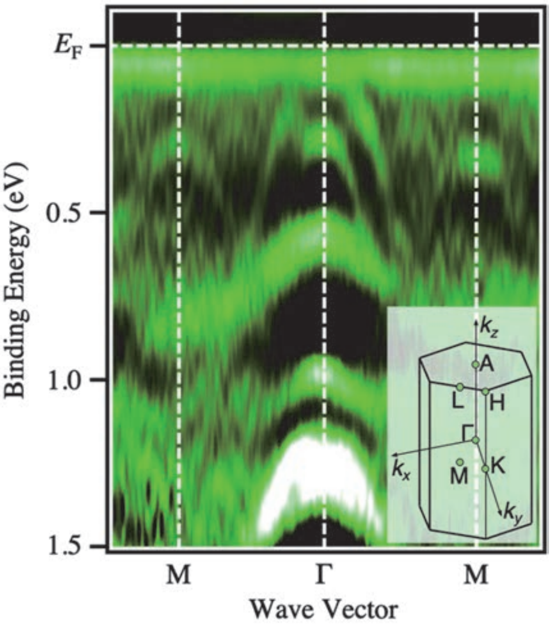

Fig. 1. Plot of second-derivative ARPES intensity measured in the normal state along the ΓM high-symmetry line in $LaRh_3B_2$.

[1] S. Chaudhary *et al.*, Phys. Rev. B **107** (2023) 085103.
[2] Y. Iida *et al.*, Physica B **351** (2004) 271.

BL5U

Band Structure of Monolayer Germanene Grown on Ag Revealed by ARPES

T. Terasawa[1,2], S.Suzuki[1], D. Katsube[3], S. Tanaka[4] and K. Tanaka[5]

[1]*Advanced Science Research Center, Japan Atomic Energy Agency, Tokai 319-1195, Japan*
[2]*Institute of Industrial Science, The University of Tokyo, Meguro 153-8505, Japan*
[3]*Japan Fine Ceramics Center, Nagoya 456-8587, Japan*
[4]*SANKEN, The Institute of Scientific and Industrial Research, The University of Osaka, Ibaraki 567-0047, Japan*
[5]*UVSOR Synchrotron Facility, Institute for Molecular Science, Okazaki 444-8585, Japan*

Germanene is a monolayer material composed of Ge atoms arranged in a honeycomb lattice. Owing to the spin–orbit interaction in Ge, germanene adopts a buckled atomic configuration. As a result, it is predicted to exhibit a Dirac cone like that of graphene with a high Fermi velocity while also possessing a band gap of 23.9 meV [1]. These characteristics have spurred interest in germanene as a next-generation semiconductor material.

We have developed a novel synthesis method to produce high-quality germanene, as reported by J. Yuhara *et al.* [2]. When an Ag thin film is deposited on a Ge(111) substrate and subsequently heated, Ge atoms diffuse from the substrate to the Ag film surface. Upon cooling, a monolayer germanene forms on the Ag film surface. This segregated germanene exhibits larger domain sizes and long periodic structures. Moreover, the formation of germanene was confirmed by the characteristic Raman peaks unique to germanene [3]. The availability of high-quality germanene can facilitate angle-resolved photoemission spectroscopy (ARPES) measurements. Our ARPES measurements conducted at UVSOR BL5U in 2023 successfully observed germanene-derived bands that are distinct from those of bulk Ag or Ag–Ge alloys [4]. In this work, we aim to further refine these observations by elucidating the band structure of germanene, specifically determining whether the observed bands exhibit a cone-like or saddle-like nature. This distinction is crucial, as in the case of silicene, the saddle-like structure induced by the Ag substrate was often misinterpreted as the π-bands of silicene [5].

Figure 1(a) shows the ARPES intensity map along the Γ-K_{Ge}-M_{Ag} line (kx direction) of germanene grown on an Ag(111) thin film, obtained using 40 eV light. Here, K_{Ge} and M_{Ag} correspond to the K and M points in the Brillouin zone of germanene and Ag(111)-(1×1) surface, respectively. In addition to the prominent Ag 5sp band, a Λ-shaped structure is observed, as indicated by the red broken lines. Figure 1(b) shows the ARPES intensity map for energy (E)-ky plane at kx = 0.9 $Å^{-1}$, corresponding to a white broken line in Fig. 1(a), where the ky direction is perpendicular to the kx direction. The band around -1.5 eV, which corresponds to the Λ-shaped band in Fig. 1(a), exhibits an almost flat but slightly concave-down feature, suggesting that it is not a saddle point but rather a cone-like structure. Therefore, we attributed this band not to the Ag bands but to the π-band of germanene. The difference in the band gradients along kx and ky directions is likely due to the hybridization with Ag.

In summary, we synthesized germanene on the Ag(111) surface by Ge segregation and investigated its electronic structure using ARPES. Our results provide the first indication of a π-band in germanene segregated on Ag(111), as revealed by ARPES intensity maps in both the E-kx and E-ky planes.

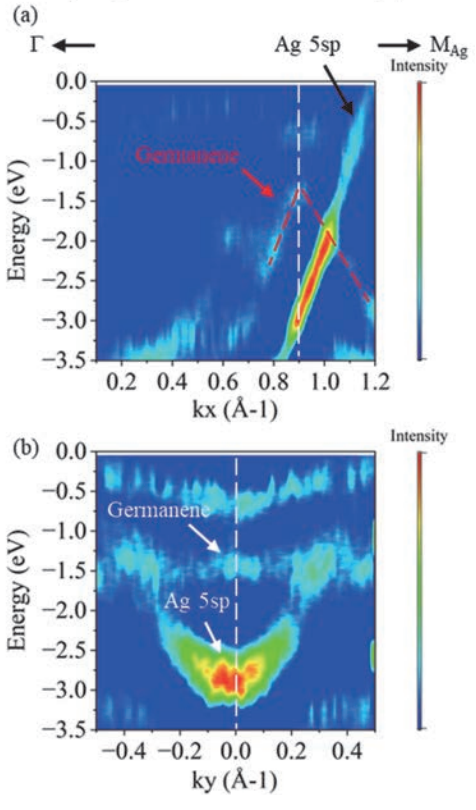

Fig. 1. (a, b) ARPES intensity plots along kx and ky lines. The plots are the second derivative of the raw data to highlight the band features.

[1] C. C. Liu *et al.*, Phys. Rev. B **84** (2011) 195430.
[2] J. Yuhara *et al.*, ACS Nano **12** (2018) 11632.
[3] S. Suzuki *et al.*, Adv. Funct. Mater. **31** (2021) 2007038.
[4] T. Terasawa *et al.*, UVSOR Activity Report **51** (2023) 97.
[5] S. K. Mahatha *et al.*, Phys. Rev. B **89** (2014) 201416.

BL5U

Spin-Polarized Band Mapping in Bi_2Sb_3 Surface States

J. Okabayashi[1] and K. Tanaka[2]

[1]*Research Center for Spectrochemistry, The University of Tokyo, Bunkyo-ku, Tokyo 113-0033, Japan*
[2]*UVSOR Synchrotron Facility, Institute for Molecular Science, Okazaki 444-8585, Japan*

Spintronics is a rapidly emerging field of science and technology that will most likely have a significant impact on the future of all aspects of electronics. Understanding magnetism of surfaces, interfaces, and nanostructures is greatly important for realizing the spintronics which aims to control and use the function of spin as well as the charge of electrons. Spin- and angle-resolved photoemission spectroscopy (spin-resolved ARPES) is one of the most powerful experimental techniques to investigate the magnetic properties of such materials, where one can know the “complete” information of the electronic states of materials, that is, energy, momentum, and spin direction. Recent development of high energy and angle-resolved photoelectron analyzer as well as the contemporary light sources makes it possible for the photoemission spectroscopy to investigate not only band structures but also many body interactions of electrons in solids. However, appending the spin resolution to photoemission spectroscopy is quite difficult because of an extremely low efficiency (10^{-4}) of Mott-type spin detections.

Recently, very low-energy electron diffraction (VLEED-type) spin detector with 100 times higher efficiency than that of conventional Mott-type has been developed and spin-resolved ARPES has been started to be realized [1-3]. So far, most of the spin-resolved ARPES systems are using the single-channel detector and efficiency is still a problem. We have developed high-efficient spin-resolved ARPES system with multi-channel detection (we call “image-spin” detection) to achieve the 100 times better efficiency and the 10 times better momentum resolution than the current spin-resolved ARPES system, which can be a breakthrough in this research field.

Figure 1 displays the ARPES and spin-resolved ARPES images of the topological surface states in Bi_2Sb_3 after cleaving the sample *in-situ* to obtain clean surface. Linearly crossing surface bands at the Dirac points are observed in ARPES, and spin-resolved states for both up and down spin states are distinctly identified with high resolution.

According to rough estimates, the efficiency of spin-resolved ARPES is 100 times greater than that of the single-channel detection systems currently in use worldwide. The imaging detection of spin-resolved mapping can be accomplished using spin manipulation techniques to separate the photoelectrons into up and down spins before their injection into the VLEED target. A new “spin manipulator” can alter the spin direction of the passing electrons in any orientation using adjustable electric and magnetic fields. The installation of the spin manipulator and the optimization of the spin target deposition conditions have significantly enhanced the spin-resolved images, allowing us to achieve spin-resolved images with momentum resolution comparable to that of conventional ARPES.

We are currently fine-tuning the lens parameters of the spin manipulator to capture spin information in the remaining three axial directions. This technique expands the research field by enabling efficient detection of spin-resolved band structures using spin-resolved ARPES.

[1] C. Bigi *et al.*, J. Synchrotron Rad. **24**, (2017) 750.
[2] T. Okuda, J. Phys.: Condens. Matter **29** (2017) 483001.
[3] F. Ji *et al.*, Phys. Rev. Lett. **116** (2016) 177601.

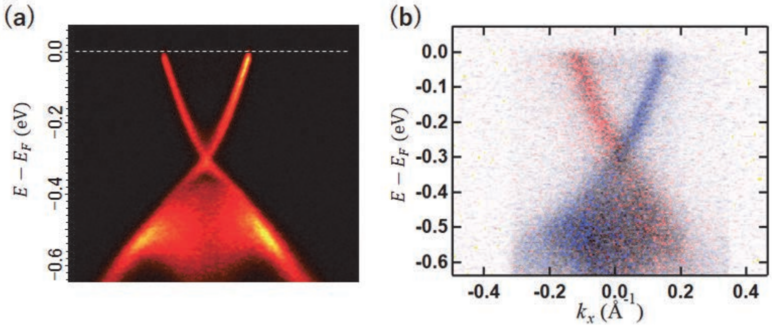

Fig. 1. Band dispersion mapping of Bi_2Se_3 taken at 55 eV photon energy. (a) ARPES and (b) Spin-resolved ARPES.

BL5U

Essential Ingredients for Pseudogap of Electron-Doped Cuprates Studied by Angle-Resolved Photoemission Spectroscopy

M. Miyamoto[1], M. Horio[1], K. Morioya[2], A. Takahashi[3], K. Tanaka[4], Y. Koike[3],
T. Adachi[2] and I. Matsuda[1]
[1]*Institute for Solid State Physics, the University of Tokyo, Kashiwa, Chiba 277-8581, Japan*
[2]*Department of Engineering and Applied Sciences, Sophia University, Tokyo 102-8554, Japan*
[3]*Department of Applied Physics, Tohoku University, Sendai 980-85879, Japan*
[4]*UVSOR Synchrotron Facility, Institute for Molecular Science, Okazaki 444-8585, Japan*

It has been widely accepted that, in addition to carrier doping, post-growth reduction annealing process is necessary to induce superconductivity in electron-doped cuprates $R_{2-x}Ce_xCuO_4$ (R: rare earth) with the so-called T'-type structure [1,2]. Neutron-scattering studies suggested that annealing removes excess impurity oxygen atoms at the apical site [3-5]. Stronger annealing, which implies further removal of apical oxygens, enhances the transition temperature T_c [6]. Horio *et al*. found that efficient annealing strongly suppresses the pseudogap, which is believed to compete with superconductivity [7]. The superconducting properties of the T'-type cuprates thus strongly depend on the degree of annealing.

On the other hand, recent studies have stressed the importance of electron doping caused by annealing. Angle-resolved photoemission spectroscopy (ARPES) studies revealed the increase of electron concentration by reduction annealing due to the creation of oxygen deficiencies in the regular sites [7-9]. Song *et al*. [10] reported that the pseudogap depends only on the electron doping level after sufficient reduction annealing. Therefore, the key factor of the pseudogap and superconductivity in electron-doped cuprates remains elusive.

To separate the effects of annealing and electron doping on the electronic structure, we previously carried out ARPES measurements on the as-grown samples of the electron-doped cuprate $Pr_{1.22}La_{0.7}Ce_{0.08}CuO_4$ and doped electrons by K adsorption on the sample surface, which should not influence the crystal structure. As a result, we found the signature of pseuedogap suppression by K adsorption [11]. In this proposal, we performed more detailed investigation into the influence of K adsorption, and also measured $Pr_{1.20}La_{0.7}Ce_{0.10}CuO_4$ annealed sample for comparison, which was annealed with an improved method called dynamic annealing [9,12,13].

ARPES measurements were performed for the as-grown $Pr_{1.22}La_{0.7}Ce_{0.08}CuO_4$ and the annealed $Pr_{1.20}La_{0.7}Ce_{0.10}CuO_4$ samples at BL5U at T = 20 K. By dosing K for the as-grown $Pr_{1.22}La_{0.7}Ce_{0.08}CuO_4$, the Fermi surface transformed from disconnected square shape [Fig. 1(a)] to continuous circular shape [Fig. 1(b)], which indicates pseudogap closing. The energy distribution curves (EDCs) at the node [Fig. 1(c)] and at the hot spot [Fig. 1(d)] show pseudogap suppression after K dosing. The increase in the electron concentration by K dosing estimated from Fermi surface area was approximately 0.12 per Cu site, which shows good reproducibility with previous measurements [11]. We further compared the results with that of the annealed $Pr_{1.20}La_{0.7}Ce_{0.10}CuO_4$ sample and evaluated the influence of apical oxygen removal by reduction annealing.

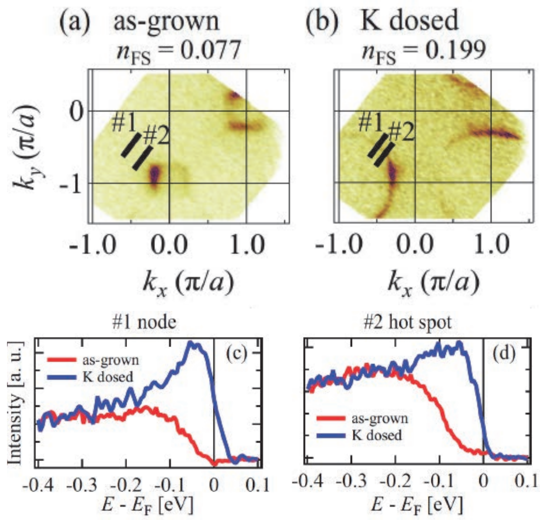

Fig. 1. Fermi surface maps for the as-grown $Pr_{1.22}La_{0.7}Ce_{0.08}CuO_4$ sample (a) before and (b) after K dosing. EDCs at the (c) node and (d) hot spot for each surface condition.

[1] Y. Tokura *et al*., Nature **337** (1989) 345.
[2] H. Takagi *et al*., Phys. Rev. Lett. **62** (1989) 1197.
[3] P. Radaelli *et al*., Phys. Rev. B **49** (1994) 15322.
[4] A. Schultz *et al*., Phys. Rev. B **53** (1996) 5157.
[5] M. Fujita *et al*. J. Phys. Soc. Jpn. **90** (2021) 105002.
[6] J. Kim *et al*., Physica C **209** (1993) 381.
[7] M. Horio *et al*., Nat, Commun. **7** (2016) 10567.
[8] M. Horio *et al*., Phys. Rev. B **98** (2018) 020505.
[9] C. Lin *et al*., Phys. Rev. Research **3** (2021) 013180.
[10] D. Song *et al*., Phys. Rev. Lett. **118** (2017) 137001.
[11] M. Miyamoto *et al*., UVSOR Activity Report **51** (2023) 98.
[12] Y.-L. Wang *et al*., Phys. Rev. B **100** (2009) 094513.
[13] Y. Lee *et al*., J. Phys. Soc. Jpn. **93** (2024) 054701.

BL5U

Resonant ARPES Study for Thermoelectric Property of Layered Ce-Based Compounds

D. Goto[1], K. Kuga[1], M. Matsunami[1,2,3] and T. Takeuchi[1,2,3]
[1]*Toyota Technological Institute, Nagoya 468-8511, Japan*
[2]*Research Center for Smart Energy Technology, Toyota Technological Institute, Nagoya 468-8511, Japan*
[3]*MIRAI, Japan Science and Technology Agency, Tokyo 102-0076, Japan*

III-2

The thermoelectric devices, which can convert heat and electricity using Seebeck and Peltier effects, have been considered as one of the most promising choices for energy saving technologies. However, such a thermoelectric generation has not been widely applied due to its low energy conversion efficiency. For evaluating a performance of thermoelectric materials directly related to conversion efficiency, the power factor $PF = S^2/\rho$ where S and ρ are Seebeck coefficient and electrical resistivity, respectively, is frequently used [1]. It is therefore necessary to search for materials possessing large PF by addressing the trade-off relationship between low ρ and large $|S|$.

It is known that in intermetallic compounds called heavy fermion systems, the low ρ and large $|S|$ coexist. This can be caused by the characteristic electronic structure formed by the hybridization between conduction (c) and f electrons. However, in heavy fermion systems, there is a serious problem concerning the sign of S, which cannot be determined solely in terms of the energy dependence of the electron density of states as in most simple metals. Therefore, the energy dependence of the relaxation time and group velocity of quasiparticles, both of which are ignored in many cases [1], should be taken into account.

The main purpose of this research is to establish a methodology for experimentally evaluating the energy dependence of the relaxation time and group velocity of quasiparticles in the vicinity of the Fermi level (E_F) using ARPES. In this study, we focus on the typical heavy fermion systems CeTIn$_5$ (T = Co, Rh, Ir) with a layered crystal structure, which show relatively high large thermoelectric performance at low temperature. In the case of Ce-based compounds, the main part of c-f hybridization bands locates just above E_F in contrast to Yb-based cases. Therefore, for clearly observing the c-f hybridization bands and analyzing them in detail, the photoemission signal Ce 4f electrons should be enhanced by using resonance condition.

Single crystals of CeTIn$_5$ (T = Co, Rh, Ir) were prepared by the In-flux method. Clean sample surfaces were obtained by *in-situ* cleaving. The ARPES measurements were performed at BL5U. The photon energies of 115 eV and 121 eV were selected as the off-resonance and on-resonance condition for Ce 4d-4f edge, respectively. The resonance energy, as generally used in previous studies [2], was also confirmed by our constant initial state (CIS) measurements.

Figure 1 shows the obtained ARPES image of CeCoIn$_5$ (001) surface at 9 K measured with the photon energy of 115 eV (off-) and 121 eV (on-resonance), respectively. The highly dispersive bands due to mainly Co 3d electrons are clearly observed and basically similar between on- and off-resonance condition [2]. The impact of nearly localized Ce 4f electrons is observed at around E_F and 0.25 eV due to spin-orbit splitting, as clearly confirmed in the angle-integrated spectra. From the linewidth of the band dispersion near E_F, the energy dependent analysis for the relaxation time and group velocity of quasiparticles for CeCoIn$_5$ can be determined, and is now in progress.

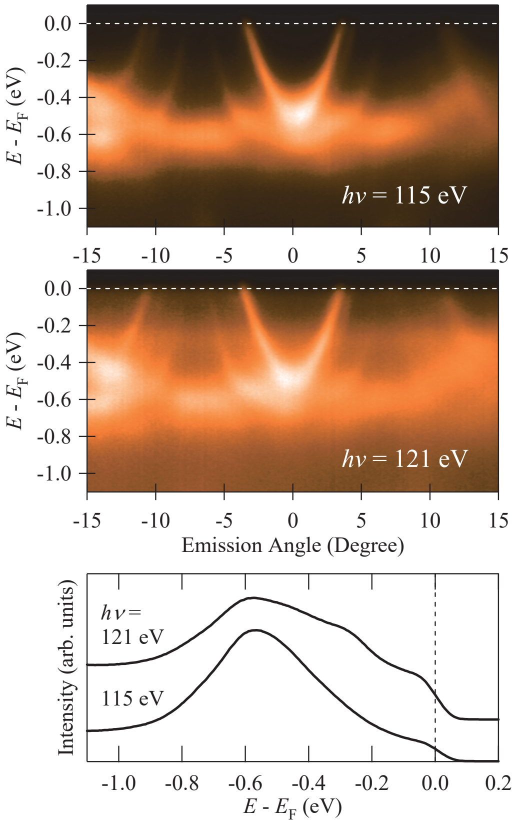

Fig. 1. ARPES image of CeCoIn$_5$ at 9 K measured with photon energies of 115 eV (top) and 121 eV (middle). The bottom figure shows the angle-integrated spectra.

[1] T. Takeuchi, J. Thermoelectrics Soc. Jpn. **9** (2012) 1.

[2] Q.Y. Chen *et al.*, Phys. Rev. B **96** (2017) 045107.

BL5U

Angle-Resolved Photoemission Study of Olivine-Type $LiMnPO_4$ Bulk Single Crystal

T. Ito[1,2], Y. Hatae[1], M. Nakatake[3], S. Takakura[2], K. Tanaka[4,5],
Y. Fujiwara[6], T. Taishi[6] and Y. Iriyama[1]
[1]Graduate School of Engineering, Nagoya University, Nagoya 464-8603, Japan
[2]Synchrotron radiation Research center, Nagoya University, Nagoya 464-8603, Japan
[3]Aichi Synchrotron Radiation Center, Seto 489-0965, Japan
[4]UVSOR Facility, Institute for Molecular Science, Okazaki 444-8585, Japan
[5]The Graduate University for Advanced Studies, Okazaki 444-8585, Japan
[6]Faculty of Engineering, Shinshu University, Nagano 380-8553, Japan

With the recent expansion of the use of lithium-ion secondary batteries, development of all-solid-state batteries using lithium-ion conductive inorganic solid electrolytes has been progressing to realize further safety, high energy density, and high output, etc. On the other hand, the valence-band electronic structure, which is essential to understand the relation between lithium-ion and electron conductivity in solid-state energy storage materials, has not been well elucidated yet, though the chemical analysis using operand X-ray photoemission has intensively been applied on the system [1,2]. To clarify the effect of lithium on the electronic structure of cathode material, we have performed angle-resolved photoemission spectroscopy (ARPES) measurements on olivine-type $LiMnPO_4$ [3], which has expected to be potential cathode material with quasi-one-dimensional Li^+ conducting path along the b axis.

ARPES measurements were performed at the UVSOR-III BL5U. Inter-plane ARPES data were acquired at the normal emission angle (θ = 0°) with using hν = 40 - 64 eV at room temperature. To minimize charging effect, we have evaporated K onto the side of sample before cleaving. Single crystals were cleaved in situ along (100) plane.

Figure 1(b) shows photon-energy dependent ARPES spectra of $LiMnPO_4$. For comparison, the density of states (DOS) of $LiMnPO_4$ calculated using density functional theory (DFT) is displayed in Fig. 1(a). From Fig.1(b), we have found that the ARPES peaks show broad dispersive features near the valence band maximum (VBM) around 4 eV and at the band bottom around 10 eV, corresponding to *hν*=62 eV and 50 eV, respectively. It should be noted that K 3p core level around 18.3 eV has not been observed at the cleaved surface, which is suggestive of negligible contribution of evaporated K at the measured spectra.

To show the dispersive features clearly, inter-plane ARPES image along ΓX line of $LiMnPO_4$ is indicated in Fig. 2(a), comparing with DFT calculation (Fig. 2(b)). From the observed symmetry around VBM, the inner potential V_0 is estimated to be 5 eV. Though the complicated dispersive features of Mn 3d-O 2sp hybridized bands have only roughly been observed on the present ARPES results, we expect there are apparent consistency between DFT and ARPES in terms of band gap size (~ 4 eV) and VB width (~ 8 eV). These results suggest the potential utility of ARPES for investigating the electronic structure of cathode material for lithium-ion battery.

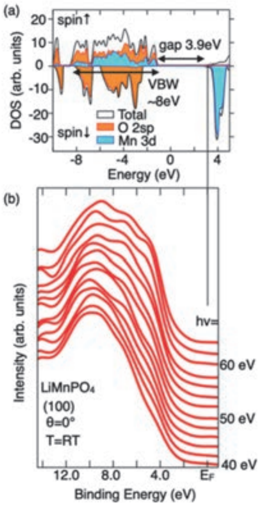

Fig. 1. (a) Density of states of $LiMnPO_4$ [3]. (b) Inter-plane ARPES spectra (θ = 0°) of $LiMnPO_4$.

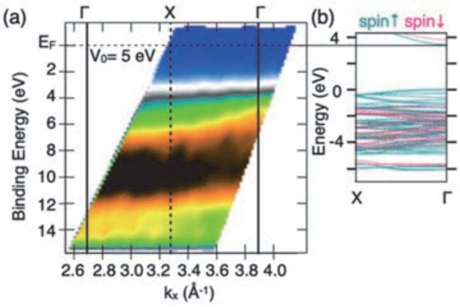

Fig. 2. (a) ARPES image along ΓX line of $LiMnPO_4$. (b) DFT calculations of $LiMnPO_4$ [4].

[1] K. Hikima *et al.*, Commn. Chem. **5** (2022) 52.
[2] K. N. Wood *et al.*, Nature Commun. **9** (2018) 2490.
[3] M. Sgroi *et al.*, Batteries **3** (2017) 11.
[4] The Materials Project. *Materials Data on LiMnPO4 by Materials Project.* United States: N. p., 2020. Web. doi:10.17188/1193777.

High-Resolution ARPES of Heavily Overdoped Bi2201 for Evaluation of Coupling Parameters

Y. Miyai[1], S. Ideta[1,2], T. Kurosawa[3], M. Oda[4], M. Arita[2], K. Tanaka[5] and K. Shimada[1,2]
[1]*Graduate School of Advanced Science and Engineering, Hiroshima University,*
Higashi-Hiroshima 739-0046, Japan.
[2]*Hiroshima Research Institute for Synchrotron Radiation Science (HiSOR), Hiroshima University,*
Higashi-Hiroshima 739-0046, Japan
[3]*Faculty of Science and Engineering, Muroran Institute of Technology, Muroran 050-8585, Japan*
[4]*Department of Physics, Hokkaido University, Sapporo 060-0809, Japan*
[5]*UVSOR Synchrotron Radiation Facility, Institute for Molecular Science, Okazaki 444-8585, Japan*

High transition-temperature (T_c) cuprate superconductors have attracted much interest since their discovery. While there have been extensive studies, there exist unsettled physical phenomena such as bad metal, density waves, magnetic fluctuations, and nematic phases [1-4]. These states are emergent from the competing charge, spin and lattice degrees of freedoms. To understand the origin of the physical properties of cuprates, it is desirable to disentangle these competing interactions and quantify each contribution. To this end, here we focus on the Bi-based high-T_c cuprate, $(Bi,Pb)_2Sr_2CuO_{6+\delta}$ (Bi2201). The Fermi surface of Bi2201 is relatively simple because there exists a single CuO_2 layer in the unit cell. In this study, we start from the overdoped region, where the electronic state is expected to behave as the Fermi Liquid [3]. However, recently, Kurashima *et al.* found a ferromagnetic fluctuation close to the vanishing T_c region, and the ground state properties in this region should be investigated [3]. Previously Meevasana *et al.* have done angle-resolved photoemission spectroscopy (ARPES) and examined the self-energy due to the electron-electron and electron-phonon interactions especially for the heavily overdoped Bi2201 with no superconducting transition [5]. However, each contribution from the electron-phonon (or electron-boson) and electron-electron interactions as a function of hole concentration is still not clearly determined. Our purpose is, therefore, to systematically clarify the evolution of these interactions as a function of hole concentrations.

To quantitatively evaluate the electron-boson interaction and the electron-electron interaction, we have focused on the Bi-based high-T_c cuprate, Pb-Bi2201 and performed high-resolution ARPES at BL5U. The low T_c (~6 K) allows us to evaluate the normal self-energy at low temperature by suppressing the thermal broadening. In addition, the Pb doping suppresses the structural modulations of the BiO layer and hence the superstructure reflections in the ARPES spectra, and therefore, the overdoped sample is expected to behave like metals enable us to extract normal self-energy. We clearly observed a parabolic quasiparticle dispersion in the nodal direction [7]. By applying tight-binding (TB) model, and we found that the evaluated real part of the self-energy crosses the zero point around $\omega \sim -0.6$ eV, where the imaginary part of the self-energy takes the minimum. The self-energy part responsible for the high-energy anomaly (HEA) is almost temperature independent and the coupling parameter is $\lambda_{\mathrm{HEA}} \sim 1$ at 300 K, indicating strongly correlated nature of the strange metal state. We have also measured fine details near the Fermi level using the μ-Laser ARPES machine and have observed a clear kink structure around -90 meV. From this experiment, we found that, the self-energy part responsible for the low-energy kink (LEK) near the Fermi level shows significant temperature dependence: it is $\lambda_{\mathrm{LEK}} \sim 0.1$ at 300 K but enhances steeply below ~150 K up to $\lambda_{\mathrm{LEK}} \sim 0.8$, leading to the total coupling strength of $\lambda_{\mathrm{tot}} = \lambda_{\mathrm{HEA}} + \lambda_{\mathrm{LEK}} = 1.8$ at 20 K.

In this study, we evaluated the self-energy due to the electron-phonon and electron-electron interactions using the two band TB model. Comparing the theoretical results, the high-energy anomaly is considered to originate from local excitations that are characterized by spin fluctuation or charge fluctuation. Our results clearly indicate distinct energy scales in the self-energy, providing insight into the strange metal state as well as the temperature-dependent interactions of many-body interactions. The details of this study have been published in Ref. [6].

[1] P. Choubey *et al.*, PNAS, **117** (2020) 14805.
[2] Y.Y. Peng *et al.*, Nature Materials **17** (2018) 697.
[3] K. Kurashima *et al.*, Physical Review Letters **121** (2018) 057002.
[4] N. Auvray *et al.*, Nature Communications **10** (2019) 5209.
[5] W. Meevasana *et al.*, Physical Review B **75** (2007) 0174506.
[6] Y. Miyai *et al.*, Phys. Rev. Research **7** (2025) L012039.

BL5U

Electronic Structure Modulation in the CDW Phase of Kagome Superconductor AV_3Sb_5 Studied by ARPES

K. Nakayama[1], S. Suzuki[1], T. Kato[2], Y. Li[3,4,5], Z. Wang[3,4,5], S. Souma[2,6], K. Tanaka[7,8],
T. Takahashi[1], Y. Yao[3,4] and T. Sato[1,2,6,9,10]
[1]Department of Physics, Graduate School of Science, Tohoku University, Sendai 980-8578, Japan
[2]Advanced Institute for Materials Research (WPI-AIMR), Tohoku University, Sendai 980-8577, Japan
[3]Centre for Quantum Physics, Key Laboratory of Advanced Optoelectronic Quantum Architecture and Measurement (MOE), School of Physics, Beijing Institute of Technology, Beijing 100081, P. R. China
[4]Beijing Key Lab of Nanophotonics and Ultrafine Optoelectronic Systems, Beijing Institute of Technology, Beijing 100081, P. R. China
[5]Material Science Center, Yangtze Delta Region Academy of Beijing Institute of Technology, Jiaxing 314011, P. R. China
[6]Center for Science and Innovation in Spintronics (CSIS), Tohoku University, Sendai 980-8577, Japan
[7]UVSOR Synchrotron Facility, Institute for Molecular Science, Okazaki 444-8585, Japan
[8]School of Physical Sciences, The Graduate University for Advanced Studies (SOKENDAI), Okazaki 444-8585, Japan
[9]International Center for Synchrotron Radiation Innovation Smart (SRIS), Tohoku University, Sendai 980-8577, Japan
[10]Mathematical Science Center for Co-creative Society (MathCCS), Tohoku University, Sendai 980-8578, Japan

The kagome lattice provides a rich platform for the exploration of unconventional quantum phenomena, including Weyl semimetals, chiral density-wave orders, fractional charges, and exotic superconductivity. These arise from the interplay of electron correlation effects with unique electronic band features like flat bands, Dirac cones, and van Hove singularities. The recently discovered materials AV_3Sb_5 (A: an alkali metal), characterized by vanadium atoms forming an ideal two-dimensional kagome network, offer a valuable opportunity to explore novel physics within the kagome lattice structure [1].

AV_3Sb_5 exhibits the charge-density wave (CDW) state defined by three-dimensional lattice distortions with a periodicity of 2 × 2 × 2 or 2 × 2 × 4, depending on the A element. The CDW transition temperature, T_{CDW}, varies according to the alkali metal, ranging from 78 K to 103 K. Within this CDW phase, AV_3Sb_5 materials often display a breaking of not only translational symmetry but also rotational symmetry. The latter phenomenon suggests the emergence of nematic states, which have occasionally been identified in strongly correlated electron systems, such as cuprates and iron-based superconductors. To verify this nematicity and elucidate its origin, a detailed investigation of the electronic band structure is essential.

In this study, we have performed high-resolution angle-resolved photoemission spectroscopy (ARPES) measurements of a series of AV_3Sb_5 (A = K, Rb, and Cs). High-resolution ARPES measurements were performed at BL5U with linearly polarized photons of 90-150 eV.

Figure 1 shows a representative band dispersion measured in the CDW state of KV_3Sb_5. Compared to the normal state, we observed doubling of some energy bands, which indicates CDW-induced electronic reconstruction [2,3]. We performed first-principles band calculations to understand the observed band doubling and found it originates from the formation of staggrred three-dimensional CDW order. This CDW state naturally breaks rotational symmetry, resulting in nematic-like responses. To amplify the nematic-like response, we developed uniaxial strain device compatible with ARPES, and studied impact of uniaxial strain on the electronic structure.

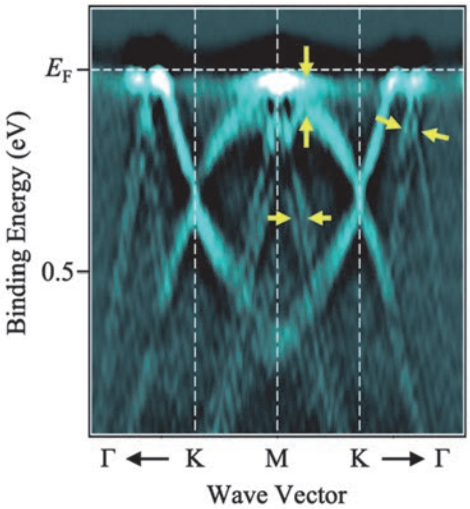

Fig. 1. Second-derivative ARPES intensity plot measured in the CDW state in KV_3Sb_5.

[1] Y. Zhong, J.-X. Yin and K. Nakayama, J. Phys. Soc. Jpn. **93** (2024) 111001.
[2] K. Nakayama *et al.*, Phys. Rev. B **104** (2021) L161112.
[3] T. Kato *et al.*, Commun. Mater. **3** (2022) 30.

BL5U

Explorations of Bandgap-Tuned Excitonic Insulator Materials by Angle-Resolved Photoemission Spectroscopy

K. Fukutani[1,2], R. Nakazawa[1], S. Makita[1], K. Tanaka[1,2] and S. Kera[1,2,3]
[1]*Institute for Molecular Science, Okazaki 444-8585, Japan*
[2]*School of Physical Sciences, The Graduate University for Advanced Studies, Okazaki 444-8585, Japan*
[3]*Graduate School of Science and Engineering, Chiba University, Chiba 263-8522, Japan*

An exciton, a bound pair of an electron and a hole, is one of the most fundamental quasiparticles in condensed matters, which forms as a result of external excitations, such as light irradiations, and plays a pivotal role not only in various electronic devices, including photovoltaic cells and light-emitting diodes, but also in biological processes like photosynthesis.

On the other hand, it is interesting to point out that in the most naïve picture, the negatively charged electrons and positively charged holes would naturally attract each other, and one may expect their bound state (excitons) to be stable in the ground state of matters. Of course, this view is, generally speaking, incorrect in that excitons would *not* form spontaneously in most materials. This is, roughly speaking, due to the effect of electrostatic screening arising from the sea of charged particles, which needs to be properly accounted for when the many-body ground state is to be determined. As it turns out, for most materials, the effect of screening is strong enough to make the binding of electrons and holes energetically more expensive than when they remain separated.

Extending along the line of thought mentioned above, an interesting question can be proposed; that is, what if we tune the bandgap of materials so as to decrease the density of carriers (i.e., source of screening) across the limit where the simple electron- hole Coulomb attraction can overcome the "barriers" of carrier screening? This question is pondered by N. F. Mott, W. Kohn, D. Jerome and others, and have led to the theoretical prediction of what is called an *excitonic insulator* (EI) [1], in which the simple Coulomb attraction between the electrons and holes manifests itself as they form a condensate of excitons in the many-body ground state.

While the charge neutrality of excitons and the lack of distinct macroscopic behaviors like superfluidity had made it difficult for the experimental probes to unambiguously detect the EI phase, various prominent candidate materials exist, such as Ta_2NiSe_5 and $TiSe_2$. In particular, $TiSe_2$ has been proposed as an EI material nearly two decades ago [2] and have been extensively investigated by various experimental probes. Nonetheless, due to the presence of both the exciton and the phonon degrees of freedom, which are closely interlinked near the quantum criticality, its true nature is still under disputes and a general consensus has not been reached.

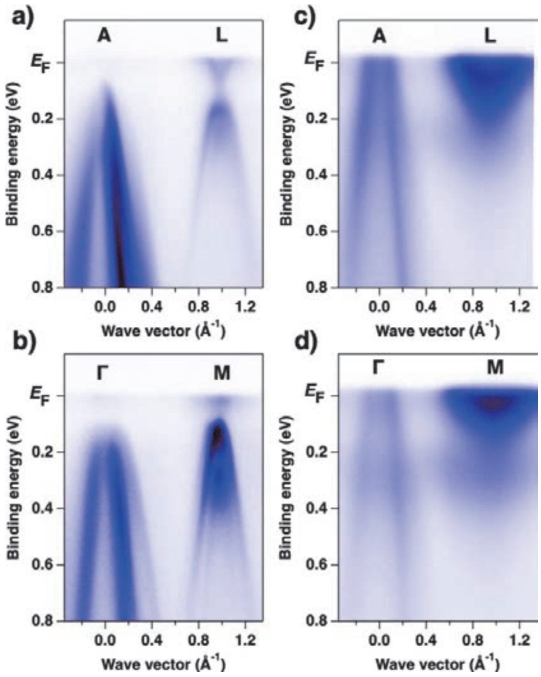

Fig. 1. ARPES intensity plots for $TiSe_2$ ($x = 0$) taken at (a) $h\nu = 44$ eV, (b) $h\nu = 58$ eV and TiSeTe ($x = 0.5$) taken at (c) $h\nu = 44$ eV, (d) $h\nu = 58$ eV near the indicated high-symmetry lines of bulk Brillouin zones at $T = 10$ K.

Thus, we once again trace back to the original question of how the bulk carrier density (closely linked to the magnitude of bandgap) affects the competition between the electron-hole Coulomb attraction and the carrier screening. In our experiments, we have performed the photon-energy- and polarization-dependent angle-resolved photoemission spectroscopy (ARPES) on $Ti(Se_{1-x}Te_x)_2$, to observe the evolution of their 3D band structures. As shown in Fig. 1, the negative bandgap is clearly enhanced as the Te-doping x increases from 0 to 0.5 and at the same time, the charge density wave, believed to be accompanied by the EI transition, is confirmed to be suppressed down to $T = 5$ K. Further investigations on various Te-doping concentrations are expected to provide important insights into one of the fundamental questions in many-body condensed matter physics.

[1] D. Jerome *et al*., Phys. Rev. **158** (1967) 462 etc.
[2] H. Cercellier *et al*., Phys. Rev. Lett. **99** (2007) 146403 etc.

BL5U

Relation between Electronic Structure and Thermopower in $YbCu_2Si_2$

D. Goto[1], S. Uchida[1], M. Matsunami[1,2,3] and T. Takeuchi[1,2,3]
[1]*Toyota Technological Institute, Nagoya 468-8511, Japan*
[2]*Research Center for Smart Energy Technology, Toyota Technological Institute, Nagoya 468-8511, Japan*
[3]*MIRAI, Japan Science and Technology Agency, Tokyo 102-0076, Japan*

Thermoelectric technology, which is capable of converting temperature differentials directly into electrical energy, can maximize the efficient use of existing energy sources. However, thermoelectric generation has not been widely applied in our society due to its energy conversion inefficiency. As evaluation criteria for the efficiency, the dimensionless figure of merit $ZT = S^2T/\rho\kappa$ or the power factor $PF = S^2/\rho$ where S, ρ, and κ are the Seebeck coefficient, electrical resistivity, and thermal conductivity, respectively, of constituent materials, are well known. It is necessary to search for materials possessing large ZT or PF.

It is known that in heavy fermion systems, the low ρ and large $|S|$ coexist, resulting in a large PF. This can be caused by the characteristic electronic structure formed by the hybridization between conduction and f electrons. However, there is a serious problem concerning the sign of S, which cannot be determined solely in terms of the energy dependence of the electron density of states as in most simple metals. Therefore, the energy dependence of the relaxation time of quasiparticles, both which are the terms in Mott formula and are neglected in many cases, should be taken into account.

The main purpose of this research is to establish a methodology for experimentally evaluating the energy dependence of the relaxation time of quasiparticles in the vicinity of the Fermi level (E_F) using angle-resolved photoemission spectroscopy (ARPES). In this study, we focus on the typical heavy fermion system $YbCu_2Si_2$, which is known to show relatively high large $|S|$ [1].

Single crystals of $YbCu_2Si_2$ were prepared by the Sn-flux method. The elements, Yb (3N) Cu (4N), Si (5N), and Sn (3N), with an off-stoichiometric ratio of Yb : Cu : Si : Sn = 1 : 15 : 2 : 50 were inserted in an alumina crucible and sealed in a quartz tube. The quartz tube was heated to 1050 °C, maintained at this temperature for two days, and cooled to 600 °C at the rate of 2 °C/h, taking about 12 days in total. The excess flux was removed using a centrifuge outside the furnace. Synchrotron ARPES measurements were carried out at the undulator beamline BL5U of UVSOR facility in the Institute for Molecular Science, using photon energies of 40 eV - 121 eV and a hemispherical electron analyzer, MBS-A1. The total energy resolution was set to 21 meV for a photon energy of 40 eV. The clean (001) surface of single crystals was obtained by *in-situ* cleaving under ultra-high vacuum condition. The Fermi level was determined by measuring a polycrystalline gold film in electrical contact with the samples.

The inset of Fig. 1 shows the Brillouin zone of $YbCu_2Si_2$. In the present study, the ARPES image is measured along the directions from Γ to X or from Z to X in the neighboring Brillouin zone corresponding to the $\bar{\Gamma}$-$\bar{X}$ direction in the surface Brillouin zone. Figure 1 shows the Fermi surface measured with a photon energy of 40 eV. According to the band calculation (LDA + U) [1], $YbCu_2Si_2$ has at least two Fermi surfaces, in which one is due to quasi two-dimensional (33th) electron band centered at X point focused in the present study and the other is due to three-dimensional (32th) hole band around Z point. By analyzing these bands, we will further investigate the relation between the electronic structure and Seebeck coefficient in $YbCu_2Si_2$.

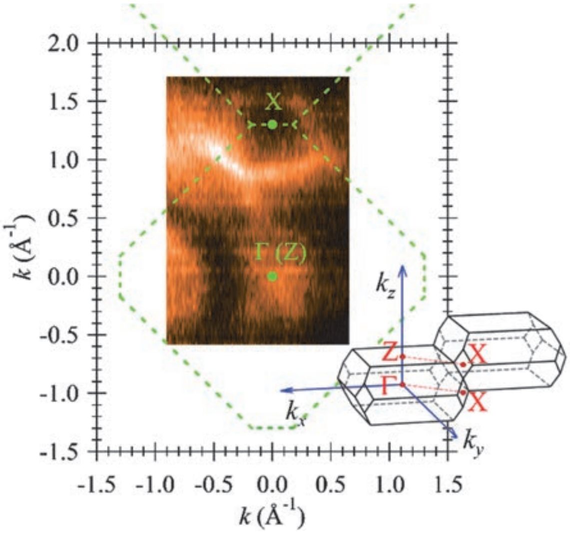

Fig. 1. (a) ARPES image of $YbCu_2Si_2$ along $\bar{\Gamma}$-$\bar{X}$ direction at 9 K measured with the photon energy of 121 eV.

[1] N.D. Dung *et al.*, J. Phys. Soc. Jpn. **78** (2009) 084711.
[2] M. Matsunami *et al.*, Phys. Rev. B **87** (2013) 165141.

BL5U

Electronic Structure Study on Novel Spin-Split Collinear Antiferromagnets

Z. Lin[1], X. Liang[1] and J. Ma[1]
[1]*Department of Physics, City University of Hong Kong, Kowloon, Hong Kong, China*

Magnetism, a foundational domain in condensed matter physics, conventionally classifies magnetic materials into two primary phases: ferromagnets and antiferromagnets (although unconventional forms like ferrimagnetism and chiralmagnetism are also recognized). Ferromagnets exhibit macroscopic magnetization in spatial space and spin splitting in reciprocal momentum space.

Conversely, typical antiferromagnets show no net macroscopic magnetization in spatial space and no spin splitting in reciprocal momentum space when time reversal symmetry combined with inversion or translation operation is preserved [1–3]. Recent theoretical investigations have identified special collinear antiferromagnetic materials with substantial spin-split band structures but no net macroscopic magnetization. This has led to the proposal of altermagnetism, a special antiferromagnetic phase that appropriately describes such materials. In contrast to conventional antiferromagnets, which have spin sublattices linked to one another through straightforward translation operations, altermagnetism involves linking sublattices with opposite spins using rotation operations. Applying the same rotational angle in momentum space causes a spin flip between up and down. As outcome of this phenomenon, even-order wave symmetries of the spin pattern appear, such as the d-, g-, and i-waves. Recently, it has even been suggested that altermagnetism can extend to include non-collinear spins and multiple local-structure variations.

In this study, we focus on d-wave altermagnet candidate RuO_2 and g-wave altermagnet candidate CrSb. We have carried out high-resolution spin angle-resolved photoemission spectroscopy (ARPES) measurements of RuO_2 and CrSb by using MBS-A1 spectrometer and customized VLEED spin detector at BL5U.

Figure 1 and 2 shows the spin ARPES result of this beamtime. Figure 1 shows that RuO_2's spin texture is symmetric about the Γ point, which conflicts with the presented result [4]. The result in Fig.1 indicates that the spin texture of RuO_2 is not from space-inversion symmetry breaking. Figure 2 shows the possible spin splitting band structure of CrSb.

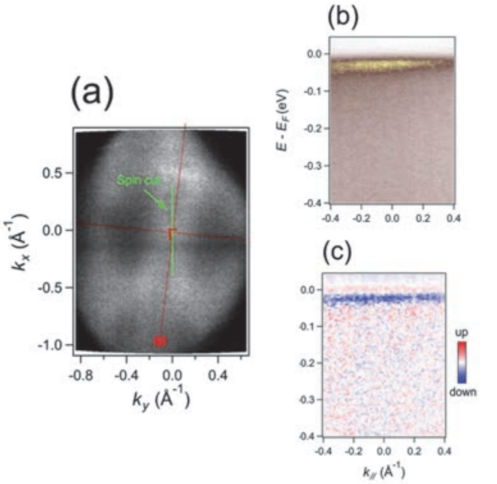

Fig. 1. (a), Fermi Surface of RuO_2. (b), The ARPES band structure of the green line in Fig. 1(a). (c), The spin resolved data of the same path band structure as (b).

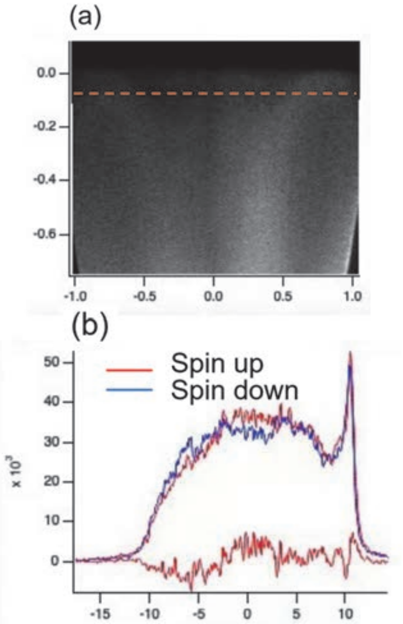

Fig. 2. (a), a high-symmetric path's band structure of CrSb. (b), The spin resolved MDC of the orange line of figure 2(a).

[1] L. Néel, Science **174** (1971) 985.
[2] L. Šmejkal, J. Sinova, and T. Jungwirth, Phys. Rev. X **12** (2022) 031042.
[3] L. Šmejkal, J. Sinova, and T. Jungwirth, Phys. Rev. X **12** (2022) 040501.
[4] J. Liu *et al*., Phys. Rev. Lett. **133** (2024) 176401.

BL5U

Photoemission Study about the Fermi Arc in Type-II Weyl Semimetal NbIrTe$_4$

S. Cho[1] and D. Shen[2]
[1]*Department of Physics Education, Sunchon National University, Suncheon57922, Republic of Korea*
[2]*National Synchrotron Radiation Laboratory, University of Science and Technology of China, Hefei 230026, China*

The unique features of topological Weyl semimetals (TWSs) arise primarily from their unusual band structure around the Weyl nodes and the topologically non-trivial surface state as Fermi arc, which connect each pair of Weyl nodes [1]. Moreover, TWSs have a family so-called type-II TWSs, where the Weyl nodes are highly anisotropic and tilted, breaking the Lorentz symmetry [2]. The Weyl nodes of type-II TWSs appear as contact points between electron and hole pocket in the bulk band structure, which result in the presence of the boundaries between these pockets. One of the promising candidates for type-II TWSs is WTe$_2$, which has the orthorhombic crystal structure with space group *Pmn2₁* and the bulk system of WTe$_2$ exhibits the non-saturating magnetoresistance [2].

Recently, NbIrTe$_4$ and TaIrTe$_4$, which crystallize in the non-centrosymmetric orthorhombic space group *Pmn2₁* (No. 31), have been suggested as possible type-II TWSs. The previous calculation result of NbIrTe$_4$ revealed a closed Fermi arc loop that connects two distinct pairs of Weyl nodes from the top and bottom surfaces in the type-II TWSs [3]. Given the symmetry of TaIrTe$_4$ (presence of time-reversal symmetry but with broken inversion symmetry) and the Berry curvature originating from its type-II Weyl nodes, TaIrTe$_4$ can expect to exhibit a large and room-temperature nonlinear Hall effect [4]. Moreover, the recent scanning tunneling microscopy results of TaIrTe$_4$ show a superconducting gap below a critical temperature 1.54 K [5]. The behavior of the normalized upper critical field and the stability of the superconductivity against the ferromagnetism suggest the unconventional superconductivity with the p-wave pairing. The results of the scanning tunneling spectroscopy and angular-dependent transport measurements show that the superconductivity is the quasi-1D and occurs in the surface states [5].

Here, we investigate the spin structure of the Fermi arc associated with the type-II Weyl nodes in NbIrTe$_4$. Given the lack of inversion symmetry, NbIrTe$_4$ is predicted to host four type-II Weyl nodes. In previous band calculation, one of these type-II Weyl points was found to show an intersection of tilted cone which lies on the Fermi energy at $E - E_F = 0.131$ eV. The electronic structure of NbIrTe$_4$ shows the different surface state at two different surface terminations (top and bottom surface in Fig. 1a), leading to distinct Fermi arc loop configuration. This is because the Fermi arc loop connects different pairs of the Weyl nodes depending on the surface termination.

Figure 1 (b) and (c) show the Fermi surface and the band structure at $k_y = 0$ (red dotted line in Fig. 1b) taken from the bottom surface termination. The Fermi arc exists near the Γ-point, consistent with the previous band calculation results in Ref. [3]. We try to measure the spin structure of the Fermi arc in Fig. 1 (d). Figure 1 (d) shows the spin-resolved momentum distribution curves (MDC) and spin polarization of the Fermi arc at EB = -0.01 eV. We found that the spin polarization taken from the left and right momentum points show opposite direction of s_y with red and blue assigned for spin-down and spin-up respectively. We hope our results on the spin-resolved MDC may provide valuable insights into the characteristics of type-II Weyl nodes.

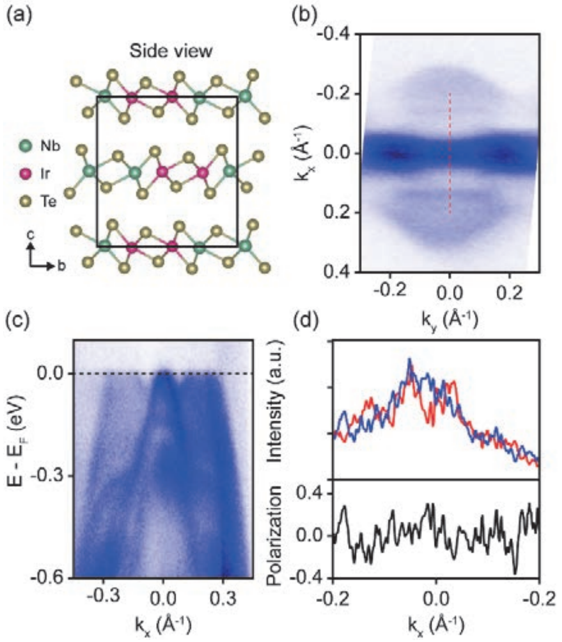

Fig. 1. (a) Crystal structure of NrIrTe$_4$ (b) The Fermi surface obtained from the bottom surface termination. (c) The band structure at the red line in b. (d) spin-resolved MDC along the s_y direction and the spin polarization at $E_B = -0.01$ eV.

[1] A. Bansil, H. Lin, and T. Das, Rev. Mod. Phys. **88** (2016) 021004.
[2] A. A. Soluyanov *et al.*, Nature **527** (2015) 495.
[3] S. A. Ekahana *et al.*, Phys. Rev. B **102** (2020) 085126.
[4] D. Kumar *et al.*, Nat. Nanotechnol. **16** (2021) 421.
[5] Y. Xing *et al.*, Natl. Sci. Rev. **7** (2020) 579.

BL6U

Accurate 2D-Momentum-Microscopy-Data Distortion Correction Method for Characterization of Valence Band Spin Polarization

F. Matsui[1,2], Y. Sato[1,2], K. Hagiwara[1], S. Tanaka[3] and S. Suga[3]
[1]*UVSOR Synchrotron Facility, Institute for Molecular Science, Okazaki 444-8585, Japan*
[2]*The Graduate University for Advanced Studies (SOKENDAI), Okazaki 444-8585, Japan*
[3]*SANKEN, The University of Osaka, Ibaraki 567-0047, Japan*

Combining a two-dimensional (2D) spin filter with a photoelectron momentum microscope (PMM) allows multi-channel detection of spin polarization data in 2D momentum and real spaces. An established method for spin polarization analysis is to measure the difference between two patterns taken at the different scattering energies corresponding to the opposite spin-dependent reflectivity [1]. On the other hand, the PMM installed at BL6U in UVSOR [2] is equipped with a spin rotator that flips the direction of the in-plane spin component by ±90°. In addition to the conventional method of taking the scattering energy dependence, the spin rotator makes it possible to detect the spin polarization pattern using a single-scattering-energy condition [3]. The spin rotator can alternate between positive and negative spin polarization detection in times less than one second, opening the door to the efficient accumulation of multi-dimensional (*kz* dispersion, position scan, time evolution, photon polarization, etc.) spin-polarized spectral data. The drawback is that the spin components rotate by ±90° due to Larmor precession in the spin rotator, and the 2D projection distributions also rotate by ±45° due to the Lorentz force simultaneously. To obtain a differential pattern of the 2D distribution of positive and negative spins, the coordinates of the two ±45° rotated patterns must be precisely rotated back to their original orientation to eliminate aberration and distortion.

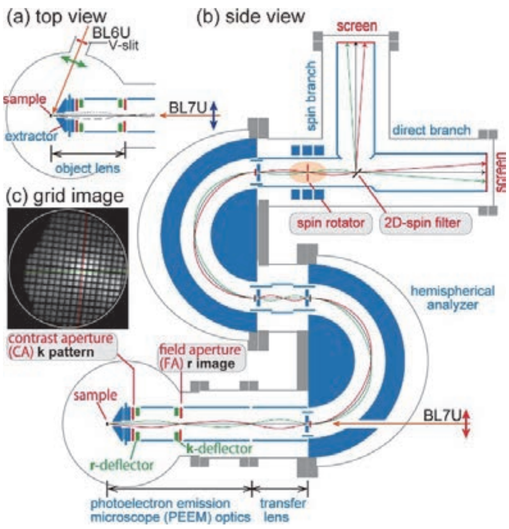

Fig. 1. (a) Top and (b) side views of the photoelectron momentum microscope. (c) The grid inserted at the location of the CA imaged by the direct branch screen.

The PMM at BL6U consists of a six-axes sample stage, PEEM optics, two concentric hemispherical analyzers, a spin rotator, a 2D spin filter, and 2D projection-type detectors in direct and spin-resolved branches as shown in Fig. 1(a) and (b). Instead of a contrast aperture and a field aperture, square grids that can be inserted in the diffraction and back focal planes, respectively, are used to correct distortions of the 2D pattern on the final detection screen. Figure 1(c) shows the image of such a grid on a direct branch screen inserted at the contrast aperture position. Note that the grid is intentionally rotated approximately 5° counter-clockwise to be offset from the pixel array of the CMOS detector.

Figure 2(a) and (b) show images of the CA grid using the ±45° rotation modes of the spin rotator by the direct branch. The latter image is rotated -90° with respect to the former. Figures 2(c) and (d) show the images after numerical correction of coordinate rotation and distortion. As shown in Fig. 2(e) and (f), the horizontal and vertical intensity profiles of the two images (blue: +45°, red: -45° rotation mode) match exactly. Since the spin rotator only affects the photoelectron trajectory after they leave the second hemispherical analyzer, the positional relationship between the valence band pattern and the grid image is not affected. Based on this correction procedure, two spin polarized images are aligned exactly the same coordinates and the spin-polarized valence band dispersion and Fermi surface data are analyzed [3].

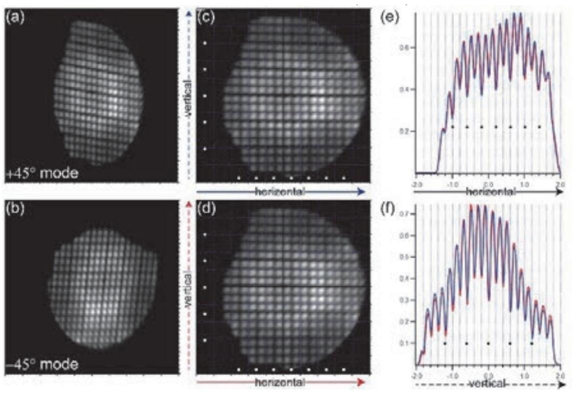

Fig. 2. (a, b) Raw and (c, d) coordinate-corrected grid images of the spin rotator ±45° modes. (e, f) Intensity profiles along the horizontal and vertical directions.

[1] C. Tusche *et al.*, Ultramicroscopy **159** (2015) 520.
[2] F. Matsui *et al.*, J. Phys. Soc. Jpn. **59** (2020) 067001.
[3] F. Matsui *et al.*, submitted (2025).

BL6U

Steady Development of the SP-PMM at UVSOR BL6U with Reliable Data Acquisition and Very High Efficiency

S. Suga[1]
[1]SANKEN, Osaka University, Mihogaoka, Ibaraki, Osaka 567-0047, Japan

In order to overcome various and serious difficulty of the single channel spin-resolved-ARPES (SP-ARPES) detection by use of a single hemispherical electron energy analyzer, much more reliable and orders of magnitude higher detection efficiency spin-resolved Photoelectron Momentum Microscope (SP-PMM) with double hemispherical electron energy analyzers (DHDAs) and PEEM type objective lens as well as two dimensional spin detector (SP-PMM) was introduced to UVSOR in 2022.

Two dimensional(2D) real space $E_B(x, y)$ is first measured with changing the sample position and the high quality homogeneous (x, y) regions (even down to 10μm) are selected. Then objective lens mode is switched to the $E_B(k_x, k_y)$ mode and their 2D patterns beyond the 1st Brillouin zone of most materials are recorded at various E_B with 2D detector without sample movement (Fig.1). Even in the case of multidomain cleaved surfaces, PEEM can select a certain particular domain region with the size larger than ~10μm. Then $E_B(k_x, k_y)$ series are integrated as functions of hν. The spatial resolution is decided by the PEEM aperture as good as 50nm. Temperature dependent PMM is feasible down to 10 K now in UVSOR BL6U. The measurements have so far been performed on variety of samples [1-3]. Since the selection rule must be taken into account for understanding several experimental results, we also realized the feasibility of the normal incidence excitation from the branched line of BL7U as shown partly in Publications.

For the spin measurement, Ir(001) clean surface has been so far utilized. This spin filter was used at around 30 eV photoelectron collision with the Ir of the life time of less than 1 day, by use of the spin rotator. Since the tuning of the collision energy down to 10eV became feasible recently after solving an instrumental problem, we will soon start the Au monolayer covered Ir spin filter in few months. Its life time is already checked to be several months. Then we will perform most experiments by this performance-upgraded SP-PMM on the materials under various hot discussions.

So far we have measured the samples with the clean surface prepared either 1) by ion sputtering and annealing or 2) cleaved by peeling off tapes. The 3) pin post pressed cleavage was also employed for wide variety of samples. In addition, the knife-edge cleavage is required for hard materials. So I designed 4) a cleavage crystal recovering box with the knife edge on it. Further the 5) flexibly adjustable knife edge cleavage system is planned to be added in the near future for much more sample cleavage.

In addition, I am preparing an operation manual to use the complex SP-PMM in UVSOR in English, since the demand from the foreign users are expected to increase dramatically in 2025 after the perfect performance of the Au/Ir(001) spin filter, and the use of flexible cleavage system.

Since the normal incidence synchrotron radiation use is very limited, I hope to introduce switchable low energy laser with variable light polarization to be set in the normal incidence configuration. If the pulsed laser is set pump-probe SP-PMM may become feasible.

The collaboration have been so far performed with the research members Prof. F. Matsui, Prof. S. Kera, Dr. Y. Sato, Dr. R. Sagehashi, Dr. K. Hagiwara in UVSOR, IMS & Prof. S. Tanaka, SANKEN, Osaka Univ. I hope to contribute to future works for the next 20 years.

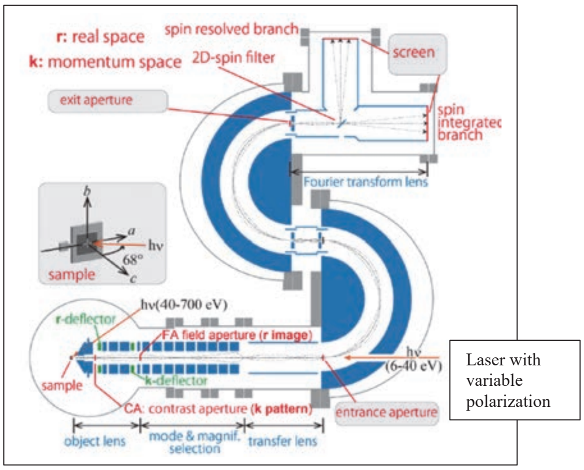

Laser with variable polarization

Target is to realize the best resolutions in x, y, k_x, k_y, k_z, Spin (Psx, Psy, Psz) from VUV to Hard X-ray region. Operand measurements are also planned. Spin rotator is in work.

Related-Publication

[1] F. Matsui, K. Hagiwara, E. Nakamura, T. Yano, H. Matsuda, Y. Okano, S. Kera, E. Hashimoto, S. Koh, K. Ueno, T. Kobayashi, E. Iwamoto, K. Sakamoto, S. Tanaka and S. Suga Rev. Sci. Instrum. **94** (2023) 083701.

[2] F. Matsui, K. Hagiwara, Y. Sato, E. Nakamura, R. Sagehashi, S. Kera and S. Suga, Synchrotron Rad. News, **37** (2024).

[3] Y. Higuchi, R. Itaya, H. Saito, T. Toichi, T. Kobayashi, M. Tomita, S. Terakawa, K. Suzuki, K. Kuroda, T. Kotani, F. Matsui, S. Suga, H. Sato, K. Sato and K. Sakamoto, Vacuum, **233** (2025) 113944.

BL6U

Three-Dimensional Fermi Surface Measurement of the Au Crystal Via the Photon-Energy-Dependent Angle-Resolved Photoelectron Spectroscopy Using the Photoelectron Momentum Microscope

S. Tanaka[1], S. Suga[1], K. Hagiwara[2], Y. Sato[2] and F. Matsui[2]
[1]*SANKEN, The University of Osaka, Mihogaoka 8-1, Ibaraki 567-0047, Japan*
[2]*UVSOR Synchrotron Facility, Institute for Molecular Science, Okazaki 444-8585, Japan*

The Fermi surface is a fundamental concept in solid-state physics, representing the boundary in momentum space that separates occupied from unoccupied electronic states. While much progress has been made in understanding the 2D Fermi surface by the angle-resolved photoelectron spectroscopy (ARPES) for materials like thin films or surfaces, obtaining the full 3D Fermi surface has remained a significant challenge, due in part to the complexity of the experimental techniques involved and the immense volume of data required to map the surface in three dimensions.

The dual-beamline photoelectron momentum microscope (PMM) developed at UVSOR is a powerful tool not only for comprehensively characterizing orbital contributions in the electronic structure, but also for determining the Fermi surface, thanks to its high efficiency and extensive momentum-space detection range [1,2]. In recent years, we have been developing methods for 3D Fermi surface determination, both experimentally and through computer-based analyses.

Figure 1 presents the photoelectron intensity maps obtained with the measurements using the PMM for the Au(111) surface, which correspond to the Fermi surface in various planes within the reciprocal lattice space of the Au crystal. Panel (a) shows the k_x–k_y plane at the indicated k_z values, while panels (b) and (c) depict k_y–k_z and k_x-k_z planes at k_x=0 and k_y=0, respectively. The k_z values were estimated using the free-electron final-state model, as

$$k_z = \sqrt{\frac{2m_e}{\hbar^2}(E_k \cos^2\theta + V_0)}$$

where E_k and θ are the kinetic energy and the polar emission angle of the photoelectron, respectively. We assumed the inner potential V_0 is 10.5 eV. Photon energies ranging from 45 eV to 100 eV were employed. Because the Au crystal has three-fold symmetry along the <111> axis, all the intensity distributions in Figs. 1 are the results of averaging over three images; the original distribution and those rotated by 120° and 240°; in order to improve statistics and to suppress the effects of photon polarization. It should be noted that generating the 3D volume data (whose cross sections are shown in Figs. 1) from a series of photon-energy–dependent ARPES measurements required the development of specialized data conversion programs using the cutting-edge AI technique.

In Fig. 1(a), small circles with a radius of approximately 0.17 Å^{-1} around the origin are visible at all k_z values. Additionally, regular hexagons of uniform size, each with an approximate radius of 1 Å^{-1}, are clearly visible in the k_z range of 4.87–4.35 Å^{-1}. As these features do not depend on k_z in terms of their shapes (though their intensity may vary with photon energy), we attribute them to the Au(111) surface states. Other features, which change with k_z, should be attributed to photoelectrons emitted from the bulk 3D-Fermi surface. We are currently developing detailed comparisons between the experimental results and density functional theory (DFT) calculations performed using Quantum Espresso package (version 7.2). While some experimentally observed features are well reproduced by the theoretical calculations, significant discrepancies remain at this stage. Further investigation will be required to refine the methodology for revealing the 3D Fermi surface by exploiting photon-energy–dependent measurements, including the adoption of a more accurate final-state model beyond the free-electron approximation that has been recently proposed [3].

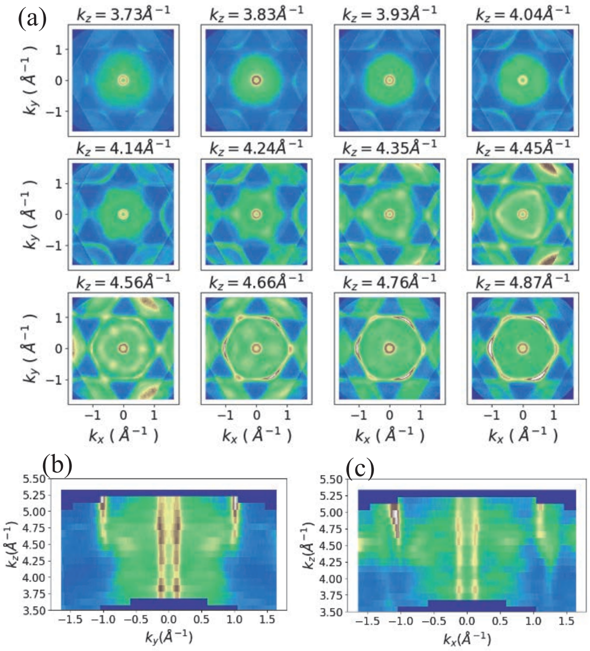

Fig. 1. Photoelectron intensity maps at the Fermi level of Au(111) for various planes in the reciprocal lattice space.

[1] F. Matsui *et al.*, Rev. Sci. Instrum. **94** (2023) 083701.
[2] K. Hagiwara *et al.*, J. Synchrotron Radi. **31** (2024) 540.
[3] V. N. Strocov *et al.*, Nat Commun. **14** (2023) 4827.

BL6U

Photoelectron Momentum Microscopy Study of Termination-Dependent Electronic Structure in $PtBi_2$

Y. Morita[1], K. Nakayama[1], T. Kato[2], S. Souma[2,3], S. Masaki[4], T. Ikushima[4], Y. Moriyasu[4],
K. Hagiwara[5], F. Matsui[5], T. Takahashi[1], K. Kudo[4] and T. Sato[1,2,3,6,7]
[1]*Department of Physics, Tohoku University, Sendai 980-8578, Japan*
[2]*Advanced Institute for Materials Research (WPI-AIMR), Tohoku University, Sendai 980-8577, Japan*
[3]*Center for Science and Innovation in Spintronics (CSIS), Tohoku University, Sendai 980-8577, Japan*
[4]*Department of Physics, Graduate School of Science, Osaka University, Toyonaka 560-0043, Japan*
[5]*UVSOR Synchrotron Facility, Institute for Molecular Science, Okazaki 444-8585, Japan*
[6]*International Center for Synchrotron Radiation Innov1ation Smart (SRIS), Tohoku University, Sendai 980-8577, Japan*
[7]*Mathematical Science Center for Co-creative Society (MathCCS), Tohoku University, Sendai 980-8578, Japan*

The discovery of exotic quantum phenomena, such as the half-integer quantum Hall effect in graphene and surface Dirac states in topological insulators, has sparked significant interest in condensed matter physics. These effects originate from novel quasiparticles associated with band degeneracies. For instance, graphene hosts two-dimensional Dirac fermions with linear band dispersion that intersect at a single point, because of the chiral symmetry of its honeycomb lattice. In topological insulators, surface conduction is driven by spin-polarized Dirac fermions, which are protected by time-reversal symmetry and nontrivial bulk topology. These findings stimulate research in exploring quasiparticles beyond Dirac fermions. Among these, Weyl fermions, 3D spin-polarized counterparts of Dirac fermions, are notable for their topological stability and unconventional phenomena such as the chiral anomaly and Fermi arc surface states. Weyl fermions can emerge when either spatial inversion or time-reversal symmetry is broken.

Among candidate Weyl semimetals, $PtBi_2$ is particularly intriguing. It consists of Bi-Pt-Bi trilayer sheets which stack along the c axis. One Bi layer is flat and the other is buckled, resulting in an A-B-C stacking sequence that naturally breaks inversion symmetry. This symmetry breaking combined with strong spin-orbit coupling from the heavy atomic masses lifts spin degeneracy in the band structure. DFT calculations predict that $PtBi_2$ hosts twelve Weyl fermions near $k_z = \pm 0.5\ \pi/c$. Moreover, this material exhibits bulk superconductivity at 0.6 K, and recent studies have suggested the existence of surface superconductivity at a significantly higher temperature (~10 K). This makes $PtBi_2$ a rare platform for exploring the interplay between Weyl fermions and superconductivity at relatively high temperatures. Such coupling could trigger the emergence of topological superconductivity with Majorana fermions, which are their own antiparticles.

In this study, we aimed to gain a comprehensive understanding of the surface-termination-dependent fermiology of $PtBi_2$. We performed photoelectron momentum microscopy measurements at BL6U and mapped the band structure over a wide momentum space. The Fermi surfaces observed for different terminations [Figs. 1(a) and 1(b)] show complex features. Spectral components common to both terminations are attributed to bulk states, while the different features are interpreted as surface states. By comparing our data with DFT-based Fermi surface calculations, we identify signatures of Fermi arc surface states, supporting the Weyl semimetal character of $PtBi_2$.

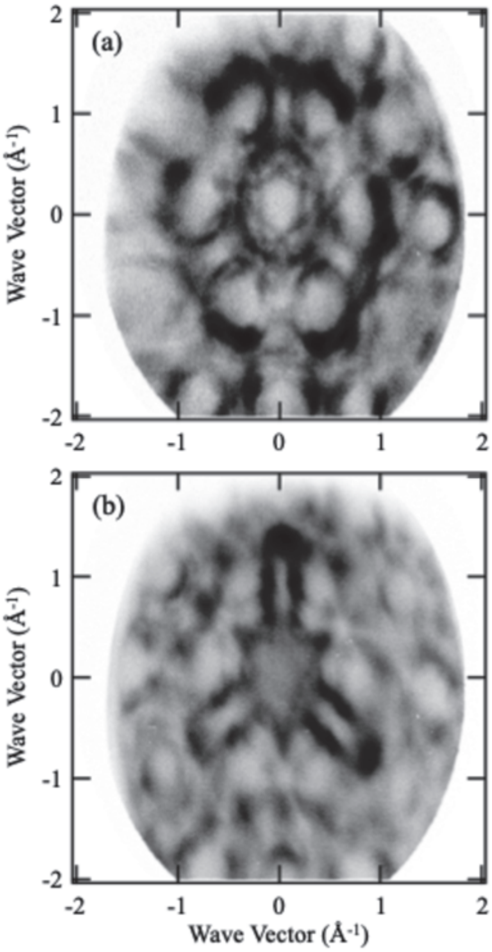

Fig. 1. (a) and (b) Two-dimensional ARPES intensity maps at a constant energy measured on different surface terminations in $PtBi_2$.

BL7U&5U

Changes in the Electronic Structure during the Charge-Density-Wave Transition Via the Well-Defined Temperature-Dependent Angle-Resolved Photoelectron Spectroscopy

S. Tanaka[1], K. Ueno[2] and K. Tanaka[3]
[1]SANKEN, The University of Osaka, Mihogaoka 8-1, Ibaraki 567-0047, Japan
[2]Department of Chemistry, Graduate School of Science and Engineering, Saitama University, Saitama 338-8570, Japan
[3]UVSOR Synchrotron Facility, Institute for Molecular Science, Okazaki 444-8585, Japan

The charge-density-wave (CDW) transition in titanium diselenide ($TiSe_2$) has attracted substantial interest due to its intriguing interplay between structural and electronic properties. Historically, X-ray diffraction studies have established a prominent structural transition near 202K [1], characterized predominantly by displacement of Ti atoms. More recently, advanced diffraction experiments revealed additional diffraction spots emerging at a lower temperature of approximately 165K, attributed primarily to the displacement of Se atoms which coincides with the peak-temperature observed in the resistivity change during the CDW transition [2]. Despite extensive structural investigations, detailed knowledge of how these distinct atomic rearrangements influence the electronic structure across the CDW transition remains incomplete.

In this study, we employ temperature-dependent angle-resolved photoelectron spectroscopy (ARPES) to investigate the electronic structure evolution of $TiSe_2$ across the CDW transition. The left panel of Fig. 1 presents ARPES spectra measured near the Γ point (top panel) and the L point (bottom panel) of $TiSe_2$, both below (left-hand side) and above (right-hand side) the CDW transition temperature. In the non-CDW phase (right-hand side), distinct features in the electronic states in $TiSe_2$ are Se4p-derived valence band and Ti3d conduction band located at the Γ and L points, respectively. The right panel of Fig. 1 displays the photoelectron intensity maps obtained along the momentum-space cuts indicated in the ARPES spectra, as a function of temperature. Our ARPES measurements reveal notable electronic signatures associated with the CDW transition including: (1) the folding of the Ti3d band from the Brillouin zone boundary (L point) toward near the zone center (Γ point), (2) the complementary folding of the Se4p band from near Γ toward the vicinity of the L point, and (3) a distinct binding energy shift of the Se4p band near the Fermi level.

Figure 2 illustrates the temperature dependence of the observed electronic signatures—specifically, the band folding intensity and energy shift—normalized such that values are set to 1 at 25 K and 0 at 200 K. The transition temperature for all the changes in the electronic structure is 165K, not the 202K. These observations indicate that the fundamental electronic reorganization in $TiSe_2$ is closely correlated with the lower-temperature structural transition involving Se atom displacement, rather than the higher-temperature transition predominantly involving Ti atom movements. Our findings clarify the relationship between electronic and structural transformations in $TiSe_2$ and underscore the critical role of Se atoms in driving the electronic properties of the CDW phase.

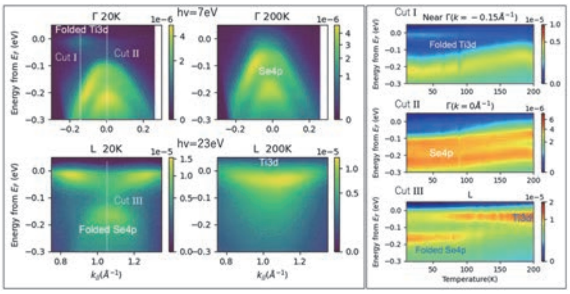

Fig. 1.
Left: the ARPES spectra near the Γ point (upper part) and L point (lower part) of $TiSe_2$ below the CDW temperature (left) and above (right).
Right: The photoelectron intensity map along the cut indicated in the ARPES spectra shown in the left panel as functions of the temperature.

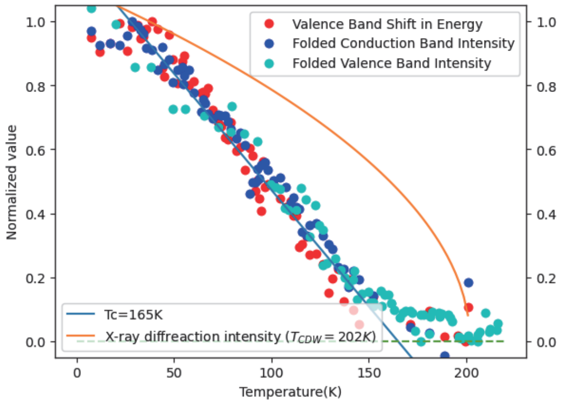

Fig. 2. Temperature dependence of the observed electronic signatures in $TiSe_2$, specifically the band folding intensity and binding energy shift, normalized to unity at 25 K and to zero at 200 K.

[1] F. J. Di Salvo, D. E. Moncton, and J. V. Waszczak, Phys. Rev. B **14** (1976) 4321.
[2] H. Ueda *et al.*, Phys. Rev. Res. **3** (2021) L022003.

BL6U

Momentum-Resolved Resonant Photoelectron Spectroscopy of Au(111) Toward Distinguishing p and d Orbital Contributions

K. Hagiwara[1], R. Sagehashi[1], Y. Sato[1,2], S. Tanaka[3], S. Suga[3] and F. Matsui[1,2]
[1]*UVSOR Synchrotron Facility, Institute for Molecular Science, Okazaki 444-8585, Japan*
[2]*The Graduate University for Advanced Studies (SOKENDAI), Okazaki 444-8585, Japan*
[3]*SANKEN, The University of Osaka, Mihogaoka 8-1, Ibaraki 567-0047, Japan*

Dual-beamline photoelectron momentum microscope (PMM) developed at UVSOR is a powerful tool for comprehensive characterization of orbital contribution to the electronic structure [1, 2]. Normal-incident VUV light from BL7U can be used to analyze atomic orbital symmetry [2]. Resonant photoelectron spectroscopy, utilizing photon-energy ($h\nu$) tunable soft X-ray from BL6U at specific core absorption edges, can provide element- and/or orbital-selective information [3]. We have determined 6p orbital arrangement in the Fermi surface of Au(111) by using horizontally and vertically polarized light from BL7U [2]. However, 5d orbital contribution to the Fermi surface was reported [4]. Therefore, light polarization dependent measurement distinguishing the p and d orbitals is challenging. Here, we have investigated the 6p and 5d orbital contributions to the Fermi surface of Au(111) by resonant photoelectron spectroscopy. Whether the 5d signal selectively enhanced when excited with the photon energy corresponding to transition from 4f to 5d was our question.

Figure 1 shows the photoemission intensity in the valence band region integrated over all momentum as a function of photon energy. One can find noticeable intensity peaks indicated by two dotted lines. These peak lines originate from the Au $4f_{7/2}$ and $4f_{5/2}$ core levels excited by the second order light. Figures 2(a) and 2(b) show the momentum map at E=E_F-0.2eV excited under the resonant ($h\nu$ = 83.9 eV, corresponding to the transition from 4f to 5d) and off-resonant ($h\nu$ = 85 eV) condition, respectively. One can see the bulk state corresponding to the cross section of the Fermi sphere of the bulk Au crystal: the nearly hexagonal contour centered at the $\bar{\Gamma}$ point. The Shockley surface state is centered at the $\bar{\Gamma}$ point as a small circular contour. The corresponding band dispersions are shown in Fig. 2 (d) and 2(e). For comparison, we chose the data taken at these photon energies and the binding energy to avoid influence of the core-level peaks excited by the second order light. As seen from their subtraction in Fig. 2(c) and 2(f), the intensity enhancement under the resonant condition was estimated to be less than 5%. We were not able to find the momentum dependence and different behavior of bulk and surface states for the intensity enhancement. From these results, we cannot conclude the 5d orbital contribution to the Fermi surface of Au(111).

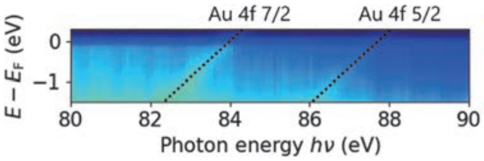

Fig. 1. Photoemission intensity of Au(111) in the valence band region integrated over all momentum as a function of photon energy. Dotted lines indicate the position of for Au $4f_{7/2}$ and $4f_{5/2}$ core levels excited by the second order light.

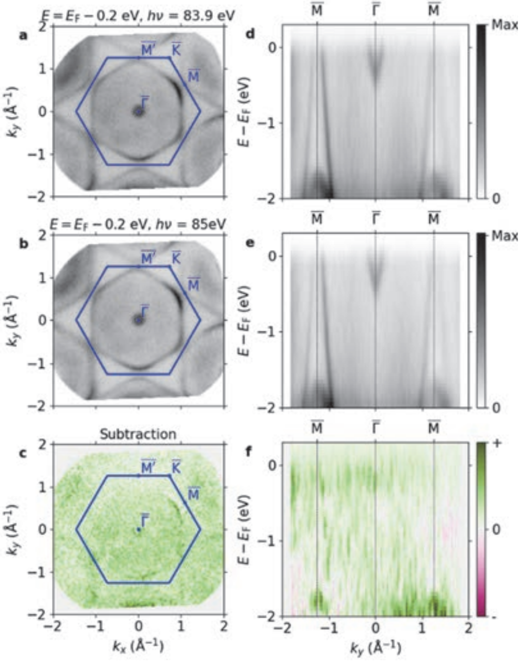

Fig. 2. Momentum-resolved resonant photoelectron spectroscopy of Au(111). (a, b) Momentum distribution at E=E_F-0.2eV excited under the resonant ($h\nu$ = 83.9 eV, corresponding to transition from 4f to 5d) (a) and off-resonant ($h\nu$ = 85 eV) conditions(b). (c) Subtraction between (a) and (b). (d-f) Same as (a-c), but the corresponding band dispersion.

[1] F. Matsui *et al.*, Rev. Sci. Instrum. **94** (2023) 083701.
[2] K. Hagiwara *et al.*, J. Synchrotron Rad. **31** (2024) 540.
[3] F. Matsui *et al.*, J. Phys. Soc. Jpn. **90** (2021) 124710.
[4] A. Sekiyama *et al.*, New J. Phys. **12** (2010) 043045.

BL6B

Infrared Absorption Measurements on Single Crystals and Amorphous Thin-Films of Rubrene

Y. Nakayama[1,2], R. Sakata[1] and Y. Baba[1]
[1]Department of Pure and Applied Chemistry, Tokyo University of Science, Noda 278-8510, Japan
[2]Institute for Molecular Science, Okazaki 444-8585, Japan

Rubrene (Fig. 1 inset) is a representative p-type organic semiconductor molecule exhibiting considerable charge carrier mobility over 10 cm^2/Vs [1] and widely dispersing intermolecular electronic bands [2] in its single-crystal (SC) phase. One peculiar character of this material is that charge carrier mobilities, crystallographic structures, and ionization energies of its vacuum-deposited thin-films (TFs) differ greatly from those of its SCs [3]. Such changes in structural and electronic properties may lead to changes in vibronic characteristics in its solid-state phases via inequivalent intermolecular interactions. In this work, infrared absorption measurements were performed on SCs and amorphous TFs of rubrene trying to compare intra-molecular vibrations depending on inter-molecular aggregation manners.

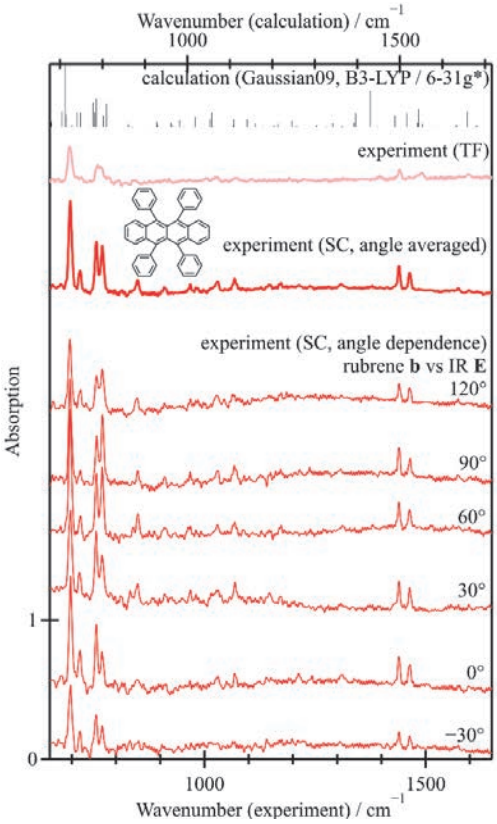

Fig. 1. Quantum chemical calculation results (black) and IR absorption spectra of an amorphous TF (pink) and SC (red) of rubrene. The bottom six curves are spectra of SC depending on orientations of the crystal principal axis **b** of rubrene to the IR **E**. The calculated wavenumber is scaled by a factor 0.9613 [5].

Rubrene SCs were produced by a horizontal physical vapor transport technique and were electrostatically fixed on polycrystalline diamond substrates. TFs of rubrene were prepared by vacuum deposition of thicknesses up to 5 μm on the polycrystalline diamond plates and were afterward taken out of the vacuum. FT-IR measurements were performed at BL6B, UVSOR. Experimental details were described previously [4].

Figure 1 shows IR absorption spectra of a TF and SC of rubrene with quantum chemical calculation results on a single rubrene molecule. While the former was much weaker than the latter due to insufficient film thickness, the peak positions were overall consistent with each other. The peak intensities of SC, especially in a low wavenumber range, clearly exhibited dependence on the in-plane orientation of the sample presumably by variations in relations between transition dipoles **μ** and the IR electric field **E** [4]. Closed-up spectra (Fig. 2) revealed that the IR absorption wavenumbers are mostly unchanged independent of the solid-state phases. Peak broadening for TFs may be caused by diverse inter-molecular conditions, whereas the emergence of peaks derived by **μ**·**E** ≈ 0 modes for SC (#66 and #73) cannot be ruled out as possible causes of the broadening at this stage.

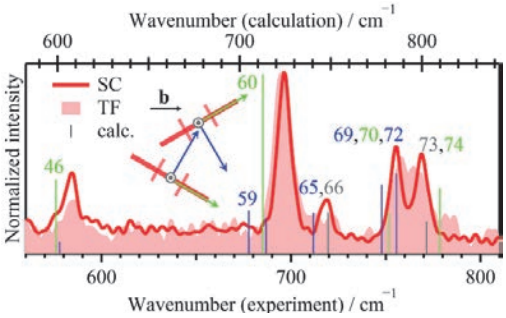

Fig. 2. Experimental and calculation results shown in extended wavenumber scales. The latter are displayed with different colors by its **μ** directions (see inset).

[1] J. Takeya, *et al.*, Appl. Phys. Lett. **90** (2007) 102120.
[2] S. Machida *et al.*, Phys. Rev. Lett. **104** (2010) 156401.
[3] Y. Nakayama, *et al.*, Appl. Phys. Lett. **93** (2008) 173305.
[4] Y. Nakayama, *et al.*, Vib. Spectrosc. **132** (2024) 103681; *idem*, Jpn. J. Appl. Phys. **63** (2024) 09SP07.
[5] J. P. Merrick, *et al.*, J. Phys. Chem. A **111** (2007) 116803.

BL7U

High-Resolution ARPES Study of Pure Electronic Nematicity in FeSe Thin Films on $LaAlO_3$

K. Nakayama[1], T. Kobayashi[2], F. Nabeshima[2], S. Souma[3,4], T. Takahashi[1],
A. Maeda[2] and T. Sato[1,3,4,5,6]
[1]*Department of Physics, Tohoku University, Sendai 980-8578, Japan*
[2]*Department of Basic Science, the University of Tokyo, 3-8-1 Komaba, Meguro, Tokyo 153-8902, Japan*
[3]*Center for Spintronics Research Network, Tohoku University, Sendai 980-8577, Japan*
[4]*Advanced Institute for Materials Research (WPI-AIMR), Tohoku University, Sendai 980-8577, Japan*
[5]*International Center for Synchrotron Radiation Innovation Smart (SRIS), Tohoku University, Sendai 980-8577, Japan*
[6]*Mathematical Science Center for Co-creative Society (MathCCS), Tohoku University, Sendai 980-8578, Japan*

The iron-based superconductor FeSe is attracting considerable attention because it exhibits unique physical properties distinct from other iron-based superconductors, such as very strong coupling superconductivity in bulk samples and high-temperature superconductivity in monolayers. A particularly intriguing property is its electronic nematic state [Fig. 1(a)], in which the rotational symmetry of the electronic state is reduced from four-fold (C_4) to two-fold (C_2) [1]. While the electronic nematic state in other iron-based superconductors typically develops concurrently with antiferromagnetic order and a tetragonal-to-orthorhombic structural transition, the nematic state in FeSe is markedly different as it is not accompanied by antiferromagnetic ordering. In nearly all high-temperature superconductors discovered thus far, an antiferromagnetic phase exists adjacent to the superconducting phase, leading to the consideration of antiferromagnetic interactions as a primary candidate mechanism for high-temperature superconductivity. In this context, the results for FeSe are puzzling. Understanding the origin of the electronic nematic state is considered a crucial step towards the full understanding of the high-temperature superconductivity mechanism in iron-based superconductors.

As described above, the electronic nematic state in bulk FeSe is not accompanied by antiferromagnetic order. On the other hand, similar to other iron-based superconductors, it is known to undergo a tetragonal-to-orthorhombic structural transition. Therefore, the lattice also possesses C_2 symmetry. In a strict sense, this means the electronic state itself does not break the rotational symmetry independently of the lattice distortion. By contrast, we recently discovered that FeSe thin films grown on $LaAlO_3$ substrates exhibit a “pure” nematic state that emerges without accompanying antiferromagnetic order or even a structural phase transition [2]. Moreover, this pure nematic state coexists with superconductivity. Elucidating the complete picture of this novel electronic nematic state and its relationship to superconductivity is a critical research task.

In this work, we utilized high energy- and momentum-resolution capabilities at low-energy beamline BL7U to perform angle-resolved photoemission spectroscopy (ARPES) measurements on FeSe/$LaAlO_3$. High-quality FeSe/$LaAlO_3$ samples, prepared by pulsed laser deposition, were cleaved *in-situ* under ultrahigh vacuum to obtain clean surfaces suitable for ARPES. As shown in Fig. 1(b), we observed two hole-like branches around the M point of the Brillouin zone. This observation indicates the lifting of band degeneracy between the Fe 3d *xz* and *yz* orbitals, a hallmark of the electronic nematic state. We carefully investigated the evolution of these bands across the nematic transition. Furthermore, high-resolution measurements were performed at very low temperatures. From these comprehensive measurements, we obtained a detailed understanding of the pure nematic state.

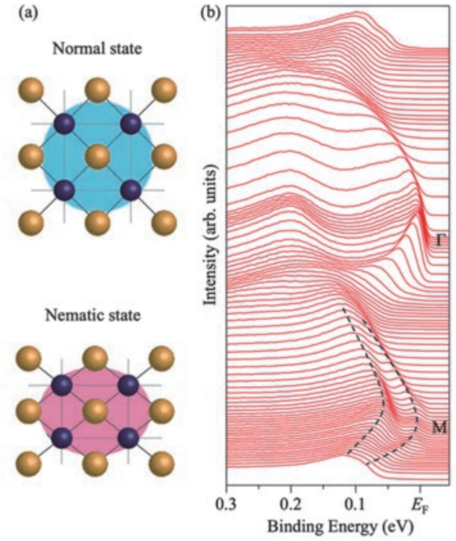

Fig. 1. (a) Schematic of crystal structure and electronic states in the normal state (top) and nematic state (bottom) in bulk FeSe [2]. (b) ARPES spectra along the ΓM high-symmetry line measured in the pure electronic nematic state of FeSe/$LaAlO_3$.

[1] K. Nakayama *et al*., Phys. Rev. Lett. **113** (2014) 237001.
[2] Y. Kubota *et al*., Phys. Rev. B **108** (2023) L100501.

BL7U

Band Dispersion of the Topological Nodal-Line Semimetal KAlGe

T. Ishida[1], S. Huh[1], T. Ikenobe[1], T. Yamada[2], J. Junhyeok[1], A. Mine[1], S. Makita[3], K. Tanaka[3],
Z. Hiroi[1] and T. Kondo[1]
[1]*Institute for Solid State Physics, The University of Tokyo, Kashiwa, Chiba 277-8581, Japan*
[2]*IMRAM, Tohoku University, Sendai 980-0812, Japan*
[3]*UVSOR Facility, Institute for Molecular Science, Okazaki, Aichi 444-8585, Japan*

The compounds NaAlSi, NaAlGe, and KAlGe are part of a family of topological nodal-line semimetals. These materials share nearly identical crystal and electronic structures according to first-principles calculations [1]. However, they display strikingly different physical properties: NaAlSi becomes superconducting below ~7 K, NaAlGe exhibits a pseudogap-like behavior near 100 K, while KAlGe undergoes a metal-to-metal transition at 89 K. This divergence in physical phenomena, despite similar electronic band topology, raises important questions about the underlying mechanisms. In NaAlSi, recent studies suggest that many-body interactions significantly enhance the effective mass of the Fermi surface, contributing to its superconductivity [2]. ARPES measurements have confirmed the existence of a flat band near or just below the Fermi level, which is interpreted as a manifestation of mass enhancement [3]. Furthermore, two topological nodal lines are clearly resolved. To understand the unique behavior of KAlGe, we aim to clarify its band dispersion, especially the position of the flat band, through angle-resolved photoemission spectroscopy (ARPES). Despite theoretical predictions, no experimental band structures for KAlGe have been reported to date, making our study the first direct observation. Single crystals of KAlGe were synthesized using a potassium–indium flux method. Owing to their air sensitivity, all handling and sample preparation were conducted in an argon-filled glovebox. The samples were cleaved *in-situ* under ultrahigh vacuum conditions (4.0×10^{-9} Pa) immediately prior to measurement to expose pristine surfaces. ARPES experiments were performed at 120 K using 17 eV photons at the UVSOR BL7U beamline. Both linear horizontal (LH) and vertical (LV) polarizations were used to probe orbital character.

Figure. 1 consents constant-energy mappings of KAlGe measured with 17 eV LH-polarized light. The overall shape and symmetry closely resemble those of NaAlSi, indicating that the bulk electronic structure is largely conserved within this family. Figure 2 shows the band dispersions along the Γ–X direction. The left and right panels correspond to LH and LV polarization, respectively. Under LH light, we observe features dominated by the Ge $4p_x$ orbital (highlighted in yellow), whereas LV polarization enhances the Ge $4p_y$ orbital (blue). The Al 3s orbital is not clearly observed under either polarization, likely due to matrix element suppression. Most notably, unlike NaAlSi, the flat band is absent below the Fermi energy in KAlGe. This suggests a crucial difference in many-body renormalization or hybridization strength. We propose that the elevated position of the flat band in KAlGe may suppress the density of states at the Fermi level, thereby inhibiting superconductivity while allowing alternative phenomena such as the observed metal-to-metal transition. The polarization dependence also supports orbital selectivity in KAlGe, possibly tied to the directionality of nodal-line dispersion and spin-orbit coupling. Further photon energy-dependent measurements are planned to confirm the three-dimensional character of the observed bands.

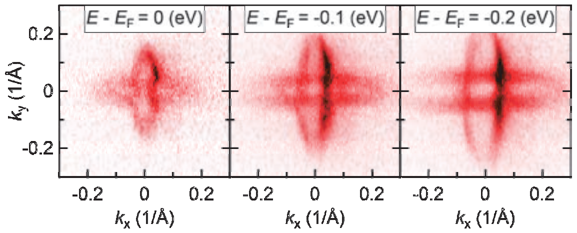

Fig. 1. Constant energy mapping of KAlGe at 120 K with 17 eV LH polarized light.

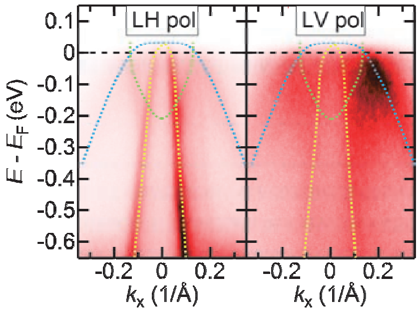

Fig. 2. Electronic structure of KAlGe at 120 K with 17 eV light in Γ-X.

[1] T. Ikenobe, *et al.*, Chem. Mater. **37**(1) (2024) 189.
[2] S. Uji, *et al*, Phys Rev B **105** (2022) 235103.
[3] C. Song, *et al.*, Phys Rev B **105** (2022) L161104.

BL7U

High-Resolution ARPES Study of Topological Superconductor Candidate $PtBi_2$

Y. Morita[1], K. Nakayama[1], T. Kato[2], S. Souma[2,3], S. Masaki[4], T. Ikushima[4], Y. Moriyasu[4],
K. Hagiwara[5], F. Matsui[5], K. Tanaka[5,6], T. Takahashi[1], K. Kudo[4] and T. Sato[1,2,3,7,8]
[1]*Department of Physics, Tohoku University, Sendai 980-8578, Japan*
[2]*Advanced Institute for Materials Research (WPI-AIMR), Tohoku University, Sendai 980-8577, Japan*
[3]*Center for Science and Innovation in Spintronics (CSIS), Tohoku University, Sendai 980-8577, Japan*
[4]*Department of Physics, Graduate School of Science, The University of Osaka, Toyonaka 560-0043, Japan*
[5]*UVSOR Synchrotron Facility, Institute for Molecular Science, Okazaki 444-8585, Japan*
[6]*School of Physical Sciences, The Graduate University for Advanced Studies (SOKENDAI),*
Okazaki 444-8585, Japan
[7]*International Center for Synchrotron Radiation Innov1ation Smart (SRIS), Tohoku University,*
Sendai 980-8577, Japan
[8]*Mathematical Science Center for Co-creative Society (MathCCS), Tohoku University, Sendai 980-8578, Japan*

Following the discovery of topological insulators, the exploration for new topological materials is actively progressing. A prime example is the Dirac semimetal, which features a Dirac-cone-type band dispersion where the bulk conduction and valence bands touch at discrete points in three-dimensional Brillouin zone. These materials hold promise for applications in next-generation ultra-high-speed electronics and spintronics. Furthermore, among topological semimetals, Weyl semimetals host spin-polarized Dirac cones (Weyl cones) in their bulk band structure. Weyl semimetals are realized in systems where spatial inversion or time-reversal symmetry is broken. Numerous quantum phenomena, such as the anomalous Hall effect and the chiral anomaly, are predicted for Weyl semimetals, and their experimental verification is actively underway. In recent years, aiming to realize even more exotic topological phases, the exploration of materials that integrate superconductivity with Dirac or Weyl semimetal states has become a key research objective. Introducing superconductivity is anticipated to facilitate the formation of unconventional Cooper pairs, potentially leading to topological superconductivity and Majorana fermions.

Here, we focus on $PtBi_2$ [Fig. 1(a)], a transition metal dichalcogenide with broken spatial inversion symmetry. This material is a Weyl semimetal candidate and exhibits bulk superconductivity below 0.6 K. Moreover, a recent report suggests potential surface superconductivity with a significantly higher transition temperature above 10 K [1]. These combined Weyl semimetallic and superconducting characteristics make $PtBi_2$ a promising platform for exploring topological superconductivity. However, key aspects of its electronic structure relevant to topological superconductivity, such as bulk Weyl cones, require further investigation.

Using bulk-sensitive low-energy photons at BL7U, we mapped the three-dimensional bulk electronic structure of $PtBi_2$. Our results shown in Fig. 1(b) reveal signatures of spin-split bulk bands, recognized from Rasha-like band dispersion observed around the M point. Such spin splitting, likely originating from the broken inversion symmetry, is a prerequisite for the predicted Weyl semimetal phase. To further investigate this phase, we performed high-resolution measurements to directly observe the Weyl cones near the Fermi level.

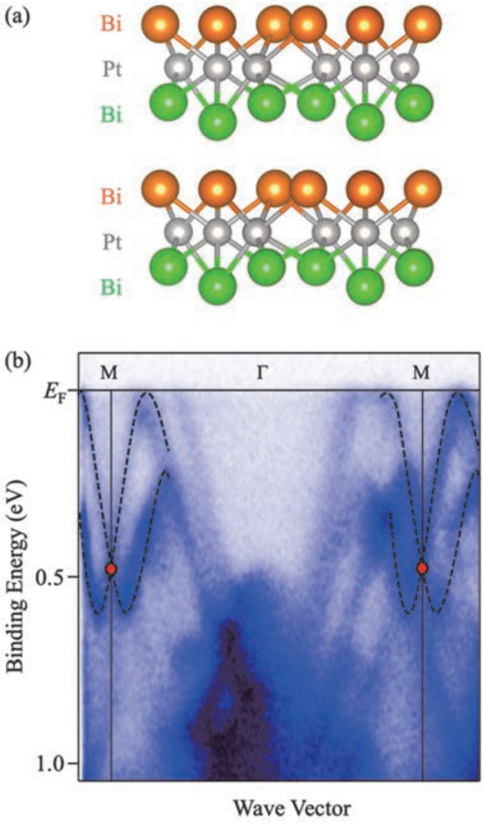

Fig. 1. (a) Crystal structure of $PtBi_2$. (b) Plot of ARPES intensity measured in the normal state along the ΓM high-symmetry line.

[1] A. Kuibarov *et al.*, Nature **626** (2024) 294.

BL7U

Probing Hole Doping Effects in Ti-Substituted Ta_2NiSe_5 Investigated by Angle-Resolved Photoemission Spectroscopy

J. Han[1], K. Aido[1], S. Tsuchida[2], Y. Hirose[2], R. Settai[2], S. Makita[3], K. Tanaka[3] and T. Kondo[1]
[1]*ISSP, University of Tokyo, Kashiwa, Chiba 277-8581, Japan*
[2]*Department of Physics, Niigata University, Niigata 950-2181, Japan*
[3]*UVSOR Facility, Institute for Molecular Science, Okazaki, Aichi 444-8585, Japan*

Ta_2NiSe_5 has emerged as one of the most prominent candidates for excitonic insulator systems. With a direct band gap, it undergoes an insulating transition accompanied solely by a $q = 0$ structural distortion at $T_s = 329$ K, without charge density wave (CDW) formation [1]. A central issue in this field is whether the transition is primarily driven by excitonic condensation or by lattice instability. Since exciton formation originates from the Coulomb attraction between electrons and holes, tuning the screening strength through carrier doping could facilitate a disentangled investigation of the respective roles played by electronic and structural degrees of freedom.

To systematically explore the effects of carrier doping, we investigated the electronic structure of Ti-substituted Ta_2NiSe_5, where Ti atoms replace Ta sites, introducing effective hole doping due to the difference in their valence electron configurations. Single crystals of pristine and Ti-substituted Ta_2NiSe_5 were synthesized by the chemical vapor transport method. The samples were cleaved *in-situ* to obtain clean surfaces for measurements. Angle-resolved photoemission spectroscopy (ARPES) measurements were performed at BL7U of UVSOR with a photon energy of 18 eV. All data were collected at a sample temperature of 83 K (below T_s). To distinguish the orbital characters associated with Ta, Ni, and Se atoms, both linear vertical (LV) and linear horizontal (LH) polarizations were employed during the measurements [2].

Figure 1 compares the band structures along the Γ-X direction for pristine and Ti-substituted Ta_2NiSe_5. Under LV polarization [Figs. 1(a) and 1(b)], bands primarily derived from Ta 5*d* orbitals are selectively enhanced, while LH polarization emphasizes the Ni 3*d*-derived bands [Figs. 1(c) and 1(d)]. In the pristine sample [Figs. 1(a) and 1(c)], the characteristic flat top of the valence band, associated with the excitonic insulating state, appears near a binding energy of approximately 170 meV. Upon Ti substitution [Figs. 1(b) and 1(d)], the overall band structure, which includes the characteristic flat band, shifts toward lower binding energies without significant deformation compared to the pristine one. This implies that the level of Ti substitution may not yet be sufficient to induce a complete insulator-to-semimetal transition.

Assuming that carrier doping suppresses exciton condensation, the upward shift of the flat-top valence band to approximately 60 meV can be regarded as an indication of gap narrowing. As highlighted by the black arrows in Figs. 1(b) and 1(d), only the spectral weight near the Fermi level (E_F) is depleted, which may suggest the emergence of a pseudogap. With a slightly higher level of Ti substitution, the bands may begin to overlap, potentially leading to a semimetallic transition. Unlike previous approaches based on potassium deposition [3], our substitution-based strategy avoids interpretational ambiguities arising from the Stark effect, thereby offering a cleaner platform to disentangle the respective roles of electronic and lattice degrees of freedom in the excitonic insulating state.

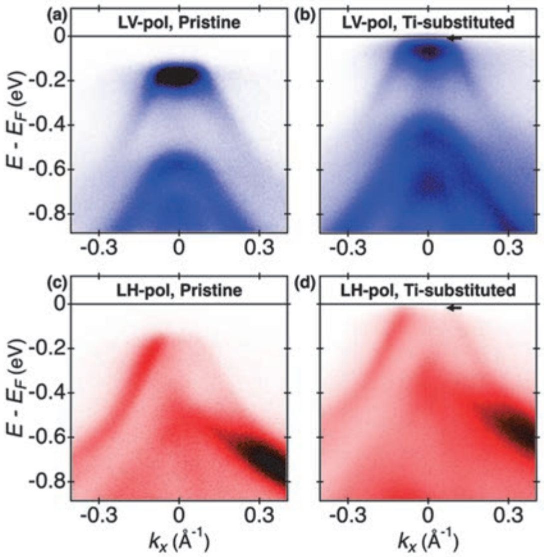

Fig. 1. Polarization-dependent ARPES spectra of pristine (a,c) and Ti-substituted (b,d) Ta_2NiSe_5 along the Γ-X direction, measured with LV (a,b) and LH (c,d) polarizations. Black arrows indicate spectral weight suppression near E_F .

[1] Y. Wakisaka *et al*., Phys. Rev. Lett. **103** (2009) 026402.
[2] T. Kaneko *et al*., Phys. Rev. B **87** (2013) 035121.
[3] X. Chen *et al*., Phys. Rev. Res. **5**,(2023) 043089.

BL7U

Observation of Electronic Structure of Organic Mott Insulator β’-(BEDT-TTF)$_2$ICl$_2$ by Angle-Resolved Photoelectron Spectroscopy

R. Nakazawa[1], K. Fukutani[1], Y. Ishida[2], S. Makita[3], K. Tanaka[3],
T. Kobayashi[4], H. Taniguchi[4] and S. Kera[1,2,3]
[1]Department of Photo-Molecular Science, Institute for Molecular Science, Okazaki 444-8585, Japan
[2]Faculty of Engineering, Chiba University, Chiba 263-8522, Japan
[3]UVSOR Synchrotron Facility, Institute for Molecular Science, Okazaki 444-8585, Japan
[4]Faculty of Science, Saitama University, Saitama 338-8570, Japan

Organic materials have the potential to promote the sustainable development of science and technology due to their flexibility and high environmental compatibility. Among them, strongly correlated organic molecular crystals exhibit a variety of quantum phases, such as superconductivity, spin liquid state, Mott insulating phase, and topological phase [1, 2].

(BEDT-TTF)$_2$X belongs to the strongly correlated organic molecular crystals and is a charge-transfer complex. Here, X means anion. Due to the electron transfer of the BEDT-TTF molecule to X, the valence band described from the highest occupied molecular orbital (HOMO) offers a half-filled or 1/4 filled. Whether the system is a metallic phase or an insulating phase depends on the microscopic electronic structure with Coulomb interaction energy. In the case of the half-filled band for a dimer state and large Coulomb interaction energy, the valence band from the anti-bonding HOMO state splits into upper and lower Hubbard bands, leading to an insulating phase which is called Mott insulator.

While the origins of the Mott insulator phase are largely encoded in the electronic structures as mentioned above, direct experimental data on the momentum-resolved electronic structure is missing. In the case of a Mott insulator, β’-(BEDT-TTF)$_2$ICl$_2$ [3, 4], electrical measurements confirm that it is an insulating phase at ambient pressure [1]. On the other hand, the band obtained by theoretical calculations crosses the Fermi level because they do not correctly account for the Coulomb interaction [5], and the true picture of electronic structure of this material is not unclear. To understand the many-body nature of β’-(BEDT-TTF)$_2$ICl$_2$, such as whether this material has the electronic states as a metallic phase or an insulating phase, first it is important to directly observe the momentum-resolved electronic structures which previous studies lack.

In this study, we observed the valence band electronic structure of β’-(BEDT-TTF)$_2$ICl$_2$ using angle-resolved photoelectron spectroscopy (ARPES) at BL7U in UVSOR.

Figure 1 shows the valence band structure observed using excitation energy of $h\nu$ = 40 eV at T = 150 K. Fig.1(a) shows the photoemission intensity plot along the short crystal axis (c-axis), and Fig. 1(b) is the corresponding second derivative plot. A dispersive band with the width of ~0.14 eV is observed at the binding energy (E_b) of ~0.7 eV. Since the observed band periodicity corresponds to the periodicity of Brillouin zone, we judged that we have successfully observed itinerant electrons in this material. In addition, the band with almost no dispersion was observed at the E_b of ~0.4 eV. These bands at the E_b of ~0.4 and ~0.7 eV are ascribed to the lower Hubbard and the bonding band, respectively. Moreover, we have successfully observed the photoelectrons along other high-symmetric momentum directions to reveal the details of the electronic structures.

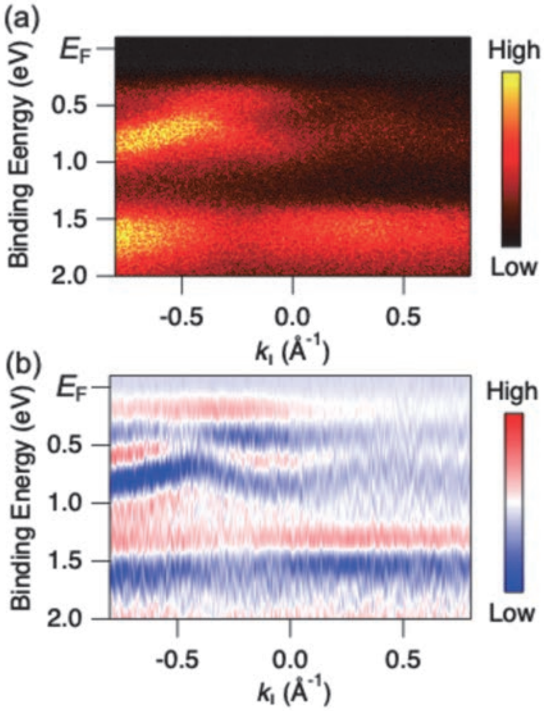

Fig. 1. (a) Photoemission intensity plot, and (b) the corresponding second derivative plot of β’-(BEDT-TTF)$_2$ICl$_2$ crystal observed at $h\nu$= 40 eV, T = 150 K.

[1] K. Kanoda, J. Phys. Soc. Jpn. **75** (2006) 051007.
[2] T. Nomoto *et al.*, Nat. Commun. **14** (2023) 2130.
[3] T. J. Emge, *et al.*, J. Am. Chem. Soc. **108** (1986) 695.
[4] H. Kobayashi, *et al.*, Chem. Lett. **15** (1986) 89.
[5] T. Koretsune, C. Hotta, Phys. Rev. B **89** (2014) 045102.

BL7U

Angle-Resolved Photoemission Study of Layered MAB Phase Compounds MoAlB

T. Ito[1,2], K. Kawano[1], N. Yuanzhi[1], M. Nakatake[3], K. Tanaka[4,5],
A. Sharma[6], H. Pazniak[6] and T. Ouisse[6]
[1]*Graduate School of Engineering, Nagoya University, Nagoya 464-8603, Japan*
[2]*Synchrotron radiation Research center, Nagoya University, Nagoya 464-8603, Japan*
[3]*Aichi Synchrotron Radiation Center, Seto 489-0965, Japan*
[4]*UVSOR Facility, Institute for Molecular Science, Okazaki 444-8585, Japan*
[5]*The Graduate University for Advanced Studies, Okazaki 444-8585, Japan*
[6]*Grenoble Alpes, CNRS, Grenoble INP, LMGP, F-38000 Grenoble, France*

MAB phase compounds are layered compounds formed by combining transition metals M and III-A (IV-A) group elements A and B, and have a layered crystal structure in which a strong MB layer and two A layers are stacked in the b-axis direction [1]. In this system, it is expected that the atomic layer system MBenes formed only from MX layers will be obtained by removing the A atoms by HF treatment or exfoliation. Therefore, this system has attracted attention in recent years as a new atomic layer system that can replace graphene [2]. Among boron compounds, MoAlB is known to be an excellent system, especially in terms of applications, due to its relatively good processability, high temperature oxidation resistance, high thermal conductivity, and high electrical conductivity. Furthermore, the results of DFT calculations [3] predict a three-dimensional Dirac semimetal nature of MoAlB. In this study, we have performed angle-resolved photoemission spectroscopy (ARPES) on MAB phase compound MoAlB to directly investigate the electronic structure of this system.

ARPES measurements were performed at the UVSOR-III BL7U. Inter-plane ARPES data were acquired with using $h\nu = 11 - 30$ eV at T = 30 K. Single crystals were cleaved in situ along (010) plane.

Figure 1(a) shows the obtained Fermi surface (FS) image on the ΓYZT plane . It has been found that the electronic structure around ΓZ line formed by two hole-like FSs with quasi-two-dimensional character, which are qualitatively reproduced by density functional theory (DFT) calculations (not shown). On the other hand, we have found three dimensional FS around Z point and $k_y \sim -0.5$ Å^{-1} around ΓY line. To elucidate three-dimensional electronic structure of MoAlB, we indicate inter-plane ARPES image along ΓZ line in Fig. 1(b). The inner potential V_0 is estimated to be 27 eV based on the symmetry of the dispersive features. From the comparison between ARPES and DFT calculation, narrow parabolic dispersions around 0.5 and 2.7 eV seem to show qualitative agreement. However, a sharp, flat pocket symmetrically observed around the Z point on the present ARPES is not predicted by the DFT calculations. Although the origin of this discrepancy remains unclear, it is plausible that the formation of the heavy electron surface is associated with a chemical potential shift of approximately 100 meV. To pursue the relation between anomalous FS and the thermodynamic properties of MoAlB, further studies are intended.

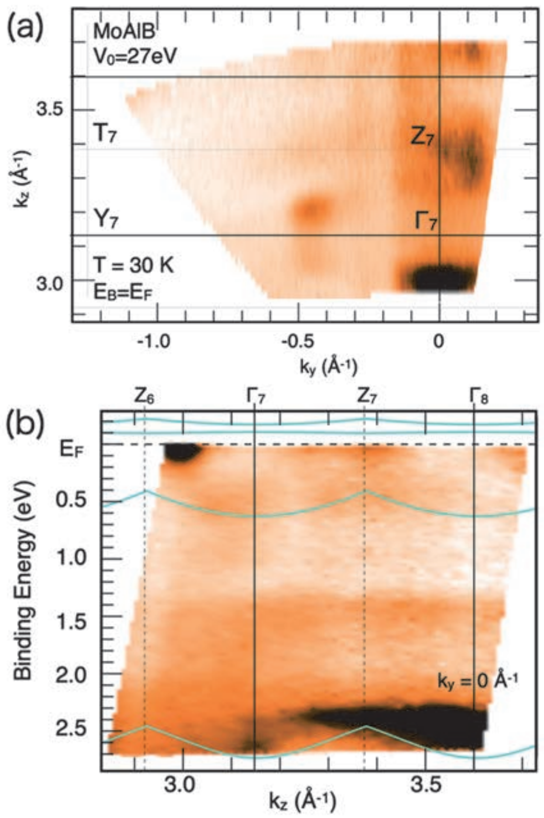

Fig. 1. (a) Fermi surface along ΓYZT plane of MoAlB obtained by inter-plane ARPES measurements. (b) Inter-plane ARPES image along ΓZ line. Solid lines are DFT calculation along ΓZ line.

[1] Y. Huang *et al.*, Small **18** (2022) 2104460.
[2] X. Zhu *et al.*, Nature Commun. **12** (2021) 4080.
[3] Y. Huang *et al.*, Materials Today Physics **33**(2023) 101060.

BL7U

Exploration of Electronic Band Structure and Topological Surface States in Ni-Doped PdSeTe

Y. Kumar[2], S. Ideta[1,2] and K. Shimada[1,2]
[1]*Graduate School of Advanced Science and Engineering, Hiroshima University, Hiroshima 739-0046, Japan.*
[2]*Hiroshima Research Institute for Synchrotron Radiation Science (HiSOR), Hiroshima University, Hiroshima 739-0046, Japan.*

In recent years, exploring the electronic structures of topological insulators and topological semimetals has become a central focus in condensed matter physics. Among these, Dirac and Weyl semimetals have attracted significant attention, particularly in the realm of spintronics, due to their unique and enhanced physical properties [1, 2]. Layered transition-metal dichalcogenides (TMDCs) with the chemical formula AB_2 (where A is a transition metal and B is a chalcogen) have been the subject of extensive research due to their diverse range of physical properties, including superconductivity and the emergence of charge density waves (CDWs).

Recently, we have reported the existence of topological surface states and enhancement of superconducting transition temperature in 1T-PdSeTe [3], which is the sister compound of $PdTe_2$ by replacing 50% of Te atoms with Se, trying to break the inversion symmetry to create a Weyl semimetal. We explored the surface and bulk electronic structures of the superconducting type-II Dirac semimetal 1T-PdSeTe, which exhibits a superconducting transition temperature (T_C = 3.2 K) nearly twice that of its counterpart 1T-$PdTe_2$ (T_C = 1.6 K). Angle-resolved photoemission spectroscopy (ARPES) and density functional theory (DFT) analyses revealed topological surface states and electronic band structures closely resembling those of 1T-$PdTe_2$. These findings suggest that the CdI_2-type lattice symmetry plays a dominant role in dictating the band dispersion, largely unaffected by atomic-scale disorder in the chalcogen layers. To the best of our knowledge, we were the first to demonstrate that the PdSeTe superconductor hosts topological surface states.

In order to break the time reversal symmetry in this material, we have tried to dope a magnetic impurity (Ni) at the Pd-site. We have successfully grown the $Ni_xPd_{1-x}SeTe$ single crystals. We have measured the electronic band structure using ARPES at BL7U at UVSOR. The objective of this study was to carry out ARPES measurements on Ni-doped PdSeTe samples to elucidate their electronic band structure. Particular emphasis was placed on analyzing the band dispersion and Fermi surface with the goal of identifying signatures of topological surface states and Fermi arcs. We have prepared $Ni_xPd_{1-x}SeTe$ samples and aligned them in a high-symmetry direction using the Laue diffraction (XRD) available at the UVSOR-III synchrotron facility to accurately measure the band dispersion in the high-symmetry direction.

We have cleaved three samples of $Ni_xPd_{1-x}SeTe$ to obtain a clean surface; the cleave was very good, resulting in the sharp band dispersion. We have performed the ARPES experiment and mapped the Fermi surface at photon energy 25 eV as shown in Fig. 1. Also, I have measured high symmetry cuts in the Γ-M direction to investigate the electronic band structure with both *s*- and *p*-polarizations. I have performed the photon energy-dependent measurement from 9 eV to 25 eV to observe the k_z dependence. We have also optimized the beam slit to improve the data quality and resolution. Detailed records of experimental procedures, sample characteristics, and measurement results were maintained during the experiment. We have to do further measurements to complete the data set.

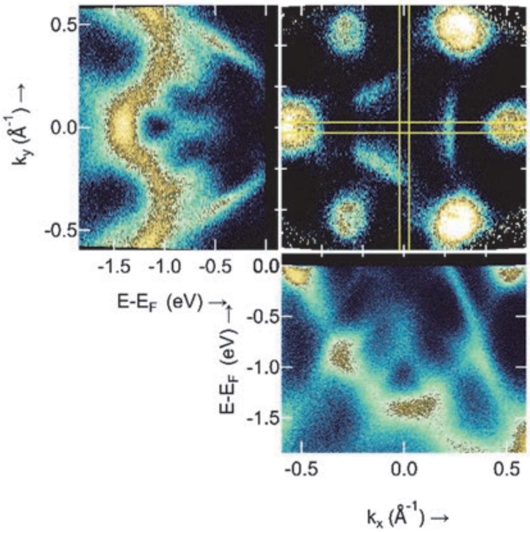

Fig. 1. Fermi Surface of $Ni_xPd_{1-x}SeTe$ single crystal at 25 eV alongside band dispersion in the K-Γ-K and M-Γ-M directions.

[1] N. P. Armitage, E. J. Mele, A. Vishwanath, Rev. Mod. Phys. **90** (2018) 015001.
[2] A. A. Burkov, Nat. Mater. **15** (2016) 1145.
[3] Y. Kumar, K. Shimada *et al*, Phys. Rev. Res. **7** (2025) 013174.

BL7U

Role of Orbital-Selective Mott Phase on Topological Properties in Iron Chalcogenide Superconductors

Y. Kim[1], J. Yoo[1], S. Kim[1] and C. Kim[1]

[1]*Department of Physics and Astronomy, Seoul National University, Seoul 08826, South Korea*

Orbital-selective Mott phase (OSMP), where one band becomes effectively localized while other bands remain metallic, emerges in correlated multiorbital systems. In electronic structures, the OSMP is characterized by a loss of spectral weight and broadening of the associated band at high temperatures [1]. This phenomenon has attracted much attention since its ubiquity; many strongly correlated multiorbital systems exhibit OSMP. Despite such interests to OSMP, research on its relation to practical physical properties remains elusive.

Here, we investigate the relationship between OSMP and non-trivial topology in $FeTe_{1-x}Se_x$ (FTS), iron chalcogenide superconductors. FTS exhibit non-trivial topology as well as unconventional superconductivity. The non-trivial topology arises from the band inversion of the odd-parity p_z and d_{xz} bands along the Γ – Z line [2]. This in turn suggest that to study the impact of the OSMP on the topological properties of FTS, it is necessary to investigate the electronic structures of FTS along the Γ – Z line.

In ARPES measurements, two aspects should be considered for the measurements; i) as the band of interest is pz band, photon energy should be lower than 20 eV considering photoionization cross section ii) photon energy should be tunable for the k_z-dependent measurements. UVSOR Beamline 7U satisfies the aforementioned conditions [3]. Here, we report successful measurement results of the electronic structures of FTS along the Γ – Z line as a function of Se/Te ratio and temperature in BL 7U.

Shown in Figs. 1**a-d** are electronic structures of FTS along the Γ – Z line with selenium contents of x = 0.04, 0.09, 0.19, and 0.31, respectively. They all show a dispersive band, which can be attributed to the odd-parity p_z band. To track the evolution of the p_z band as a function of doping, the top and bottom positions of the band at the Γ and Z points, respectively, are extracted from a two-dimensional fitting as shown in Fig. 1**e**. The p_z band overall moves towards lower energy for lower Se contents. The notable point of the doping-dependent evolution is that the band at the top of the p_z band at the Γ point goes below the Fermi level at x = 0.04. If the p_z band goes below the d_{xz} band which is near the Fermi level, this makes the inversion parities of the Γ and Z both odd, resulting in trivial topology. This suggests that topological phase transition occurs between x = 0.04 and 0.09, resulting in trivial topology at x = 0.04.

Figures 1**f–i** show temperature-dependent ARPES results for the sample with x=0.19 measured at temperatures of 30 K, 50 K, 90 K, and 175 K, respectively. Unlike the doping-dependent behavior, the position of the odd-parity band does not change with temperature.

In summary, we have successfully measured the odd-parity band in FTS, providing insights into its topology. These results may shed light on the role of OSMP in determining the system's topological properties.

[1] M. Yi *et al.*, npj Quantum Mater. **2** (2017) 57.
[2] P. Zhang *et al.*, Science **360** (2018) 6385.
[3] Y. Kim *et al.*, Nat. Commun. **14** (2023) 4145.

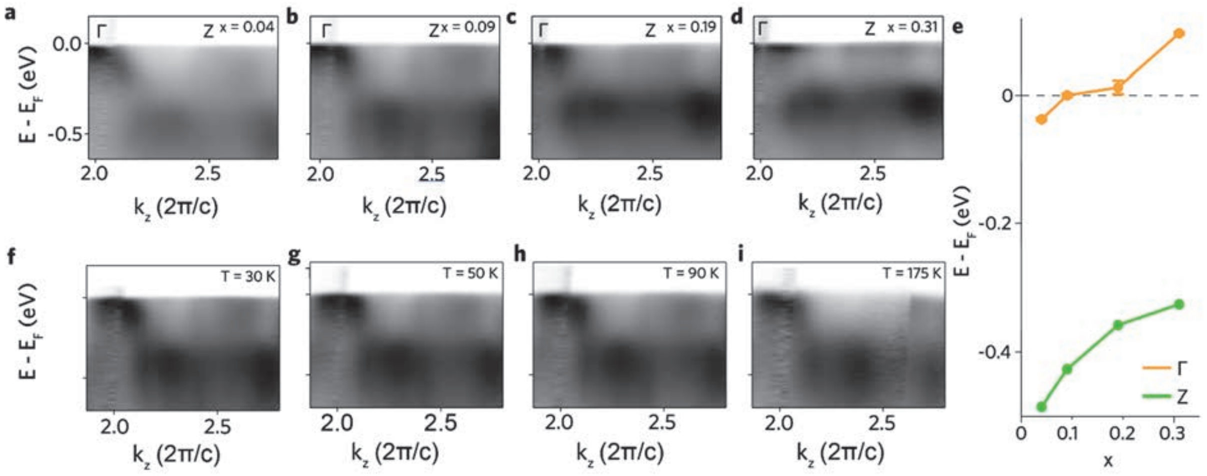

Fig. 1. **a-d** Band dispersion along Γ − Z, with selenium contents of x = 0.04, 0.09, 0.19, and 0.31, respectively. e Position of the p_z band at the Γ and Z points. **f-i** Band dispersion along Γ − Z, with temperatures of 30 K, 50 K, 90 K and 175 K, respectively.

BL7B

Evaluation of Fluorescence Lifetimes of UV-Cured Scintillators for the Next K_L^0 Rare Decay Experiment at J-PARC

Y. Tajima[1], R. Abe[1], T. Naito[1], Y. Honma[1], N. Izawa[1], S. Yamamoto[1] and H. Y. Yoshida[1]
[1]*Department of Science, Yamagata University, Yamagata 990-8560, Japan*

J-PARC E14 KOTO [1] is the current running experiment of searching for the direct CP violating decay $K_L \to \pi^0\nu\bar{\nu}$ decay. This decay mode is considered to be sensitive to new physics beyond the Standard Model (SM), and its branching ratio is predicted to be 3.0×10^{-11} in the SM with about 2% theoretical uncertainly. The upper limit currently obtained on the branching fraction of $K_L \to \pi^0\nu\bar{\nu}$ decay is 2.2×10^{-9} at the 90% confidence level [2].

We are planning the next generation $K_L \to \pi^0\nu\bar{\nu}$ experiment, called KOTO-II [3]. KOTO-II experiment uses a beam intensity about three times higher and a decay volume about five times longer than that of KOTO. The operation of the detectors in KOTO-II are required higher counting rates. To satisfy this requirement, the scintillators need to have a short fluorescence lifetime, which enables fast time response.

Recently, a new UV-cured scintillator with high light yield has been developed [4]. The scintillators are expected to be easy to fabricate and low cost.

We are currently evaluating its various characteristics for use in KOTO-II experiment. For this purpose, the fluorescence spectrum and decay curve of a newly developed high light yield UV-cured plastic scintillator were measured in this experiment.

The fluorescence decay curves were measured by using light pulses from visible to near ultraviolet under single bunch operation, which enables a time-correlated single-photon counting.

In this experiment, ethoxylated bisphenol A diacrylate (EBECRYL 150 supplied from Daicel Allnex) was used as the host polymer, Irgacure TPO as the photoinitiator, DPO and POPOP as wavelength shifters.

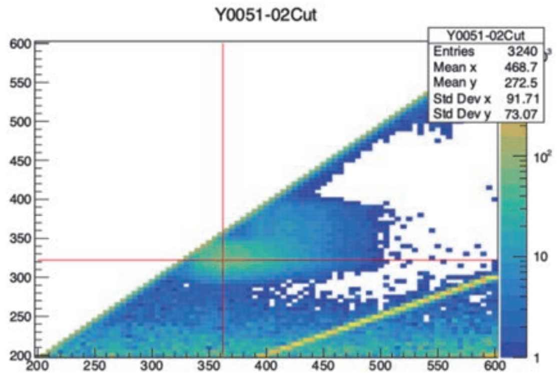

Fig. 1. 2D fluorescence spectra of the UV-cured host polymer. Y-axis is excitation wave length (nm) and X-axis is emission wave length (nm).

Figure 1 shows the 2D fluorescence spectra of the UV-cured host polymers and Fig. 2 shows of the UV-cured scintillator. Figure 3 shows the decay curves. The blue line is the data of the host polymer for the 392 nm band under excitation at 240 nm, the red line is the data of the scintillator data for the 450 nm band under excitation at 322 nm.

Now that we have established a basic evaluation method for UV-cured scintillators, we plan to evaluate other UV-cured scintillators.

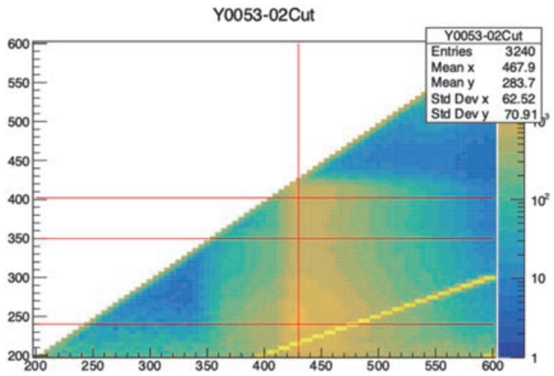

Fig. 2. 2D fluorescence spectra of the UV-cured host polymer with DPO and POPOP.

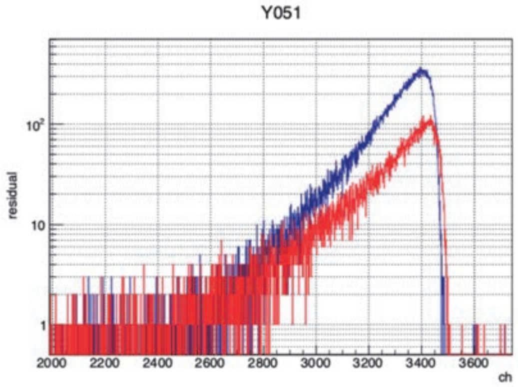

Fig. 3. Decay curve of the UV-cured host polymer (blue) and UV-cured scintillator (red). (946ch/ns)

[1] J. Comfort *et al.*, Proposal for $K_L \to \pi^0\nu\bar{\nu}$ Experiment at J-PARC (2006).
[2] J.K. Ahn *et.al.*, Phys. Rev. Lett. **134** (2025) 081802.
[3] J.K. Ahn *et.al.*, J-PARC PAC (arXiv 2501.14827).
[4] N. Hayashi and M.Koshimizu, J. Lumin. **277** (2025) 120993.

Excitation Spectra of Plastic Scintillators Based on PVK Containing Different Organic Fluorescent Molecules

M. Koshimizu[1]
[1]*Research Institute of Electronics, Shizuoka University, 3-5-1 Johoku, Chuo-ku, Hamamatsu 432-8011, Japan*

Scintillators are a kind of phosphors that can be used for radiation detection in combination with photon detectors (e.g. photomultiplier tubes) to form scintillation detectors, where scintillation photons upon impinge of ionizing radiation are converted and amplified into electric pulsed signals. Because the response speed of the photon detectors is faster than the decay of the scintillation of scintillators in most cases, scintillators exhibiting fast scintillation decay is necessary to achieve excellent timing resolutions or detection capability at high counting rate with short dead time. From the viewpoint of fast response, plastic scintillators are favorable owing to their fast scintillation decay with typically < 10 ns, which is much faster than those of inorganic scintillators [1, 2]. In addition, scalability and low production cost of the plastic scintillators are favorable to large-scale detectors used in high-energy and particle physics. A significant drawback of the plastic scintillators is low scintillation light yield of typically ~10,000 photons/MeV or less, which is significantly smaller than those of inorganic scintillators. A cause of this low scintillation yield is the formation of triplet excited states in the host polymer, which is formed upon recombination of electron–cation pairs after ionization. The use of the triplet states is the key to enhance the scintillation light yield of plastic scintillators.

Recently, triplet excited states have been efficiently used for photon emission in organic light-emitting diodes via efficient phosphorescence or thermally activated delayed fluorescence. If such utilization of triplet excited states is possible in plastic scintillators, one can enhance scintillation light yield in plastic scintillators. To achieve the scintillation light yield in this approach, it is necessary to develop appropriate fluorescent molecules that can convert the energy of triplet excited states into photons via delayed fluorescence or phosphorescence and a technique to analyze the contribution of photon emission originated from triplet excited states. Recently, we found that the contribution of emission originating from singlet and triplet excited states can be analyzed based on excitation spectra in VUV region [3] and difference in the decay behavior at different excitation wavelengths in VUV—UV region [4]. In the previous study, we have analyzed the properties of plastic scintillators based on polystyrene. In this study, the emission properties of plastic scintillators based on polyvinyl carbazole (PVK) were analyzed.

The samples were plastic scintillators based on PVK containing POPOP, bis-MSB, TPB, or DPA as the fluorescent molecules. The photoluminescence spectra of the samples under VUV irradiation at different wavelengths were obtained at BL7B of UVSOR, Institute for Molecular Science, Japan. Based on the photoluminescence spectra and the excitation light intensity as functions of excitation wavelength, we obtained excitation spectra in VUV region.

Excitation spectra of the samples containing bis-MSB and DPA are presented in Figs. 1 and 2, respectively. The spectra were similar regardless of the contained organic fluorescent molecules. The spectra were also similar to those of polystyrene-based plastic scintillators [3].

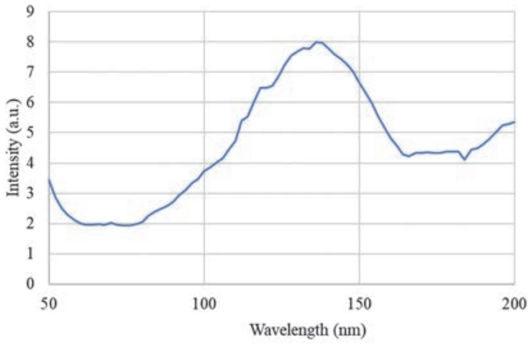

Fig. 1. Excitation spectra of PVK-based plastic scintillators containing bis-MSB.

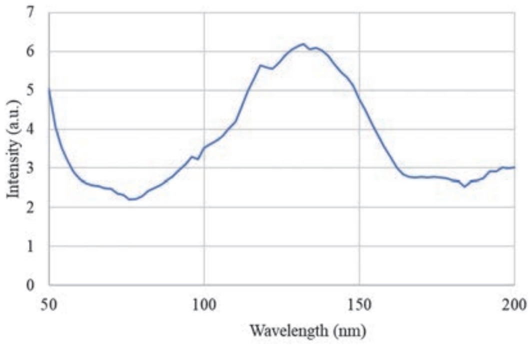

Fig. 2. Excitation spectra of PVK-based plastic scintillators containing DPA.

[1] M. Koshimizu, Jpn. J. Appl. Phys. **62** (2023) 010503.
[2] M. Koshimizu, J. Lumin. **278** (2025) 121008.
[3] M. Koshimizu, Y. Fujimoto, and K. Asai, UVSOR Activity Report **50** (2022) 111.
[4] M. Koshimizu, UVSOR Activity Report **51** (2023) 118.

BL7B

Vacuum Ultraviolet Characterization of Li-Glass as a Potential Neutron Scintillator

T. Shimizu[1], K. Shinohara[1], K. Yamanoi[1] and N. Sarukura[1]

[1]*Institute of Laser Engineering, The University of Osaka, 2-6 Yamadaoka Suita, Osaka 565-0875 Japan*

In nuclear fusion experiments, neutron detection plays a vital role in monitoring both operational efficiency and radiation safety. Primary neutrons, being high in flux, are typically detected using conventional plastic scintillators. However, scattered neutrons, generated through secondary nuclear reactions and arriving with a time delay, are present in much smaller quantities. Their reliable detection demands scintillators with high neutron sensitivity and fast optical response to distinguish their signals from primary neutrons and associated X-rays.

Scattered neutrons generally possess energies in the range of 0.2 to 0.6 MeV. ^{6}Li is known to have a high neutron absorption cross-section within this energy range, and ^{6}Li-containing glass scintillators doped with Ce^{3+} have long been employed for thermal neutron detection. Commercial products such as GS2, GS20, and KS20 are based on Ce^{3+}-doped Li_2O–SiO_2 glass matrices. However, these materials exhibit luminescence decay times of 50–70 ns, insufficient for the 25 ns time resolution required in time-of-flight (TOF) neutron measurements.

To address this issue, a new type of scintillator based on a $20Al(PO_3)_3$–80LiF (APLF) glass matrix was developed. This material offers superior UV transparency and minimal self-absorption, making it ideal for shorter-wavelength luminescence. By replacing Ce^{3+} with Pr^{3+}, the emission wavelength was shifted from 300–350 nm to 250–300 nm, effectively shortening the luminescence decay time.

Previously, We have compiled the analysis and discussion of the X-ray absorption near edge structure (XANES) spectroscopy for the presence of Pr ions in the glasses with a oxidation state.[1] .

In addition to APLF, we investigated alternative lithium glass matrices for scintillator use. Collaborative efforts led to the development and evaluation of various Pr-doped lithium glasses: $20Li_2O$–$20CaO$–$60SiO_2$+ $0.3Pr_2O_3$(LCSO+0.3Pr), $30Li_2O$–$70B_2O_3$+$0.3Pr_2O_3$ (LBO+ 0.3Pr), $30Li_2O$–$60P_2O_5$–$10Al_2O_3$ + $0.3Pr_2O_3$ (LPA+ 0.3Pr).[2]

In FY2024, we will focus on LPA-type glasses with varied Pr concentrations, as they have shown promise in luminescence control. The samples under evaluation include: LPA10+0.1Pr, LPA10+0.3Pr, LPA10+0.5Pr, LPA10+1Pr, LPA10+2Pr. All samples are solid, non-volatile, and pose no safety concerns.

Spectral measurements were conducted at the UVSOR synchrotron facility using the VUV beamline. A combination of spectrometers, cooled CCD cameras, and photomultiplier tubes (PMTs) was used to measure transmission, absorption, and emission spectra. The samples were placed in a vacuum chamber (pressure < 1.0×10^{-5} Pa) and irradiated with 100–180 nm synchrotron radiation. Si photodiodes were used for transmission measurements, while luminescence was detected using PMTs and CCD cameras. Temperature-controlled experiments were performed from liquid helium temperature up to room temperature, and emission was recorded in the 200–800 nm range. The excitation wavelengths were selected based on prior photoluminescence excitation spectra.

The transmission spectra for the LPA samples showed a systematic shift in the absorption edge corresponding to varying Pr concentrations, indicating successful doping (Fig.1). However, attempts to measure luminescence spectra were hindered by reduced system sensitivity. The resulting emission signals were too weak for reliable detection under the current measurement setup.

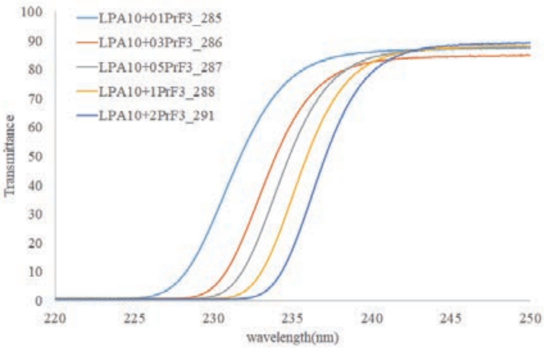

Fig. 1. Transmission spectrum for the LPA.

Although the absorption behavior of the Pr-doped LPA glasses was clearly characterized, luminescence measurements remain inconclusive due to instrumentation limitations. Future experiments will focus on improving measurement conditions and signal screening methods to enable effective evaluation of emission and excitation spectra. Once optimized, these measurements will guide the assessment of scintillator performance and help identify the most suitable material composition for scattered neutron detection.

[1] K. Shinohara *et al.*, the 9th International Symposium on Optical Materials (IS-OM'9), Tarragona (Spain), from June 26 to 30, 2023.

[2] T. Shimizu *et al.*, UVSOR Activity Report **51** (2023) 119.

BL7B

Optical Properties of Rare-Earth Doped La$(BO_2)_3$ Phosphor for Radiation Detection

J.Y. Cho[1], E.J. Choi[1], D.W. Jeong[1], N.D. Ton[1] and H.J. Kim[1]
[1]Department of Physics, Kyungpook National University, Daegu 41566, Republic of Korea

Borate-based materials are of considerable interest due to their optical transparency, wide bandgap, and thermal and chemical stability, making them ideal hosts for rare-earth dopants in luminescent applications. In particular, lanthanum borates such as La$(BO_2)_3$ offer a stable crystal environment that supports efficient energy transfer and emission. When doped with rare-earth ions like Nd^{3+}, Eu^{3+}, and Pr^{3+}, these materials exhibit promising luminescence properties suitable for lasers, phototherapy, and radiation detection [1–3].

However, studies on La$(BO_2)_3$ phosphors doped with Ce^{3+} and Tb^{3+} remain limited. This work focuses on investigating the luminescence behavior of Ce, Tb co-doped La$(BO_2)_3$ using PL, PLE, and VUV excitation (BL7B beamline), aiming to elucidate their emission mechanisms and assess their potential for optical applications.

In addition, since La$(BO_2)_3$ can be fabricated both as glass and as a crystalline phosphor, we aim to investigate the differences in their luminescence properties through VUV spectroscopy.

The samples were prepared via solid-state reaction at 900 °C for 10 hours from La_2O_3 and H_3BO_3 powder as starting materials and $CeBr_3$/Tb_4O_7 activator. After the mixing process,the mixtures were loaded in alumina crucibles and placed in a high-temperature round furnace where the solid-state reactions occurred. Finally, the products were ground in an agate mortar then introduced to XRD measurement to confirm the crystallization structures before pelletized with a hydraulic press.

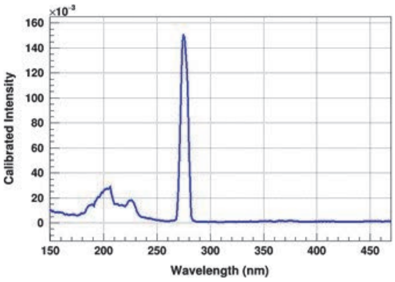

Fig. 1. Calibrated excitation spectrum of La$(BO_2)_3$:Tb phosphor.

Under the excitation measurement of 545 nm emission on La$(BO_2)_3$:Tb phosphor, broad bands from 180-240 and an intense peak of 270-285 nm were observed as shown in Fig.1. The broad band at 180-240 nm could be explained by the transitions from low energy levels to 4f levels of Tb^{3+} while the prominent peak appears at 270–280 nm, indicating the most efficient excitation wavelength for terbium (Tb^{3+}) emissions at 545 nm is characteristic of 4f → 5d transitions for Tb^{3+}. The PL excitation spectrum of La$(BO_2)_3$:Tb confirms that the material can be efficiently excited at 270–285 nm to produce the 545 nm emission then making it the potential choice for applications like phosphors in lighting or display technologies where Tb^{3+}'s green emission is desired.

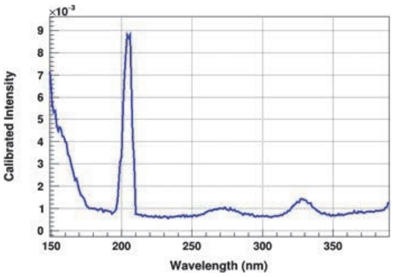

Fig. 2. Calibrated excitation spectrum of La$(BO_2)_3$:Ce phosphor.

Meanwhile, the excitation spectrum of La$(BO_2)_3$: Ce corresponding to 400 nm emission as shown in Fig. 2 is primarily dominated by a strong transition near 200 nm, making it effective for deep-UV-excited blue emission applications. Besides, weak bands from 260 - 290 nm and 320-350 nm were observed. The weak response at higher wavelengths limits its efficiency under near-UV excitation sources but could still contribute to broad-spectrum phosphor applications.

[1] X. Wang *et al*., Mater. Res. Bull. **52** (2014) 112.
[2] J. Guohua *et al*., Crystal Opt. Commun. **242** (2004) 79.
[3] T. Dogan *et al*., Ceram. Int. **45** (2019) 4918.

UVSOR User 9

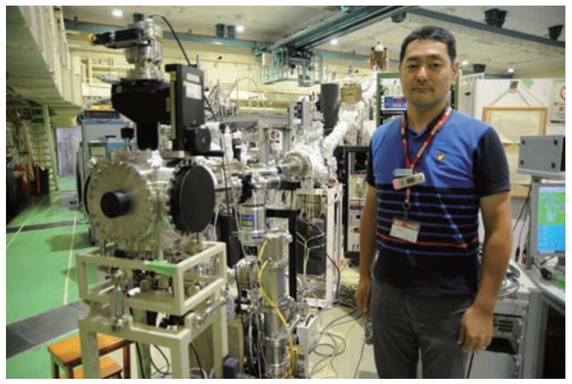

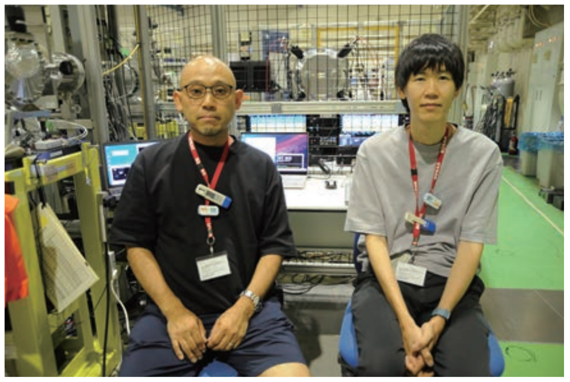

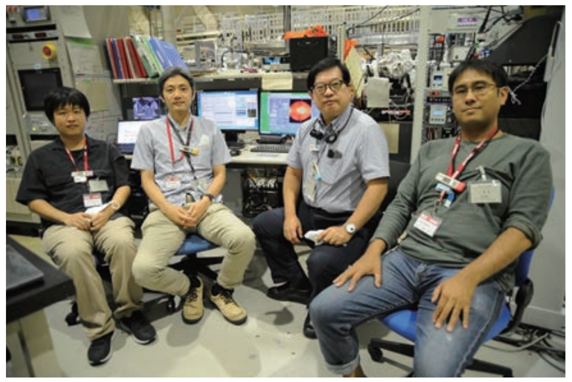

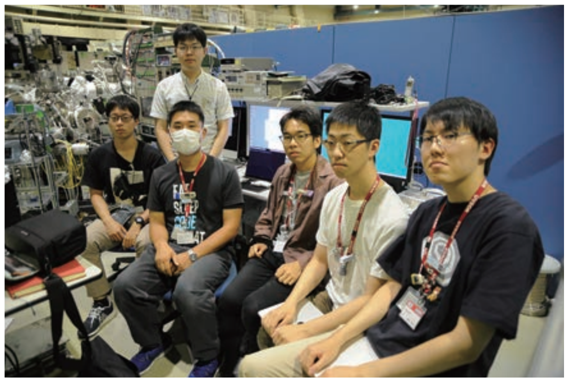

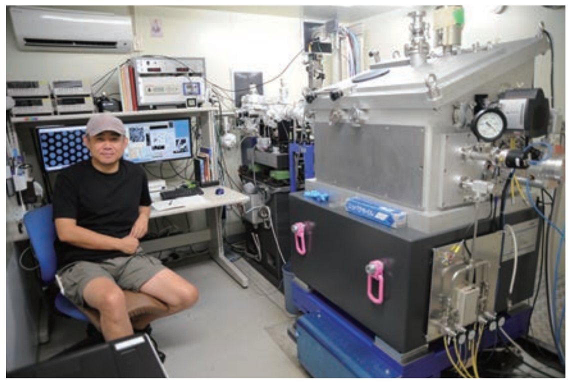

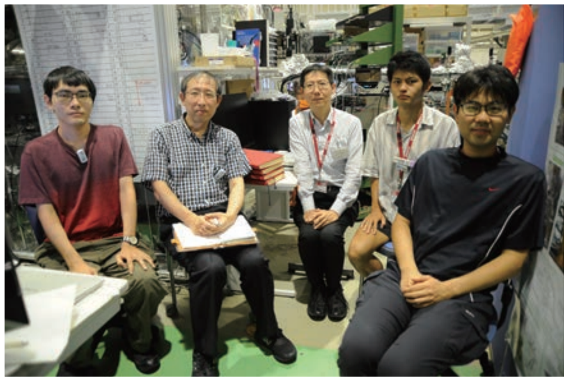

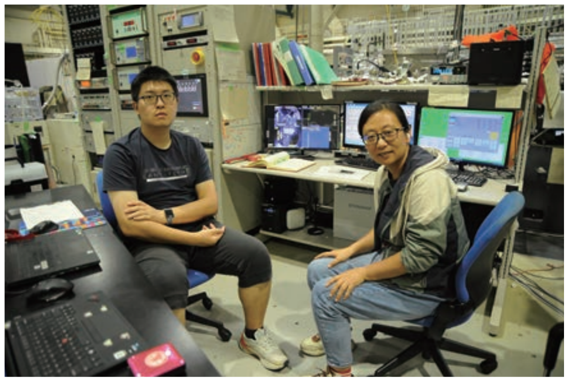

UVSOR User 10

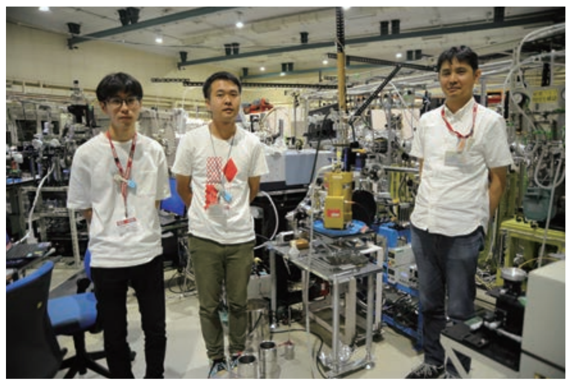

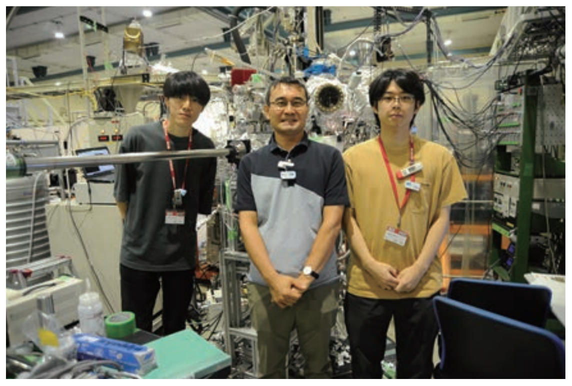

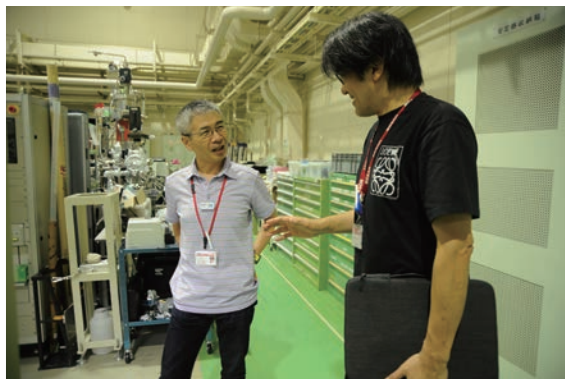

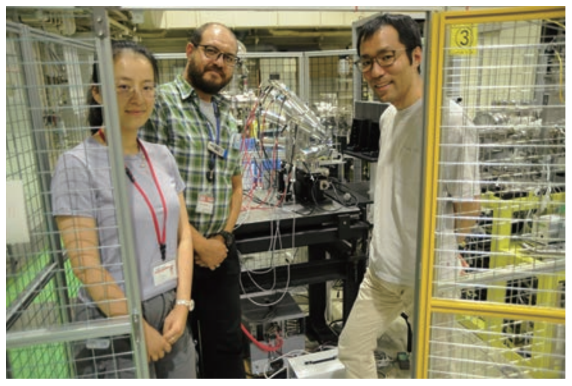

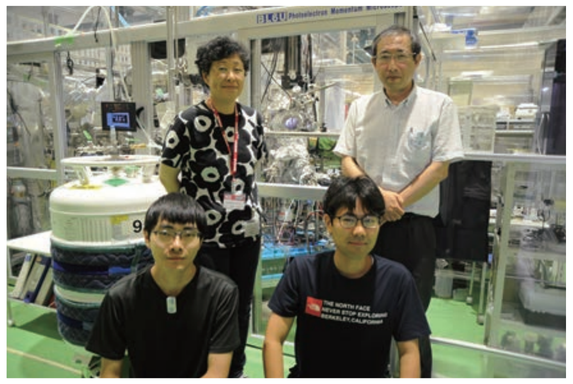

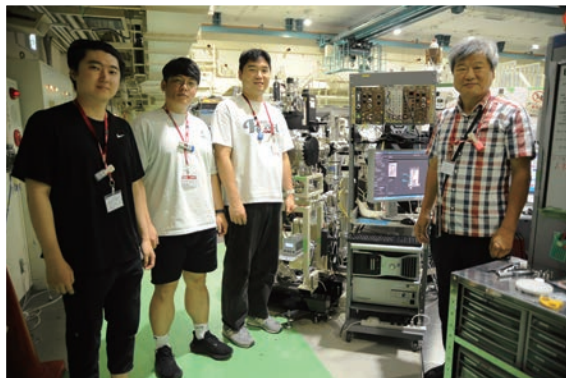

III-3

Chemistry

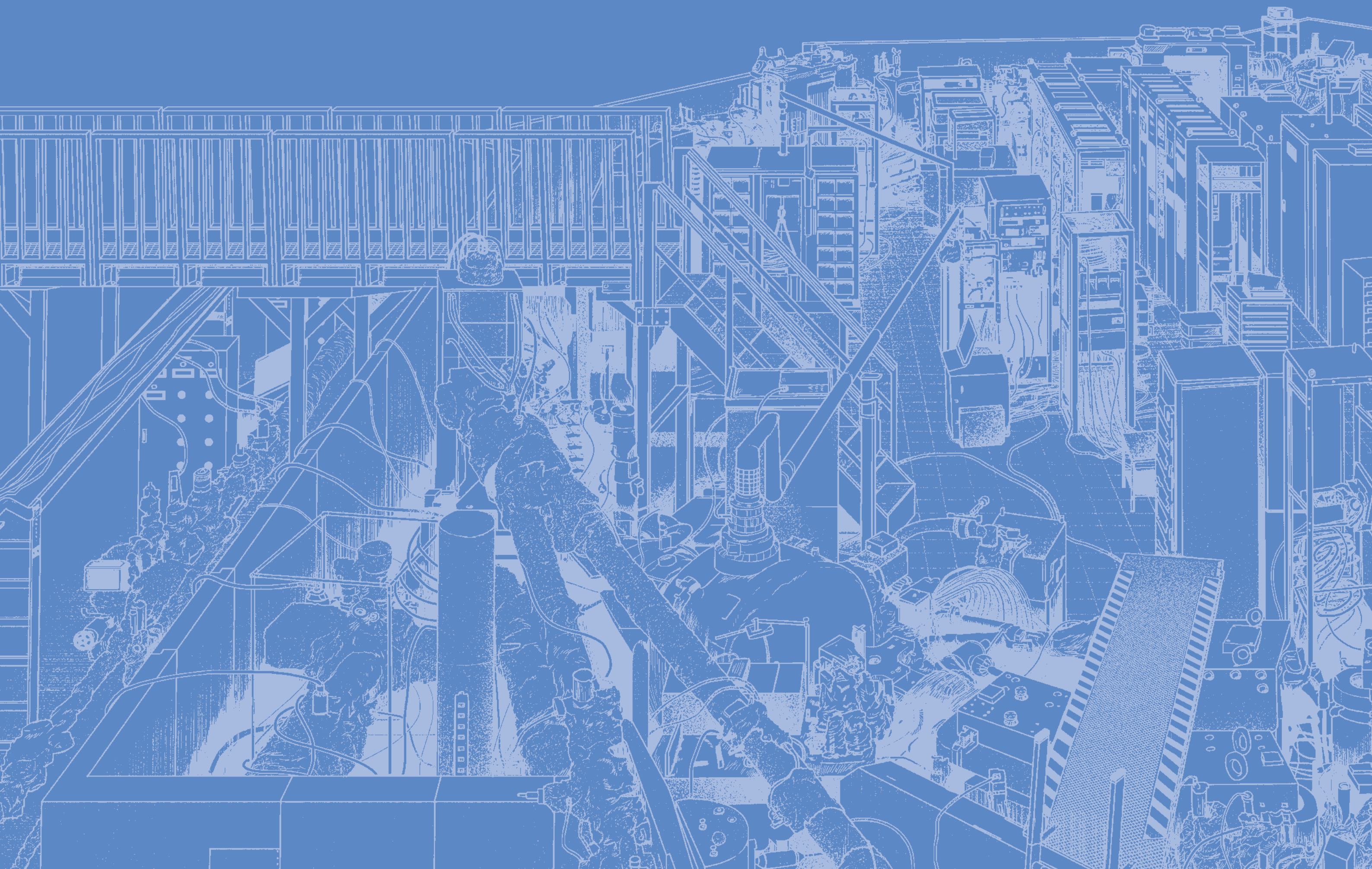

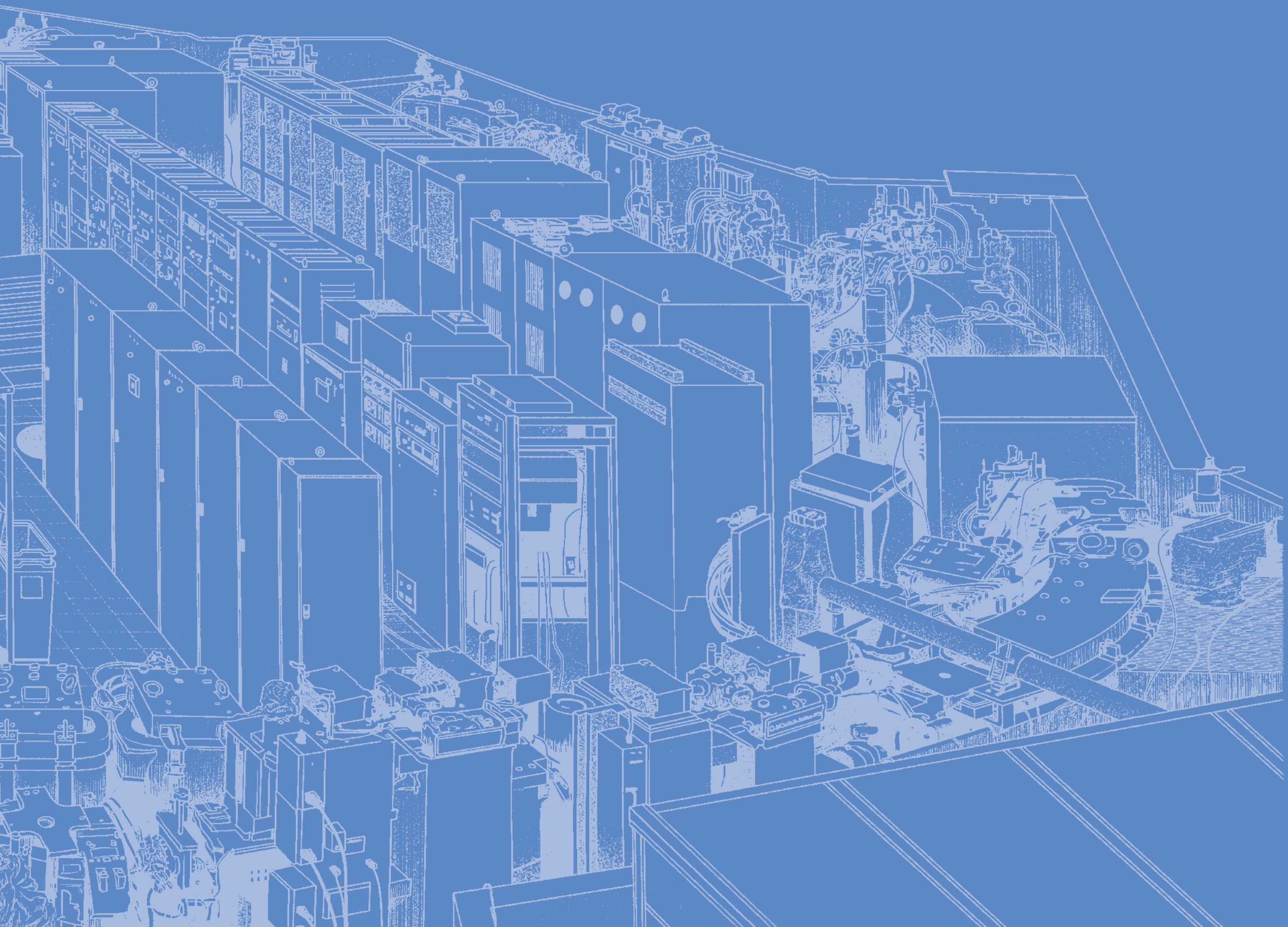

BL1U

Photoionized Plasma Production Experiments in the Synchrotron Light Source UVSOR

M Kobayashi[1], S Yoshimura[1], H Ota[2,3], H Chimura[1], K Shimizu[3], T Kaneyasu[3,4] and M Katoh[3,5]
[1]*National Institute for Fusion Science, Toki city 509-5292, Japan*
[2]*Japan Synchrotron Radiation Research Institute, 1-1-1, Kouto, Sayo-cho, Sayo-gun, Hyogo 679-5198, Japan,*
[3]*UVSOR Synchrotron Facility, Institute for Molecular Science, Okazaki city 444-8585, Japan*
[4]*SAGA Light Source, Tosu city 841-0005, Japan*
[5]*Reserach Institute for Synchrotron Radiation Science, Hiroshima University, Higashi-Hiroshima 739-0046, Japan*

Photoexcitation and photoionization are important processes in space to produce plasmas. The photoinduced processes will also become important in divertor region of nuclear fusion reactors due to both the increase in gas pressure and in the emission from plasmas. In the photoionized plasmas, there is no threshold energy to initiate discharge such as Paschen's law in the electric field application. The cross section of the photoionization decays rapidly with increasing photon energy. The photon energy exceeding the ionization potential is converted to kinetic energy of electrons. Owing to these features, photoionized plasmas are expected to have distinct characteristics from those produced by electric field application, which is usual scheme to produce plasmas in laboratory experiments. In particular, the photoionization rate coefficients become large at several tens eV range for most of atoms and molecules. However, photoionized plasma experiments with systematic scan of photon energy in this range have not been performed so far. Therefore, understanding plasma properties, particularly in terms of plasma as collective phenomena of charged particles, is still very limited. In these contexts, we are developing experimental apparatus that can generate photoionized plasmas by using the synchrotron light source [1], which is capable to change the energy of the beam continuously in a wide range, from X-ray, EUV, VUV, visible, to infra-red ranges.

The VUV/EUV beam was produced in the undulator beam line BL1U in UVSOR. The higher-order light of the undulator beam is cut by gold and an aluminum mirror located on the upstream gas cell, as shown in Fig.1. The cut-off energy is selectable by changing an incident angle of the beam to the mirrors, and it was set to 40eV in the present experiments. The gas cell is connected to the beamline with a multi-step differential exhaust system without a vacuum shielding with a window or film, to avoid flux attenuation caused by the window or film. The photon flux of an order of 10^{15} photons/sec/mm^2 with a beam radius of about 1 mm is obtained at the center of the gas cell. Sample gas was introduced to the gas cell in a range from 1 to 10 Pa, while keeping the high vacuum condition, an order of $10^{-6} \sim 10^{-7}$ Pa, at the upstream chamber connected to the storage ring.

The beam energy was scanned from 16 to 36 eV. The production of photoionized plasmas was detected with emission spectra of the gas and the Langmuir probe measurements. Figure 2 shows a camera image of the Ar plasmas produced by beam energy of 22 eV, where the emission along the beam is clearly observed. The estimated plasma parameters are electron density of order of 10^{13} m^{-3} and electron temperature of about 1 eV at a position 1 mm away from the beam axis. The density decays quickly within 2 mm away from the beam, while temperature is almost constant in space. Analysis of emission spectra to evaluate plasma parameters will be conducted for comparison with the Langmuir probe measurements.

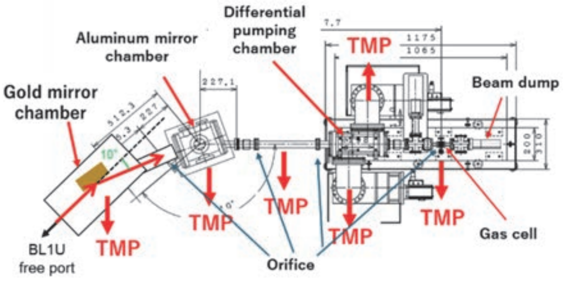

Fig. 1. Schematic of experimental set of photoionized plasma experiments. TMP denotes turbo molecular pump.

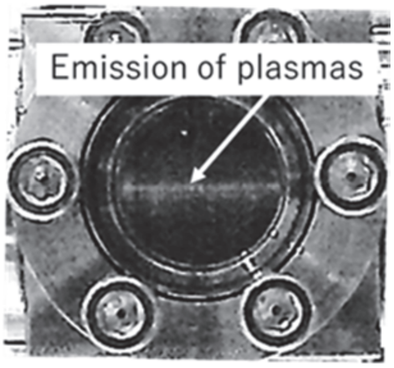

Fig. 2. Visible camera image of photoionized plasmas produced with argon gas of 10 Pa and beam energy of 22 eV. Emission along the beam is clearly observed.

[1] M. Kobayashi *et al.*, Plasma Fusion Res. **19** (2024) 1301038.

BL1U

State-Resolved Molecular Chirality Based on the High-Precision Measurements of Photoelectron Circular Dichroism

H. Kohguchi[1], Y. Hikosaka[2], T Kaneyasu[3], S. Wada[1], K. Shimizu[4],
M. Katoh[1,4] and Y-I. Suzuki[5]

[1]*Graduate School of Advanced Science and Engineering, Hiroshima University,*
Higashi-Hiroshima 739-8526, Japan
[2]*Institute of Liberal Arts and Sciences, University of Toyama, Toyama 930-0194, Japan*
[3]*SAGA Light Source, Tosu 841-0005, Japan*
[4]*UVSOR Synchrotron Facility, Institute for Molecular Science, Okazaki 444-8585, Japan*
[5]*School of Medical Technology, Health Sciences University of Hokkaido, Tobetsu 061-0293, Japan*

Molecular chirality is generally defined by the molecular structure regarding whether the configuration has a right-handed or left-handed form. Photoelectron circular dichroism (PECD) has been developed as a new approach to examining electronic molecular chirality, which is state-specific and energy-dependent. The BL1U beamline with the undulator is most suited for the PECD study since the circularly polarized light for photoionization is available with the light source in a broad wavelength region. Especially, the BL1U beamline is advantageous for circularly polarized light in the VUV region where PECD is maximized in most chiral molecules [1]. We have investigated the PECD of oxirane with the BL1U beamline and the photoelectron imaging apparatus based on the VMI method.

Oxiranes are typical chiral molecules exhibiting PECD, for which we have conducted the precise measurements of the state- and energy-dependence to compare with our accurate theoretical calculations. The circularly polarized radiation at several wavelengths from 50 nm to 130 nm was used for photoionization. Examples of the observed photoelectron images at various photoionization wavelengths are shown in Fig. 1. The PECD data are difference images between the photoelectron images with the right- and left-circular polarization. The total image intensity was normalized before subtraction. A possible source of inaccuracy occurs in the normalization and background correction of the single polarization image data. The error due to the image data analysis most seriously appears in the highest photoelectron kinetic energy (PKE) region. The photoelectron count rate was suppressed to be lower than 10 kcps by reducing the pulse energy, although the much higher count rate was easily obtained with the BL1U beamline. The number of photoelectrons was limited because our imaging system was too slow to detect correctly more photoelectron spot images on the phosphor screen than 10 kcps. These technical problems could be serious only for the determination of the highly precise PECD parameters. We examined the source of the problems and the solution to improve the accuracy based on the experimental data [2].

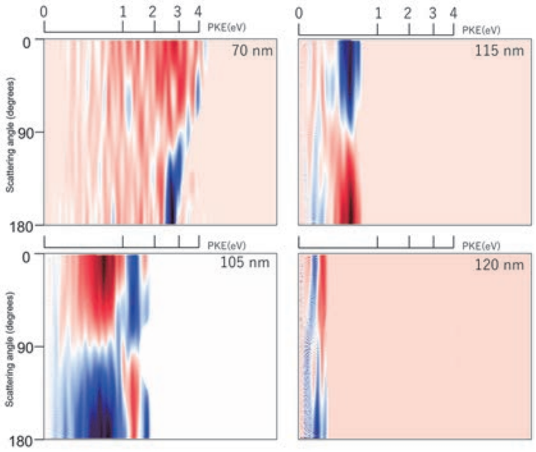

Fig. 1. Photoelectron circular dichroism of methyl oxirane at photoionization wavelengths of 70 nm, 105 nm, 115 nm, and 120 nm. The photoelectron kinetic energy (PKE) is denoted on the upper bar and the scattering angle is indicated on the vertical axis. The partly missing signal region in the largest PKE edge is due to the image data subtraction.

Nevertheless, the state- and energy-dependence of the PECD data are observed (Fig. 1). The PECD was the largest in the low PKE region at the longest photoionization wavelength, which was assigned to the emitted electron from the HOMO and HOMO-1. The sign of PECD (blue/red in Fig. 1) was altered depending on the ionization final states, and the degree of PECD of the particular state varied with the photon energy, therefore PKE. Overall, the PECD decreased with the higher PKE. In the high photon energy (ex. 70 nm in Fig. 1), although the PECD almost disappeared, the highest PKE component exhibited substantially large intensity, indicating a particular state- and energy dependence to reveal the origin of PECD.

[1] H. Kohguchi *et al.*, UVSOR Activity Report **51** (2023) 138.
[2] H. Kohguchi, Y. Hikosaka, T Kaneyasu, S. Wada, and Y-I. Suzuki, UVSOR Activity Report **50** (2022) 136.

BL1U

Inner-Shell Photoelectron Wave Packet Interference by Attosecond Phase Control of XUV Synchrotron Radiation

T. Kaneyasu[1,2], Y. Hikosaka[3], S. Wada[4], H. Ota[5,2], H. Iwayama[2], K. Shimizu[2],
M. Fujimoto[6,7] and M. Katoh[8,2,6]
[1]SAGA Light Source, Tosu 841-0005, Japan
[2]Institute for Molecular Science, Okazaki 444-8585, Japan
[3]Institute of Liberal Arts and Sciences, University of Toyama, Toyama 930-0194, Japan
[4]Graduate School of Advanced Science and Engineering, Hiroshima University,
Higashi-Hiroshima 739-8526, Japan
[5]Japan Synchrotron Radiation Research Institute, Hyogo 679-5198, Japan
[6]Synchrotron Radiation Research Center, Nagoya University, Nagoya 464-8603, Japan
[7]Aichi Synchrotron Radiation Center, Seto 480-0965, Japan
[8]Research Institute for Synchrotron Radiation Science, Hiroshima University, Higashi-Hiroshima 739-0046, Japan

The sequential interaction of an atom with a pair of coherent light pulses results in the production of a pair of photoelectron wave packets which interfere with each other during the propagation in a free space. The control and observation of photoelectron wave packet interference has been achieved by using coherent pulse pairs generated by laser sources [1]. Recently, we have shown that the phase coherent double pulses generated by synchrotron light source can be used for controlling the photoelectron wave packet interference in the extreme ultraviolet wavelength [2].

As a next step, we applied this method to the inner-shell ionization of atoms for probing the ultrafast electronic rearrangement processes following the inner-shell ionization of atoms. The experiment was performed by using coherent double pulses generated by a tandem undulator at BL1U. The central photon energy of the pulse was set to approximately 93 eV. The time delay between the pulses was adjusted in femtosecond range with an attosecond resolution. The photoelectron interferogram which comprises of photoelectron spectra measured as a function of time delay, was obtained for helium 1s and xenon 4d photoelectrons.

Figure 1 shows the measured photoelectron interferograms. The interferogram exhibits a periodic modulation due to the interference with a period of approximately 45 as, which corresponds to the photon frequency calculated as $\omega = (E+E_{\mathrm{IP}})/\hbar$ where E and E_{IP} are the kinetic energy of the photoelectron and the ionization potential of the atom, respectively. When comparing the two measurements, the contrast of interference quickly decreases as the time delay increases for xenon atoms. This can be explained by the femtosecond Auger decay following the inner-shell ionization. Moreover, the interferogram exhibits intensity modulation with a period of about 2 fs. This effect can be attributed to the evolution of the spin-orbit wave packet produced in the Xe^+ ion, suggesting that this method could be used to explore ultrafast quantum state dynamics with attosecond resolution.

[1] M. Wollenhaupt *et al*., Phys. Rev. Lett. **89** (2002) 173001.
[2] T. Kaneyasu *et al*., Sci. Rep. **13** (2023) 6142.

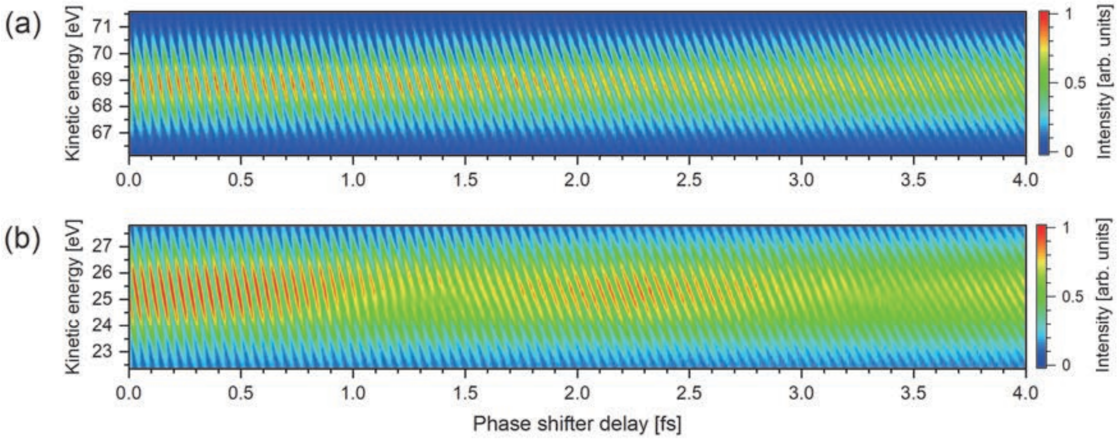

Fig. 1. Photoelectron interferograms measured for (a) helium 1s and for (b) xenon 4d photoelectrons.

BL3U

Oxygen K-Edge Soft X-Ray Absorption Spectroscopy of Pd/CeO$_2$ Catalyst for DC-Assisted Dry Reforming of Methane

H. Tedzuka[1], N. Matsumoto[1], H. Saito[2], T. Sugimoto[2,3], M. Nagasaka[2,3] and Y. Sekine[1]
[1]*Department of Applied Chemistry, Waseda University, 3-4-1, Okubo, Shinjuku, Tokyo 169-8555, Japan*
[2]*Institute of Molecular Science, Myodaiji, Okazaki 444-8585, Japan*
[3]*Graduate Institute for Advanced Studies, SOKENDAI, Myodaiji,Okazaki 444-8585, Japan*

Chemical utilization of methane (CH_4) and carbon dioxide (CO_2) is of great importance because both are greenhouse gases. Catalytic dry reforming of methane (DRM; $CH_4+CO_2 \rightarrow 2CO+2H_2$) is therefore much attractive reaction in which CH_4 and CO_2 are converted syngas, i.e., the mixture of carbon monoxide (CO) and hydrogen (H_2). In particular, DRM can be a powerful solution of biogas (the mixture of CH_4 and CO_2) utilization [1].

In the conventional DRM induced by thermal catalysis, high reaction temperatures above 973 K are required for activation of CH_4 and CO_2 because both molecules are highly stable. From the thermodynamic point of view, high reaction temperatures are also profitable for achieving high equilibrium conversion. However, under the harsh reaction conditions, catalysts are rapidly deactivated by carbon deposition through CH_4 decomposition ($CH_4 \rightarrow C+2H_2$) and CO disproportionation ($2CO \rightarrow C+CO_2$). Therefore, non-thermal catalytic DRM processes at low temperatures are desirable for suppression of the coke formation and efficient energy utilization.

To promote DRM at low temperatures, we have developed DC-assisted catalysis in which constant DC of the order of a few mA is applied to the catalyst [2]. In this catalytic system, ceria (CeO_2)-supported metal catalysts exhibit high catalytic performance [2]. However, it remains a challenge to elucidate why DRM can be driven at low temperatures, although we reported the key role of surface lattice oxygen species [3]. In this study, to obtain microscopic insight into the reaction mechanism, we performed oxygen *K*-edge soft X-ray absorption spectroscopy (SXAS) of the CeO_2-supoorted palladium (Pd) catalyst.

Pd/CeO_2 was prepared by an impregnation method; firstly, CeO_2 (JRC-CEO-1; Catalysis Society of Japan) and distilled water were added to a flask and were stirred for 2 h, then palladium acetate (Kanto Chemical Co. Inc.) solved in acetone was added into the flask and was further stirred for 2 h. After the suspension was evaporated, the obtained powder was dried at 393 K and calcined at 773 K. For the SXAS measurement, the calcined powder was formed into a pellet.

The SXAS measurement was performed at the BL3U beamline of UVSOR-III synchrotron. After the sample was put on the cell, the chamber was evacuated by a turbomolecular pump. Then, the mixture of CH_4, CO_2 and He, was introduced in the chamber and DRM was induced by applying DC to the sample. SXAS spectra were measured in fluorescence yield mode with a silicon drift detector.

Figure 1 shows the O *K*-edge SXA spectra of the Pd/CeO_2 before and after the reaction. In the spectra before the reaction, two peaks at 529.8 and 532.9 eV were observed. These peaks are attributed to the hybridized O2p-Ce4f state at 529.8 eV and the hybridized O2p-Ce5d(e_g) state at 532.9 eV [4].

Compared with the spectra before the reaction, the two peaks derived from CeO_2 were shifted to the lower energy after the DRM reaction. The shift of the hybridized O2p-Ce5d(e_g) state indicates that a part of Ce^{4+} was reduced to Ce^{3+} during the reaction [5] whereas the shift in the hybridized O2p-Ce4f state suggest the change in the local environment of Ce^{4+}. These results suggest that the redox properties of Ce play a crucial role in the DC-assisted DRM reaction.

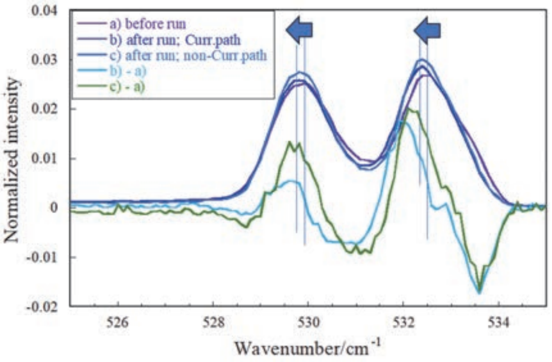

Fig. 1. Oxygen *K*-edge spectra of 1wt%Pd/CeO_2 before and after the DRM reaction. The spectra were measured in fluorescence mode using a silicon drift detector. The DRM reaction was performed by applying DC to the catalyst at $P_{CO2}=P_{CH4}=P_{He}=$ 5 kPa.

[1] M. Usman *et al.*, Renew. Sustain. Energy Rev. **45** (2015) 710.
[2] A. Motomura *et al.*, RSC Adv. **12** (2022) 28359; A Motomura *et al.*, Chem. Lett. **52** (2023) 259.
[3] N. Nakano *et al.*, RSC Adv. **12** (2022) 9036.
[4] L. Amidani *et al.*, J. Phys. Chem. *C* **127** (2023) 3077.
[5] A.B. Altman *et al.*, Dalton Trans. **45** (2016) 9948.

BL3U

XAS Measurements for Grahpene Oxide Aqueous Solutions

T. Sasaki[1] and H. Xu[1]

[1]*Department of Complexity Science and Engineering, Graduate School of Frontier Sciences,*
The University of Tokyo, Kashiwa 277-8561, Japan

XAS measurements for liquid samples have been enabled at UVSOR BL3U, giving new insights for physicochemical properties of materials [1]. We have achieved O-K edge XAS measurements for cellobiose aqueous solutions and found that XAS signals can be simulated with CP2K and hydrogen bonding with water molecules affect the relative intensity of XAS peaks [2]. In this study Graphene oxide (GO) was chosen as a target molecule. GO is widely used as a catalyst support due to its hydrophilic, acidic, large surface area, and easy modification properties. However, although several structural models have been proposed, none have been conclusively established. We are searching for a suitable structural model for graphene oxide based on quantum chemical calculations, clarifying the dependence of the model on the carbon number, oxygen content, and degree of unsaturation. In particular, we will clarify the functional group structure and carbon defects contained therein and the associated structural features. To verify this, we will perform measurements using soft X-ray absorption spectroscopy and perform simulation calculations of the spectra to experimentally verify the structural model.

XAS measurements for liquid samples were conducted at UVSOR BL3U using facilities developed by Nagasaka et al. [1]. The liquid sample cell with Si3N4 membranes was adopted, where the thickness of the liquid layer was controlled by the He gas pressure around the cell. GO was prepared by the modified Hummers method [3] and aqueous solution was prepared by sonication of 2 hours.

Figure 1 shows C-K XAS spectrum for GO (14 mg) in 10 ml water at room temperature. Three peaks at 285, 287 and 291 eV were observed. O-K XAS measurement was also achieved but due to the dominant contribution by water molecules it was difficult to assign peaks originated from GO (not shown).

We are also conducting computational study for obtaining typical structural formula of GO. In order to clarify the structure of graphene oxide, we performed a structure search using l-ADDF calculations using GRRM, sorted the resulting equilibrium structures (EQs) in order of energy, and enumerated the partial features within the structure for each EQ as structural features, thereby summarizing the energetically stable EQs and their structural features. Multiple l-ADDF calculations with different calculation conditions were conducted, and the trends was clarified as to the results of the structure search (calculation time, number of EQs obtained, number of structural features obtained, and energy width of the EQs obtained) when changing LADD, Nlowest, and calculation level. We also compared previously proposed structures and found the modified structure which exhibits the stabilized total energy with a modified partial structure as shown in Fig. 2. XAS simulation calculation using the obtained GO formula is undertaken to assign the peaks in the experimental result.

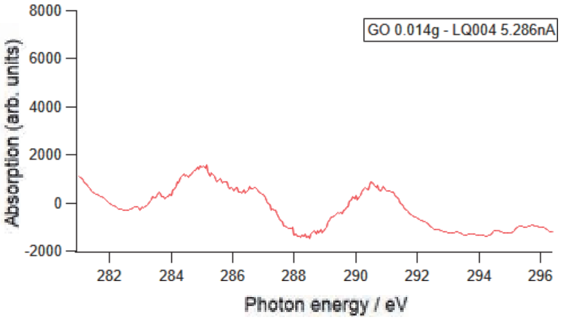

Fig. 1. C-K XAS spectrum for GO (14 mg) in 10 ml water at room temperature.

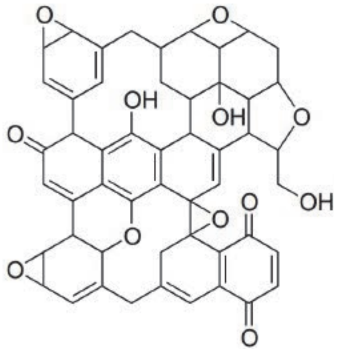

Fig. 2. One of the GO models obtained by GRRM calculation.

[1] M. Nagasaka *et al.*, J. Electrosc. Relat. Phenom. **200** (2015) 293.
[2] D. Akazawa *et al.*, J. Chem. Phys. **156** (2022) 044202.
[3] V.B. Saptal *et al.*, Chem. Sus. Chem. **9** (2016) 644.

BL3U

Salt-Specific Effect on the Solubility and Aggregation of 1-butanol in Water

Y. Yao[1], M. Nagasaka[2,3] and K. Mochizuki[1]
[1]*Department of Chemistry, Zhejiang University, Hangzhou 310028, RP China*
[2]*Institute for Molecular Science, Okazaki 444-8585, Japan*
[3]*Graduate Institute for Advanced Studies, SOKENDAI, Okazaki 444-8585, Japan*

The Hofmeister series has continued to a topic of interest across a variety of fields [1], and the Hofmeister anion series is typically represented by $CO_3^{2-} > SO_4^{2-} > S_2O_3^{2-} > H_2PO_4^- > F^- > Cl^- > Br^- > NO_3^- > I^- > ClO_4^- > SCN^-$. The solubility and aggregation of solute molecules in water has been influenced with the addition of these Hofmeister anions. In this study, the salt-specific effect on the degree of aggregation of 1-butanol molecules in aqueous solutions were studied using C K-edge X-ray absorption spectroscopy (XAS) [2].

The C K-edge XAS experiments were performed at BL3U using the transmitted-type liquid cell, whose details were described previously [3, 4]. The liquid cell was at an ambient pressure in helium gas, where a liquid layer was sandwiched between two Si_3N_4 membranes with a thickness of 100 nm. The thickness of the liquid layer was precisely controlled by adjusting the helium pressure for obtaining appropriate absorbance of soft X-rays. XAS spectra were obtained using the Lambert-Beer law, $\ln(I_0/I)$, where I and I_0 are the transmission signals of aqueous butanol solutions including salts and the solutions without 1-butanol, respectively.

Figure 1 shows C K-edge XAS spectra of 0.2 M aqueous 1-butanol solutions including different salts, where 1 M $NaClO_4$, 1 M NaCl, and 1 M Na_2SO_4 are dissolved. The temperatures of aqueous solutions were kept at 25 °C. The XAS spectra consists of five broad peaks, which were assigned using the inner-shell calculations: The lowest peak is assigned to the transition of the CH_3 C1s electrons to the 3s-type Rydberg orbitals. The second peak is assigned to the transitions of the CH_2 C1s electrons in the center part of the butyl group to the 3s-type Rydberg orbitals. The third peak is assigned to the transitions of the CH_3 C1s electrons to the 3p-type Rydberg orbitals. The fourth peak is assigned to the transitions of the CH_2 C 1s electrons in the center part of the butyl group to the 3p-type Rydberg orbitals. The fifth peak is assigned to the transitions of the CH_2 C1s electrons connected to the hydroxyl groups to the 3s-type Rydberg orbitals.

The peak intensity at 288.5 eV in the XAS spectrum of 0.2 M aqueous 1-butanol solution is higher than that in the spectrum of neat 1-butanol liquid. It is because 1-butanol molecules are remarkably isolated in the dilute aqueous solution. This tendency is same as the C K-edge XAS spectra of aqueous methanol and ethanol solutions [5, 6]. It means that the aggregations of 1-butanol molecules in aqueous solutions would be evaluated from the peak intensities at 288.5 eV.

In the C K-edge XAS spectra of 0.2 M aqueous 1-butanol solutions shown in Fig. 1, the peak intensities at 288.5 eV are decreased with the order of $NaClO_4$, NaCl, and Na_2SO_4 from those with no salt condition. It means that the aggregations of 1-butanol molecules by adding salts are increased with the order of $NaClO_4$, NaCl, and Na_2SO_4. It means that the aggregations of 1-butanol molecules follow the Hofmeister anion series. These results provide molecular insights into how ions affect solute solubility and solute-solute aggregations for other hydrophobic molecules. The C K-edge XAS measurements are useful for evaluating the aggregations of hydrophobic molecules in aqueous solutions.

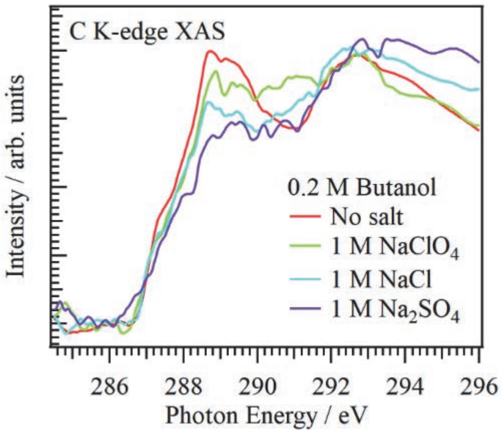

Fig. 1. C K-edge XAS spectra of 0.2 M aqueous 1-butanol solutions including different salts (1 M $NaClO_4$, 1 M NaCl, and 1 M Na_2SO_4).

[1] F. Hofmeister, Arch. Exp. Pathol. Pharmakologie **24** (1888) 247.
[2] Y. Yao *et al*., Physica A **647** (2024) 129917.
[3] M. Nagasaka *et al*., Anal. Sci. **36** (2020) 95.
[4] M. Nagasaka and N. Kosugi, Chem. Lett. **50** (2021) 956.
[5] M. Nagasaka *et al*., J. Phys. Chem. B **118** (2014) 4388.
[6] M. Nagasaka *et al*., J. Phys. Chem. B **126** (2022) 4948.

BL3U

Structure Analysis of Organic Thin-Film Solar Cells Using Resonant Soft X-ray Scattering Technique

H. Iwayama[1] and A. Sugishima[2]

[1]*UVSOR Synchrotron Facility, Institute for Molecular Science, Okazaki 444-8585, Japan*
[2]*Analysis Technology Center, Fujifilm Corporation, Minamiashigara 250-0193, Japan*

Resonant soft X-ray scattering is an innovative technique for analyzing chemical-specific structures in material science. Conventional small-angle X-ray scattering (SAXS) has been widely used to analyze nanostructures within materials. However, when analyzing polymer composites, SAXS faces significant challenges due to the lack of contrast between polymers composed mainly of light elements. This makes it difficult to determine how these polymers mix and interact. For instance, in organic thin-film solar cells, efficient charge transfer is achieved when two molecules form a bulk heterojunction structure. However, this structure is challenging to measure using conventional SAXS.

Resonant soft X-ray scattering (RSoXS) enhances scattering from specific molecules by utilizing their resonant energy differences. This technique takes advantage of the slight differences in resonant X-ray energies between two molecules to clarify their structures and arrangements. This allows for detailed analysis of the internal structures of polymer composites. In this work, we show an example application of RSoXS in the analysis of organic thin-film solar cells.

Our sample is an organic thin film composed of [6,6]-Phenyl-C61-butyric Acid Methyl Ester (PCBM) and Poly(3-hexylthiophene-2,5-diyl) (P3HT) spin-coated on a 100 nm thick Si_3N_4 membrane, and has a bulk heterojunction structure separated at the nanoscale as shown in Fig. 1. The thickness of this film is about 200 nm.

The experiment was performed at UVSOR BL3U. The soft X-ray energy was 260 eV for non-resonance and 284 eV and 286 eV for resonance, respectively. The camera length was 100 mm, and the scattered light was observed with a soft X-ray camera (Andor BN940P).

Figure 2 shows the scattering profile at the photon energy of 260, 284, and 298 eV. The horizontal axis is the scattering vector q [nm^{-1}], and the vertical axis is the scattering intensity. No strong scattering peak was observed in the non-resonance case of 260 eV. This means that there is no difference in the complex dielectric constant of the two molecules, so there is no contrast in the scattering process. On the other hand, at 284 eV, close to the resonance energy of PCBM, a strong peak was observed at q=0.2 nm^{-1}. This indicates that PCBM has a spatial scale of about 30 nm. On the other hand, at 298 eV, where scatterings from P3HT are enhanced, a peak was also observed at q=0.1 nm^{-1}. This means that P3HT has a spatial scale of about 60 nm.

In our work, it has been shown that the structure of each polymer can be analyzed by using resonant soft X-ray scattering. We will continue to conduct detailed analysis.

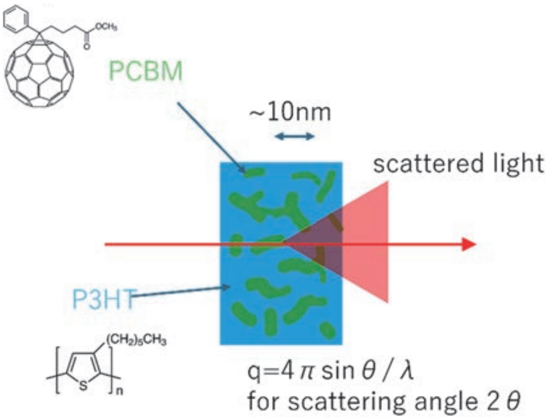

Fig. 1. Schematic view of the organic thin film, where bulk heterojunction of PCBM and P3HT is formed.

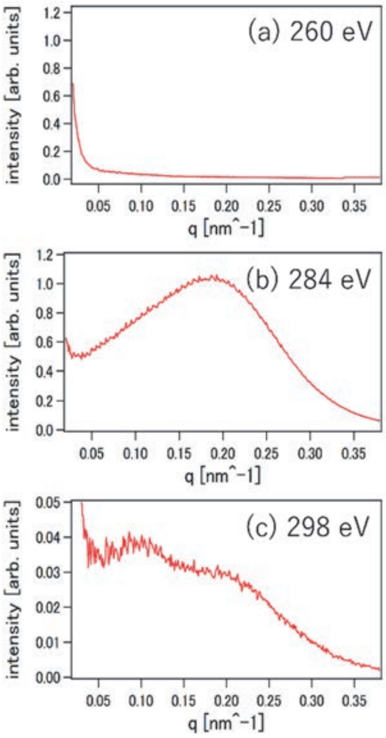

Fig. 2. Scattering profiles for the organic thin film at the photon energies of (a) 260 eV, (b) 284 eV and (c) 298 eV.

BL3U

Observation of O K-Edge X-Ray Absorption Spectrum of μ-Oxo-Bridged Iron Phthalocyanine Dimer

Y. Yamada [1,2] and M. Nagasaka[3]

[1]*Department of Chemistry, Graduate School of Science, Nagoya University, Furo-cho, Chikusa-ku, Nagoya 464-8602, Japan*

[2]*Research Center for Materials Science, Nagoya University, Furo-cho, Chikusa-ku, Nagoya 464-8602, Japan*

[3]*Institute for Molecular Science, Myodaiji, Okazaki 444-8585, Japan*

Coordination of oxygen atoms to the iron porphyrinoids has long been attracted interests of chemists since interactions of oxygen atoms with iron center of iron porphyrin are quite important in various biological processes such as oxygenation, oxygen carrying, and so on. It is well-known that iron(II) porphyrinoids including iron porphyrin and iron phthalocyanine tend to form μ-oxo-bridged dimers as described in Fig. 1 under air [1]. These μ-oxo-bridged dimers of iron porphyrinoids can act as an oxygenation catalyst for various organic chemicals under photoirradiation in the presence of O_2.

To the best of our knowledge, soft X-ray XAS studies of μ-oxo-bridged iron porphyrinoid dimers have not been reported yet, although there are some reports on hard X-ray XAS studies. Therefore, the purpose of this work is to investigate μ-oxo-bridged iron phthalocyanine dimer by soft X-ray XAS. We prepared a μ-oxo-bridged iron phthaloycyanine dimer having 8 peripheral *tert*-butyl units **1** and a monomeric iron(III) phthalocyanine chloride having 4 peripheral *tert*-butyl units **2**. The use of soft X-ray XAS is advantageous because direct and selective observation of both oxygen and iron atoms in an μ-oxo-bridged dimer become possible since the soft-X-ray region include both of the K-edge of oxygen and L-edge of iron.

O K-edge XAS measurements of **1** and **2** in solution were performed by using a beamline equipped with a transmission-type liquid flow cell in BL3U of UVSOR [2]. The spectra were obtained based on the Lambert-Beer law, $\ln(I_0/I)$, where I_0 is the transmission signals of benzonitrile and I is those of **1** or **2**.

Fig. 2 shows a comparison of the O K-edge XAS spectra obtained for **1** and **2** in benzonitrile (30 mM). The blue spectrum represents that of **2** having no oxygen-containing moieties, where small amount of silicon oxide on Si_3N_4 membrane and H_2O in benzonitrile were observed. It is considered that the μ-oxygen of **1** should show double bond character due to the interaction of p-orbitals of the μ-oxygen atom with the d-orbitals of the iron atom of two iron porphyrins. It is known that, generally in the O K-edge XAS spectra, the peaks of oxygen having double bond character tend to appear at lower energy than 534 eV, whereas the peaks of oxygen having single bond character appears at higher energy than 535 eV [3]. By comparing the spectra of **1** and **2**, we considered that the peak at 527 eV and/or 532–534 eV could be assigned to those of μ-oxygen of **1**. In order to identify the peaks of μ-oxygen of **1**, we are going to measure the soft X-ray XAS of the solids of **1** and **2**. In addition, DFT calculations of XAS of **1** and **2** are also underway.

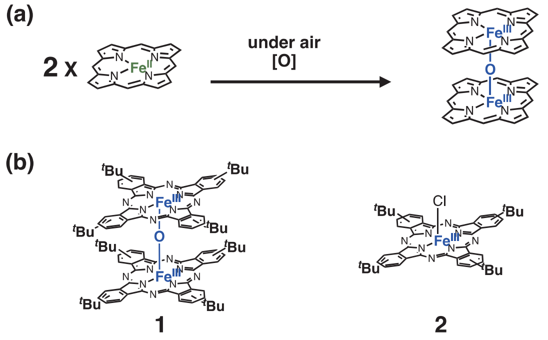

Fig. 1. Generation of μ-oxo-bridged iron porphyrin dimer from iron porphyrin.

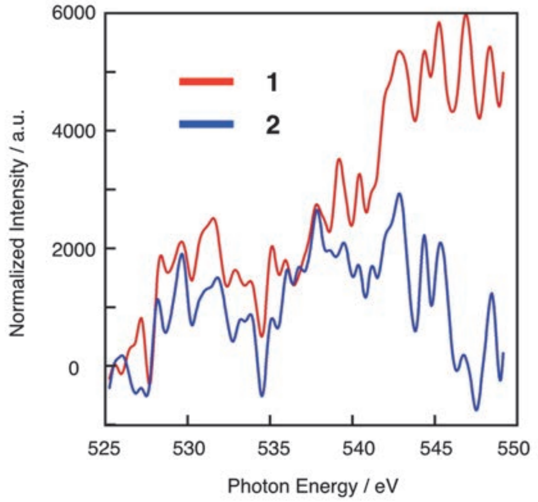

Fig. 2. Comparison of O K-edge XAS spectra of **1** and **2** in benzonitrile (30 mM) at 25 °C.

[1] S. P. Rath *et al.*, Coord. Chem. Rev. **337** (2017) 112.
[2] M. Nagasaka and N, Kosugi, Chem. Lett. **50** (2021) 956.
[3] M. Nagasaka *et al.*, Phys. Chem. Chem. Phys. **26** (2024) 13634.

BL3U

Soft X-ray Absorption Study of a Titanium-Oxide Photocatalyst Suspended in Water

Yi Hao Chew[1], N. Ichikuni[2], T. Yoshida[3] and H. Onishi[1,4]
[1]Graduate School of Science, Kobe University, Kobe 657-8501, Japan
[2]Graduate School of Engineering, Chiba University, Chiba 263-8522, Japan
[3]Graduate School of Engineering, Nagoya University, Nagoya 464-8603, Japan
[4]Division of Advanced Molecular Science, Institute for Molecular Science, Okazaki 444-8585, Japan

Material conversion on semiconductor photocatalysts is intensively studied worldwide. Downhill reactions, in which the Gibbs free energy decreases during the conversion of reactants to products, have been successfully integrated into our society [1]. Artificial photosynthesis, a category of uphill reactions involving the oxidation of water, is being developed for societal implementation in the near future [2]. In addition, fundamental studies are being conducted to uncover new scientific discoveries related to light-driven, efficient materials conversion.

In collaboration with Prof. Masanari Nagasaka of UVSOR, we apply soft X-ray absorption to the *in-situ* characterization of semiconductor photocatalysts suspended in water. An anatase TiO_2 photocatalyst (JRC-TIO-19 provided by Catalysis Society of Japan), was suspended in water. The suspended solution was adjusted with NaOH to pH 13. The pH adjustment was critical to suspend 100 nm TiO_2 particles long enough to pass through a liquid cell.

The liquid cell was mounted in BL3U. Oxygen K-edge and titanium L-edge absorption spectra were observed with a transmission setup [3] in the presence and absence of ultraviolet (UV) light for band-gap excitation. Soft X-rays transmitted through the suspended solution were detected with a silicon photodiode. The photodiode was capped with a 150 nm thick aluminum film (LUXEL, TF110) to minimize the contribution of stray UV light to the detector response (Fig. 1). The capping device is deposited at UVSOR. Users are encouraged to use the device when operating the photodiode under UV or visible light irradiation.

Figure 2 shows a Ti L-edge spectrum observed in the presence of UV light provided by a Hg–Xe lamp (200 W). In the Ti L-edge, electron transition from Ti2s and 2p to 3d orbitals of TiO_2 particles appears at 455–470 eV [4]. The Ti3p orbitals are hybridized with O2s and 2p orbitals to form the conduction band in TiO_2. The hybridized orbitals are split into t_{2g} and e_g levels according to the ligand field in TiO_6 octahedra.

The soft X-ray absorption of solutions has been successfully studied. Here, transmission measurement was achieved with a suspension. The extension to an *operando* study of the suspension under UV irradiation is possible.

This study was supported by JSPS KAKENHI (grant number 22H00344).

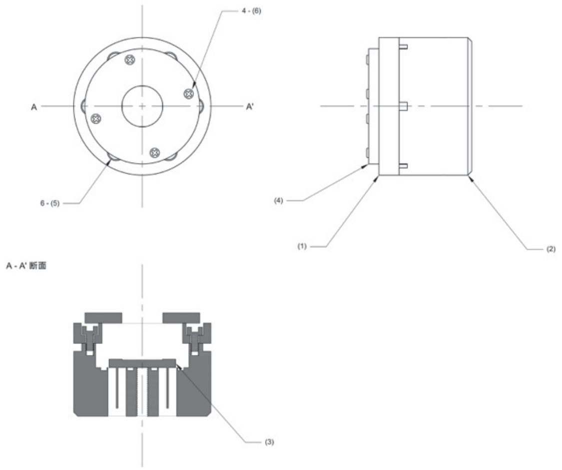

Fig. 1. A devise capping the photodiode with the aluminum filter for transmission detection of soft X-ray absorption spectrum under UV-light irradiation.

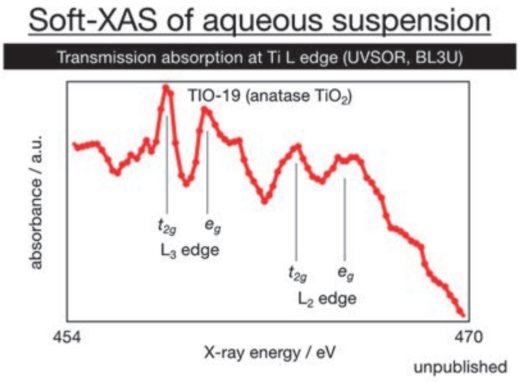

Fig. 2. Soft X-ray absorption of anatase TiO_2 photocatalyst particles (JRC-TIO-19) suspended in water at pH 13. Titanium L-edge spectrum was observed under UV light irradiation.

[1] A. Fujishima *et al.*, J. Photochem. Photobio. C **1** (2000) 1.
[2] H. Onishi, ChemSusChem **12** (2019) 1825.
[3] T. Petit *et al.*, J. Phys. Chem. Lett. **6** (2015) 2909.
[4] S. C. Ray *et al.*, J. Phys. Chem. C **126** (2022) 8947.

BL3U

Direct Observation of Solvation of Redox Species by Soft X-ray Spectroscopy toward Development of High Performance Thermo-Electrochemical Cells

H. Yoshikawa[1], K. Wakamatsu[1], Z. Hongyao[2], T. Yamada[2] and M. Nagasaka[3]
[1]*Program of Materials Science, School of Engineering, Kwansei Gakuin University, Sanda, Hyogo 669-1330, Japan*
[2]*Division of Chemistry, Graduate School of Science, The University of Tokyo, Bunkyo-ku, Tokyo 113-0033, Japan*
[3]*UVSOR Synchrotron Facility, Institute for Molecular Science, Okazaki, Aichi 444-8585, Japan*

In the utilization of primary energy, approximately 50–60 % is discarded as unused waste, with around 70 % of this being low-grade waste heat. The recovery and reuse of low-grade waste heat using thermoelectric devices, which convert thermal energy into electrical energy, present an effective solution to the energy problem. Among various thermoelectric devices, thermochemical cells (TECs) utilizing liquid electrolytes have recently gained attention due to their high thermoelectric conversion efficiency [1]. The efficiency of thermoelectric conversion is evaluated by the dimensionless figure of merit as following:

$$ZT = \frac{S_e^2 \sigma T}{\kappa} \quad (1)$$

where S_e is Seebeck coefficient, σ is electrical conductivity, T is temperature, and κ is thermal conductivity. To enhance thermoelectric conversion efficiency, the material must exhibit a high S_e, excellent σ, and low κ. However, achieving all these properties simultaneously in a single material remains a significant challenge. To establish an ideal reaction mechanism and molecular design guidelines, it is crucial to observe the reaction field. However, X-ray structural analysis of fluids, particularly liquids, is challenging and remains largely unexplored. In this study, we identified the redox pair quinone/hydroquinone in sodium chloride solution under flow conditions.

The functional group discrimination of quinone/hydroquinone in aqueous NaCl solution was investigated by measuring carbon (C) *K*-edge X-ray absorption spectroscopy (XAS) spectra. The XAS measuremnt was conducted at BL3U of UVSOR equipped with a transmission liquid flow cell [2]. The energy range was set to 280–300 eV, with grating widths of 129 μm/61 μm (S_0/S_1). A 100 mM NaCl solution served as the standard (baseline) sample, to which 10 mM quinone and hydroquinone were added, respectively. The XAS spectra were analyzed based on Lambert-Beer's law as following:

$$\mu t = \ln \frac{I_0}{I_1} \quad (2)$$

where μ is absorption coefficients, t is sample thickness, and I_0 and I_1 represent the incident and transmitted light intensities, respectively. The XAS spectra of 10 mM quinone/hydroquinone in aqueous NaCl solution were applied baseline correction using those of the 100 mM NaCl solution.

The peaks observed at 285.9 eV and 293.0 eV correspond to C1s–π* of C=C and C1s–σ* of C=C resonances, respectively (Fig. 1), indicating their origin from the six-membered rings of quinone and hydroquinone. The intense peak at 288.4 eV corresponds to a C1s–π* of C=O resonance (Fig. 1), suggesting its association with the quinone functional group. These findings confirm the detection of quinone and hydroquinone signatures in the spectrum, demonstrating that their functional groups can be observed in the fluid phase.

Future studies will use electrochemical measurements and XAS analysis at BL3U to further clarify the redox mechanism in TECs with quinone-based systems. Solvation by redox species and solvents is crucial for TEC performance. To explore solvation effects, including hydrogen bonding, *operando* soft X-ray XAS will be conducted on solutions with dissolved redox species. We will examine how solvation influences redox behavior under different solvent compositions, acidity levels, and electrolyte concentrations. These insights will aid in optimizing thermochemical energy conversion systems.

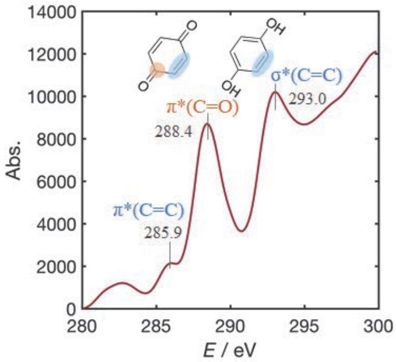

Fig. 1. C *K*-edge XAS spectra of 10 mM quinone/hydroquinone in 100 mM NaCl solution.

[1] H. Zhou *et al.*, Angew. Chem. Int. Ed. **62** (2023) e202213449.
[2] M. Nagasaka *et al.*, Chem. Lett. **50** (2021) 956.

BL3U

The Electronic States of 1-Methylimidazole in the Acetic Acid/1- Methylimidazole Mixture

Y. Horikawa[1], Y. Shiro[1] and M. Nagasaka[2]

[1]*Graduate School of Sciences and Technology for Innovation, Yamaguchi University, Yamaguchi 753-8512, Japan*
[2]*Institute for Molecular Science, Okazaki 444-8585, Japan*

We have observed the electronic structure of acetic acid and 1-methylimidazole (1-MI) molecules in their solution by soft X-ray spectroscopy to investigate the cause of the change in electrical conductivity of 1- MI/acetic acid mixtures [1, 2]. The electrical conductivity of the solutions changes drastically when the mixing ratio is changed, with maxima at mole fractions of acetic acid (χ_{AcO}) of 0.65 and 0.85. The results of previous analyses showed that the ionic content of acetic acid and 1-MI was maximum around $\chi_{\mathrm{AcO}} = 0.70$, while the ionic content decreased at concentrations of $\chi_{\mathrm{AcO}} = 0.85$. The reason why the electrical conductivity reaches a maximum value at the high acetic acid concentration, despite the decreasing amount of ions, is thought to be due not only to the diffusion of the ionic molecules (acetic acid ions and 1-MI ions) themselves, but also to the proton hopping between the acetic acid monomers and 1-MI or through acetic acid chain clusters. However, the previous measurements have only been made to analyze the molecular species in the mixed solution under steady-state conditions. Since an electric field is applied to the solution when electrical conduction occurs, the application of an electric field generates acetate ions that do not exist under steady-state conditions, and the possibility of an increase in electrical conductivity due to the diffusion of these ions was considered. In this experiment, the electronic state of acetic acid molecules in the mixed solution was observed in an electrochemical cell during the application of an electric field to confirm whether new ions were generated.

Soft X-ray absorption spectroscopy measurements at the O K-edge were performed using a transmission electrochemical cell for the solution. Fig. 1 and 2 show the absorption spectra of acetic acid at $\chi_{\mathrm{AcO}} = 0.70$ and 0.85 with and without the application of an electric field. As 1-MI dose not contain any oxygen atoms, the absorption spectra at the O K-edge only reflect information about the acetic acid molecules. Previous studies have shown that absorption peaks originating from the $\mathrm{O}_{\mathrm{C=O}}\ 1s \rightarrow \pi^*_{\mathrm{OCO}}$ and $\mathrm{O}_{\mathrm{OH}}\ 1s \rightarrow \pi^*_{\mathrm{OCO}}$ transitions appear at around 532.6 eV and 535 eV for molecules containing the COOH group. When the carboxy group ionises to COO^-, the two oxygen atoms become chemically equivalent, the positions of the two absorption peaks coincide and the second peak no longer appears [1]. In other words, as the acetate neutral molecules in solution become acetate ions, or as more acetate ions come close to the electrode surface, the intensity of the second peak is expected to decrease as the overall spectral shape. Figure 1 shows that the intensity of the second peak was 0.50 relative to the first peak without the application of an electric field, while the intensity of the second peak was 0.36 when an electric field of 0.7 V was applied, indicating a clear decrease in the intensity of the second peak. However, no effect of the electric field application was observed for the solution with mole fraction $\chi_{\mathrm{AcO}} = 0.85$, and it was experimentally confirmed that the application of the electric field caused the formation of acetate ions and that the increase in conductivity due to the increase in ion content was unlikely to have occurred. This result supports the idea that proton hopping is the cause of the increase in conductivity in the solution with mole fraction $\chi_{\mathrm{AcO}} \sim 0.85$.

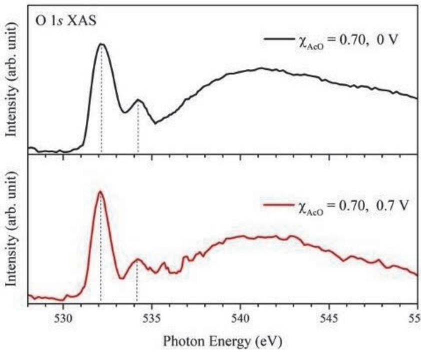

Fig. 1. O K-edge X-ray absorption spectra of acetic acid in the solution of $\chi_{\mathrm{AcO}} = 0.70$ with and without the application of an electric field.

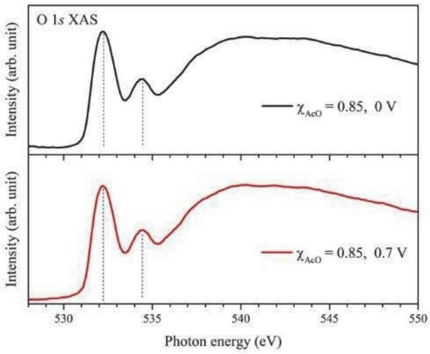

Fig. 2. O K-edge X-ray absorption spectra of acetic acid in the solution of $\chi_{\mathrm{AcO}} = 0.85$.

[1] N. Yoshimura *et al*., J. Phys. Chem. B **123** (2019) 1332.
[2] Y. Horikawa, M. Okazaki and M. Nagasaka, UVSOR Activity Report **51** (2023) 129.

Valence Fragmentation Dynamics of a Promising Low Global Warming Etching Gas CF_3CHCF_2

Tran T. Nguyen[1], T. Hayashi[1], H. Iwayama[2] and K. Ishikawa[1]
[1]*Nagoya University, Furo, Chikusa, Nagoya 464-8601, Japan*
[2]*UVSOR Synchrotron Facility, Institute for Molecular Science, Okazaki 444-8585, Japan*

The semiconductor industry faces significant challenges in etching high-aspect-ratio (HAR) structures for fabrication of 3D flash memory. Traditional reactive ion etching (RIE) processes struggle with issues on aspect-ratio-dependent etching and require precise control to maintain high-quality profiles [1]. Hydrofluorocarbons (HFCs) and perfluorocarbons (PFCs) gases are widely used in the HAR etching processes; despite their impact on global warming. To address these environmental concerns, the industry is exploring alternative gas chemistries and process techniques, including low-GWP fluorocarbons [2, 3].

In this study, we have investigated dissociation of C_3HF_5 by the PEPICO (Photo Electron Photo Ion CO incidence) technique using synchrotron radiation [4]. Identifying key dissociative fragments provided valuable insights for optimization of the etching results and minimization of their environmental impact.

The PEPICO experiments were conducted at the UVSOR facility in Japan, utilizing a 2.5 m off-plane Eagle-type monochromator to generate tunable vacuum ultraviolet (VUV) light in the energy range of 10-26 eV. C_3HF_5 gas was introduced into a high-vacuum chamber and irradiated with the VUV light. A time-of-flight mass spectrometer was employed to detect the resulting fragment ions. By analyzing the ion yield curves as a function of photon energy, appearance energies were determined, providing valuable insights into the dissociation pathways and energetics of C_3HF_5 molecules.

The dissociative photoionization of C_3HF_5 was systematically characterized across 10–26 eV using PEPICO spectroscopy. At 20 eV, the mass spectrum revealed dominant fragment ions such as $C_3HF_4^+$ and $C_3F_4^+$, alongside significant contributions from CF_3^+ and $C_2F_3^+$. The parent ion $C_3HF_5^+$ persisted at this energy, while weaker signals for smaller fragments (e.g., $C_3F_3^+$, $C_2F_2^+$) suggested secondary dissociation pathways. Figure 1 shows a breakdown diagram constructed from the ion yield curves. The breakdown diagram illustrated a photon-energy-dependent evolution in fragmentation: below 14 eV, the parent ion dominated (~80% abundance), with minor $C_3F_5^+$ (~20%) from H loss. Above 14 eV, a sharp transition occurred, with $C_3HF_4^+$ (F loss) and $C_3F_4^+$ (HF loss) emerging as primary products, collectively contributing ~54% of the ion yield by 15.5 eV. Notably, CF_3^+ became increasingly prominent above 15.2 eV, reaching ~25% abundance at 19–26 eV. Appearance energies (AEs), derived from ion yield thresholds, confirmed sequential fragmentation: the parent ion $C_3HF_5^+$ originated at 10.6 ± 0.06 eV, followed by $C_3F_5^+$ (10.7 ± 0.03 eV). $C_3HF_4^+$ exhibited dual pathways (13.7 ± 0.02 eV and 14.2 ± 0.04 eV), attributed to distinct C–F bond cleavages in CF_3 and CF_2 groups, while $C_3F_4^+$ showed similar dual thresholds (13.5 ± 0.02 eV and 14.5 ± 0.03 eV). Secondary fragments (e.g., CF^+) emerged above 17.9 eV but contributed minimally (<3%), underscoring the dominance of primary dissociation channels.

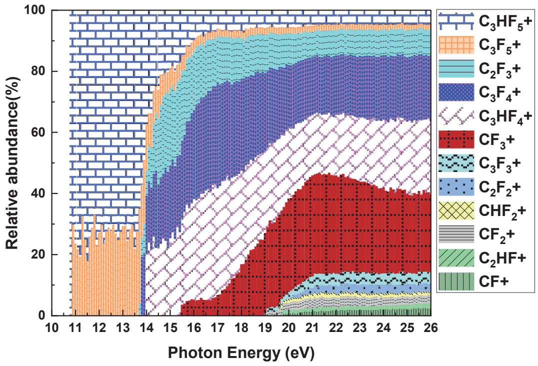

Fig. 1. Relative abundance curves of the fragment ions produced from the photoionization of C_3HF_5.

C_3HF_5 fragmentation balances fluorine-rich (CF_3^+, $C_3F_4^+$) and hydrogen-containing ($C_3HF_4^+$) species, critical for SiO_2/SiN etching. Fluorine radicals enhance SiO_2 etching, while hydrogen promotes polymer deposition for selectivity. Below 14 eV, minimal fragmentation favors parent ions; higher energies (>15 eV) optimize reactive fragment yields. The AE data align with plasma conditions (1–5 eV electron energies), suggesting C_3HF_5 efficiency in generating key etching species at low thresholds.

C_3HF_5 low-energy fragmentation pathways, characterized by PEPICO, validate its suitability as an eco-friendly etching gas. Optimizing photon energy controls reactive species, advancing high-aspect-ratio etching in semiconductor manufacturing. This study provides a framework for designing next-generation low-GWP etching gases.

[1] S. N. Hsiao *et al.*, Appl. Surf. Sci. **542** (2021) 148439.
[2] T. N. Tran *et al.*, Appl. Surf. Sci. **684** (2025) 161815.
[3] C. Abe *et al.*, Jpn. J. Appl. Phys. **63** (2024) 06SP10.
[4] T. N. Tran, *et al.*, Sci. Rep. **15** (2025) 9507.

BL4B

Dissociation Following Double Auger Decay of Xenon Difluoride Molecules

Y. Hikosaka[1]

[1]*Institute of Liberal Arts and Sciences, University of Toyama, Toyama 930-0194, Japan*

Molecular inner-shell photoionization is usually followed by Auger decay, where occasionally two Auger electrons are emitted, resulting in the formation of triply-charged molecular ions. These ions are energetically unstable due to Coulomb repulsion among the three positive charges and typically fragment immediately after their formation. In this study, we employed multielectron-ion coincidence spectroscopy with a magnetic bottle electron spectrometer equipped with ion detection [1,2] to explore the dissociation of triply-charged states in xenon difluoride (XeF_2) [3], a molecule characterized by weak bonding between the central rare-gas atom and fluorine ligands.

The double Auger decay processes of the XeF_2 4d core-hole state can be isolated through electron triple coincidence which includes a 4d photoelectron. Figure 1 (top) displays the energy sum of the two other electrons detected in coincidence with a $4d_{3/2}$ photoelectron as a function of the XeF_2^{3+} binding energy, determined by the relationship: (XeF_2^{3+} binding energy) = ($4d_{3/2}^{-1}$ binding energy) − (sum of two Auger electrons' energy). The ratio of double to single Auger decay in the $4d_{3/2}^{-1}$ state is determined to be 33% ± 5%, considering electron detection efficiency. The XeF_2^{3+} spectrum generally shows a gradual rise from around 60 eV without distinct peaks. The triple ionization threshold is about 4 eV lower than that of atomic Xe. The observed triple ionization threshold for double Auger decay can be less than the vertical triple ionization energy. This discrepancy arises because the double Auger decay involves sequential processes that pass through the intermediate XeF_2^{2+} states, which lie below the vertical triple ionization energy. The second Auger steps originating from these XeF_2^{2+} states occur outside the Franck–Condon region of neutral ground state XeF_2.

Four ion species, Xe^{2+}, Xe^{+}, F^{+}, and XeF^{2+}, were detected in coincidence with the triple electrons including a $4d_{3/2}$ photoelectron. The dissociation pathways potentially forming these four ions are $Xe^{2+} + F^{+} + F$, $Xe^{+} + 2F^{+}$, and $XeF^{2+} + F^{+}$. To elucidate the contributions from these pathways, XeF_2^{3+} spectra filtered with these four ion species were obtained from fourfold coincidences between the three electrons and an ion. Figure 1 illustrates the coincidence spectra. The spectra corresponding to Xe^{2+}, Xe^{+}, and XeF^{2+} delineate the contributions from the dissociation pathways of $Xe^{2+} + F^{+} + F$, $Xe^{+} + 2F^{+}$, and $XeF^{2+} + F^{+}$, respectively. The spectrum coincident with F^{+} includes contributions from all the dissociation pathways.

Dissociation to $XeF^{2+} + F^{+}$ occurs just above the triple ionization threshold and peaks around 60 eV. Dissociation to $Xe^{+} + 2F^{+}$ begins around 62 eV and reaches its maximum near 68 eV. The onset of dissociation to $Xe^{2+} + F^{+} + F$ is around 65 eV, with yield rapidly increasing as binding energy increases.

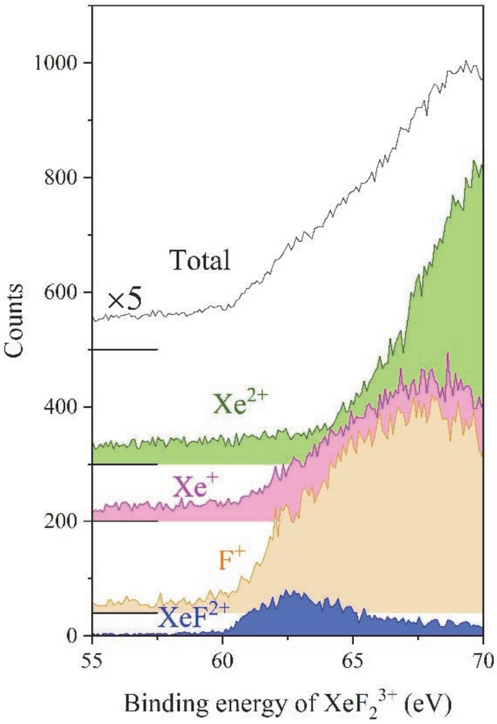

Fig. 1. Spectra of XeF_2^{3+} states selected by coincidence with fragment ions and the overall XeF_2^{3+} spectrum resulting from the $4d_{3/2}$ double Auger decay.

[1] Y. Hikosaka and E. Shigemasa, Int. J. Mass Spectrom. **439** (2019) 13.

[2] Y, Hikosaka, J. Electron Spectrosc. Relat. Phenom. **255** (2022) 147158.

[3] Y. Hikosaka, J. Chem. Phys. **160** (2024) 024304.

BL4B

X-ray Absorption Spectroscopy in Ferroelectric Nematic Liquid Crystals

F. Araoka[1], Y. Takanishi[2] and H. Iwayama[3]
[1]RIKEN Center for Emergent Matter Science, Hirosawa 2-1, Wako, Saitama 351-0198, Japan
[2]Department of Physics, Kyoto Prefectural University of Medicine,1-5,
Shimogamohangi-cho, Sakyo, Kyoto 606- 0823, Japan
[3]UVSOR Synchrotron Facility, Institute for Molecular Science, Okazaki 444-8585, Japan

Ferroelectric nematics (NF) are a new group of polar fluid liquid crystals (LCs), wherein liquid-like fluidity and ferroelectricity co-exist. Such polar ordering was first predicted by the well-known physicist, Max Born, in the early 20th century. However, it had not been realized for a long time until its coincident discoveries in 2017 by two independent groups [1,2]. There are many fascinating physical properties of NF such as huge apparent permittivity values, large spontaneous polarization, strong nonlinear optical effects, and so on. Because of both scientific curiosity and vast potential for applications, it has attracted broad attention in the field of liquid crystal sciences.

Recently, we reported cybotactic cluster formation stabilizing the NF phase in diastereomeric DIO mixtures [3]. In this case, anisotropy of the smectic clusters, estimated from small/wide angle X-ray analysis, clearly shows growth of clusters as temperature decreases. This suggests a possibility that the side-by-side interaction may be an important role in stabilizing the polar ordering of the NF phase. Motivated by this, we have tackled resonant X-ray scattering to resolve polar distribution at the nanoscopic scale. However, due to strong absorption at the carbon K-edge, yet it is too difficult to detect a clear scattering pattern. Thus, we need to seek the possibility to use other resonant conditions in other elements, such as fluorine, or oxygen, which also takes a part of the molecular structure of the NF molecule.

In this study, we performed X-ray absorption spectroscopy for the NF liquid crystal, DIO-C3 (Fig. 1, left). The carbon, fluorine, and oxygen K-edge absorption spectra were taken by scanning the photon energy of the soft X-ray irradiated on the sample sandwiched between two silicon nitride (SiN) membrane films (Fig. 1). The sample film was heated by a hot stage which equips input/output window to allow the X-ray beam to pass through. The transmitted X-ray was detected by a photodiode instead of a cooled CCD used in the scattering experiment, and the generated photocurrent was recorded by a signal counter.

Plotted in Fig. 2 are typical carbon K-edge absorption spectra taken using the soft X-ray beam at BL3U. The spectra show two signature peak regions; one appearing in the lowest photon energy region (285~6 eV) is corresponding to the π-electrons in the molecule, the other in the higher energy region (above~286.5eV) to the α-electrons. Interestingly, the latter shows notable peak shift at the phase transition temperature between the nematic, antiferroelectric meso- and NF phases, while the former shows only scarce change either in the peak position or shape. This means, the head-to-tail dipolar interaction, which affects the longitudinal α-orbitals, is stronger than the effect of the side-by-side attraction contributed from the π-π interaction, in the present system. Thus, this is different from our expectation, described in the above introduction part. Based on this result, we further conducted K-edge absorption measurements for fluorene and oxygen by using the soft X-ray available at BL4B. The result will be discussed with a theoretically computed spectrum obtained with a density functional theory (DFT). Further calculation and analysis are currently on-going.

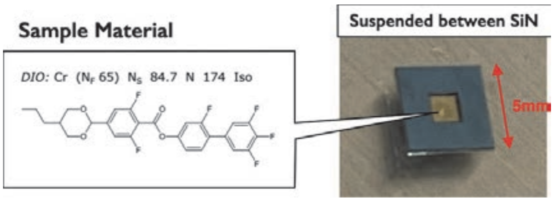

Fig. 1. Chemical structure of the NF molecule, DIO-C3 (Left), introduced between two SiN membrain films (Right).

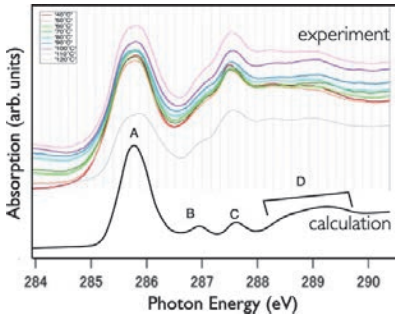

Fig. 2. Typical temperature-dependent absorption spectrum in the NF material, DIO-C3. The region A is corresponding to the π-orbital, and B, C and D are to the α-orbitals of alkyls and dioxanes.

[1] H. Nishikawa *et al.*, Adv. Mater. **29** (2017) 1702354.
[2] R. Mandle *et al.*, Chem. Eur. J. **23** (2017) 14554.
[3] H. Nishikawa *et al.*, Commun. Mater. **3** (2022) 89.

BL4B

Fragmentation Processes of 2-Iodothiophone in Doubly Charged States Studied by Multielectron-Ion Coincidence Spectroscopy

M. Fushitani[1], Y. Hikosaka[2], Y. Kimura[1] and A. Hishikawa[1,3]
[1]*Graduate School of Science, Nagoya University, Nagoya 464-8602, Japan*
[2]*Institute of Liberal Arts and Sciences, University of Toyama, Toyama 930-0194, Japan*
[3]*Research Center for Materials Science, Nagoya University, Nagoya 464-8602, Japan*

Breaking chemical bonds in a cyclic structure is an important step for ring-opening reactions. Among others, 2-iodothiophene (2-C_4H_3SI) is one of the prototype heterocyclic compounds which have been used to clarify the elementary processes in photoinduced ring-opening. Site-selective probing using ultrashort laser pulses in the extreme ultraviolet (EUV) and X-ray region is a promising method to directly capture details of the reaction [1, 2]. Such inner-shell probing often leads to the formation of highly charged states followed by ultrafast dissociation into different channels. Since the fragmentation pathways could be dependent on the initial geometry, it offers a unique approach to understand photoinduced processes in neutral states, including the ring-opening. Herein, we carried out multielectron-ion coincidence spectroscopy of I 4d inner-shell photoionization of 2-C_4H_3SI in the ground state to study the fragmentation processes after the core-hole decay.

Synchrotron radiation at 105 eV (single bunch mode) was used to ionize isolated 2-C_4H_3SI molecules and the produced electrons and ions were detected in coincidence by using a magnetic bottle type electron spectrometer with an ion-collecting electrodes [3,4].

The measured ion time-of-flight mass spectrum identifies formations of C_n (n = 1-4) hydrocarbons with a specific number of H atoms. Figure 1(a) shows I $4d_{5/2}$ Auger electron spectrum obtained in coincidence with I $4d_{5/2}$ photoelectrons and the parent 2-$C_4H_3SI^{2+}$ ions in the ground state while those with pairs of I^+ and the counterpart fragment ions are shown in Figs.1(b)-(i). All the Auger signals for the ion pairs appear in the lower energy region than the Auger peak at 33.1 eV of the parent 2-$C_4H_3SI^{2+}$, showing that these fragmentations take place mainly in electronically excited states in the doubly charged states. The Auger signals associated with the fragment ions can be classified into the 0-20 eV (Region I) and 20-32 eV (Region II) energy regions. It is found in Fig. 1(c) that $C_3H_3^+$ ions are selectively produced with I^+ ions in Region II while in Region I the fragment ions become C_3H^+ species instead of $C_3H_3^+$. On the other hand, C_4 and C_2 hydrocarbons in Figs. 1(b) and (d), appear as C_4H^+ and $C_2H_2^+$ ions, both of which are identified in Region I only. This suggests that a three-body fragmentation, 2-$C_4H_3SI^{2+} \rightarrow C_3H_3^+ + I^+ + CS$, is a main channel to break the ring structure in Region II.

Auger signals for the fragment ions containing the S atom in Figs. 1(e)-(i), it turns out that $C_3H_3S^+$, C_2HS^+, CHS^+, and S^+ ions with a fixed number of H atoms are dominant products as the I^+ counterpart while for $C_4H_nS^+$ (n = 0-3) ions the number of the H atom depends on the Auger electron energies. It is noted that the Auger peak at 30.4 eV for the (I^+, $C_4H_3S^+$) ion in Fig. 1(e) exhibits much narrower spectral width compared to the other Auger peaks. This indicates that the $C_4H_3S^+$ moiety could keep its cyclic structure after the C-I bond fission, 2-$C_4H_3SI^{2+} \rightarrow C_4H_3S^+ + I^+$.

The present study reveals which electronic energy region of 2-$C_4H_3SI^{2+}$ preferentially produces specific fragment pair of ions with the characteristic numbers of C and H atoms, providing crucial information on the ring-opening processes.

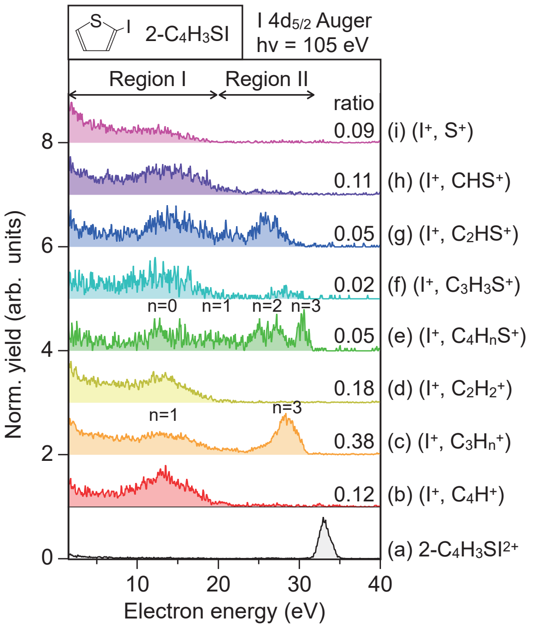

Fig. 1. Auger electron spectra of 2-iodothiophene by I $4d_{5/2}$ inner-shell photoionization at 105 eV, detected in coincidence with (a) 2-$C_4H_3SI^{2+}$, (b) (I^+, C_4H^+), (c) (I^+, $C_3H_n^+$(n = 1,3)), (d) (I^+, $C_2H_2^+$), (e) (I^+, $C_4H_nS^+$(n = 0-3)), (f) (I^+, $C_3H_3S^+$), (g) (I^+, C_2HS^+), (h) (I^+, CHS^+), and (i) (I^+, S^+) ions. The values for traces (b)-(i) represent the relative yield among these ion pairs.

[1] B. W. Toulson *et al.*, J. Chem. Phys. **159** (2023) 034304.
[2] W. O. Razmus *et al.*, Phys. Chem. Chem. Phys. **26** (2024) 12725.
[3] Y. Hikosaka, J. Electron Spectrosc. Rel. Phenom. **255** (2022) 147158.
[4] M. Fushitani *et al.*, J. Chem. Phys. **160** (2024) 174307.

BL5B

Development of the Fast Camera System for High-Precision Photoelectron Imaging

H. Kohguchi[1], Y. Hikosaka[2], T Kaneyasu[3], S. Wada[1], K. Shimizu[4],
M. Katoh[1,4] and Y-I. Suzuki[5]
[1]Graduate School of Advanced Science and Engineering, Hiroshima University,
Higashi-Hiroshima 739-8526, Japan
[2]Institute of Liberal Arts and Sciences, University of Toyama, Toyama 930-0194, Japan
[3]SAGA Light Source, Tosu 841-0005, Japan
[4]UVSOR Synchrotron Facility, Institute for Molecular Science, Okazaki 444-8585, Japan
[5]School of Medical Technology, Health Sciences University of Hokkaido, Tobetsu 061-0293, Japan

Recent development of photoelectron circular dichroism (PECD) studies significantly relies on photoelectron VMI (Velocity Map Imaging) measurements as well as circularly polarized radiation generated with undular light sources, which is especially advantageous for one-photon ionization in the vicinity of the molecular photoionization threshold region. On the other hand, multi-photon ionization based on laser-based photoionization has also been subject to the PECD research. Molecular electronic chirality can be further understood in comparison with the PECD data of one-photon and multi-photon ionization.[1, 2]

We have so far used the camera system of the VMI apparatus common for laser and synchrotron light sources, although the synchrotron measurements and laser-based measurements were executed in UVSOR and the Hiroshima University laboratory, respectively. Besides the wavelength regions, the critical difference of the UVSOR beam line and the pulsed laser system regarding our PECD study lies in the repetition rate and the photoelectron count rate. The pseudo-continuous radiation provided by the UVSOR beam line can generate photoelectrons with more than 100 kcps (counts per second) under our experimental conditions. The pulsed laser system runs in a 10 Hz repetition rate, where a single laser shot provides less than 100 photoelectrons corresponding to the 10 cps. The photoelectron count rate should be reduced to a rate so low that the light spots due to a single photoelectron arrival at the detector do not overlap each other, otherwise, the accurate photoelectron distributions are not obtained. The higher count rate, ensuring the better signal statistics, is especially critical in PECD measurements, where the difference of independently measured image data is analyzed. In place of the conventional frame-transfer type camera (1000 x 1000 pixels, 33 frames/s rate), which was matched with the low repetition pulsed laser, we introduced an event-driven type camera, whose nominal signal transfer rate is sufficiently fast to fully capture the signals provided by the UVSOR beam line.

The performance of the event-driven camera was examined with the BL5B beam line. The camera equipped with the VMI apparatus was linked with the local Ethernet LAN to store the event data. The sensitivity, temporal response, and transfer rate were methyl oxirane at 120 nm (Fig. 1). Although the photoelectron spot images were overlapped in a frame-type camera display (Fig. 1(a)-(c)), the stored event data were confirmed to be isolated from each other by the fast time resolution of 1 μs (Fig. 1(d)). We developed a program code to recover the image data from the event data. The results indicated the good linearity of the image intensity up to the photoelectron count rate of 500 kcps, which is nearly the upper limit of the detector damage.

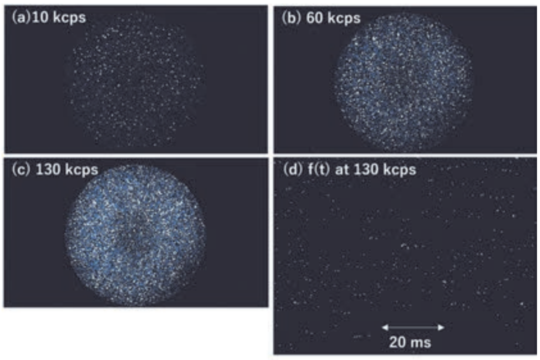

Fig. 1. Photoelectron image data measured with the event-driven camera equipped with the synchrotron radiation light source. The light spots due to photoelectron hitting on the imaging detector (1280 x 720 pixel size) accumulated in 33 camera frames are shown at a photoelectron count rate of (a) 10 kcps, (b) 60 kcps, and (c) 130 kcps. A time profile of the event-camera output in a particular pixel column of (c) is shown in (d).

[1] H. Kohguchi *et al,*, UVSOR Activity Report **50** (2023) 138.
[2] H. Kohguchi *et al.*, UVSOR Activity Report **50** (2022) 136.

BL3B, 5B, 7B

Delayed Fragmentation of Ethanol Molecules Induced by Photoionization

T. Nakao[1], T. Kaneyasu[2,3], H. Iwayama[3], T. Yanagawaya[4] and T. Majima[1]
[1]Department of Nuclear Engineering, Kyoto University, Kyoto 615-8540, Japan
[2]SAGA Light Source, Tosu 841-0005, Japan
[3]Institute for Molecular Science, Okazaki 444-8585, Japan
[4]Faculty of Engineering, Kyoto University, Kyoto 606-8501, Japan

Characterizing the intermediate states of ionized and excited molecules before dissociation is a key to understanding the fragmentation mechanism. Valuable insights into the intermediate states can be obtained through an analysis of the delayed fragmentation processes. We investigated the delayed fragmentation from various singly charged intermediate ions by coincidence measurement of product ions and neutral fragments using time-of-flight (TOF) mass spectrometry [1]. We have observed delayed fragmentation from nucleobase (adenine, guanine, cytosine, thymine, and uracil) and alcohol (ethanol, 1-propanol, and 2-propanol) molecules induced by MeV-energy fast ion collisions so far. The results indicated that large degrees of freedom are essential to the delayed fragmentation from singly charged intermediate ions. However, due to the complexity of fast-ion-induced processes, the characteristics of intermediate ions are not fully understood. In this study, we carried out photoionization experiments in the vacuum ultraviolet (VUV) region.

The experiments were performed at the bending magnet beamlines BL3B, BL5B, and BL7B of the UVSOR III facility. The main measurement was performed at BL7B after the test experiments at BL3B and BL5B. Monochromatic VUV light in the range of 13.0–23.0 eV photon energy was delivered to the experimental apparatus equipped with a TOF mass spectrometer. Effusive molecular beam of ethanol was used as the target. Fragments were detected with a microchannel plate (MCP) detector and recorded in event-by-event mode by a multichannel scaler.

Figure 1 shows TOF correlation spectra of the two fragments measured at a photon energy of 18.0 eV. Delayed fragmentation processes from singly charged intermediate ions are clearly visible as long diagonal tails extend from spots. Note that in this experiment neutral fragments are detectable in the delayed fragmentation, although the detection efficiency of them is relatively low due to the insufficient impact energy to be detected by the MCP. This is because they are generated during the extraction from the ionization region to the drift tube.

The delayed fragmentation channels were identified by comparing the experimental results and the calculated curves shown on the right side of Fig.1. The numbers in the figure correspond to the following channels: (1) $C_2H_5O^+ \rightarrow CHO^+ + CH_4$, (2) $C_2H_5O^+ \rightarrow C_2H_3^+ + H_2O$, (3) $C_2H_5O^+ \rightarrow H_3O^+ + C_2H_2$, and (4) $C_2H_3O^+ \rightarrow CH_3^+ + CO$. These pathways are the same as the MeV-energy fast ion collisions. The delayed fragmentation events at the tails in Fig. 1 indicate that the intermediate ions remain undissociated for submicroseconds.

The photon energy dependence of each delayed fragmentation channel was investigated, except for channel 2 because of the low statistics. Channel 1 and channel 3 show a similar energy dependence: the tail appears rapidly at about 14 eV. For channel 3, the tail appears gradually at about 17 eV. Since the vertical ionization potential of ethanol is about 10.6 eV [2], the results indicate that these delayed fragmentation processes can be induced with an internal energy of a few eV. These threshold energies are consistent with the preliminary results of the quantum chemical calculations we performed.

The photon energy dependence of the decay curve of the intermediate ion $C_2H_5O^+$ on channel 3 was also obtained by analyzing TOF spectra. The decay curve shows a $1/t$ dependence above 15 eV. This result indicates that the internal energy transferred to vibrational excitation is the key to delayed fragmentation.

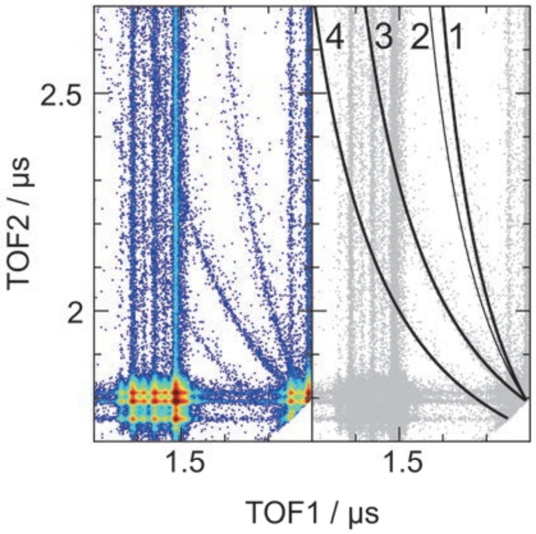

Fig. 1. TOF correlation spectra at 18.0 eV. Four delayed fragmentation channels were determined by comparing the experimental results (left) and the calculated curves (right). The numbers correspond to each dissociation channel.

[1] T. Nakao *et al.*, J. Chem. Phys. **161** (2024) 054302.
[2] P. Linusson *et al.*, Phys. Rev. A **80** (2009) 032516.

BL7B

High-Resolution Photoelectron Spectroscopy of Functional Compounds with High Melting Points

H. Kohguchi[1], Y. Hikosaka[2], T Kaneyasu[3], S. Wada[1], K. Shimizu[4], M. Katoh[1,4] and Y-I. Suzuki[5]
[1]*Graduate School of Advanced Science and Engineering, Hiroshima University,*
Higashi-Hiroshima 739-8526, Japan
[2]*Institute of Liberal Arts and Sciences, University of Toyama, Toyama 930-0194, Japan*
[3]*SAGA Light Source, Tosu 841-0005, Japan*
[4]*UVSOR Synchrotron Facility, Institute for Molecular Science, Okazaki 444-8585, Japan*
[5]*School of Medical Technology, Health Sciences University of Hokkaido, Tobetsu 061-0293, Japan*

Photoelectron circular dichroism (PECD) has been investigated with a photoelectron imaging apparatus based on the velocity-mapping imaging (VMI) methodology. The targets of the PECD study have been mostly limited to gaseous or volatile samples since photoelectron imaging relies on electron detection under high vacuum conditions. Chiral compounds in solid form are not subjects of the PECD study, although much more chiral species with novel chirality are stable than gaseous and volatile liquid samples. We have developed the VMI photoelectron imaging apparatus for PECD measurement, providing high-quality PECD data for gaseous chiral molecules [1]. Application of the VMI apparatus to solid chiral samples requires the generation of the molecular beam by heating solid samples. The molecular beam intensity was found to be much weaker than that of the gaseous beams in our previous studies [2]. Thus, efficient photoelectron data collection is a key to PECD measurements of solid chiral species as well as intense beam sources with a heat nozzle.

A photoelectron count rate for gaseous samples is typically several hundred kcps under our experimental conditions. Although the count rate can be increased by more than 1000 kcps, our previous image detection system could only acquire less than 100 kcps photoelectrons because of the slow frame transfer rate (33 frames/s) of the camera system. In the present measurement with the BL7B beamline, we have adopted an event-driven camera to a spot image of a photoelectron arrival on the phosphor screen, whose nominal response time is potentially one microsecond.

We examined the sensitivity and operative limitation of the event-driven camera for the actual PECD measurement conditions but the Ar sample was used for evaluation. The results of photoelectron imaging of Ar at 76 nm photoionization are shown in Fig. 1. The photoelectron image obtained with the conventional frame camera exhibited noticeable background noise outside of photoelectron scattering distribution (Fig. 1a). The background, which originated from the analog recording, was found to be critical for in our previous PECD study because difference image data between right- and left circularly polarization ionization is heavily affected by preceding signal normalization. It is noted that the electron background, which originates from the photoionization of the imperfectly evacuated samples in the vacuum chamber subtraction, is not problematic in image subtraction. The image data captured with the event-driven camera at various count rates (Fig. 1b-1d) indicated that no photoelectron arrival position on the phosphor screen was lost up to the count rate of 180 kcps. The photoelectron spectra and the angular distributions with 5 kcps, 40 kcps, and 180 kcps are identical other than the signal statistics. Application of the event-driven camera to the photoelectron imaging with synchrotron radiation, especially to the image subtraction, is thus confirmed.

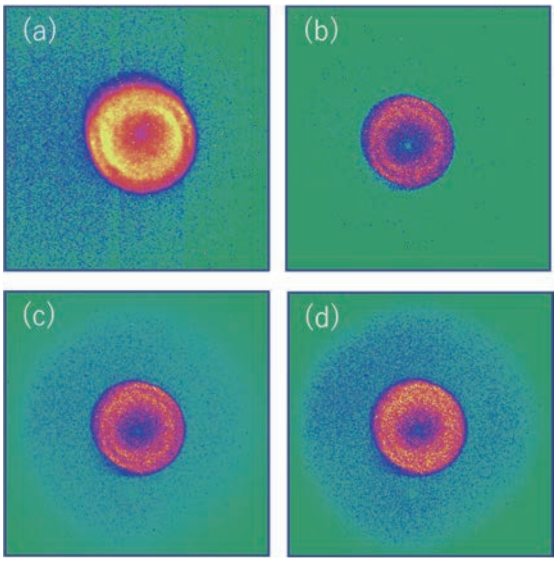

Fig. 1. Photoelectron scattering images of Ar at 76 nm photoionization with (a) the frame-camera (conventional) and (b)–(d) the event-driven camera. The electron count rate is (b) 5 kcps, (c) 40 kcps and (d) 180 kcps. The outside of the double-ring image is especially emphasized to display the background level.

[1] H. Kohguchi *et al,*, UVSOR Activity Report **50** (2023) 138.

UVSOR User 11

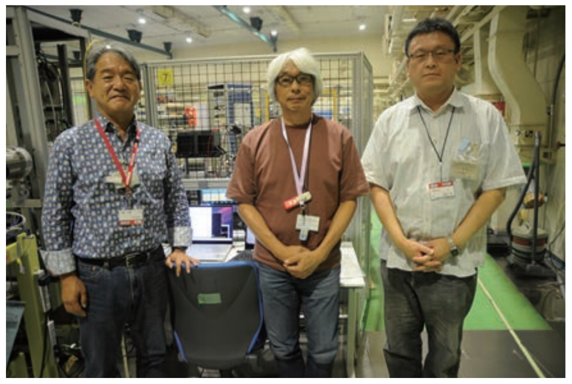

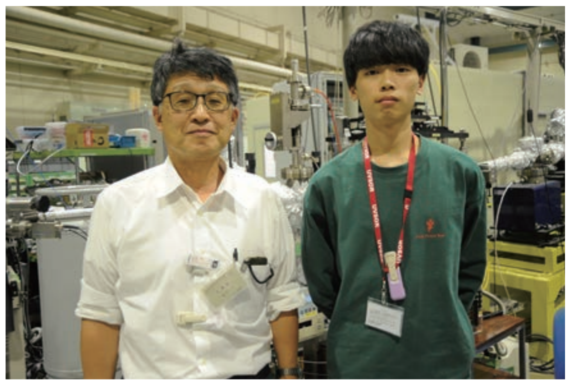

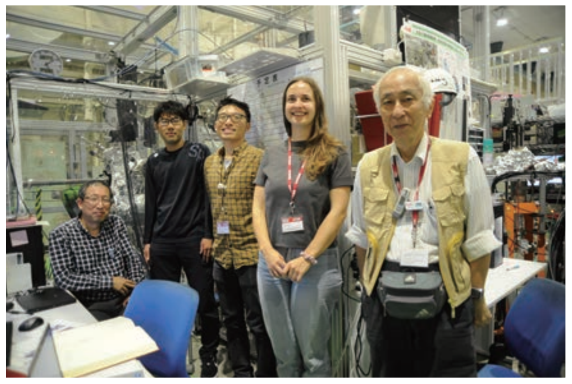

UVSOR User 12

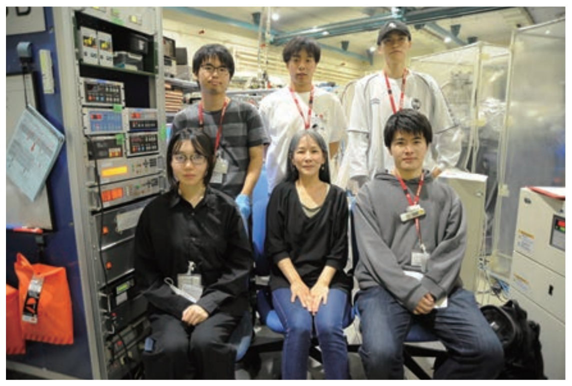

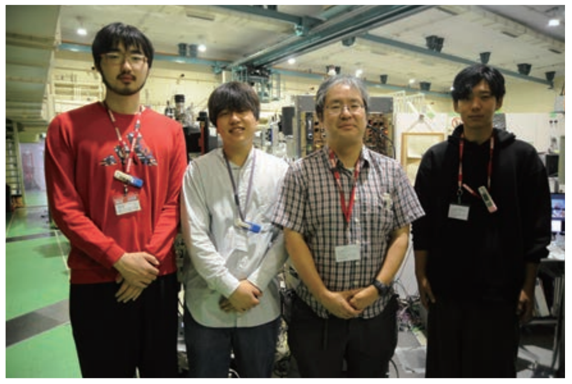

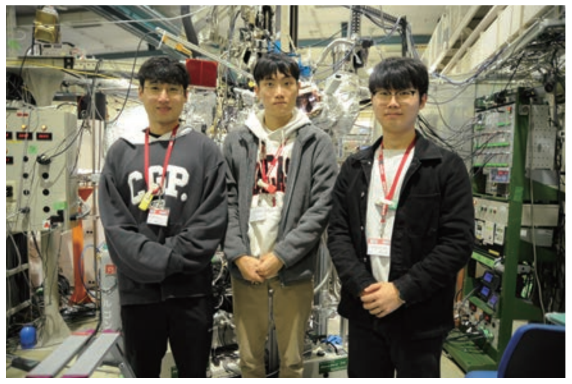

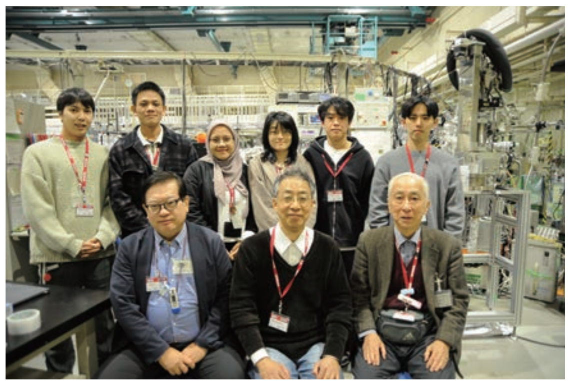

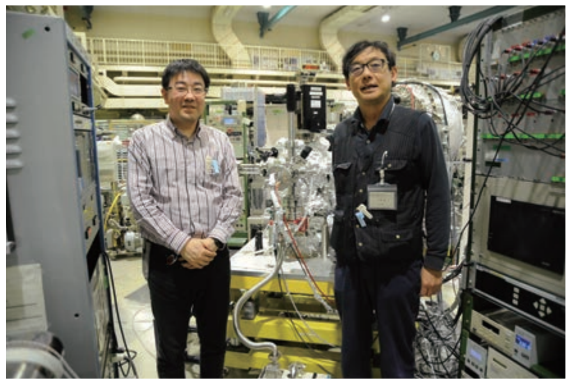

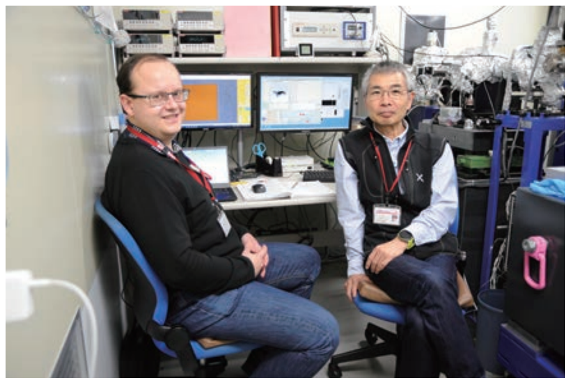

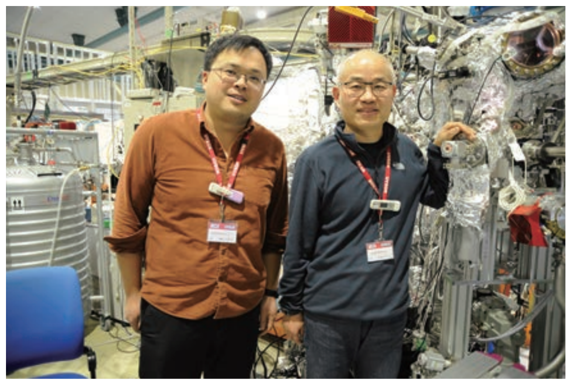

III-4

Surface,
Interface and
Thin Films

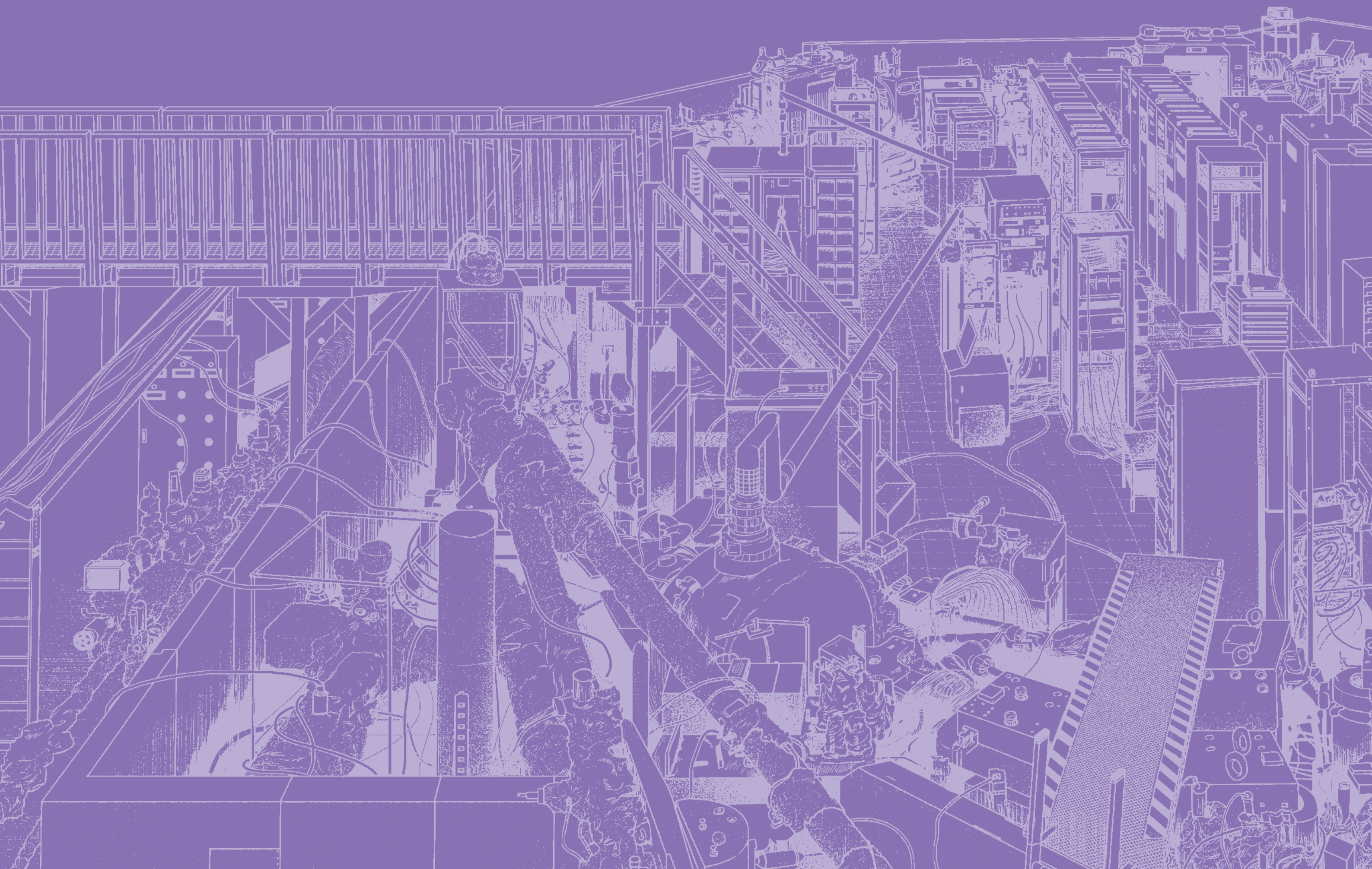

BL2A

Analysis of Electronic Structure of P3HT/ MoO_x Interface by Soft X-ray Absorption Spectroscopy

K. K. Okudaira[1], S. Yoshioka [2] and E. Kobayashi [3]
[1]Graduate School of Science and Engineering, Chiba University, 1-33 Yayoi-cho Inage-ku,
Chiba 263-8522, Japan
[2]Graduate School of Engineering, Kyushu University, 744 Motooka Nishi-ku Fukuoka 819-0395 Japan
[3]Kyushu Synchrotron Light Research Center, 8-7 Yayoigaoka, Tosu, Saga 841-0005, Japan
1-33 Yayoi-cho Inage-ku, Chiba 263-8522, Japan

Organic thin-film solar cells are advantageous due to their low manufacturing costs; however, their low power conversion efficiency remains a challenge. One approach to improve efficiency is the introduction of metal oxides like MoO_3 as hole extraction layers or electron extraction layers between the organic layer and the two electrodes[1,2]. Furthermore, doping metal oxides to control their valence band structures and achieve appropriate energy alignment with the HOMO and LUMO of organic semiconductor layers is expected to lead to high-efficiency organic thin-film solar cells. However, when doped metal oxides are stacked with organic semiconductors, the formation of new interfacial electronic states is considered.

This study investigates the electronic states at the interface between molybdenum oxide, known as a hole extraction layer, and the organic film using soft X-ray absorption spectroscopy. To obtain insights into the buried interface, measurements utilizing the partial fluorescence yield method in soft X-ray absorption spectroscopy are effective. However, there are very few examples of incorporating such techniques into the development of organic thin-film solar cells

The sample are thin molybdenum oxide film fabricated on silicon using the RF magnetron sputtering method. One of the films was cleaned with neutral detergent, distilled water, acetone and UV ozone. P3HT was dissolved in chlorobenzene and deposited onto the thin film by spin coating. NEXAFS spectra of the MoO_x film using both total electron yield (TEY) and partial fluorescence yield (PFY) modes were measured at the beamline 2A of the UVSOR in the Institute of Molecular Science. For TEY, the drain current from the sample was measured. For PFY, fluorescence X-rays were collected using an energy dispersible silicon drift detector (SDD). All experiments were performed at room temperature.

Figure 1 shows the NEXAFS spectrum of P3HT/ MoO_x/Si thin film in PFY mode. The observed spectrum is considered to consist of two components, Peak A and Peak B[3]. Adsorbing P3HT onto the MoOx thin film resulted in Peak A becoming more intense than Peak B. This suggests that electronic states were generated at the interface between the organic film and the oxide film. Furthermore, when P3HT was adsorbed onto a cleaned thin film, the intensity ratio changed, indicating that surface treatment of the oxide film alters the interfacial electronic states. This finding implies the possibility of controlling interfacial electronic states.

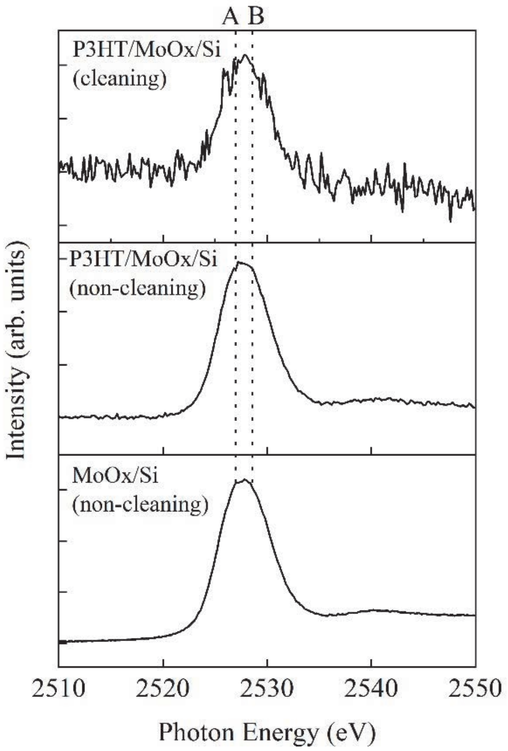

Fig. 1. Mo L-edge NEXAFS spectra of P3HT/MoO_x/Si thin film in PFY mode.

[1] D. W. Zhao *et al.*, Appl. Phys. Lett. **95** (2009) 153304.
[2] X. Hu, *et al.*, J. Phys. Chem. C **118** (2014) 9930.
[3] A. Svyazhin *et al.*, Inorg. Chem. **61** (2022) 869.

BL3U

Oxygen K-Edge XAS-Evidenced Specific Hydrogen-Bonded Water inside Hydrophobic Single-Walled Carbon Nanotubes

Y. Kawamata[1], H. Otsuka[1], M. Nagasaka[2] and K. Kaneko[1,3]
[1]*Research Initiative for Supra-Materials Shinshu University, Nagano 380-8553, Japan*
[2]*Institute for Molecular Science, Okazaki 444-8585, Japan*
[3]*Institute for Aqua Regeneration Shinshu University, Nagano 380-8553, Japan*

Understanding the properties of hydrogen-bonded water molecules around functional groups on nanopores of hydrophobic carbon surfaces or biological substances is crucial. Although presence of only trace amounts of water molecules around functional groups on the hydrophobic surfaces are presumed, their effects should dominate the important phenomena such as water/ion permeation and energy storage in the electrical double layer [1, 2]. The direct observation of the hydrogen-bonded structure of only slight amount of water molecules inside nanopores is very challenging with conventional diffraction technique or Raman/IR spectroscopy because the background of solid hinder the signals of trace amount of water molecules. However, X-ray absorption spectroscopy (XAS) is a powerful tool for investigating the hydrogen-bonded structure of only a tiny water molecules inside nanopores, as it selectively detects specific atoms of interest [3]. In this study, we applied XAS to water molecules inside highly hydrophobic single-walled carbon nanotubes (SWCNTs). SWCNT has well-defined hydrophobic cylindrical nanopores, enabling to investigate the interactions between trace amount of water molecules and isolated functional groups on the graphene wall.

SWCNT with a diameter of 2 nm were purified by heating at 2073 K in vacuo for 3 hours, removing most of impurities. End-caps were removed by air oxidation at 823 K, enabling water molecules to access the SWCNT internal pores. The SWCNTs were dispersed in EtOH at a concentration of 0.01 wt%, and the dispersion was casted onto a SiN membrane with a thickness of 100 nm. EtOH were removed by vacuum evaporation at room temperature, producing a thin SWCNTs film with a thickness of 3 μm on the SiN membrane. The SWCNTs film on the SiN were placed in a XAS measurement chamber. O K-edge XAS spectrum of SWCNTs were measured in the range of 525 – 550 eV under water vapor introduced into the chamber via He bubbling of pure water.

Figure 1 shows the water adsorption isotherm of the SWCNTs. At the relative pressure (P/P_0) below 0.65, the water adsorbed amount is very small, suggesting the water exists as isolated water clusters inside SWCNT [4]. We carried out XAS measurement at $P/P_0 = 0.5$, where the water adsorbed amount is 20 mg g^{-1}, being only 4 % of the fractional filling against saturated adsorbed amount.

Figure 2 shows Oxygen K-edge XAS spectrum of SWCNTs. At $P/P_0 = 0$, two peaks are observed. A sharp peak at 532 eV and a broad peak at 539 eV are assigned to C=O and C-O, respectively. At $P/P_0 = 0.5$, the sharp peak at 532 eV broadens, evidencing the interactions between C=O and water molecules via hydrogen bonding. Furthermore, the intensity of the broad peak increases in the range of 536 – 542 eV due to the presence of water clusters. The increase of the broad peak intensity suggests that the intermolecular distance of water molecules fluctuates from the equilibrium distances. This is the direct evidence on water-surface oxygen groups interactions inside highly hydrophobic carbon spaces.

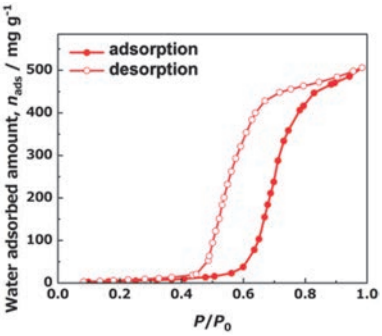

Fig. 1. Water adsorption isotherm of SWCNT at 298 K.

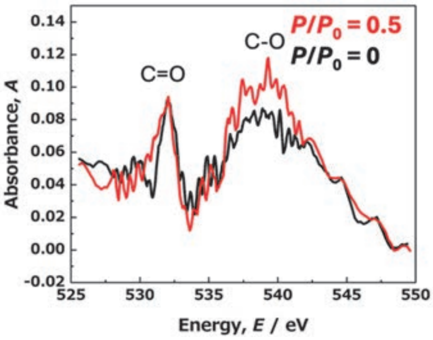

Fig. 2. O K-edge XAS spectrum of SWCNT.

[1] D. A. Doyle *et al.*, Science **280** (1998) 69.
[2] P. Simon and Y. Gogotsi, Nat. Mater. **19** (2020) 1151.
[3] T. Fransson *et al.*, Chem. Rev. **116** (2016) 7551.
[4] T. Ohba, H. Kanoh and K. Kaneko, J. Am. Chem. Soc. **126** (2004) 1560.

BL3U

Ionic Layers at the Electrode Interface of Ionic Liquids Studied Using Interface-Selective Soft X-ray Absorption Spectroscopy

K. Yamaguchi[1], T. Furuya[1], M. Nagasaka[2] and N. Nishi[1]
[1]*Graduate School of Engineering, Kyoto University, Kyoto 615-8510, Japan*
[2]*Institute for Molecular Science, Okazaki 444-8585, Japan*

Ionic liquids (ILs), which are entirely composed of cations and anions, are appealing materials as electrolytes for energy devices. In such devices, the electrochemical interface between ILs and electrodes is an electrochemical reaction field that strongly influences the local reaction rate and thereby the net ones such as charging speed for batteries. Thus, it is of crucial importance to study, and further control, the interfacial structure of ILs at the electrode interface. In the present study, we adopted soft X-ray absorption spectroscopy (XAS) to reveal the interfacial structure of ILs at the electrode interface in an interface-selective manner [1].

1-Butyl-1-methylpyrrolidinium bis(fluorosulfonyl) amide ([C4mpy$^+$][FSA$^-$]) that contained Li$^+$[FSA$^-$] at a concentration of 0.5 M was used as IL [2]. *In-situ* XAS measurements for the IL/electrode interface were performed at BL3U at UVSOR-III, by using an electrochemical liquid flow cell [1]. The IL was sandwiched with two SiC membranes in the He-filled chamber and XA spectra were measured in transmission mode for the nitrogen, oxygen, and fluorine K-edge regions. The photon energy was calibrated by the first peak in the nitrogen or oxygen K-edge region for a ProLINE polymer thin film in a vacuum chamber [3]. The thickness of the IL film was controlled with the He pressure [4]. The platinum film deposited at the inner surface of one of the two SiC membranes was used as the working electrode. Pt wires, as the quasi-reference and counter electrodes, were located aside the film region inside the electrochemical cell. The potential of the working electrode with respect to the quasi-reference electrode was controlled using a potentiostat.

Figure 1 shows fluorine K-edge XA spectra for the IL/platinum interface at three different potentials. At 0 V (black dashed line), where no IL-ion accumulation/depletion occurs at the interface and therefore the interfacial structure corresponds to the bulk one, double sharp peaks were discernible at the absorption edge around 688 and 692 eV, both of which originate from FSA$^-$, according to a prediction using the GSCF3 code for inner-shell excitation [5]. When negative potentials were applied at the IL/platinum interface, the XA spectra (Fig.1, blue and green lines) showed three potential-dependent features. First, the lowest-energy peak decreased in intensity and blue-shifted. Second, the second lowest-energy peak was broadened. Third, the intensity at the high-energy region became higher. These three features demonstrate that the present XAS measurements in transmission mode with a nm-scale thin film setup sensitively detect the interfacial structure, which is different from the bulk one and is also potential-dependent. Oxygen and nitrogen K-edge XA spectra (data not shown) exhibited similar potential-dependent features, although the behavior for the lowest-energy peak was element-dependent. Furthermore, the oxygen K-edge spectra at negative potentials showed an evolution of pre-edge peak, which clearly indicates the formation of solid electrolyte interphase (SEI). SEI, which is indispensable for a stable battery anode and therefore has been extensively studied, is generally difficult to investigate in an *in-situ* manner, illustrating the powerfulness of the present *in-situ* XAS method. The SEI formation is highly likely to cause the intensity increases at the high-energy region observed for all three elements, as exemplified in Fig.1 for the fluorine case.

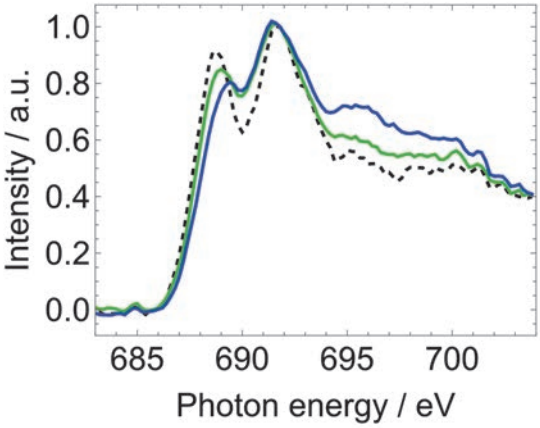

Fig. 1. Fluorine K-edge XA spectra for the IL/platinum interface at 0 (black dashed), −2 (green), and −2.5 V (blue).

[1] M. Nagasaka *et al.*, Rev. Sci. Instrum. **85** (2014) 104105.
[2] S. Kato *et al.*, J. Electrochem. Soc. **169** (2022) 076509.
[3] M. Nagasaka *et al.*, J. Electron Spectrosc. Relat. Phenom. **224** (2018) 93.
[4] M. Nagasaka *et al.*, J. Electron Spectrosc. Relat. Phenom. **117** (2010) 130.
[5] N. Kosugi, Theor. Chim. Acta **72** (1987) 149.

BL3U

Cation-Specific Effects on Interfacial Water Structure Around Silica Nanoparticles Probed by O K-edge NEXAFS

X.Kong[1], N. Faure[1], M. Nagasaka[2] and Z. Abbas[1]
[1]*Department of Chemistry and Molecular Biology, Atmospheric Science, University of Gothenburg,*
SE-413 90 Gothenburg, Sweden
[2]*UVSOR Synchrotron, Institute for Molecular Science, Okazaki 444-8585, Japan*

Understanding the interfacial water structure at the nanoparticle-electrolyte interface is essential for advancing applications in catalysis, separation science, environmental remediation, and biomedicine. Silica nanoparticles (SiO_2), which develop surface charge through silanol group deprotonation, offer a model system for such studies. The organization of water around these charged particles—strongly influenced by particle size, shape, concentration, and particularly the type of counterion, remains poorly resolved, especially at the nanoscale [1].

In this beamtime at the BL3U beamline (UVSOR-III), we investigated cation-specific effects on interfacial water structures in colloidal dispersions of silica nanoparticles using oxygen K-edge Near Edge X-ray Absorption Fine Structure (NEXAFS) spectroscopy. In this preliminary study, nanoparticles (8-10 nm) were suspended in aqueous media with Na^+ as the stabilizing counterion at various concentrations (10-30 wt%). The experiment builds on recent studies showing interfacial water perturbations induced by nanodiamond surfaces [2] and is a precursor to planned systematic studies involving a full alkali series (Li^+, Na^+, K^+, Rb^+, Cs^+).

Measurements were performed in a liquid flow cell configuration, where liquid samples were sandwiched between two 100 nm thick Si_3N_4 membranes (window area: 2 × 2 mm²) with 100 μm Teflon spacers. Liquid exchange was achieved in situ via tubing pump, with temperature controlled at ~25°C. A 200 × 200 μm² beam spot was selected to optimize photon flux.

Oxygen K-edge NEXAFS spectra were collected and analyzed to investigate the characteristic spectral features corresponding to different water environments: the pre-edge (~535 eV), main-edge (~537 eV), and post-edge (~540 eV), as shown in Fig. 1. These features provide insight into the electronic structure and hydrogen bonding states of water molecules near nanoparticle surfaces. To correct for potential variations in liquid film thickness and to enable direct comparison across different conditions, the spectra were normalized either to the intensity at the pre-edge or post-edge region.

In this study, the SiO_2 nanoparticle concentration was fixed at 15 wt%, and the key variable was the type of dissolved cation—Li^+, Na^+, K^+, Cs^+, NH_4^+, as well as multivalent anion-containing salts like Na_2SO_4 and K_2SO_4. Despite the constant nanoparticle loading, the post-edge intensities exhibited noticeable variation depending on the cation present. In general, larger or less strongly hydrated cations (e.g., Cs^+, NH_4^+) led to enhanced post-edge features, which suggests a more ordered or polarized water structure at the nanoparticle interface. This may be attributed to differences in ion hydration behavior and their impact on the arrangement of water molecules in the electrical double layer.

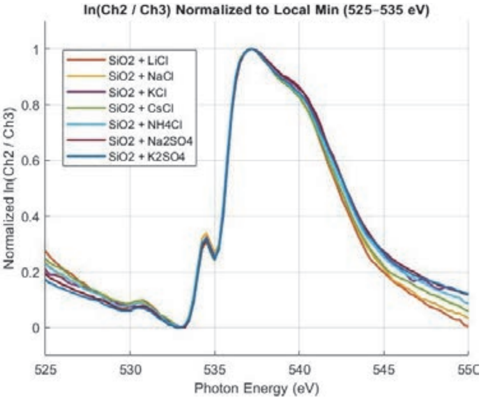

Fig. 1. O K-edge NEXAFS spectra of 15 wt% SiO_2 nanoparticle solutions in the presence of different salts: LiCl, NaCl, KCl, CsCl, NH_4Cl, Na_2SO_4, and K_2SO_4. All measurements were conducted at 25 °C. The spectra have been normalized both to the post-edge maximum and the pre-edge feature to account for differences in sample thickness and to facilitate comparison of spectral features across different ionic conditions.

Conversely, the pre-edge intensity—which reflects contributions from distorted or weakly hydrogen-bonded water species—was found to decrease for certain salts, indicating that specific cations can promote stronger hydrogen bonding or more structured water layers near the surface. These ion-specific trends point to the subtle yet significant influence of cation size, charge density, and hydration enthalpy on interfacial water structuring.

These results are consistent with prior molecular dynamics simulations and spectroscopic studies showing that cation identity modulates interfacial water orientation and hydrogen bonding patterns. The findings reinforce the capability of soft X-ray absorption spectroscopy to sensitively detect changes in interfacial solvent structure induced by ion-specific interactions, even in complex colloidal systems.

[1] Abbas *et al.*, J. Phys. Chem. C **112** (2008) 5715.
[2] T. Petit *et al.*, J. Phys. Chem. Lett. **6** (2015) 2909.

BL3B

Evaluation of Properties of Inner Region of Zinc Aluminate Thin Film for Ultra violet Emission

H. Kominami[1,2,3], J. Kamikawa[1], T. Sadamori[1], D. Takeya[1], M. Yasuda[1], N. Yoshimura[1],
K. Kamiya[2], H. Nagao[2], K. Murata[2], K. Yamaguchi[2] and S. Kurosawa[4,5]
[1]Graduate School of Integrated Science and Technology, Shizuoka University,
[2]Faculty of Engineering, Shizuoka University,
[3]Graduate School of Science and Technology, Shizuoka University,
[1~3]3-5-1 Johoku, Chuo-ku, Hamamatsu 432-8651 Japan
[4]New Industry Creation Hatchery Center (NICHe), Tohoku University 6-6-10 Aza-Aoba,
Aramaki, Aoba-ku, Sendai, Miyagi 980-8579, Japan
[5]Faculty of science, Yamagata University, 1-4-12, Kojirakawa-machi, Yamagata 990-8560, Japan

In the fields of sterilization and water purification, conventional sterilization methods using chemicals and heat are concerned about the effects of deterioration, toxicity to the human body, and the effects of resistant bacteria. For this reason, sterilization methods using ultraviolet light are becoming more widespread. It is said that ultraviolet light around 260 nm has the strongest effect. Mercury lamps and other devices are used as ultraviolet light sources for sterilization, but their use is concerned from the perspective of environmental impact. Under these circumstances, we aim to develop a new ultraviolet light-emitting device for sterilization that is highly efficient, low-cost, and has a low environmental impact. As one of these devices, we focused on a device that uses $ZnAl_2O_4$, which emits deep ultraviolet light around 250 nm when excited by electron beams, as the emitting layer. We are currently working on the fabrication of a double-insulated electroluminescence (EL) lamp, which is one of the solid-state display elements. There are many challenges in developing this device, such as improving the sterilization ability, controlling the voltage applied to the emitting layer, and fabricating an ultraviolet-transparent electrode. In particular, it is necessary to know the dielectric constant of the emitting layer to control the applied voltage, but the dielectric constant of the emitting layer $ZnAl_2O_4$ is currently unknown. Therefore, we attempted to obtain the refractive index from the fluctuation of the transmittance spectrum of the emitting layer, and from that, to obtain the dielectric constant.

On a c-plane sapphire substrate (c-Al_2O_3), he deposited about 300 nm of ZnO by magnetron sputtering, and on top of that he deposited about 25 nm of Al_2O_3 as a cap layer. After sputtering, he fabricated $ZnAl_2O_4$ thin films by annealing (990°C, 50 hours) under atmospheric conditions in a muffle furnace and by thermal diffusion. In addition, the thin film surface of the prepared sample was etched using hydrochloric acid to expose the inside of the film, and its characteristics were evaluated using cathodoluminescence (CL), thin film X-ray diffraction measurement (XRD), analytical FE-SEM, and transmission.

The transmission spectrum of the sample etched for 0 to 300 minutes (0 to 450 nm) is shown in Fig. 1. Interference was observed at wavelengths of 180 to 350 nm. Here, the wavelengths of the peaks of the spectrum fluctuation are λ1, λ3, and λ5 from the short wavelength side, and the wavelengths of the valleys are λ2 and λ4, and we tried to derive the refractive index from these wavelengths.

From the cathodoluminescence measurement, the emitting layer region is calculated to be about 1200 nm. Therefore, calculations were performed assuming that Zn diffusion is 1000 and 1400 nm. As a result, when the diffusion length is assumed to be 1000 nm, the refractive index is about 4 to 5. On the other hand, when the diffusion length is assumed to be 1400 nm, the refractive index is about 3. From past research, it is thought that a layer of Zn diffused into the sapphire substrate is formed inside the thin film. In addition, the dielectric constant of the sapphire substrate is 9, and the refractive index is converted to about 3 without considering the extinction coefficient. From these facts, it is considered appropriate to assume that the refractive index after 450 nm etching is about 3, and that the Zn diffusion length is 1400 nm. In addition, because a good $ZnAl_2O_4$ layer is formed from the surface to about 400 nm, the refractive index is thought to be about 1.9 to 2.3, and the dielectric constant is thought to be about 3.6 to 5.3.

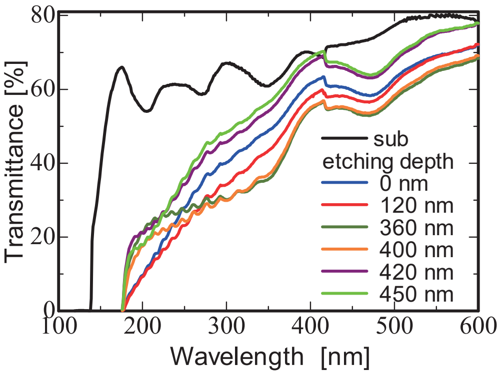

Fig. 1. Transmission spectra of etched $ZnAl_2O_4$ thin films.

BL4U

Scanning Transmission X-ray Microscopy (STXM) Study of Co Oxidation State Evolution in Nano- and Micro-Sized $LiCoO_2$ During Alkaline OER

Y. Zhang[1], J. Lei[1], T. Araki[2] and J. Wang[1]
[1]*City University of Hong Kong, Kowlong, Hong Kong*
[2]*UVSOR Synchrotron Facility, Institute for Molecular Science, Okazaki 444-8585, Japan*

Layered $LiCoO_2$ (LCO), well-known as a cathode in lithium-ion batteries, also shows promise as an alkaline oxygen evolution reaction (OER) electrocatalyst due to its Co^{3+}↔Co^{4+} redox activity and robust Co–O framework [1]. Studies have demonstrated that Na^+ or K^+ incorporation in LCO can enhance Co–O covalency, boosting OER activity while preserving structural integrity [2]. Nanoscale LCO, in particular, offers abundant Co^{3+}-rich surface facets and favorable electronic structures for redox kinetics. Conversely, micro-sized LCO (mLCO) often suffers from limited lithium diffusion, surface Co dissolution, and structural reconstruction under prolonged OER conditions [3,4].

To explore how particle size influences Co valence state distribution during OER, we performed STXM with Co L_3-edge XANES on nanoparticulate LCO (nLCO, ≈ 50 nm) and micron-sized LCO (mLCO, ≈ 1 μm). Samples were polarized in 1 M KOH at 1.5 V vs. RHE for 10 min and 30 min. We aimed to determine: (i) initial oxidation homogeneity, (ii) short-term oxidation evolution, and (iii) spatial heterogeneity after prolonged exposure.

STXM maps of pristine samples showed that nLCO consistently exhibited an XANES peak at 778.0 eV, indicating a homogeneous Co^{3+} oxidation state (Fig. 1a). In contrast, mLCO displayed a broader peak around 776.8 eV, signifying mixed Co^{2+}/Co^{3+} states and a lower overall oxidation level (Fig. 1b). The enhanced surface energy and electronic coupling in nLCO likely stabilize Co^{3+}, consistent with previous findings on size-dependent structural robustness [1, 3].

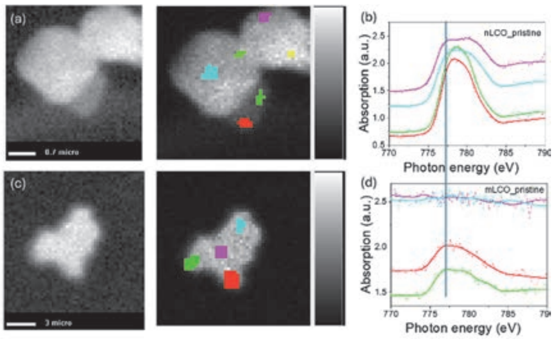

Fig. 1. STXM of nLCO pristine (a-b) and mLCO pristine (c-d).

After 10 minutes of OER polarization, the Co peak in nLCO slightly shifted to ~777.8 eV but remained indicative of Co^{3+} (Fig. 2a). Remarkably, mLCO's peak shifted from 776.8 to ~777.9 eV (Fig. 2b), aligning with nLCO. This reveals rapid oxidation of surface Co^{2+} to Co^{3+} in mLCO, demonstrating that even micro-sized particles can achieve surface valence homogenization under short-term OER conditions.

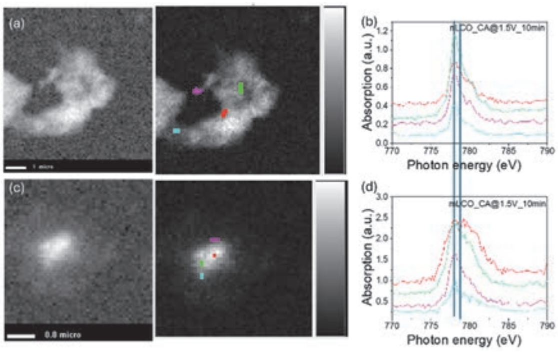

Fig. 2. STXM of nLCO (a-b) and mLCO (c-d) after CA at 1.5V for 10min.

Prolonged polarization showed divergent trends: nLCO retained uniform Co^{3+} distribution with no spatial variation (Fig. 3a) while mLCO developed clear spatial heterogeneity—edge regions exhibited peaks at ~778.0 eV (possibly over-oxidized Co^{3+}), while core areas remained around ~777.8 eV (Fig. 3b). This behavior results from rapid edge oxidation by OH^- and slower lithium deintercalation in the core, leading to non-uniform internal oxidation—a phenomenon observed in larger LCO crystals [4].

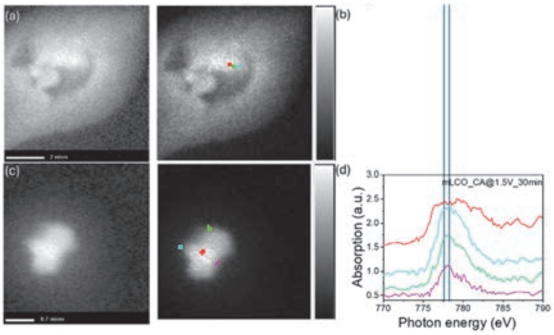

Fig. 3. STXM of nLCO (a-b) and mLCO (c-d) after CA at 1.5V for 30min.

[1] Y. Kim *et al.*, J. Mater. Chem. A **10** (2022) 10967.
[2] J. Qian *et al.*, Nat. Commun. **9** (2018) 4918.
[3] Y. Kim *et al.*, J. Phys. Chem. Lett. **6** (2015) 1357.
[4] T. Maiyalagan *et al.*, Nat. Commun. **6** (2015) 3949.

BL4U

In Situ STXM-Based Approach to Visualize Polymer Fracture: Demonstration with Polystyrene

T. Ejima[1,2], E. Sasaki[2] and Y. Tamura[3]
[1]SRIS & [2]IMRAM, Tohoku University, Sendai 980-8577, Japan
[3]ENEOS Materials Corp., Yokkaichi 510-0871, Japan

Polystyrene (PS) is a widely used thermoplastic owing to its low cost, high transparency, and ease of processing. The fracture behavior of PS is primarily attributed to main-chain scission, in which carbon–carbon bonds within the polymer backbone are ruptured—a phenomenon widely observed in polymeric systems. Although molecular probes such as fluorescent dyes and stabilized radicals have facilitated the visualization of such events, methods for directly detecting main-chain scission remain limited [1].

Carbon K-edge spectral imaging at sub-micron resolution is expected to reveal stress-induced electronic structural changes and elucidate fracture mechanisms, with a particular focus on main-chain scission [2]. The objective of this study is to visualize polymer fracture without the use of dyes or radicals by performing in situ stress-application experiments using scanning transmission X-ray microscopy (STXM). To this end, a custom-designed sample holder was developed by integrating the STXM frame from BL4U (UVSOR) with a cartridge designed for simultaneous tensile deformation and TEM observation [3]. The holder incorporates a piezo-linear actuator (Picomotor™, Model 8302, Newport) connected to a lever, enabling precise displacement control (Fig. 1a). The cartridge contains a flexure structure that is actuated by the lever, thereby applying stress to the sample (Fig. 1b). Polymer samples were mounted on parallel TEM grids and secured with double-sided adhesive tape. The conversion of vertical lever motion into horizontal displacement resulted in an opening displacement of 9.02 ± 0.18 nm per actuator pulse.

The measurements were conducted using injection-grade polystyrene (HF77, PS Japan Corporation), which was sectioned into 100 nm-thick slices using an ultramicrotome. These slices were mounted on TEM grids (40 µm bar width, 62 µm pitch) and affixed to the cartridge. During STXM, soft X-rays from the BL4U monochromator were focused to a 50 nm spot using a zone plate. The images were acquired with a pixel exposure time of 2 ms.

Two stress-application measurements were conducted, both showing PS fracture at strain levels between 0.327 and 0.460. Below 0.327, the STXM spectra from the PS region exhibited consistent profiles (Fig. 2) corresponding to previously reported PS spectra [2]. Normalized absorption spectra revealed a strain-dependent increase near 285 eV (inset of Fig. 2), consistent with π* orbitals from benzene rings [2, 4], indicating alignment of the ring along the X-ray direction [4]. These results suggest that stress-application STXM offers enhanced potential for elucidating polymer fracture mechanisms.

Acknowledgement:
The authors thank the Machine Shop of IMRAM, Tohoku University for their support in fabricating the STXM holder.

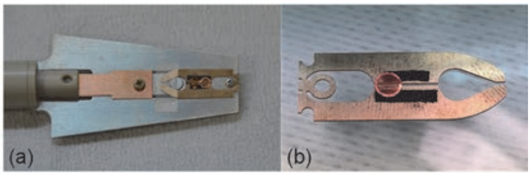

Fig. 1. (a) STXM holder frame with a piezo-linear actuator, (b) Sample cartridge: Stress is applied to the sample by opening and closing the flexure structure.

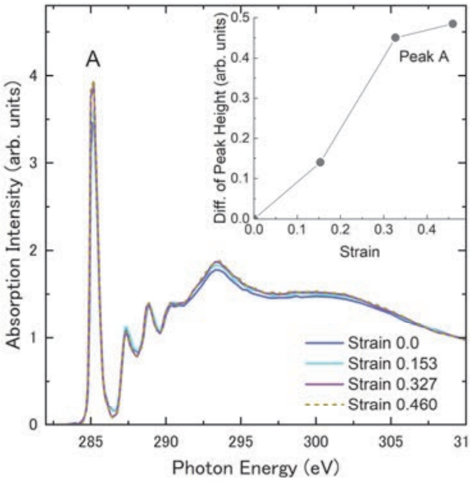

Fig. 2. Spectral shape the major area is the same of PS [2]. Inset is the intensity change of peak A.

[1] T. Yamamoto, D. Aoki and H. Otsuka, ACS Macro Lett. **10** (2021) 744.
[2] J. Stöhr, *NEXAFS Spectroscopy* (Springer, Berlin & Heidelberg, 1992) §7.4, p.230.
[3] T. Higuchi *et al*., Microscopy **67** (2018) 296.
[4] J. A. Horsley *et al*, J. Chem. Phys., **83**(12) (1985) 6099.

BL4B

Coverage-Dependent Spin Reorientation Transition in Ni Thin Films on Cu(001) Induced by Pd Overlayers

T. Miyamachi[1,2], N. Okamura[1], A. Iwai[1], H. Ono[1], N. Maejima[3,4], O. Ishiyama[3,4], E. Nakamura[5], H. Iwayama[5], T. Yokoyama[3,4] and M. Mizuguchi[1,2]

[1]*Department of Materials Science and Engineering, Nagoya University, Nagoya 464-8603, Japan.*
[2]*Institute of Materials and Systems for Sustainability (IMaSS), Nagoya University, Nagoya 464-8601, Japan.*
[3]*Institute for Molecular Science, Myodaiji-cho, Okazaki 444-8585, Japan*
[4]*The Graduate University for Advanced Studies, Myodaiji-cho, Okazaki 444-8585, Japan*
[5]*UVSOR Synchrotron Facility, Institute for Molecular Science, Okazaki 444-8585, Japan*

Thin film heterostructures have been widely studied because of novel phenomena developed by the formation of the heterointerface. Especially for the heterostructure composed of magnetic materials, interface conditions such as lattice strain, mixing drastically change magnetic properties of the whole system [1]. In this study, we fabricate Pd/Ni thin film heterostructures on Cu(001) and investigate their structural, electronic, and magnetic properties by low energy electron diffraction (LEED) and x-ray absorption spectroscopy/magnetic circular dichroism (XAS/XMCD). Ni thin films grown on Cu(001) are known to exhibit the spin reorientation transition (SRT) from in-plane magnetization to out-of-plane magnetization with increasing the coverage [2]. Since the SRT is associated with changes in the lattice constant near surface, adding Pd overlayers with significantly larger lattice constant than Ni can modify magnetic properties of Ni thin films by the formation of Pd/Ni heterointerface.

To fabricate Pd/Ni thin film heterostructures, we grow 6 and 12 monolayer (ML) Ni thin films on Cu(001) at room temperature. Then, 2, 6 and 12 MLs of Pd overlayers are grown onto each Ni thin film. LEED patterns of Pd/Ni thin-film heterostructures reveal that both Ni and Pd layers grow epitaxially on Cu(001) but the surface lattice constant of Ni expands by adding Pd overlayers. To investigate electronic, and magnetic properties of Pd/Ni thin film heterostructures, XAS/XMCD measurements are performed at BL4B in UVSOR by total electron yield mode at B = 0 - ± 5 T and T = 6.6 K. The XMCD spectra are obtained at the normal (NI: θ = 0°) and the grazing (GI: θ = 55°) geometries by detecting $\mu_+ - \mu_-$, where μ_+ (μ_-) denotes the XAS recorded at Ni and Pd L adsorption edges with the photon helicity parallel (antiparallel) to the sample magnetization. Note that θ is the angle between the sample normal and the incident x-ray. Element specific magnetization curves of Ni layers are also recorded by plotting the Ni XAS L_3 peak intensity normalized by L_2 one as a function of the magnetic field. The deposition rates and coverages of Ni and Pd layers are crosschecked by the quartz-crystal microbalance (QCM) and XAS edge jumps at L-edges of Ni and Pd relative to of Cu L-edge [3].

We first investigate magnetic properties of bare Ni thin films on Cu(001) by XAS/XMCD. Comparing XAS/XMCD spectra recorded in the NI and GI geometries, we reveal that 6 ML Ni thin films show strong in-plane magnetization the easy magnetization direction of 12 ML Ni thins film is slightly toward the out-of-plane direction, which is in good agreement with previous work investigated by ferromagnetic resonance measurements [2].We find from Pd coverage dependence of Ni magnetization curve that adding Pd overlayer modifies the magnetic anisotropy of Ni thin films. For 12 ML Ni thin films, the easy magnetization direction gradually shifts from out-of-plane to in-plane direction with increasing Pd coverage. On the other hand, adding Pd overlayer further stabilizes the in-plane magnetization of 6 ML Ni films. Interestingly, the stabilization of the in-plane magnetization is completed when 2 MLs of Pd are deposited no further changes are recognizable with increasing Pd coverage. The results indicate that the degree of lattice strain of Ni induced by Pd overlayers and the hybridization strength at the Pd/Ni heterointerface, which both modify the magnetic anisotropy of Ni thin film, are strongly dependent on Ni coverage.

[1] S. Nakashima *et al*., Adv. Funct. Mater. **29** (2019) 1804594.
[2] B. Schulz *et al*., Phys. Rev. B **50** (1994) 13467.
[3] H. Ono *et al*., J. Phys. Chem. C **127** (2023) 23935.

BL4B

Spin Reorientation Transition of Co Nano Islands by the Formation of Organic-Inorganic Hybrid Interface

T. Miyamachi[1,2], H. Ono[1], K. Fujimoto[1], K. Yoshida[1], N. Maejima[3,4], O. Ishiyama[3,4],
E. Nakamura[5], H. Iwayama[5], T. Yokoyama[3,4] and M. Mizuguchi[1,2]
[1]*Department of Materials Science and Engineering, Nagoya University, Nagoya 464-8603, Japan.*
[2]*Institute of Materials and Systems for Sustainability (IMaSS), Nagoya University, Nagoya 464-8601, Japan.*
[3]*Institute for Molecular Science, Myodaiji-cho, Okazaki 444-8585, Japan*
[4]*The Graduate University for Advanced Studies, Myodaiji-cho, Okazaki 444-8585, Japan*
[5]*UVSOR Synchrotron Facility, Institute for Molecular Science, Okazaki 444-8585, Japan*

An organic-inorganic hybrid interface has attracted attention due to its controllable interface electronic state by the proper choice of organic and inorganic materials. Especially for the system composed of organic molecules and an inorganic magnetic material, a variety of novel spin functionalities with the help of long spin diffusion length of organic molecule can emerge via the magnetic interaction at the organic-inorganic interface. Since the degree of the magnetic interaction strongly replies on the spin polarization of the inorganic magnetic material near the Fermi energy, element specific investigations of the organic-inorganic hybrid interface are important to understand the impact of the formation of the organic-inorganic hybrid interface on the magnetic properties of the inorganic magnetic material. In this work, we fabricate the organic-inorganic hybrid interface composed of [1,2,5] Thiadiazolo [3,4-f][1,10]phenanthroline 1,1-dioxide (tdapO_2) and Co nano island and investigate its electronic/magnetic properties element specifically by x-ray absorption spectroscopy/x-ray magnetic circular dichroism (XAS/XMCD).

XAS/XMCD measurements are conducted at BL4B in UVSOR by total electron yield mode at B = 0 - ± 5 T and T = 7.7 K. The XMCD spectra are obtained at the normal (NI: $\theta = 0°$) and the grazing (GI: $\theta = 55°$) geometries by detecting $\mu_+ - \mu_-$, where μ_+ (μ_-) denotes the XAS recorded at Co L adsorption edges with the photon helicity parallel (antiparallel) to the sample magnetization. Note that θ is the angle between the sample normal and the incident x-ray. Magnetization curves of Co nano islands are recorded by plotting the L_3/L_2 Co XAS peak intensity as a function of the magnetic field.

Co islands are first grown by deposition of 0.4 monolayer Co onto Cu(111) at room temperature. We investigate the morphology of Co islands by scanning tunneling microscopy (STM) in advance, and confirm the formation of isolated bilayer Co nano islands at Co coverage of 0.4 monolayer. The deposition rate of Co is evaluated by the quartz-crystal microbalance (QCM) and XAS edge jump [1]. Then, tdapO_2 molecules are sublimated by heating at 380 K and deposited onto Co islands. The deposition amount of tdapO_2 is evaluated by QCM and set to several molecular layers in this study.

In XAS/XMCD measurements, we focus on the remanent magnetization and coercivity in the Co magnetization curve. While the Co magnetization curve recorded in the GI geometry shows a clear hysteresis loop, reduced remanent magnetization and a smaller hysteresis loop are observed for that recorded in the NI geometry. The results reveal in-plane magnetic easy axis of Co nano islands, which is consistent with previous study [2]. After the deposition of tdapO_2, significant changes are observed for Co magnetization curve recorded in the NI geometry. We find that the remanent magnetization increases by a factor of two, and the coercivity by a factor of seven, which induces the spin reorientation transition (SRT) of Co nano islands from in-plane direction to out-of-plane direction. These results indicate that substantial enhancement of perpendicular magnetic anisotropy of Co nano island is caused by the interface formation with tdapO_2. In future work, we will investigate the adsorption geometry and electronic structures of tdapO_2 molecules by STM and discuss the origin of the SRT of Co nano islands.

[1] H. Ono *et al.*, J. Phys. Chem. C **127** (2023) 23935.
[2] M. Zhang *et al.*, J. Phys.: Condens. Matter **12** (2000) 783.

BL4B

Angle-Resolved Photoemission Circular Dichroism for Chiral Molecule Overlayer on Monolayer WS_2

F. Nishino[1,2], K. Fukutani[1,2], P. I. Jaseela[1,2], J. Brandhoff[3], F. Otto[3], M. Grünewald[3], M. Schaal[3], J. Picker[4], Z. Zhang[5], A. Turchanin[4], S. Makita[6], H. Iwayama[6], T. Hirose[5], T. Fritz[3] and S. Kera[1,2,6]
[1]*Institute for Molecular Science, Okazaki 444-8585, Japan*
[2]*School of Physical Sciences, The Graduate University for Advanced Studies, Okazaki 444-8585, Japan*
[3]*Institute of Solid State Physics, Friedrich Schiller University Jena, Helmholtzweg 5, 07743 Jena, Germany*
[4]*Institute of Physical Chemistry, Friedrich Schiller University Jena, Lessingstraße 10, 07743 Jena, Germany*
[5]*Institute for Chemical Research, Kyoto University, Gokasho, Uji, Kyoto 611-0011, Japan*
[6]*UVSOR Synchrotron Facility, Institute for Molecular Science, Okazaki 444-8585, Japan*

A chirality-induced spin selectivity (CISS) effect with controlled chiral molecules on various solid surfaces has been actively studied for various applications, such as for spintronics and enantio-separations [1]. On the other hand, many aspects of this phenomenon, including its mechanism underlying its extraordinarily large spin polarization effects, remain unknown.

Our approach to this challenge is to fabricate well-defined chiral molecular systems on solid surfaces with known spin-polarized electronic band structures, and to investigate how the surface chirality affects the emitted electrons from the solid by angle-resolved photoemission spectroscopy (ARPES).

As a preliminary study, in this work, we used angle-resolved photoemission circular dichroism (CD-ARPES) for the system of chiral molecular overlayer on achiral substrate possessing fully spin-polarized electrons to assess how the electrons emitted from the substrate recognize the surface chirality.

The enantiopure chiral molecule, thiadiazole-[9] helicene (TD[9]H) [2], was used in this study as show in Fig. 1(a). The substrate used was a monolayer WS_2/Au(111) (ML-WS_2) with fully spin-polarized bands at $\overline{\mathrm{K}}$' and $\overline{\mathrm{K}}$ points [3]. After depositing the enantiopure TD[9]H on the ML-WS_2 under ultra-high vacuum condition, low-energy electron diffraction (LEED) showed an ordered molecular overlayer with broken mirror-symmetry, indicating the surface chirality has been induced on the system.

Following the confirmation of the surface chirality, CD-ARPES measurements were performed, using left circularly polarized (LCP) and right circularly polarized (RCP) lights for both the clean substrate and the (*M*)-TD[9]H/ML-WS_2 samples, as shown in Fig. 1(b).

Figures 1(c)-(e) show the CD-ARPES maps obtained for clean ML-WS_2 substrate. It can be seen that the dichroic signals at the $\overline{\Gamma}$-$\overline{\mathrm{M}}$ plane [black dotted lines in Figs. 1(c), 1(d) and the entire map in Fig. 1(e)], which is the mirror plane of the substrate, is very weak. Furthermore, the dichroic signals in the $\overline{\Gamma}$-$\overline{\mathrm{K}}$ and $\overline{\Gamma}$-$\overline{\mathrm{K}}$' directions are seen to be generally anti-symmetric with respect to the $\overline{\Gamma}$-$\overline{\mathrm{M}}$ plane.

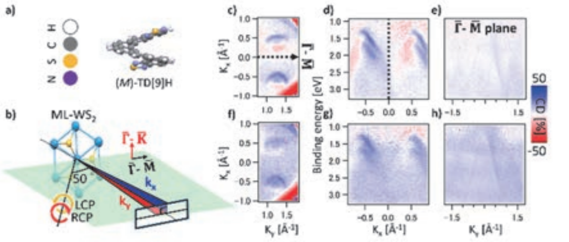

Fig. 1. (a) Molecular structures of (*M*)-TD[9]H. (b) Schematic illustration of CD-ARPES setup. The relative orientations of the sample and the photoelectron analyzer slit are shown. (c)-(e) CD-ARPES map of ML-WS_2. (f)-(h) CD-ARPES map of (*M*)-TD[9]H/ML-WS_2. (c) and (f) shows constant-energy cut and (d), (g) is the intensity plots in E-k_x slice. (e) and (h) is the intensity plots in E-k_y slice.

These characteristics of dichroic signals from substrate can readily be understood from the point of view of symmetry. Since the substrate is achiral and the mirror plane of the crystal coincides with the plane of light incidence, it must hold that $I_{\mathrm{RCP}}(k_x, k_y) = I_{\mathrm{LCP}}(-k_x, k_y)$ (Equation 1), where I_{RCP} and I_{LCP} are the photoelectron intensities with RCP and LCP lights, respectively. That is, the achirality of substrate is reflected in our CD-ARPES results.

Next, the CD-ARPES results after the deposition of (*M*)-TD[9]H are shown in Figs. 1(f)-(h). Unlike the CD-ARPES results from the clean substrate, finite (blue) dichroic signals were observed uniformly in the substrate bands, molecular orbitals and inelastic scattering regions even in the E-k slice of the $\overline{\Gamma}$-$\overline{\mathrm{M}}$ plane as can be seen in Fig. 1(h). While more investigations are necessary, the apparent violation of equation 1 above could arise from the loss of achirality (i.e., emergence of chirality) for the electrons in the system of chiral molecular overlayer on achiral substrate.

[1] S.-H. Yang *et al.*, Nat. Rev. Phys. **3** (2021) 328.
[2] Z. Zhang *et al.*, Tetrahedron **142** (2023) 133514.
[3] P. Eickholt *et al.*, Phys. Rev. Lett. **121** (2018) 136402.

BL5U

Growth of P Ultra-Thin Film on Cu(111)

N. Maejima[1] and T. Yokoyama[1]
[1]Institute for Molecular Science, Myodaiji-cho, Okazaki 444-8585, Japan

Two-dimensional single-element materials, such as graphene, silicene and germanene etc., have attracted much attention owing to their unique physical and chemical properties. Phosphorene, has attracted attention due to its high mobility and variable band gap depending on the number of atomic layers. Blue phosphorene with a Dirac cone, produced by evaporation of P on a heated Cu(111) substrate, was recently reported [1]. The 1 ML and 1.5 ML blue phosphorene samples show 10√3x 10√3 and 13 x 13 moire LEED patterns, respectively. The formation of self-assembled P nanodots on top of the phosphorene sheet of 13x13 sample was clearly observed in the study. In this report,1ML phosphorene was grown on Cu(111) which shows 13x13 moire LEED pattern in different fabrication process.

Experiments were performed at BL5U of the UVSOR facility. The Cu(111) surface was cleaned by cycles of Ar^+ ion spattering (0.75 keV) and annealing (600 °C). P atoms were deposited by directly heating of a piece of GaP wafer. The Cu(111) substrate was kept at 300 °C during the P atoms deposition. The prepared Cu(111) and P deposited Cu(111) samples showed 1x1 and 13x13 moire LEED patterns, respectively. The P deposited sample were post-annealed at 500°C. The LEED pattern was not changed from of this sample consisted of 1x1 spots arising from 13x13 moire LEED pattern. P 2p and valence band photoelectron spectroscopy (PES) measurements were performed by an MBS A-1 analyzer.

Figure 1 shows the P 2p spectrum obtained from P deposited during 300°C annealing and 500°C post-annealing samples with black and red solid lines, respectively. In the spectrum of the P deposited sample during 300°C annealing, P 2p 3/2 peak of shoulder and main components were observed at 128.3 eV and 128.8 eV, respectively. These peak components were attributed to the P nanodot and blue phosphorene layer, respectively, in the previous study [1]. The 500°C post-annealing sample have only the main component at 128.8 eV. The total area of the P 2p spectrum was reduced to 80% by 500°C post- annealing process. The P nanodot component observed in the spectra of 300°C annealing sample has disappeared, indicating that the whole surface is simply covered with blue phosphorene monolayer. The band dispersion of the valence band of the sample post-annealed at 500 °C showed a linear band around the Cu(111) $\overline{K}$ point. This result is similar to the band structure of 10√3x10√3 1ML Blue Phosphorene sample structure previously reported. Combining these results and the fact that the LEED pattern was not changed by the 500 °C post-annealing process indicates that the 13x13 structure is not due to nanodot origin but to a blue phosphorene monolayer. There are several lattice constants for phosphorene reported ranging from 3.4 Å to 4.2 Å [1]-[3]. Such flexible lattice constants are attributed to differences in the planarity of the phosphorene layers and surface super structure.

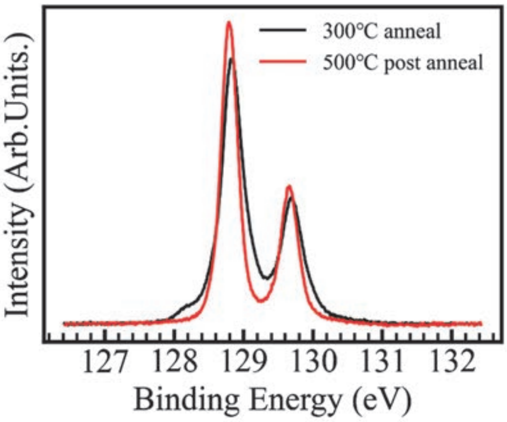

Fig. 1. Figure 1 shows the P 2p spectrum of P deposited during 300°C annealing (black solid line) and 500°C post- annealing samples (red solid line).

[1] Y. Kaddar *et al., Adv. Funct. Mater.* **33** (2023) 2213664.
[2] YH. Song, *et al.,* Nat Commun. **15** (2024) 1157.
[3] D. Zhou, *et al.,* ACS Nano **14** (2020) 2385.

BL5U

Spin-Resolved Electronic Structure of Altermagnet MnTe and CrSb

M. Zeng[1] and C. Liu[1]

[1]*Southern University of Science and Technology (SUSTech), Shenzhen, Guangdong 518055, China*

Magnetic materials play a crucial role in modern technology, and controlling spins in these materials remain a central challenge in spintronics [1–3]. Large spin-splitting has been observed primarily in ferromagnetic materials and system with strong spin-orbit coupling (SOC). However, strong SOC is typically found in heavy elements, which are often toxic and prone to defects, limiting their practical applications.

Recently, researchers have discovered that light-element collinear antiferromagnets could also exhibit properties that are traditionally inherit to ferromagnets [4–9]. In these systems, SOC is negligible, allowing the spin and lattice degree of freedom to be decoupled. This unique property enables e.g. anomalous Hall effect [10-11] and giant spin splitting [12] in antiferromagnetic materials. Specifically, collinear members of spin-split antiferromagnets are termed *altermagnets* due to their alternatively patterned spin polarization.

Among the many proposed altermagnets, MnTe and CrSb have emerged as key candidates due to their simple magnetic structures, high Néel temperatures, and substantial spin splitting. However, direct spectroscopic measurements of their spin textures remain scarce.

To test the predictions of altermagnetism and provide experimental insights for future applications, we performed spin-ARPES (SARPES) measurements on MnTe and CrSb at this beamtime. The results are presented in Fig. 1 and Fig. 2.

For MnTe, traces of faint bulk bands can be observed [Fig. 1(a)]. However, as shown in Fig. 1(b), SARPES measurements reveal a uniform spin-up polarization within the reliable momentum range, contradicting the theoretical expectation of an antisymmetric spin polarization around the Γ point.

For CrSb, a clear holelike band is visible [Fig. 2(a)]. S_z-resolved MDCs were subsequently measured on the bands near the Fermi level, with an energy integration window of $E_B = 0 – 0.5$ eV. The SARPES result shows exclusively spin-up polarization, again inconsistent with the altermagnet theory.

To assess potential instrumental artifacts, we measured the spin polarization of polycrystalline gold, which should ideally yield zero spin signal. However, Fig. 3 reveals strong spin polarization on the gold sample, indicating a significant instrumental bias.

Given that the intrinsic spin polarization in altermagnets is inherently weak, this instrumental background likely dominates the spin signal, masking the spin polarization of the materials. This explains why Fig. 1 and Fig. 2 display similar spin polarization patterns despite their different electronic structures.

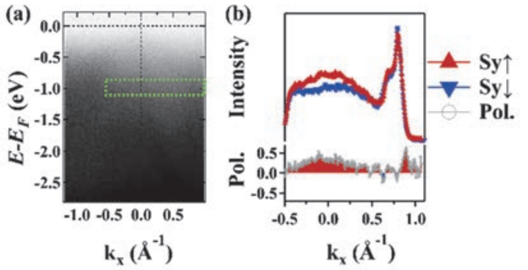

Fig. 1. The SARPES result on MnTe. (a) Spin-integrated ARPES band dispersion acquired at $h\nu = 74$ eV ($k_z = 8.5\ \pi/c$). k_x is parallel to $\overline{\Gamma}-\overline{M}$.Green dash frame represents the spin-MDC measurement region in (b). (b) Representative S_y-resolved MDC. Red lines with up-triangle / blue lines with down-triangle correspond to SARPES signals for opposite S_y components.

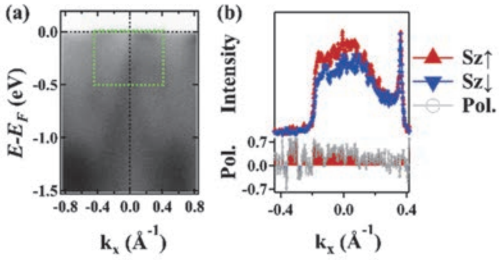

Fig. 2. The SARPES result on CrSb. (a) Spin-integrated ARPES band dispersion acquired at $h\nu = 45$ eV ($k_z = 6.5\ \pi/c$). k_x is parallel to $\overline{\Gamma}-\overline{M}$. Green dash frame represents the spin-MDC measurement region in (b). (b) Representative S_z-resolved MDC. Red lines with up-triangle / blue lines with down-triangle correspond to SARPES signals for opposite S_z components.

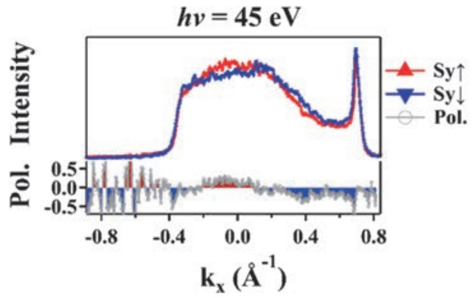

Fig. 3. Representative S_y-resolved MDC on polycrystalline Au at $h\nu = 45$ eV, $E_B = 0.5$ eV.

[1] I. Žutić *et al.*, Rev. Mod. Phys. **76** (2004) 323.
[2] A. Fert, Thin Solid Films **517** (2008) 2.
[3] C. Chappert *et al.*, Nat. Mater. **6** (2007) 813.
[4] L.-D. Yuan *et al.*, Phys. Rev. B **102** (2020) 014422.
[5] L.-D. Yuan *et al.*, Phys. Rev. Mater. **5** (2021) 014409.
[6] L.-D. Yuan *et al.*, Phys. Rev. B **103** (2021) 224410.
[7] S. Hayami *et al.*, Phys. Rev. B **101** (2020) 220403.
[8] S. Hayami *et al.*, J. Phys. Soc. Jpn. **88** (2019) 123702.
[9] C. Wu *et al.*, Phys. Rev. B **75** (2007) 115103.
[10] Z. X. Feng *et al.*, Nat. Electron. **5** (2022) 735.
[11] B. R. Gonzalez *et al.*, Phys. Rev. Lett. **130** (2023) 036702.
[12] L. Šmejkal *et al.* Phys. Rev. X **12** (2022) 031042.

BL5U, 7U

Interfacial Heavy Fermion in Moiré Kondo Lattice $YbCu_2$/Cu(111)

T. Nakamura[1,2], H. Sugihara[2], Y. Chen[2], K. Nishihara[2], R. Ichikawa[2], H. Yamaguchi[2],
K. Tanaka[3] and S. Kimura[1,2,3]
[1]*Graduate School of Frontier Biosciences, The University of Osaka, Suita 565-0871, Japan*
[2]*Department of Physics, Graduate School of Science, The University of Osaka, Toyonaka 560-0043, Japan*
[3]*Institute for Molecular Science, Okazaki 444-8585, Japan*

Heavy fermion (HF) systems originate from a translocation between localized and iterant characters due to the Kondo effect being the host of fertile exotic quantum phases of matter [1]. The Kondo lattice, where rare-earth elements containing localized *f*-electrons are periodically arranged, is the most typical system for investigating HF physics. Recently, HF in stacked layered materials with flat bands near the Fermi level (E_F), such as twisted bilayer graphene and transition metal dichalcogenides, have been actively studied [2-4]. The correlated effect at the interface leads to rich and exotic electronic quantum phases.

Among those correlated stacked systems, the moiré Kondo lattice, a coupled system of two kinds of layered materials by exchange interaction, has been proposed as a new concept in the Kondo lattice model [5-7]. The two layered materials have independent roles for the localized magnetic moment and itinerant conduction electrons. However, the interfacial HF band structure has not been observed experimentally because of poor candidates to satisfy the condition of the moiré Kondo lattice and tiny sample pieces, even in known systems. In this study, we investigated the electronic structure of a novel moiré Kondo lattice $YbCu_2$/Cu(111) by high-resolution synchrotron-based angle-resolved photoemission spectroscopy (ARPES). The $YbCu_2$/Cu(111) is the family of rare-earth-based surface alloy on noble-metal substrates with a moiré superstructure due to the lattice mismatch between the $YbCu_2$ layer with a coherence temperature of 30 K [8] and the Cu(111) substrate.

Figure 1(a) shows the high-resolution ARPES image of $YbCu_2$/Cu(111) near the Fermi level (E_F) taken with linearly polarized 33-eV photons at 15 K. Several hole bands clearly across E_F at around the $\overline{\Gamma}$ point. Note that an asymmetric photoelectron intensity of the Yb^{2+} $4f_{7/2}$ states would be due to a photoexcitation selection rule. In addition to the steep hole band at $k_x = \pm 0.05$ Å^{-1}, which is the upper branch of the 2DHF state on the $YbCu_2$ layer [8], the hole band at $k_x = \pm 0.2$ Å^{-1}, which is folded *sp*-band from Cu(111) substrate [8], was newly observed. Figure 1(b) shows the energy distribution curves of Fig. 1(a) at 0.0 Å^{-1} ($\overline{\Gamma}$ point) and 0.4 Å^{-1} where the peaks originate from the Yb^{2+} $4f_{7/2}$ states. The binding energy at the $\overline{\Gamma}$ point is slightly shifted to the higher by about 10 meV than that at 0.4 Å^{-1}. Such a momentum-dependent energy shift of the Yb^{2+} $4f_{7/2}$ state never appears in the disorder cases, such as single atom adsorption and a randomly diffused Yb atom in a Cu(111) substrate. Furthermore, the left part of the lower branch of the hole band from the Cu(111) substrate smoothly connects to the Yb^{2+} $4f_{7/2}$ flat band, pronouncing band hybridization. These results suggest that a further hybridization between the heavy fermion band of $YbCu_2$ and the bulk *sp*-band derived from Cu(111) substrate is established at the $YbCu_2$/Cu(111) interface.

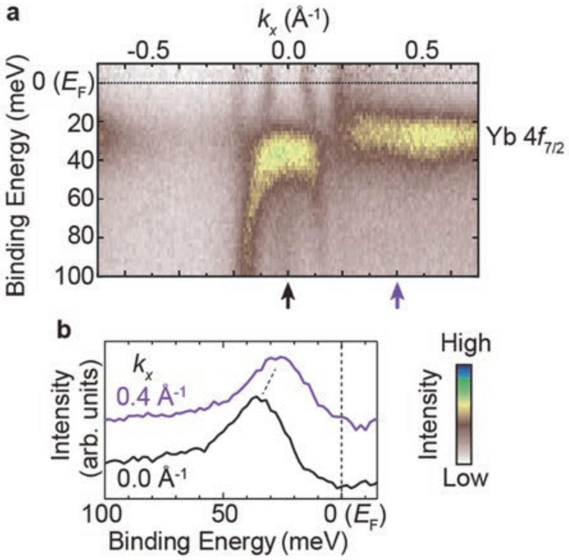

Fig. 1. (a) High-resolution ARPES image near the $\overline{\Gamma}$ point taken with linearly polarized 33-eV photons at 15 K. ARPES intensities are divided by the Fermi–Dirac distribution function convolved with the instrumental resolution. (b) Energy distribution curves at k_x = 0.0 and 0.4 Å^{-1}. The k_x positions are indicated by arrows in (a).

[1] G. R. Stewart, Rev. Mod. Phys. **56** (1984) 755.
[2] Y. Cao *et al.*, Nature **556** (2018) 43.
[3] Y. Cao *et al.*, Nature **556** (2018) 80.
[4] L. Wang *et al.*, Nat. Mater. **19** (2020) 861.
[5] V. Vaño *et al.*, Nature **599** (2021) 582.
[6] W. Zhao *et al.*, Nature **616** (2023) 61.
[7] W. Zhao *et al.*, Nat. Phys. **20** (2024) 1772.
[8] T. Nakamura *et al.*, Nat. Commun. **14** (2023) 7850.

Transmission Spectra of Amorphous Chalcogenide Thin Films in the Vacuum Ultra-Violet Region

K. Hayashi[1]
[1]*Department of Electrical and Electronic and Computer Engineering, Gifu University, Gifu 501-1193, Japan*

Amorphous chalcogenide semiconductor materials, such as amorphous $GeSe_2$, amorphous As_2Se_3 and amorphous Se etc., show a variety of photoinduced phenomena. Therefore, these materials are expected as materials for optoelectronic devices. A lot of work has been done on the photoinduced phenomena of these amorphous semiconductor materials and various mechanisms have been proposed for these photoinduced phenomena [1]. Among those phenomena, the most prominent phenomena are the so-called photodarkening and photobleaching, which are parallel shifts of the optical absorption edge to lower and higher energy sides, respectively, after irradiation with light whose energy corresponds to the optical bandgap. These darkened and bleached states are removed by annealing near the glass-transition temperature. The X-ray diffraction and the volume change of the films before and after irradiation with bandgap light suggest that these phenomena result from the change in the local structure of the amorphous network. However, the details of the mechanisms are still unknown. We are interested in the changes in the optical properties at the higher energy regions. To obtain a wide knowledge of photoinduced phenomena, it is necessary to investigate the photoinduced effects over a wide energy region. In the previous reports, we reported the annealing effect on the VUV transmission spectrum of amorphous selenium [2]. In this report, we focus on the a-$GeSe_2$ thin film that exhibits photobleaching, and report on the investigation of its fundamental optical properties by measuring the VUV transmission spectrum.

Samples used for the measurement of the VUV transmission spectra were thin films of amorphous $GeSe_2$ deposited on a thin aluminum film by conventional evaporation technique. The sample thickness was about 180 nm. An aluminum film of the thickness of 200 nm was used to eliminate the higher order light from the monochromator in the VUV region. These measurements were carried out at room temperature on the BL5B beam line of UVSOR. The spectrum was measured with a silicon photodiode as a detector. Two 1.5mm diameter pinholes were inserted between the monochromator and sample to remove stray light. The intensity of the VUV light was monitored by measuring the TPEY of a gold mesh. The positions of the core levels for the samples were calibrated with reference to the 2p core level absorption of the aluminum film.

Figure 1 shows the VUV transmission spectrum of the amorphous $GeSe_2$ thin film in the wavelength range of 18 to 24 nm. For comparison, the VUV transmission spectra of amorphous As_2Se_3 and amorphous Se are also shown in the figure. As shown in the figure, each spectrum is very broad and multiple shoulders are observed. Main absorption peaks around 22nm correspond to the 3d core level of Se atoms. The absorption spectra observed in amorphous As_2Se_3 and amorphous Se are roughly consistent with the previous report [3]. Although the wavelength resolutions in the spectral measurements are all the same, the spin-orbit splitting of the $3d_{5/2}$ and $3d_{3/2}$ levels of Se atoms is clearly resolved in amorphous $GeSe_2$ and amorphous As_2Se_3, while it is not clearly resolved in as-deposited amorphous Se. The origin of broad spectra and several peaks is not clear. I think that these origins are related to the local structures of the amorphous network. The detailed experiments and analysis will be done in the next step. More detailed experiments are necessary to clarify the origin of the VUV transmission spectra.

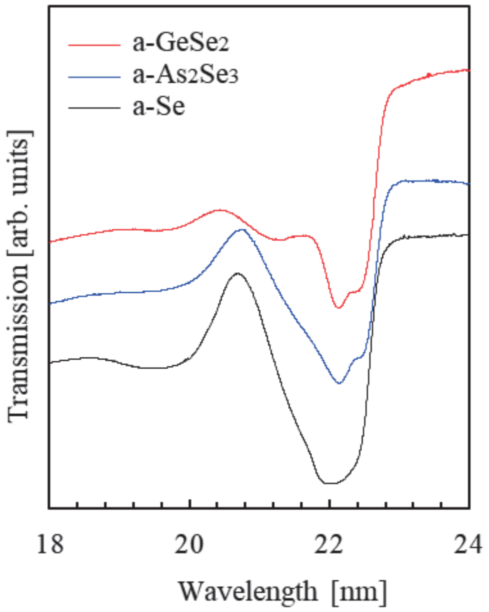

Fig. 1. VUV transmission spectra of amorphous $GeSe_2$, amorphous As_2Se_3, and amorphous Se thin films.

[1] Ke. Tanaka, Rev. Solid State Sci. **4** (1990) 641.
[2] K. Hayashi, UVSOR Activity Report **50** (2022) 152.
[3] J. Bordas and J. B. West, Phil. Mag. **34** (1976) 501.

BL5B

Reflectance of La/B_4C Reflective Multilayers

T. Ejima[1,2], R. Nakamura[3] and T. Hatano[1,2]
[1]*SRIS & [2]IMRAM, Tohoku University, Sendai 980-8577, Japan*
[3]*Dept. Appl. Physics, Tohoku University, Sendai 980-8577, Japan*

A wavelength in the soft X-ray (SX) region around 6.x nm has been proposed as a candidate for next-generation semiconductor lithography [1]. In this wavelength range, light penetration is significantly limited, necessitating the use of reflective optics based on multilayer structures. These multilayers typically consist of alternating layers of two materials that exhibit both low absorption and a large difference in refractive index. Ensuring a sharp interface between these materials is paramount for preserving the index contrast. Given that the periodic thickness of the film is approximately half the target wavelength at near normal incidence, the influence of the interface becomes increasingly critical as the wavelength decreases.

Currently, LaN/B-based multilayers are among the most reflective near 6.x nm [1]. These are fabricated via reactive magnetron sputtering using N_2 gas. However, the reactive gas can also interact with B, forming BNx compounds at the LaN/B interface and thereby degrading reflectance. To address this issue, we investigated La/B_4C multilayers as a promising alternative that eliminates the need for reactive sputtering (Fig. 1). B_4C has a negative enthalpy of formation and is thermodynamically stable in its standard state [2], while La is defined in its most stable phase [3]. This suggests that the La/B_4C pair can form stable, sharply defined interfaces in thin-film form.

The multilayers were deposited using ion beam sputtering at acceleration voltages of 1.0, 1.5, and 2.0 kV. X-ray reflectometry revealed the corresponding period lengths to be 3.63 nm, 3.52 nm, and 3.80 nm, respectively, indicating that ion energy primarily affects the interfacial structure.

Figure 2 presents preliminary reflectance spectra near 6.x nm for samples deposited at 1.0 kV and 2.0 kV. The observed variations in reflectance are believed to result from differences in interface quality induced by the ion energy.

In summary, the La/B_4C multilayer system demonstrates promising reflectance performance without the complications associated with reactive sputtering. The correlation between ion energy and interface sharpness highlights a critical parameter for further optimization. Ongoing and future work will aim to systematically improve reflectance by refining deposition conditions and enhancing interface control in La-based multilayers.

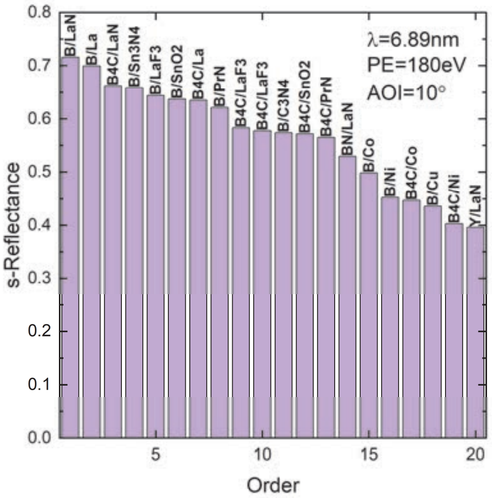

Fig. 1. A comparison of s-polarized reflectance for each material pair, with the horizontal axis indicating rank and the vertical axis displaying s-polarized reflectance. It is notable that the maximum value is B/LaN.

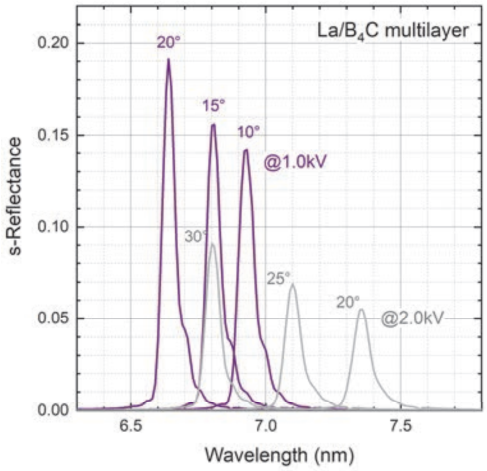

Fig. 2. A comparison of s-polarized reflectance for La/B_4C multilayers measured in the near normal incidence geometry (AOI: 10° – 30°).

[1] D. Kuznetsov *et al*., Opt. Lett. **40** (2015) 3778.
[2] M. W. Chase Jr., J. Phys. Chem. Ref. Data, Monograph **9** (1998) 1.
[3] R. H. Schumm, D. D. Wagman, S. Bailey, W. H. Evans, and V.B. Parker in National Bureau of Standards (USA) Technical Notes, (1973) 270.

BL6U

Conduction Band of Single Crystal Graphite Embedded in Photoemission Energy-Loss Electrons Visualized by Photoelectron Momentum Microscope

F. Matsui[1], R. Sagehashi[2] and Y. Sato[1]

[1]*UVSOR Synchrotron Facility, Institute for Molecular Science and School of Physical Sciences, The Graduate University for Advanced Studies (SOKENDAI), Okazaki 444-8585, Japan*

[2]*Department of Photo-Molecular Science, Institute for Molecular Science, Okazaki 444-8585, Japan*

The interaction of secondary electrons (SEs) with the conduction band in the photoemission process reduces the emission intensity into the vacuum and produces a negative conduction band pattern contrast [1,2]. This process is very similar to the generation of negative photoelectron diffraction patterns observed in the angular distribution of energy-loss electrons accompanying core-level photoelectron excitation [3]. This means that the same setup as a standard photoelectron spectroscopy system for the characterization of occupied states can be used to visualize the electron-unoccupied conduction band.

Photoelectron momentum microscopy is a suitable system to measure comprehensive band dispersion structure in multiple dimensions (*kx*, *ky*, *kz*, *E*). Here we show that the conduction band of graphite are embedded in the angular and energy distribution of SEs. In addition, the experiment was performed in single-bunch mode, which has a photon flux one order of magnitude lower than the conventional multi-bunch mode. Since the SE intensity is very strong, low photon flux conditions are rather suitable for measuring such bulk crystal conduction band dispersion.

Figure 1(a) shows the overall dispersion of the valence band of graphite. Darker features correspond to directions of larger photoelectron signals. The photon energy was set to 68 eV to match the bulk L symmetry point. The selective detection of photoelectrons from a terrace with a single type of termination confirms that L and L’ are not equal, as shown in Figure 1(b) [4]. At the binding energy (BE) of 2.8 eV, the triangles around point K touch each other at point L but are separated at point L’.

Figure 1(c) shows the momentum- resolved kinetic energy distribution of SE electrons. The unoccupied band dispersion appeared as a negative contrast due to the photoelectron absorption process by the conduction band states. Figure 2(d) shows a series of angular patterns at several kinetic energies. The key finding here is that most of the patterns appear with six-fold symmetry, but at kinetic energies of about 20 eV, the patterns become three-fold symmetric. The mechanism by which the three-fold symmetric structure of the top surface of graphite affects the conduction band remains an open question.

[1] V. N. Strocov *et al.* Phys. Rev. B **63** (2001) 205108.
[2] T. Takahashi *et al.*, Phys. Rev. B **32** (1985) 8317.
[3] F. Matsui *et al*., J. Phys. Soc. Jpn. **81** (2012) 013601.
[4] F. Matsui and S. Suga, Phys. Rev. B **105** (2022) 235126.

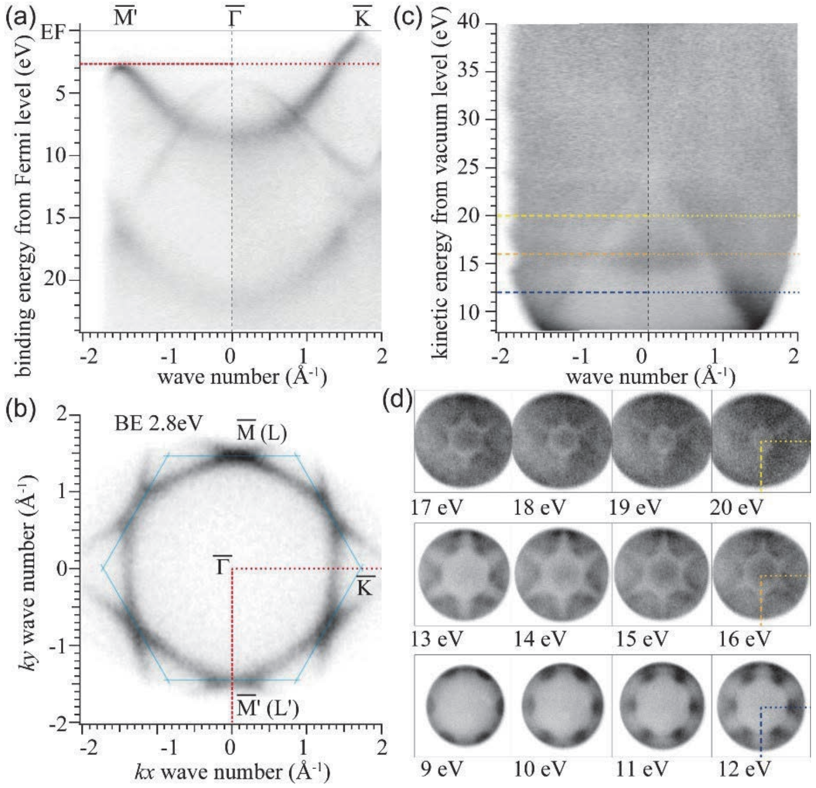

Fig. 1. (a) The overall dispersion of the valence band of graphite. Darker features correspond to directions of larger photoelectron signals. (b) Momentum distribution at the binding energy of 2.8 eV. A red line in (a) corresponds to that in (b). (c) The momentum-resolved kinetic energy distribution of SE electrons. The conduction band signature appears as a lighter grey contrast. (d) A series of SE momentum patterns at several kinetic energies. Note that at kinetic energies of 19 and 20 eV, the patterns appear as three-fold symmetric.

BL6U

Photoelectron Momentum Maps of MnPc on Single Crystal Graphite

R. Sagehashi[1], Y. Sato[2], F. Matsui[2] and S. Kera[1,2]
[1]*Department of Photo-Molecular Science, Institute for Molecular Science, Okazaki 444-8585, Japan*
[2]*UVSOR Synchrotron Facility, Institute for Molecular Science, Okazaki 444-8585, Japan*

Metal complex molecules form ligand fields, which resolve *d*-orbital degeneracy of their metal atoms. Metal-phthalocyanine (MPc) has planar structure and a transition metal atom is located at the center (shown in the inset of Fig. 1). Since MPc molecules are stacked on top of each other via π-π interaction, the ligand field is also formed between layers [1]. Therefore, the electronic and spin state is affected by the film formation significantly.

In this study, we investigated the influence of Mn-phthalocyanine (MnPc) adsorption and film formation on its electronic state by using photoelectron momentum microscopy (PMM) at BL6U. Here, single crystal graphite (SCG) for the substrate was cleaved in vacuum ($< 9.90\times10^{-8}$ Pa). MnPc was in-situ deposited ca. 6.0 Å by deposition rate of 0.30 Å/min measured by quartz crystal microbalance. In this PMM experiment, incoming light had photon energy of 54.0 eV and incident with 68° to the surface normal. The sample temperature was controlled by liquid helium during the measurements.

Figure 1 shows photoelectron spectroscopy (PES) spectra on cleaved SCG and MnPc/SCG taken at room temperature (RT) and ca. 10 K. Peak A is derived from Pc π-orbital as found for other MPcs. Peak B is uniquely observed for the MnPc as the highest occupied molecular orbital (HOMO) which is contributed strongly from Mn 3*d*-orbital. These peaks are shifted and become sharper at 10 K. Figures 2 (a-c) are the momentum maps at the energy of peak A (ΔE = 0.20 eV). In Fig. 2 (a), the intensity pattern from the SCG π-bands can be confirmed clearly. By adsorption of MnPc, the ring-like pattern along the π-bands of SCG at RT appeared (Fig. 2 (b)). On the other hand, the momentum map of MnPc/SCG at 10 K (Fig. 2 (c)) shows another intensity patterns with several lobes, where the faint ring-like pattern of the RT sample is superimposed. According to DFT calculations on MPc, the momentum map at HOMO shows the specific intensity patterns reflected C_{4v} symmetry [2]. Ring-like pattern suggests that π-orbital planes of the MnPc molecules are not ordered azimuthally on SCG at RT, then the several molecules make stable structure upon the cooling to give a specific lobe pattern. The presence of some disordered domains is indicated by the faint ring-like pattern at 10 K.

Additionally, another intensity pattern by six lobes appeared inside of the ring-like pattern at 10 K. Figures 2 (d-f) show band distribution maps corresponding to the momentum maps, respectively. In the distribution map of MnPc/SCG at 10 K (Fig. 2 (f)), another band dispersion can be confirmed inside of SCG π-bands and the value of k_x is coincident with the six-lobe pattern in the momentum map.

Since the interaction between MnPc and graphite is so weak [3], it is unlikely that a chemical change occurred between them. It is possible to consider that the appearance of band dispersion is due to phonon scattering at MnPc layers and derived from SCG π-bands. The reason for the appearance at 10 K may be due to the formation of oriented MnPc layers by cooling. These results lead to deeper understanding of weak molecule-substrate interactions.

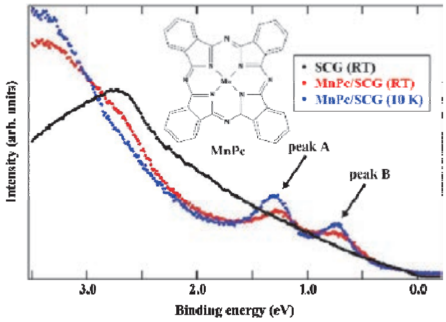

Fig. 1. Photoelectron spectra on the cleaved SCG and MnPc/SCG integrated over the whole angle. The structural formula of MnPc is shown in the inset.

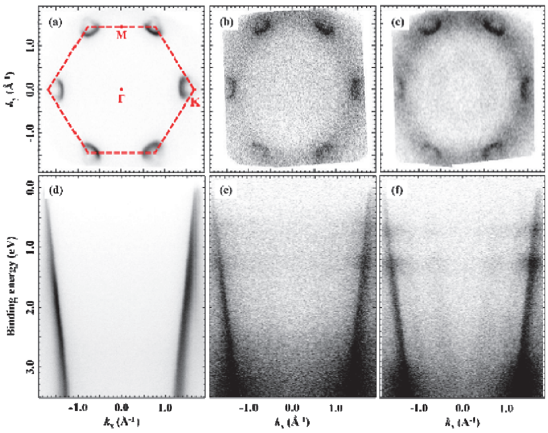

Fig. 2. (a-c): Momentum maps at peak A in Fig. 1. (a): Cleaved SCG and schematic image of hexagonal Brillouin zone. (b): MnPc/SCG at RT. (c): MnPc/SCG at 10 K. (d-f): Band distribution maps integrated over the range of k_y = (0.0±0.3) Å^{-1}. (d): Cleaved SCG. (e): MnPc/SCG at RT. (f): MnPc/SCG at 10 K.

[1] K. Nakamura *et al.*, Phys. Rev. B **85** (2012) 235129.
[2] D. Lüftner *et al.*, J. Elec. Spec. **195** (2014) 293.
[3] C. Isvoranu *et al.*, J. Chem. Phys. **131** (2009) 214709.

BL6U

Imaging the Domain Boundary of Ir(111) Thin Films by Momentum-selective PEEM Using Photoelectron Momentum Microscope

E. Hashimoto[1], H. Kurosaka[1], Y. Nishio[1], K. Hagiwara[2], F. Matsui[2] and S. Koh[1]
[1]*Department of Electrical Engineering and Electronics, College of Science and Engineering, Aoyama Gakuin University, 5-10-1 Fuchinobe, Chuo-ku, Sagamihara, Kanagawa 252-5258, Japan*
[2]*UVSOR Synchrotron Facility, Institute for Molecular Science, Okazaki 444-8585, Japan*

Iridium (Ir) is a transition metal belonging to the platinum elements group. Ir(111) is promising as a substrate for graphene growth by chemical vapor deposition (CVD). In addition, Ir(001) is used as a growth substrate for CVD diamond and a spin filter with high spin detection efficiency in spin-resolved photoemission spectroscopy. It is desired to establish methods for fabricating high quality Ir thin films at a few Å thick near the surface that can replace expensive bulk-single-crystals and methods for their characterization. In this study, we deposited Ir(111) thin films with high single-crystallinity by molecular beam epitaxy (MBE) and visualized the domain structure by momentum selective photoelectron emission microscopy (PEEM) using photoelectron momentum microscope [1,2].

We deposited Ir(111) thin films on α-Al_2O_3(0001) substrates by MBE method. First, the low-temperature buffer layer was deposited with the temperature of the substrate holder set at 500°C for 180 min. Then, the temperature of the sample holder was raised to 950°C, and the Ir(111) thin films were deposited for 120 min. By deposition for a total of 300 min, thin films with a thickness of 60 nm were grown. Afterwards, Ir(111) thin films were annealed under H_2 atmosphere at 1000°C for 60 min. Figures 1(a) and (b) show the XRD diffraction for the Ir layers on α-Al_2O_3(0001). Diffraction peaks caused by Ir(111) and α-Al_2O_3(0001) were observed in the $2\theta/\omega$ profile (Fig.1(a)). The XRD pole figure along Ir[111] is shown in Fig.1(b). The observed Bragg peaks displayed 6-fold symmetry, whereas the ideal Bragg peaks for Ir{111} exhibit 3-fold symmetry, thus indicating that Ir(111) contained twin domains.

Figures 2(a)-(c) show the band structures of Ir(111) thin films at Fermi energy by momentum-resolved photoelectron spectroscopy (MRPES). The field of view of MRPES is φ5 μm The photon energy was set to 100 eV. As shown in Fig. 2(a), we observed a 3-fold symmetry pattern of Ir. At the different measurement point 100 μm apart from the initial point, a 6-fold symmetry pattern corresponding to a domain boundary was observed (Fig.2(b)). With further movement of the measurement point, a 3-fold symmetry pattern rotated by 180 degrees from the 3-fold symmetry pattern at the initial point was observed (Fig.2(c)).

Momentum-selective PEEM images were acquired by inserting the contrast aperture into momentum space with the strongest photoelectron intensity in the MΓM direction ($E = E_F - 1$ eV, $k_x \simeq 0$ Å^{-1}, $k_y \simeq 1$ Å^{-1}, in Fig. 2(a)). Without inserting the aperture, the PEEM image without contrast was obtained, which did not reflect the domain structure, as shown in Fig.3(a). In Fig. 3(b), when the aperture was inserted, we observed that the bright region corresponded to the domain with band structure, as shown in Fig.2(a). On the contrary, when an aperture is inserted in the domain with Fig. 2(c), a PEEM image with inverted contrast can be imaged, as shown in Fig. 3(c). Repeating similar PEEM measurements in different regions, found that unidirectional domains exist over several hundred μm × several hundred μm. We successfully observed twin-domain structures with no chemical shifts and only geometric differences in band structure using momentum-selective PEEM measurements.

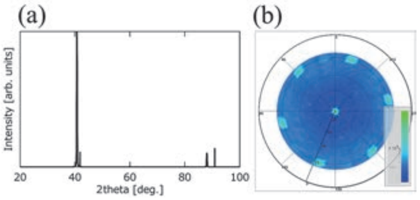

Fig. 1. (a) 2θ/ω profile and (b) pole figure of Ir(111) thin films deposited by MBE.

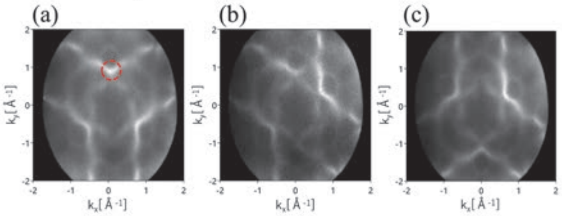

Fig. 2. The band structures of Ir(111) at Fermi energy. The observation point of (b) was moved 100 μm from (a), and (c) was moved 100 μm from (b).

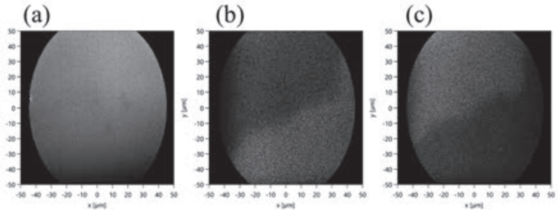

Fig. 3. PEEM images of Ir(111) thin films. (a) without inserting aperture, (b) and (c) with inserting aperture.

[1] F. Matsui *et al*., J. Phys. Soc. Jpn. **91** (2022) 097403.
[2] F. Matsui *et al*., Rev. Sci. Instrum. **94** (2023) 083701.

BL6B

Probing Molecular Vibration Dynamics of Layered Borophene Oxide Thin Films using *In-Situ* Variable-Temperature Infrared Spectroscopy

K. Kaminaga[1], K. Sasaki[1], H. Murakami[1], F. Teshima[2], A Kikuchi[1],
K. Tanaka[2], S. Maruyama[1] and Y. Matsumoto[1]
[1]*Department of Applied Chemistry, Tohoku University, Sendai 980-8579, Japan*
[2]*Institute for Molecular Science (IMS), National Institutes of Natural Sciences, 38 Nishigonaka, Myodaiji, Okazaki 444-8585, Japan*

Liquid crystals represent a distinctive mesophase exhibiting properties characteristic of both fluids and crystalline solids, and they are well-established as functional materials in electronic display technologies. While the field has historically been dominated by organic compounds due to their molecular flexibility, the synthesis of inorganic liquid crystals has proven challenging, largely attributed to the rigidity inherent in inorganic bonding. Nevertheless, the development of stable inorganic liquid crystals holds significant promise for applications in extreme environments where organic materials often prove inadequate.

A key advancement occurred in 2022 with the report of layered borophene oxide (BoL), synthesized from potassium borohydride (KBH_4) [1]. This material undergoes a structural phase transition to a liquid crystalline state at approximately 120°C, a process associated with dehydration reactions [2]. Notably, this liquid crystalline phase can be rendered metastable at ambient temperature through supercooling. Recognizing the potential for semiconductor applications, our research group has developed a vapor-phase synthesis protocol for BoL thin films using infrared laser deposition. This method involves the selective oxidation of KBH_4 precursor molecules, catalyzed by acetonitrile vapor under vacuum conditions (Fig.1 inset).

Previous infrared spectroscopic studies on bulk BoL characterized the modulation of O-H and B-O vibrational modes during the transition between crystalline and liquid crystalline phases [2]. However, despite X-ray diffraction analyses confirming the reversibility of this phase transition in thin films, the specific molecular-level structural alterations occurring within these films remain insufficiently understood.

To address this gap, the present investigation utilized temperature-variable Fourier-transform infrared (FT-IR) spectroscopy to analyze BoL thin films deposited on double side polished Si substrates. FT-IR spectroscopy was performed with a FT-IR microscope (JASCO, IRT-7000) at beamline BL6B. Infrared radiation was directed through a Michelson-type interferometer (JASCO, FT/IR-6100). The measurements were conducted in a reflectance configuration, with the incident IR beam aligned perpendicular to the surfaces of samples. To mitigate atmospheric interference, the IR absorbance spectra were derived by normalizing the reflectance spectra of the KBH_4 samples against that of a gold (Au) film. Measurements performed under atmospheric conditions successfully detected the characteristic B-O (~1500 cm^{-1}) and O-H (~3000 cm^{-1}) vibrational modes, thereby confirming the successful synthesis of the target thin films (Fig.1). On the other hand, attempts to perform measurements under vacuum were hindered by instrumental difficulties related to optical alignment.

In conclusion, future experimental work will focus on implementing refined optical axis calibration procedures to enable reliable vacuum-environment FT-IR measurements. This refinement is crucial for facilitating comprehensive in-situ observation of the temperature-dependent phase transition, free from atmospheric interference. Such optimized methodology will permit a systematic vibrational spectroscopic analysis of the structural reversibility between the crystalline and liquid crystalline phases at the molecular level.

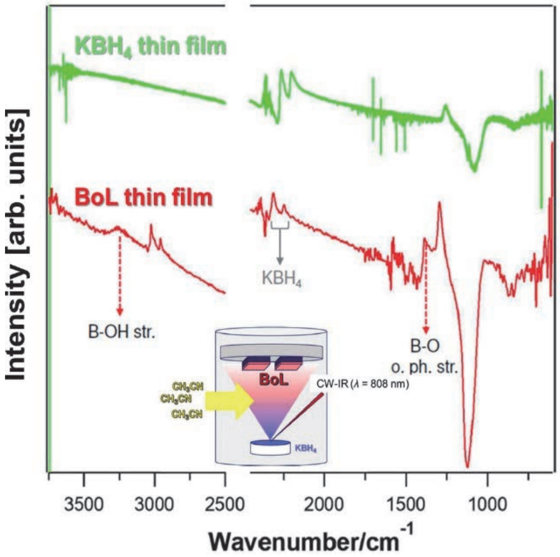

Fig. 1. IR spectra of KBH_4 thin film (green) and BoL thin film (red) under atmospheric conditions. Inset: Schematic of the experimental setup for BoL thin film growth.

[1] T. Kambe *et al*., J. Am. Chem. Soc. **141** (2019) 12984.
[2] T. Kambe *et al*., Nat Commun. **13** (2022) 1037.

BL7U

Electronic Structure Study of Topological Materials $Ge_2Bi_2Te_5$ and $Ge_3Bi_2Te_6$

Y. Dai[1], X. M. Ma[1] and C. Liu[1]
[1]*Southern University of Science and Technology (SUSTech), Shenzhen, Guangdong 518055, China*

The $MnBi_2Te_4(Bi_2Te_3)_n$ compounds, with $MnBi_2Te_4$ being a prototypical member, have been established as model systems of intrinsic magnetic topological insulators [1-3]. The characteristic van der Waals structure of $MnBi_2Te_4$ comprises alternating Te-Bi-Te-Mn-Te-Bi-Te layers with single Mn layers per unit cell, supporting antiferromagnetic (AFM) ordering below 24 K and manifesting intricate magneto-topological coupling [4, 5]. However, a fundamental constraint arises from the limited magnetic layer density: the single-Mn-layer configuration leads to weak interlayer magnetic coupling and suppresses Neel temperatures, hindering potential applications.

Recent theoretical works propose that structural engineering through magnetic layer stacking – as exemplified in $Mn_2Bi_2Te_5$ and $Mn_3Bi_2Te_6$ derivatives – could enhance magnetic ordering temperatures [6, 7]. On one hand, $Mn_2Bi_2Te_5$ has been predicted to host a *dynamic axion insulator* state, offering an unprecedented platform for exploring topological electromagnetic responses [6]. On the other hand, first-principles calculations reveal a magnetic-order-dependent topological phase transition in $Mn_3Bi_2Te_6$, with the AFM configuration remaining topologically trivial while the ferromagnetic (FM) ordering induces nontrivial topology [7]. Despite these compelling predictions, experimental verification remains elusive due to formidable single-crystal growth challenges.

To circumvent the synthesis bottleneck, we adopt a chemical substitution strategy leveraging the structural stability of isostructural germanium analogs $Ge_2Bi_2Te_5$ and $Ge_3Bi_2Te_6$ [8, 9]. Through progressive substitution of Ge with Mn in $(Ge_{1-x}Mn_xTe)_mBi_2Te_3$ (m = 2, 3), we aim to engineering systems combining robust magnetic ordering with topological functionality.

Our experimental investigation combines angle-resolved photoemission spectroscopy (ARPES) measurements at UVSOR BL7U with systematic Mn doping. Initial characterization of parent compounds $Ge_2Bi_2Te_5$ (Fig. 1a) and $Ge_3Bi_2Te_6$ (Fig. 2a) established baseline electronic structures. Subsequent doping studies focus on nominal Mn concentration of 20% and 30% in $(Ge_{1-x}Mn_x)_2Bi_2Te_5$, and 30% in $(Ge_{1-x}Mn_x)_3Bi_2Te_6$. ARPES data reveal progressive Fermi level upshifting with increasing Mn content, indicative of n-type dosage. The $(Ge_{1-x}Mn_x)_3Bi_2Te_6$ system manifests electronic features suggestive of hole-doped analogs to its m = 2 counterpart. While both systems preserve threefold rotational symmetry in constant-energy contours (Fig. 3d), subtle differences in their band dispersion await theoretical interpretation.

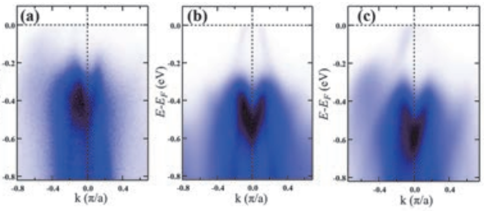

Fig. 1. Band evolution on $(Ge_{1-x}Mn_x)_2Bi_2Te_5$ with different nominal Mn doping levels $x = 0$ (a), $x = 0.2$ (b) and $x = 0.3$ (c) ($h\nu = 20$ eV). The measurement direction is Γ-M for (a) and (c), and Γ-K for (b). As x increases, the Fermi level moves upward.

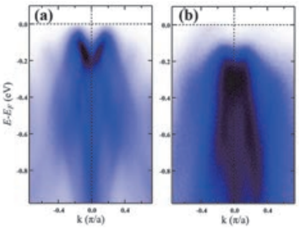

Fig. 2. Band evolution on $(Ge_{1-x}Mn_x)_3Bi_2Te_6$ with different nominal Mn doping levels $x = 0$ (a) and $x = 0.2$ (b) ($h\nu = 20$ eV). The measurement direction is Γ-K for (a) and Γ-M for (b). As x increases, the Fermi level moves upward.

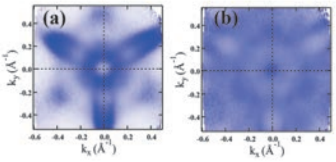

Fig. 3. ARPES constant-energy contour of $(Ge_{0.8}Mn_{0.2})_2Bi_2Te_5$ with $h\nu = 21$ eV. The binding energy of each penal is 0.25 eV (a) and 1.35 eV (b).

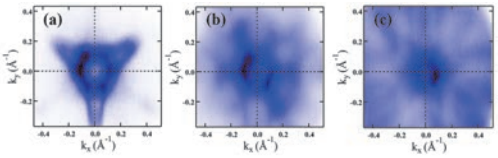

Fig. 4. ARPES constant-energy contour of $Ge_3Bi_2Te_6$ with with $h\nu = 19$ eV. The binding energy of each penal is 0.05 eV (a), 0.35 eV (b) and 1.45 eV (c).

[1] D. Zhang *et al.*, Phys. Rev. Lett. **122** (2019) 206401.
[2] Klimovskikh *et al.*, npj Quantum Mater. **5** (2020) 54.
[3] H. Deng *et al.*, Nat. Phys. **17** (2021) 36.
[4] J. Zhang *et al.*, Chin. Phys. Lett. **37** (2020) 077304.
[5] A. Gao *et al.*, Nature **595** (2021) 521.
[6] J. Zhang *et al.*, Chin. Phys. Lett. **37** (2020) 077304.
[7] W. Wu *et al.*, J. Phys.: Condens. Matter **36** (2024) 125701.
[8] Matsunaga *et al.*, Acta Cryst. B **63** (2007) 346.
[9] L. E. Shelimova *et al.*, Inorganic Materials **36** (2000) 235.

BL7U

Electronic State Analysis of Bcc-Cu Thin Film on FeCo/MgO(100)

S. Takezawa[1,2] and N. Nagamura[1,2,3]
[1]*Graduate School of Advanced Engineering, Tokyo University of Science, Tokyo 125-8585, Japan*
[2]*Center for Basic Research on Materials, National Institute for Materials Science, Tsukuba 305-0003, Japan*
[3]*Research Institute of Electrical Communication, Tohoku University, Sendai 980-0812, Japan*

Copper typically crystallizes in a face-centered cubic (fcc) structure as its most stable phase. However, in nanocrystalline systems or certain ultrathin films, it can adopt a metastable body-centered cubic (bcc) structure[1,2]. Notably, bcc-Cu/FeCo multilayers have been reported to exhibit high magnetoresistance (MR) ratios in three-layer giant magnetoresistance (GMR) devices[3]. This enhancement in MR ratio is strongly influenced by modulation of the electronic states at the Cu/FeCo interface, which arises from the formation of the metastable Cu phase. Nevertheless, there have been no experimental reports directly observing the electronic structure of bcc-Cu and its thickness-dependent modulation. This is primarily due to the difficulty in fabricating clean bcc-Cu(001) surfaces using conventional sputtering techniques.

In this study, we performed angle-resolved photoemission spectroscopy (ARPES) measurements on bcc-Cu/FeCo/MgO(001) thin films grown *in-situ* by molecular beam epitaxy (MBE) at the UVSOR BL7U beamline. The MgO(001) substrates were annealed at 500 °C for 60 minutes to clean the surface. The FeCo underlayer was deposited at a substrate temperature of 300 °C. The epitaxial growth of the FeCo layer and the cleanliness of the FeCo(001) surface were confirmed by low-energy electron diffraction (LEED) measurements (Fig. 1). Subsequently, a 1 nm-thick Cu layer was deposited at room temperature, and the formation of a clean bcc-Cu(001) surface was confirmed by LEED (Fig. 1). For comparison, an additional 20~ nm of Cu was deposited at room temperature to intentionally induce a structural transition to fcc-Cu, thereby fabricating fcc-Cu/FeCo/MgO(001) thin films. ARPES measurements were performed immediately after each deposition step.

Figure 2 (c)-(e) shows the ARPES results for FeCo(001), bcc-Cu(001), and fcc-Cu(001). ARPES measurements of FeCo ware performed at T = 250 K, ARPES measurements of bcc-Cu and fcc-Cu were performed at T = 15 K. Upon Cu deposition, a flat band attributed to Cu 3*d* electrons appeared near a binding energy = 2–3 eV. Furthermore, the electronic structure of Cu was found to be modulated as the film thickness increased. This modulation is considered to reflect the structural phase transition from the metastable bcc phase to the stable fcc phase. In addition, the spectra exhibited photon energy dependence, suggesting the presence of a three-dimensional electronic structure. These results not only provide fundamental insights into the electronic properties of bcc-Cu but also indicate the potential for tuning the electronic structure of Cu through thickness modulation.

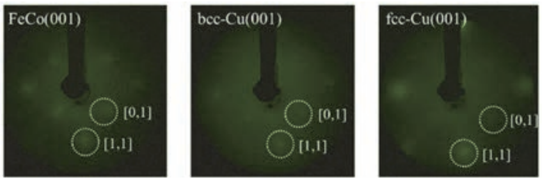

Fig. 1. LEED patterns of FeCo(001), bcc-Cu(001), fcc-Cu(001). Clean surfaces are observed respectively. All images are taken at incident electron beam energy = 210 eV.

[1] H. Li *et al*, Phys. Rev. B, **43**, (1991) 8.
[2] Z. Wang *et al*, Phys. Rev. B, **35**, (1987) 17.
[3] K. B. Fathoni *et al*., APL Mater., **7**, (2019) 111106.

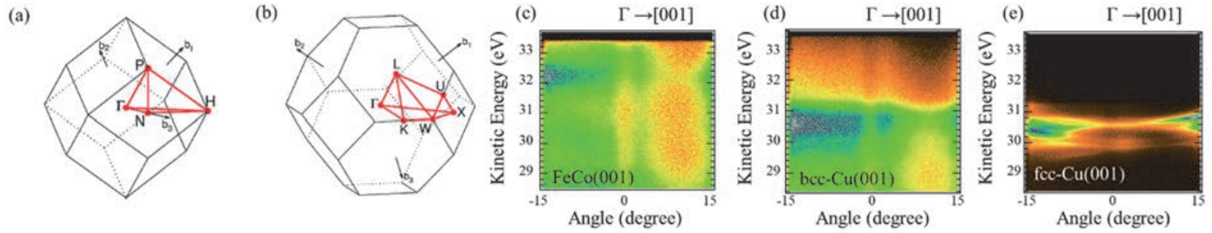

Fig. 2. (a) Brillouin zone of bcc lattice. (b) Brillouin zone of fcc lattice. (c)-(e)ARPES spectra of each sample along [001] axis. All spectra are measured at hν = 38 eV. Modulation of electronic states depending on the thickness of the Cu film was observed.

BL7U

Thin-Film Growth and Electronic Structure Study on YbSb/GaSb(110)

Y. Chen[1], T. Nakamura[2,1], R. Ichikawa[1], H. Yamaguchi[1], K. Nishihara[1],
K. Tanaka[3] and S. Kimura[2,1,4]
[1]*Department of Physics, Graduate School of Science, The University of Osaka, Toyonaka 560-0043, Japan*
[2]*Graduate School of Frontier Biosciences, The University of Osaka, Suita 565-0071, Japan*
[3]*UVSOR Synchrotron Facility, Institute for Molecular Science, Okazaki 444-8585, Japan*
[4]*Department of Material Molecular Sciences, Institute for Molecular Science, Okazaki 444-8585, Japan*

Rare-earth mono-pnictide (*REPn*: *RE* = rare-earth element, *Pn* = pnictogen (Group V element)) exhibits a variety of magnetic properties, such as extreme magnetoresistance (XMR) reaching up to more than 10^6 % of the value at zero field [1], and a complicated magnetic phase transition in CeSb [2]. These characteristic physical properties originate from the hybridization between localized 4*f* orbitals in rare-earth elements and *p* orbitals in pnictogen elements, namely *p*-*f* mixing [3]. Recently, the existence of spin-polarized surface states in some *RE*Sbs and *RE*Bis [4] and the high-quality epitaxial thin-film grown by a molecular beam epitaxy (MBE) method were reported [5]. These novel studies lead us to anticipate possibilities as potential applications in spintronics devices. Meanwhile, despite the intense study on the *REPn* family, the knowledge of Yb mono-pnictides, such as YbSb, is still limited because of the difficulty in bulk single-crystal synthesis due to the high vapor pressure of Yb. We are focusing on the MBE growth and the electronic structure study on YbSb thin film. So far, we have tried the growth of YbSb thin film on the GaSb(001)-c(2×6) surface cleaned by Ar^+ sputtering and annealing. The obtained thin film shows an unexpected (2×1) reconstructed surface and a Fermi surface with 2-fold rotational symmetry [6]. Here, we fabricated YbSb thin films on another GaSb surface (110) to understand the origin of the anisotropy of YbSb/GdSb(001)-c(2×6).

To clarify the role of the surface-preparing method, we used two cleaning methods; one is Ar^+ sputtering at the substrate temperature of 720 K for 30 minutes, and the other is direct cleaving along the (110) plane. Yb and Sb were co-evaporated onto the cleaned substrates at 570 K with the flux-rate ratio of Yb and Sb as 1:1.1. Figure 1 shows LEED patterns measured after the deposition of YbSb for ~15 ML. For the thin-film growth on both substrates, streaks along the [001] direction with the same spacing as the diffraction spots of GaSb(110) on the $[\bar{1}10]$ direction are observed. This result suggests that the substrate-preparing method is not essential for the sample quality.

Electronic structures of the differently prepared samples were detected with a synchrotron-based ARPES measurement. In the ARPES measurement, no clear dispersion could be observed along the [001] direction because of the lack of the long-range periodicity. On the other hand, as shown in Fig. 2, three hole bands and one electron pocket can be easily identified along the $[\bar{1}10]$ direction for both substrates. The obtained ARPES image is consistent with the band calculation of YbSb [7] and the ARPES results of other *RE*Sbs [8]. These results suggest that the fabricated films are YbSb with a 1D-like growth along the $[\bar{1}10]$ direction. One possible explanation could be dimer rows along the $[\bar{1}10]$ direction form a staircase-like structure with two different heights along the [001] direction. Another possibility is that the obtained Yb-Sb thin film is a different compound, $YbSb_2$, reported in a recent paper [9]. To clarify the origin of the 1D-like feature, further detailed studies on chemical composition and crystallography by XPS and XRD are needed.

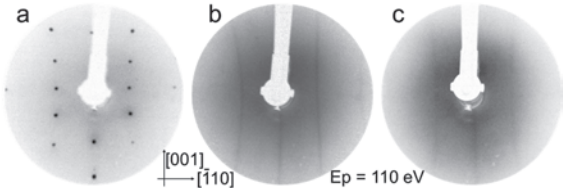

Fig. 1. LEED patterns of GaSb(110) cleaving surface (a), YbSb thin film growth on GaSb(110) substrates prepared by cleaving (b), and by Ar^+ sputtering (c), measured at 14 K.

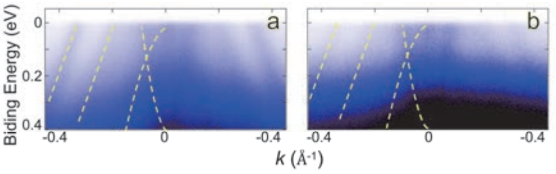

Fig. 2. ARPES intensity plots along the $[\bar{1}10]$ direction and measured with 21-eV photons at 14 K of the YbSb thin-films growth on GaSb(110) substrates prepared by cleaving (a) and by Ar^+ sputtering (b).

[1] L. Ye *et al.*, Phys. Rev. B **97** (2018) 081108.
[2] J. Rossat-Mignod *et al.*, J. Magn. Magn. Mater. **52** (1985) 111.
[3] H. Takahashi and T. Kasuya, J. Phys. C: Solid State Phys. **18** (1985) 2697, 2709, 2721, 2731, 2745, 2755.
[4] K. Kuroda *et al.*, Phys. Rev. Lett. **120** (2018) 086402.
[5] S. Chatterjee *et al.*, Phys. Rev. B **99** (2019) 125134.
[6] Y. Chen *et al.* UVSOR Activity Report **51** (2024) 164.
[7] X. Duan *et al.*, Commun. Phys. **1** (2018) 71.
[8] P. Li *et al.*, npj Quantum Mater. **8** (2023) 22.
[9] R. Dhara *et al.*, Phys. Rev. Mater. **9** (2025) 034801.

BL7U

Observation of Electronic Structure of Chiral Magnet $GdNi_3Ga_9$ by ARPES

Y. Tanimoto[1], Y. Nakashima[1], H. Sato[2], K. Tanaka[3], S. Nakamura[4] and S. Ohara[4]
[1]*Graduate School of Advanced Science and Engineering, Hiroshima University,*
Higashi-Hiroshima 739-8526, Japan
[2]*Hiroshima Research Institute for Synchrotron Radiation Science, Higashi-Hiroshima 739-0046, Japan*
[3]*UVSOR Synchrotron Facility, Institute for Molecular Science, Okazaki 444-8585, Japan*
[4]*Graduate School of Engineering, Nagoya Institute of Technology, Nagoya 466-8555, Japan*

Trigonal $GdNi_3Ga_9$ has a chiral crystal structure belonging to space group of $R32$ (No. 155) [1] and is of interest as a 4*f* chiral metallomagnetic compound [2]. The localized Gd 4*f* spins are magnetically ordered below T_N=19.5 K, forming an antiferromagnetic structure in the *ab*-plane, and exhibiting left- or right-handed helimagnetism with a propagation vector $\boldsymbol{q}$=(0, 0, 1.485) [2]. Spin-polarized conduction electrons are thought to be responsible for this phenomenon. $GdNi_3Ga_9$ has the same crystal structure as $YbNi_3Al_9$, the first discovered 4*f* chiral metallomagnetic compound [3]. $YbNi_3Al_9$ exhibits helimagnetism with $\boldsymbol{q}$=(0, 0, 0.82) [4], while ferromagnetic order in the *ab*-plane, in contrast to $GdNi_3Ga_9$. Thus, a comparative study for $GdNi_3Ga_9$ is expected.

We have previously performed angle-resolved photoemission spectroscopy (ARPES) on $YbNi_3Al_9$ and observed five hole-like Fermi surfaces around the $\overline{\Gamma}$ point and one electronic-like Fermi surface around the $\overline{K}$ point [5]. In this study, we conducted ARPES on $GdNi_3Ga_9$ to investigate the Fermi surface and band structure of conduction electronic states near the Fermi level (E_F). The experiments were carried out at BL7U of UVSOR-III using an electron analyzer (A-1, MB-Scientific). Single crystals for the ARPES measurements were synthesized by the flux-method using gallium as the solvent [2] and were cleaved *in situ* under an ultrahigh vacuum of ~5×10^{-9} Pa.

Figures 1(a) and 1(b) present ARPES intensity plots of $GdNi_3Ga_9$ measured at $h\nu$=24 eV with *p*-polarized and *s*-polarized geometries, respectively, along the $\overline{\Gamma}$-$\overline{M}$ direction of the surface Brillouin zone. Measurements were performed at 7 K, below T_N. At least three hole-like bands were observed around the $\overline{\Gamma}$ point in Fig. 1(a). On the other hand, Fig. 1(b) clearly shows two hole-like bands crossing E_F at k_x=0.3 and 0.5 Å^{-1}, as well as a convex-upward band around the $\overline{\Gamma}$ point. The shape of the observed bands closely resembles those of $YbNi_3Al_9$ [5].

Figures 2(a) and 2(b) show the Fermi surfaces of $GdNi_3Ga_9$ measured at $h\nu$=24 eV and T=7 K with *p*-polarized and *s*-polarized geometries, respectively. In Fig. 2(a), at least three hole-like Fermi surfaces, corresponding to the bands in Fig. 1(a), exhibit an approximately six-fold symmetry. In Fig. 2(b), two hole-like Fermi surfaces are observed, and that around k_x=0.4 Å^{-1} appears three-fold symmetric. The hole-like Fermi surfaces of $GdNi_3Ga_9$ appear larger compared to those of $YbNi_3Al_9$.

We have also measured ARPES spectra at 25 K above T_N. A remarkable change in the shape of the bands was not detected.

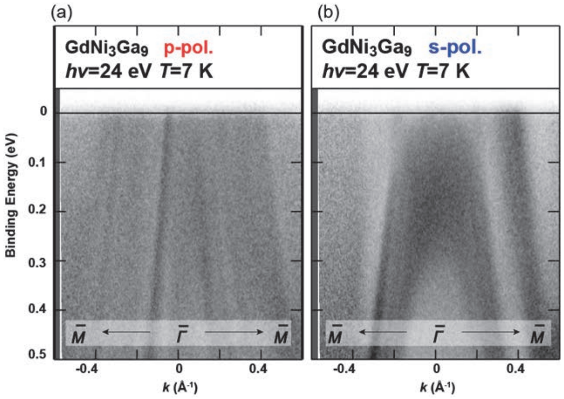

Fig. 1. ARPES intensity plots of $GdNi_3Ga_9$ measured along the $\overline{\Gamma}$-$\overline{M}$ direction at $h\nu$=24 eV and T=7 K with (a)*p*- and (b)*s*-polarized geometry.

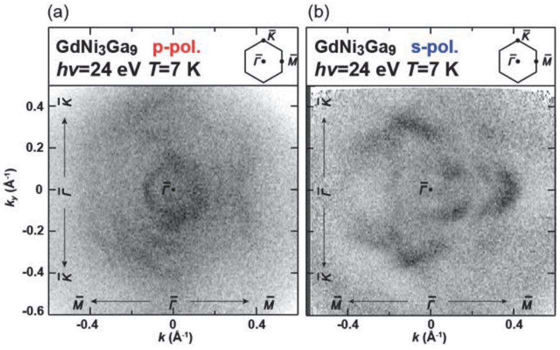

Fig. 2. The Fermi surfaces of $GdNi_3Ga_9$ measured at $h\nu$=24 eV and T=7 K with (a)*p*- and (b)*s*-polarized geometry.

[1] V. Topertser *et al.*, Chem. Met. Alloys **12** (2019) 21.
[2] S. Nakamura *et al.*, Phys. Rev. B **108** (2023) 104422.
[3] S. Ohara *et al.*, JPS Conf. Proc. **3** (2014) 017016.
[4] T. Matsumura *et al.*, J. Phys. Soc. Jpn. **86** (2017) 124702.
[5] Y. Tanimoto *et al.*, in preparation.

BL7U

Photon Energy-dependent ARPES Study of Secondary Photoemission on $CaTiO_3$ and $BaTiO_3$

C.Z. Huang[1], C.Y. Hong[1], C.Y. Jiang[1,2], X.N. Zheng[1,2] and R.-H. He[1]
[1]*School of Science, Westlake Institute for Advanced Study, Westlake University, Hangzhou 310064, China*
[2]*Department of Physics, Fudan University, Shanghai 200433, China*

The discovery of the anomalous photocathode quantum material $SrTiO_3$ (STO) has garnered significant interest, yet the mechanism behind its extraordinary properties remains unclear[1]. Recently, a theoretical model introducing a novel Auger process that recycles secondary electrons and induces the emission of tertiary electrons has been proposed to explain the intense coherent photoemission in STO[2]. This model also predicts other perovskite oxides as candidate photocathode quantum materials and calls for further explorations.

As a technique that can directly probing the electronic structure of materials, Angle-resolved photoemission spectroscopy (ARPES) serves as a powerful tool for studying and discovering novel quantum materials. Photon energy-dependent ARPES measurements on STO have revealed that the intensity of the coherence peak is influenced by the excitation photon energy, with a threshold beyond which the peak intensity increases significantly[3]. $CaTiO_3$ (CTO) and $BaTiO_3$ (BTO), as perovskite oxides, are predicted to exhibit secondary photoemission characteristics similar to those of STO. Investigations into these materials may offer valuable insights into the mechanism underlying the exotic properties of these quantum materials.

Here, we report photon energy-dependent measurements on CTO and BTO thin films. The thin films were prepared by pulsed laser deposition and annealed at 1100-1200 °C for several hours to achieve clean surfaces for ARPES measurements. ARPES measurements were conducted at the BL7U beamline of UVSOR, utilizing photon energies ranging from 7.1 to 22 eV, with a sample temperature of 11 K.

Figure 1(a) shows the secondary photoemission spectrum (SPS) of CTO measured with photon energies ranging from 7.1 to 22 eV. The SPS peak at a kinetic energy of 4.3 eV remains nearly unchanged in position despite varying photon energy, while its intensity exhibits a clear photon energy dependence. As the photon energy increases to 8.1 eV, the peak intensity rapidly rises, reaching its maximum at a photon energy of 8.6 eV, and then begins to decrease. When the photon energy exceeds 12 eV, the peak intensity stabilizes.

For BTO, the variation of SPS peak intensity at a kinetic energy of 3.6 eV with photon energy follows a trend similar to that of CTO, exhibiting a threshold of 8.1 eV, a maximum of 8.8 eV, and stabilization above 12 eV.

The photon energy dependence of SPS peak intensity in CTO and BTO closely resembles that of STO, indicating a common origin for the anomalous secondary photoemission in these materials. Further investigations, such as examining the film thickness-dependence of SPS peak intensity, may provide more insights for understanding and utilizing these novel quantum materials.

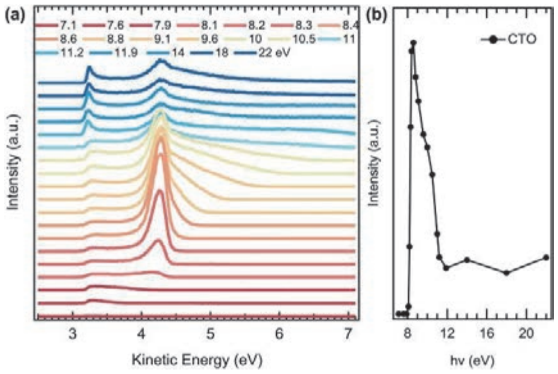

Fig. 1. (a) The secondary electron emission spectra of CTO measured with different photon energies. (b) The intensity of the peak at 4.3 eV as a function of photon energy.

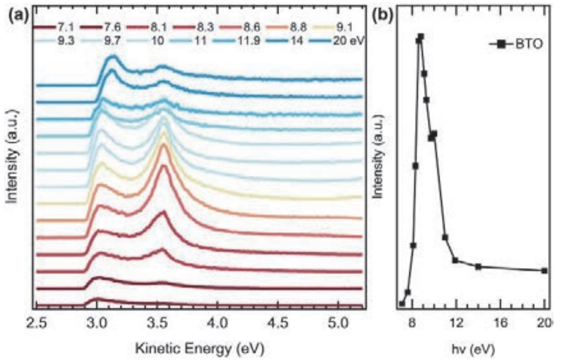

Fig. 2. (a) The secondary electron emission spectra of BTO measured with different photon energies. (b) The intensity of the peak at 3.6 eV as a function of photon energy.

[1] C. Hong *et al.*, Nature **617** (2023) 493.
[2] M. Matzelle *et al.*, arXiv:2405.06141 (2024).
[3] C. Hong *et al.*UVSOR Activity Report **51** (2023) 162.

BL7B

Polarization Dependence of Solid-Liquid Interfaces Probed by Attenuated Total Reflectance Ultraviolet (ATR-UV) Spectroscopy

I. Tanabe[1], T. Kakinoki[2] and K. Fukui[2]
[1]*Department of Chemistry, College of Science, Rikkyo University, Toshima 171-0021, Japan*
[2]*Department of Materials Engineering Science, Graduate School of Engineering Science,*
The University of Osaka, Toyonaka 560-8531, Japan

Electric double-layer organic field-effect transistors (EDL-OFETs) have garnered significant interest for their ultra-low operating voltage (<1 V), which is markedly lower than that of conventional SiO_2-gated OFETs (>10 V). This reduced voltage is achieved through the formation of a high electric field within the electric double layer (EDL), which accumulates at the interface between the organic semiconductor and the electrolyte. Consequently, understanding and optimizing the organic semiconductor/electrolyte interface is crucial for the performance of EDL-OFETs.

Attenuated Total Reflection (ATR) spectroscopy is a useful method for studying interfaces. In particular, in the ultraviolet (UV) region, it provides valuable information about the electronic states of materials. We have previously utilized ATR-UV spectroscopy with a deuterium lamp as a light source to investigate the interfaces between organic semiconductors or metals and electrolytes [1, 2]. Through this approach, we have elucidated the electronic states of organic semiconductors and interfacial electrolytes depending on the applied voltage. While a deuterium lamp emits unpolarized light, the use of polarized light is expected to provide insights into the orientation of organic semiconductors and interfacial electrolytes. Therefore, in this study, we aimed to develop a new spectroscopic system utilizing polarized light obtained from BL7B at UVSOR.

A thin film of C9-DNBDT-NW (Figure 1a), a material reported to exhibit excellent mobility, was deposited onto a sapphire ATR prism and measured using ATR setup. By adjusting the orientation of the prism relative to the incident light, the polarization characteristics of the spectra were investigated. The results, shown in Figures 1b and 1c, reveal a clear polarization dependence. As shown in Figure 1b, *s*-polarized incident light produced distinct absorption peaks within the 200–500 nm range, whereas *p*-polarized light exhibited no such prominent features(Figure 1c).

Figures 1d and 1e illustrate the polarization-dependent absorption spectra of C9-DNBDT-NW, as calculated using time-dependent density functional theory (TD-DFT). The results indicate that along the x-axis (Figure 1d), multiple strong absorption features were predicted, whereas along the z-axis, almost no absorption was observed. Considering the experimental results, it is suggested that this thin film is structured with the x-axis oriented perpendicularly to the substrate.

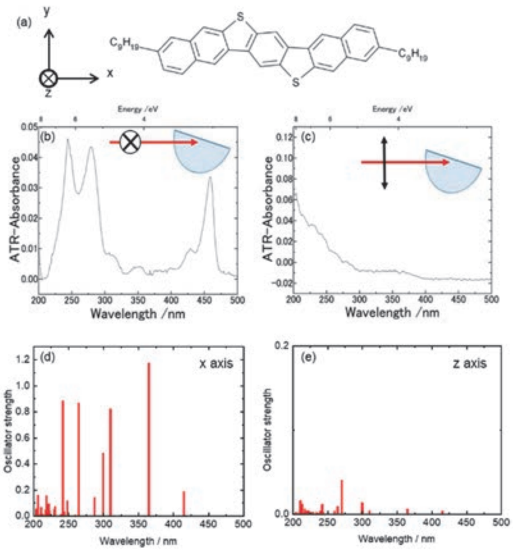

Fig. 1. (a) The structural formula of C9-DNBDT-NW. (b, c) Polarization dependence of ATR spectra of C9-DNBDT-NW on a sapphire prism. (d, e) Calculated vertical transitions along (d) x- and (e) z-axis of a C9-DNBDT-NW molecule.

Thus, polarization-dependent ATR spectroscopy enables the determination of the molecular orientation in organic thin films deposited on a sapphire substrate. Additionally, a key feature of ATR spectroscopy in the ultraviolet region is its short probing depth, limited to tens of nanometers due to the penetration depth of the evanescent wave. Moreover, by adjusting the incident angle, this probing depth can be finely controlled on the nanometer scale. Further advancements in this technique are expected to enable the investigation of electrochemical responses and the organic semiconductor-electrolyte interface.

[1] I. Tanabe *et al.*, Anal. Chem. **91** (2019) 3436.
[2] I. Tanabe *et al.*, Commun. Chem. **4** (2021) 88.

UVSOR User 13

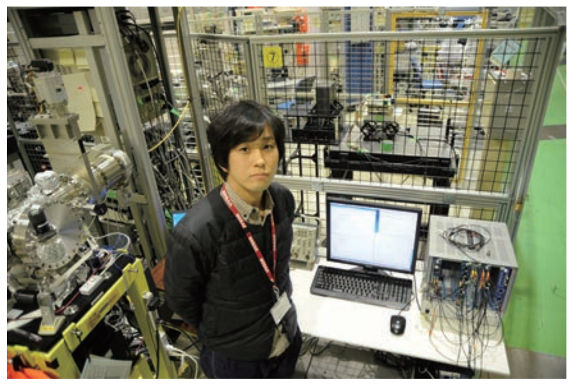

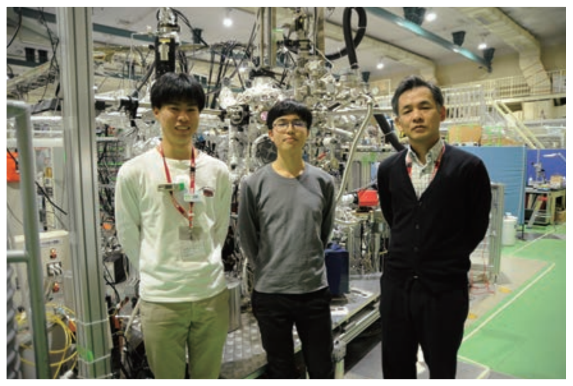

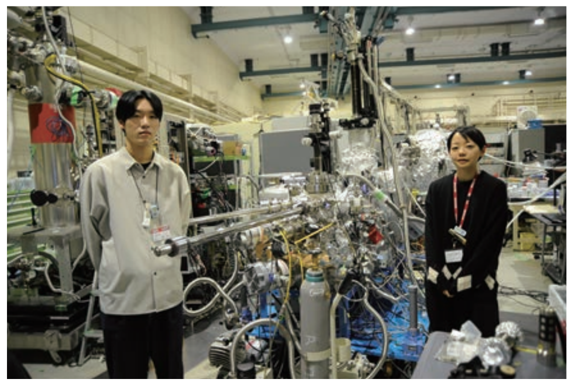

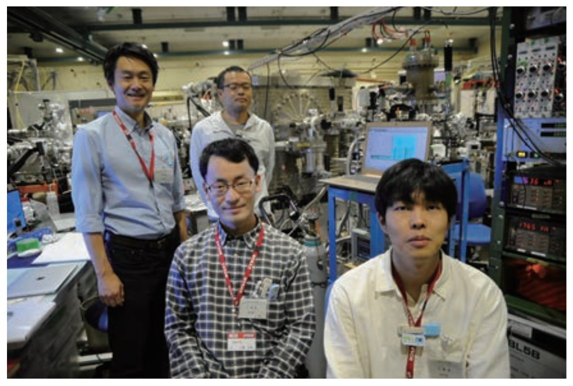

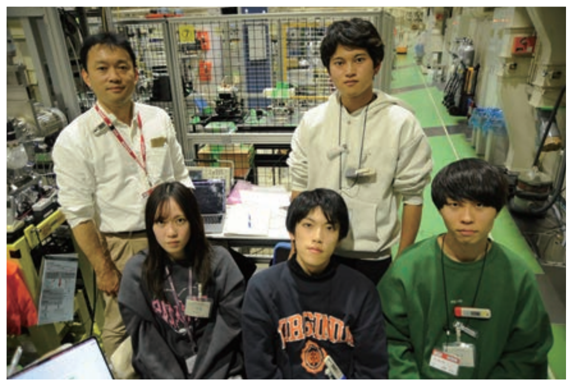

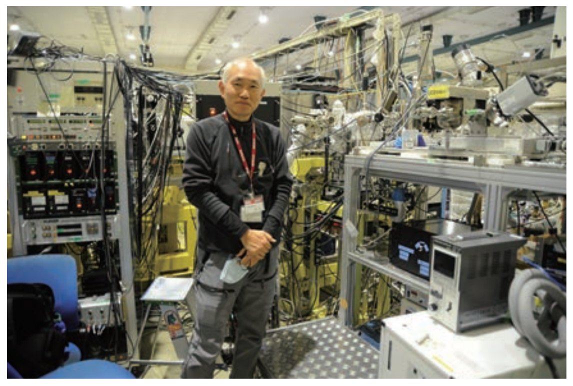

III-5

Life, Earth and Planetary Sciences

BL1U

Circularly Polarized Lyman-α Light Irradiation on Racemic Amino Acid Film to Verify the Cosmic Scenario of Origin of Homochirality

M. Kobayashi[1], K. Matsuo[2], M. I. A. Ibrahim[2], H. Chimura[1], J. Takahashi[3], K. Shimizu[4], H. Ota[4,5], Y. Satake[6], T. Minato[7], N. Takada[7], G. Fujimori[7], K. Kobayashi[8,9], Y. Kebukawa[9], M. Katoh[2,4] and H. Nakamura[1,6]

[1]*National Institute for Fusion Science, Toki city 509-5292, Japan*
[2]*Reserach Institute for Synchrotron Radiation Science, Hiroshima Univ., Higashi-Hiroshima 739-0046, Japan*
[3]*Graduate School of Maritime Sciences, Kobe University, Kobe 658-0022, Japan*
[4]*UVSOR Synchrotron Facility, Institute for Molecular Science, Okazaki city 444-8585, Japan*
[5]*Japan Synchrotron Radiation Research Institute, 1-1-1, Kouto, Sayo-cho, Sayo-gun, Hyogo 679-5198, Japan*
[6]*Nagoya University, Furo-cho, Chikusa-ku, Nagoya 464-8601, Japan*
[7]*Institute for Molecular Science, Okazaki city 444-8585, Japan*
[8]*Department of Chemistry and Life Science, Yokohama National University, Yokohama 240-8501, Japan*
[9]*Department of Earth and Planetary Sciences, Institute of Science Tokyo, Meguro-ku, Tokyo 152-8550 Japan*

The homochirality of life remains one of the most enigmatic issues in the study of the origin of life. A proposed mechanism for symmetry breaking involves irradiation by circularly polarized light (CPL). To investigate the photoreaction of amino acids induced by vacuum ultra-violet (VUV) CPL irradiation, we performed experiments where amino acids in a solid state were irradiated with CPL. This study focuses on Lyman-α (121.6 nm in wavelength), a leading candidate for selective photolysis when circularly polarized.

To investigate the photoreaction of amino acids caused by VUV CPL irradiation, we developed a VUV CPL irradiation system at the beamline BL1U in UVSOR at the Institute for Molecular Science [1]. Lyman-α CPL was generated in BL1U, and racemic alanine film specimens were irradiated with this CPL beam. After irradiation, distinct optical activity was observed, with positive and negative values of the optical anisotropy factor for right-handed (R) -CPL and left-handed (L) -CPL irradiation, respectively. However, the anisotropy factor spectra are broad in the measured wavelength range of 180–240 nm, differing from those of enantiopure alanine samples [1]. These results suggest that Lyman-α CPL irradiation not only caused simple preferential photolysis of enantiopure alanine molecules but also introduced additional effects such as oligomerization or polymerization.

These effects were corroborated by LC-MS analysis. The non-irradiated alanine sample predominantly displayed a single peak corresponding to the protonated alanine monomer $[\mathrm{Ala} + \mathrm{H}]^+$ ($\mathrm{NH_3^+}$-$\mathrm{CHCH_3}$-COOH) of m/z = 90. In contrast, the Lyman-α light-exposed samples exhibited additional complex peaks, which suggest the formation of larger molecules, such as oligomeric alanine adducts or modified oligomers, as inferred from their fragmentation patterns with high abundances of m/z values in the range 170 – 450.

It was also observed that Lyman-α CPL irradiation induced the formation of circular network ag-aggregates on the order of 100 nm in the surface of the alanine film with scanning probe microscopy (SPM) measurements, as shown in Fig.1. These results may suggest dimerization, polymerization, or micro-crystallization induced by the high photon energy of the Lyman-α CPL. Further investigations are ongoing to study the photoreaction of amino acids caused by VUV CPL irradiation.

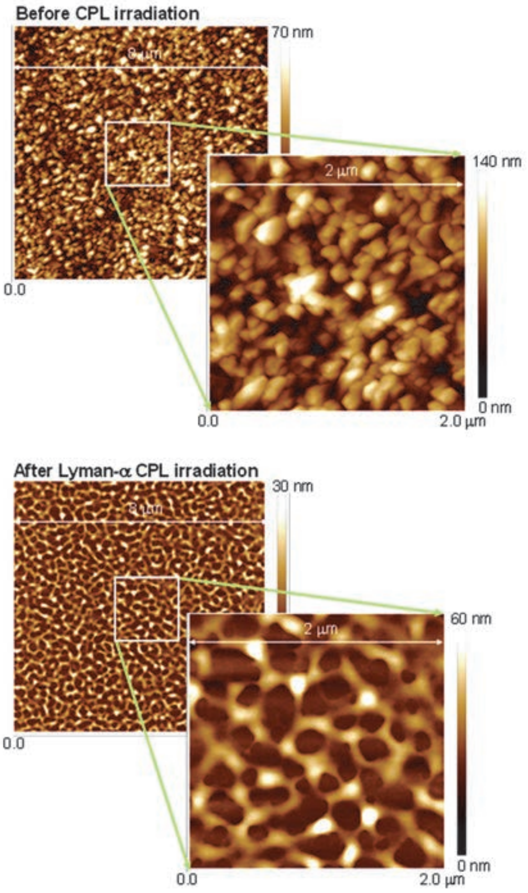

Fig. 1. Topographic images of the DL-alanine film obtained by SPM before (upper) and after (lower) CPL irradiation.

[1] M. Kobayashi *et al.*, Chirality **36** (2024) e70004.

BL1U

Experimental and Theoretical Studies Towards Observing Interactions between Biomolecules and Ultraviolet Optical Vortex

K. Matsuo[1,3,4], H. Kawaguchi[2], R. Imaura[3], S. Hashimoto[3], Y. Nishihara[4],
H. Ota[5] and M. Katoh [1,3,4,5]
[1]*Reseach Institute for Synchrotron Radiation Science, Hiroshima University, Higashi-Hiroshima 739-0046, Japan*
[2]*Muroran Institute of Technology, Muroran 050-8585, Japan*
[3]*Graduate School of Advanced Science and Engineering, Hiroshima University,*
Higashi-Hiroshima 739-8526, Japan
[4]*School of Science, Hiroshima University, Higashi-Hiroshima 739-8526, Japan*
[5]*UVSOR Synchrotron Facility, Okazaki 444-8585, Japan*

Chirality is an important structural factor in understanding the properties and functions of materials. Circular dichroism spectroscopy using right- and left-handed circularly polarized light with spin angular momentum (SAM: s) can observe the chirality of biomolecules in the ultraviolet region below 300 nm. On the other hand, right- and left-handed optical vortex with orbital angular momentum (OAM: l) are also expected to be a method for observing chirality, but there are few reports of observations of the interaction between the chirality of biomolecules and optical vortex [1-3], because a method for generating optical vortex in the ultraviolet region has not been established. In this study, in order to observe the interaction between an ultraviolet optical vortex and a biomolecule, we constructed an experimental system which can monitor the ultraviolet absorption of optical vortex using a synchrotron radiation undulator [4-5], and theoretically verified the interaction between an optical vortex and a chiral structure using a finite-difference time-domain method [6].

The second-harmonic light from the helical undulator, which is circularly polarized optical vortex ($s = l = +1$; $s = l = -1$) in the ultraviolet region, is introduced to an optical system consisting of a sample holder, a focusing lens, and a mini-monochromator, which enable the absorption measurement of the circularly polarized optical vortex. To confirm the generation of an optical vortex in the ultraviolet region, a triangular aperture was placed at the sample position, and the optical image was observed with a CCD camera, revealing characteristic scattering patterns indicating right- and left-handed optical vortex [7].

As a chiral sample, the absorption of right- and left-handed optical vortex of + (plus) and – (minus) type *10* camphorsulfonic acid (CSA) was observed at 290 nm. Both the circular dichroism and helical dichroism (Differences in absorbance between right- and left-handed optical vortex) of CSA showed positive and negative values for the + and – types, respectively, but an increase in the intensity of the helical dichroism was observed.

Using the moment method, a type of finite-difference time-domain method, we placed a helical coil at the center of a circularly polarized optical vortex field (or circularly polarized field) (Fig. 1) and theoretically observed the helical dichroism (or circular dichroism) from the scattering intensity of the interaction between the optical vortex (or circularly polarized light) and the coil. With a single coil, the intensity of the helical dichroism was smaller than the circular dichroism, but with two or three parallel coils, the difference between the helical and circular dichroism became smaller. Furthermore, when one coil was moved to the radial direction from the center point of the vortex field, the difference between the helical and circular dichroism became smaller. These theoretical results suggest that the position of a chiral sample relative to the optical vortex field strongly affects their interaction, and indicate the need to take the sample position into account when measuring optical vortex absorption.

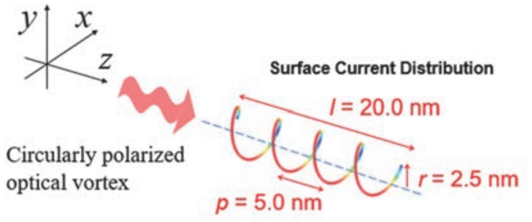

Fig. 1. Helical coil at the center of a circularly polarized optical vortex field for theoretical calculations of helical dichroism (or circular dichroism).

[1] Brullot *et. al.*, Sci. Adv. **2** (2016) e1501349.
[2] Ni *et. al.*, ACS Nano **15** (2021) 2893.
[3] Rouxel *et. al.*, Nat. Photonics **16** (2022) 570.
[4] Katoh *et. el.*, Sci. Rep. **7** 6130 (2017) & Phys. Rev. Lett. **118** (2017) 094801.
[5] Kaneyasu and Katoh *et. al.*, Phys. Rev. A, **95** (2017) 023413.
[6] Kawaguchi, Int. J. Appl. Electromagn. Mech., **65** (2021) 17.
[7] Y. Nishihara *et al.*, UVSOR Activity Report **51** (2024) 47.

BL4U

X-ray Absorption Spectroscopic Analysis of Spatial Distribution of Water Molecules in Deep-Sea White Smoker Chimney Minerals

H. E. Lee[1], T. Araki[2] H. Takahashi[1], and A. Koishi[3]
[1]*Editorial Board, Earth-Life Science Institute (ELSI), Institute of Science Tokyo, Tokyo 152-8550, Japan*
[2]*UVSOR Synchrotron Facility, Institute for Molecular Science, Okazaki 444-8585, Japan*
[3]*RIKEN Center for Sustainable Resource Science, Wako, Saitama 351-0198 Japan*

This study successfully conducted the world's first spatially-resolved soft X-ray absorption spectroscopy (STXM) analysis on minerals collected from the White Smoker Chimney located in the Mariana Trench (depth: 5743 meters)[1]. The primary aim was to investigate the chemical state and two-dimensional spatial distribution of water molecules within the nano-confined spaces of $Mg(OH)_2$ based mineral structures that constitute the chimney. Utilizing the oxygen K-edge spectra, the measurements allow us to map the presence and orientation of water molecules under both dry and humidified conditions.

Our findings reveal that water confined in the nanoscale environments created by oriented $Mg(OH)_2$ exhibits distinct molecular orientations and hydrogen bonding characteristics that differ markedly from bulk water. These altered properties are critical because they suggest the possibility of facilitating dehydration-condensation reactions, such as those involved in the formation of peptides or nucleic acids, which are generally inhibited in bulk aqueous environments. This insight directly addresses the long-standing "Water Paradox" in the origin of life research, where water is essential for life but simultaneously suppresses key synthetic reactions[2].

By employing a soft X-ray beam at BL4U (UVSOR), the study achieved high resolution in visualizing the distribution of water at the nanoscale in a wet environment. The spectroscopic features observed in the pre-edge (~535 eV), main-edge (~537 eV), and post-edge (~540 eV) regions provided detailed information on the saturation level of hydrogen bonds and surface interactions. An increased peak intensity was observed around 536~537 eV, which is expected to be associated with the characteristics of confined water[3].

As only a few research groups worldwide possess samples from the White Smoker Chimney, the structural and chemical insights provided by this study are both novel and significant. The experimental techniques developed and applied here offer a powerful platform for future exploration of water–mineral interactions and their role in supporting life-like chemical processes in extreme environments. This research not only opens new avenues in catalytic chemistry by highlighting the functional potential of mineral-bound nano-confined water but also contributes fundamentally to the field of prebiotic chemistry and the study of life's origins.

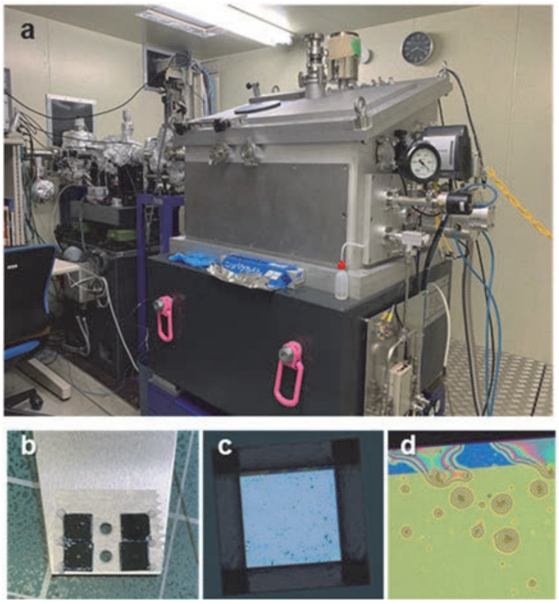

Fig. 1. a. Photograph of the STXM setup at UVSOR. b. Wet cell mounted on the sample holder. c, d. Samples enclosed within a wet cell, prepared by sandwiching them between two SiNx windows.

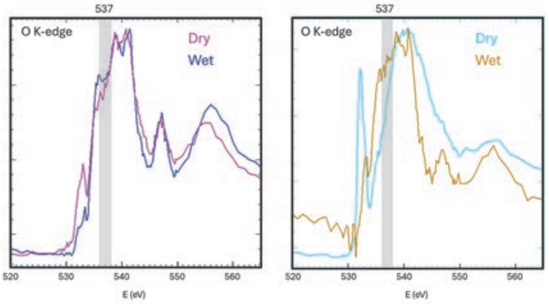

Fig. 2. O K-edge spectra of two different samples with wet and dry conditions.

[1] H.-E. Lee *et al.*, Nat. Commun. **15** (2024) 8193.
[2] M. Marshall, Nature **588** (2020) 210.
[3] K. Yamazoe *et al.*, Langmuir **33** (2017) 3954.

BL4U

Nocturnal Aerosol Growth in New Delhi – A Microscopic Investigation

M. Wickramanayake[1], E. Tsiligiannis[1], T. Araki[2] and X. Kong[1]
[1]*Department of Chemistry and Molecular Biology, University of Gothenburg, SE-412 96 Gothenburg, Sweden*
[2]*UVSOR Synchrotron, Institute for Molecular Science, Okazaki 444-8585, Japan*

This study explores the nighttime growth of atmospheric aerosol particles in New Delhi, one of the most polluted megacities globally, using advanced synchrotron-based techniques. The research addresses a significant knowledge gap in understanding the molecular composition and growth mechanisms of aerosols [1], particularly during nocturnal hours in winter when air pollution events intensify [2]. Sampling was conducted in February and March 2023 from the rooftop of the Indian Institute of Technology (IIT) Delhi, and analytical measurements were carried out at the UVSOR-III synchrotron facility in Japan in March 2024. The primary tools used were Scanning Transmission X-ray Microscopy (STXM) and Near Edge X-ray Absorption Fine Structure (NEXAFS) spectroscopy, enabling high-resolution imaging and chemical speciation of individual aerosol particles.

This investigation examines the diurnal variation of aerosol particle morphology and composition in New Delhi using STXM images at 300 eV, an energy optimal for detecting carbonaceous materials. Three particle types were identified by color: black (carbon- rich soot), grey (inorganics like potassium), and mixed (organic-inorganic combinations). Black particles often appeared chain-like, grey ones polygonal, and mixed particles suggested internal mixing due to condensation or fog processing.

Figure 1 captured during four different conditions (polluted day, clean day, polluted night, and clean night) show significant changes in particle abundance and morphology. Notably, the nighttime images showed a higher degree of spherical structures and internal mixing, supporting the idea of aqueous-phase processing under high humidity conditions, which is common at night in winter.

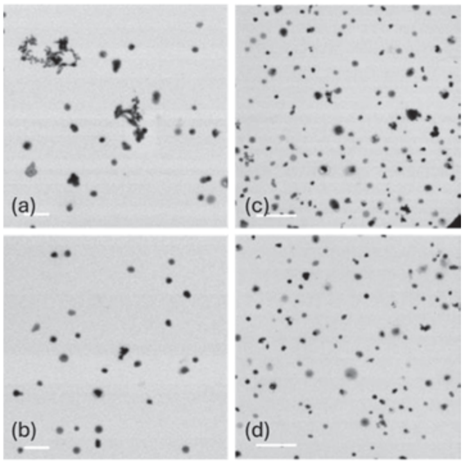

Fig. 1. STXM images of particle morphology during (a) polluted day, (b) clean day, (c) polluted night, and (d) clean night. The scale bar of each is in the bottom left corner showing as a white strip, where (a) and (b) are 2 µm, (c) and (d) are 5 µm.

A key observation lies in the change in particle composition. During both night conditions, the proportion of mixed particles increased, while the number of black (carbonaceous) particles decreased. In the polluted scenario, mixed particles increased by 13%, while black particles dropped by 8% and grey particles by 5%. For the clean scenario, the increase in mixed particles was even more prominent (15%) while grey particles rose by 13%, and black particles showed a sharp 28% decline. This suggests that nighttime conditions favor the transformation of pure carbonaceous or inorganic particles into more internally mixed forms, likely due to condensation of organic vapors and moisture.

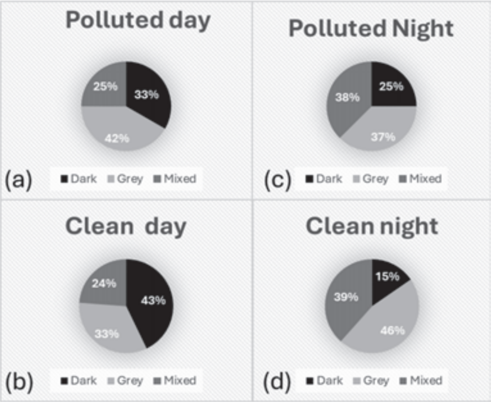

Fig. 2. The fractions of particles distributed into three categories.

The mixing state, which influences how particles interact with solar radiation and water vapor, shifts notably at night. The presence of internally mixed, spherical particles suggests fog or aqueous-phase processing, where particles absorb or coat one another, altering their chemical composition. This affects both climate forcing and health, as internally mixed particles have different optical and hygroscopic properties than externally mixed ones. STXM image analysis and particle count data show that nighttime conditions in New Delhi led to more internally mixed aerosols with larger sizes and distinct compositions. These changes are driven by lower temperatures, higher humidity, and emissions from biomass burning. The results underscore the need to consider diurnal variation in air quality assessments and control strategies.

[1] M.Hallquist *et al*., Atmos. Chem. Phys. **9** (2009) 5155.
[2] J. K. Kodros *et al*., PNAS **117** (2020) 33028.

BL4U

Trial of Molecular Mapping for Thin Sections of Isolated Mammalian Nuclei Embedded in Paraffin Using STXM

A. Ito[1], K. Shinohara[2], A. Matsuura[2], S. Toné[3], S. Ohira[4], A. Nagai[4], Y. Asada[2], T. Ohigashi[5],
H. Yuzawa[6] and T. Araki[6]
[1]*School of Engineering, Tokai University, Hiratsuka 259-1292, Japan*
[2]*Graduate School of Health Sciences, Fujita Health University, Toyoake 470-1192, Japan*
[3]*School of Science and Engineering, Tokyo Denki University, Hatoyama 350-0394, Japan*
[4]*Kawasaki Medical School, Kurashiki 701-0192, Japan*
[5]*Photon Factory, Institute of Materials Structure Science, Tsukuba 305-0801, Japan*
[6]*UVSOR Synchrotron Facility, Institute for Molecular Science, Okazaki 444-8585, Japan*

Spectromicroscopy using STXM is one of the most effective tools for molecular mapping at high spatial resolution. For the application to biological specimens, we have developed an image processing method for a quantitative distribution of constituent molecules, and successfully obtained molecular images in chromosomes, mammalian cells, and mammalian isolated normal and apoptotic nuclei [1-3]. However, due to low transmission of soft X-rays to thick areas in the isolated nucleus, reliable analysis for molecular distribution could not be achieved [3]. To try to solve this problem, thin sections of isolated nuclei with the thickness around 200 nm were prepared by embedding in resin [4]. Although the transmission was greatly improved, we could not exclude the possibility that significant amount of resin in the sections might interfere in the analysis for molecular distribution. In the present study, we adopted paraffin in place of resin, because paraffin in the thin section can be removed by soaking in xylene. In contrast, paraffin section is not so thin as resin section; around 2 μm thickness would be lower limit of the thickness. This report is the first preliminary results using paraffin embedded section.

Isolated nuclei from human HeLa S3 cells were fixed with glutaraldehyde followed by mixing with agarose to confine to a limited volume, and then embedded in paraffin. The paraffin sections were prepared with thicknesses of 5, 3 and 2 μm, and found that 2 μm was the best choice from the transmitted intensity. The section was attached directly on SiN membrane and then soaked in xylene to remove paraffin from section samples.

We basically applied the SVD (Singular Value Decomposition) method to obtain molecular distributions [3]. Energy stack images obtained at the C, N and O-K edges were analyzed using NEXAFS spectra of nucleic acids (DNA and RNA), proteins (histone and actin), and agarose.

Figure 1a shows an X-ray transmission image of a 2 μm-thick thin section of an isolated nucleus observed at 285 eV, where the dense area in the center of nucleus may be assigned to be a nucleolus. The image has somewhat irregular jagged boundary, which may result from sectioning technique of challenging thin thickness. Molecular images of DNA, RNA, histone, and actin were shown in the same OD scale for quantitative comparison, in the panel b, c, d, and e, respectively. RNA is likely to be localized in the nucleolus. Actin is known as one of nuclear proteins as well as cytoplasmic cytoskeletal protein. Although the present analysis is preliminary, because residual molecules are found to exist with significant quantity, the result indicated that the present preparation of the thin section with paraffin for imaging nucleus will be successful. Analysis including paraffin spectra is in progress.

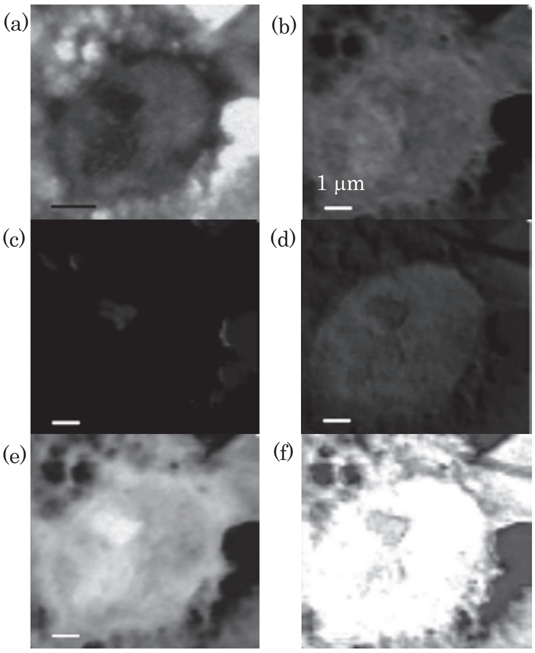

Fig. 1. Molecular distributions in an isolated human nucleus. (a) X-ray image at 285 eV, (b-e) molecular distribution of DNA, RNA, histone and actin, (f) residual molecules.

[1] K. Shinohara *et al.*, Ultramicrosc. **194** (2018) 1.
[2] K. Shinohara *et al.*, J. X-Ray Sci. Technol. **26** (2018) 877.
[3] K. Shinohara *et al.*, Cells **8** (2019) 164.
[4] A. Ito *et al.*, UVSOR Activity Report **48** (2020) 130.

BL4U

Investigation of the Terrestrial Weathering Process of Ryugu Grains

M. Miyahara[1] and T. Araki[2]
[1]*Graduate School of Advanced Science and Engineering, Hiroshima University, 1-3-1 Kagamiyama, Higashi-Hiroshima, Hiroshima 739-8526, Japan*
[2]*UVSOR Synchrotron Facility, Institute for Molecular Science, Okazaki 444-8585, Japan*

Ryugu grains, which are collected from the asteroid Ryugu, mainly consist of saponite, serpentine, magnetite, sulfides, carbonates, and phosphates, closely resembling CI-group carbonaceous chondrites [1]. CI chondrites are highly susceptible to terrestrial weathering, making it difficult to study their original features. Even Antarctic meteorites, despite better preservation, experience long exposure to water and ice. To understand early-stage terrestrial weathering of CI chondrites, this study proposes to expose Ryugu grains to atmospheric conditions and monitor surface changes, providing insights into weathering processes not possible from meteorites alone.

The sample plate C0105-042, previously analyzed by the Hayabusa2 Initial Analysis “Sand” Team, was used in this study [2]. It contains small Ryugu grains from chamber C of the second touchdown. After allocation by JAXA, over 24 grains were mounted onto C0105-042 with minimal epoxy in an N_2-filled glove box. Following approval of our terrestrial weathering AO proposal, the sample plate C0105-042 was sent to Hiroshima University. The sample plate C0105-042 was exposed to air in a desiccator. FE-SEM observations were done 104 and 245 days after exposure began. For TEM and STXM analysis, ultrathin foils were prepared using a FIB system. TEM observations and SAED pattern analysis were conducted for structural and chemical analysis, with quantitative EDS analysis. STXM analysis was conducted at BL4U, UVSOR Synchrotron facility to analyze C K-, S L-, and Fe L-edges using energy stacking methods. Elemental maps and NEXAFS spectra were processed using aXis2000.

FE-SEM observations of the C0105-042 Ryugu grains showed significant surface changes after exposure experiments. Cracks widened, some grains fragmented, and fine-grained precipitates (Fig. 1a) formed on mineral surfaces. Pyrrhotite surfaces were entirely covered by amorphous, amoeboid precipitates (Fig. 1b), obscuring their original outlines. With longer atmospheric exposure, precipitate sizes increased (>200–300 nm), and cracked grains detached completely. TEM analysis revealed that these precipitates were mostly amorphous, carbon- and oxygen-rich layers about 100 nm thick. The amoeboid precipitates on pyrrhotite were iron- and sulfur-depleted, oxidized or hydrated.

Based on the Fe L_3-edge XANES spectra, Fe^{2+} is dominant in the pyrrhotite ($Fe_{1-x}S$)-dominated regions, whereas Fe^{3+} is dominant in the saponite–serpentine matrix. S L-edge XANES spectrum indicate that at pyrrhotite-dominated regions, minor absorption peaks appear around 162 eV and 164 eV (Fig. 1c), corresponding to S^{2-} and elemental sulfur (S^0), respectively [3, 4]. Additionally, a broad absorption band between 167–174 eV is observed (Fig. 1c), attributed to oxidized sulfur species such as S^{4+} and S^{6+} [4]. C K-edge XANES spectrum show that at saponite–serpentine matrix that include carbonaceous material an absorption near 290.5 eV is observed, corresponding to carbonate (CO_3^{2-}) groups [5]. The absorption peak corresponding to the carbonate becomes weaker and an absorption peak corresponding to the C=C bond appears instead as the fine-grained precipitate layer is close to the surface of minerals

Considering the TEM observations and STXM analysis, the terrestrial weathering of Ryugu grains is initiated by the natural oxidation of pyrrhotite. It is highly probable that pyrrhotite reacts with atmospheric moisture, leading to the oxidation of sulfur into sulfate ions, which in turn may cause the decomposition of surrounding saponite, serpentine, and carbonaceous materials. The mechanism and rate by which sulfur leached from pyrrhotite affects these adjacent materials are currently under investigation.

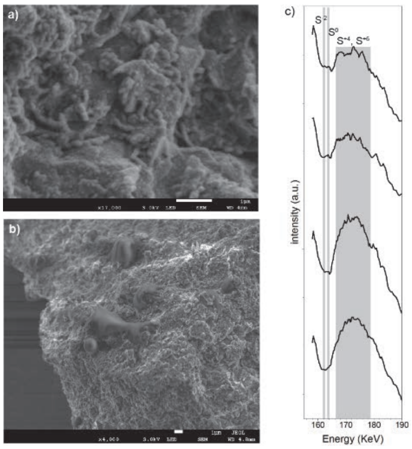

Fig. 1. SE images of a) fine-grained precipitates and b) amoeboid precipitates and c) Representative S L-edge XANES spectrum.

[1] T. Nakamura *et al*., Science **379** (2023) eabn8671.
[2] T. Noguchi *et al*., Nat. Astron. **7** (2023) 170.
[3] S. P. Farrell *et al*., Am. Mineral. **87** (2002) 1321.
[4] D. Li *et al*., Can. Mineral. **33** (1995) 949.
[5] J. A. Brandes *et al*., J. Synchrotron Radiat. **17** (2010) 676.

BL4U

Inorganic Nitrogen in Springtime Aerosol Particles over the Arctic Ocean

N. Fauré[1], T. Araki[2], R. Pohorsky[3], G. P. Freitas[4], J. Schmale[3], P. Zieger[4], J. Creamean[5],
E. S. Thomson[1] and X. Kong[1]
[1]*Department of Chemistry and Molecular Biology, University of Gothenburg, Gothenburg SE-412 96, Sweden*
[2]*UVSOR Synchrotron, Institute for Molecular Science, Okazaki 444-8585, Japan*
[3]*Extreme Environments Research Laboratory, EPFL, Sion 1950, Switzerland*
[4]*Department of Environmental Science, Stockholm University, Stockholm SE-106 91, Sweden*
[5]*Department of Atmospheric Science, Colorado State University, Fort Collins CO 80523, USA*

The Arctic region is warming at a rate two to four times faster than the global average, a phenomenon known as Arctic Amplification (AA). Aerosol particles play an important role in this accelerated warming. However, the extent of their impact depends on their physicochemical properties (e.g., chemical composition, size, and hygroscopicity). [1] Here, we utilize STXM/NEXAFS to investigate the chemical composition of both ambient and laboratory-generated Arctic springtime aerosol particles. These aerosol particles were collected during the Atmospheric Rivers and the Onset of Sea Ice Melt (ARTofMELT) expedition, which took place in the Fram Strait from May to June 2023 onboard the Swedish icebreaker Oden. Ambient aerosol particles were collected at surface level (at sea ice edge) and in clouds at higher altitudes (with a tethered balloon). Laboratory-generated aerosol particles were produced using a Sea Spray Chamber (SSC) onboard the vessel, which was filled with freshly collected seawater and melted snow.

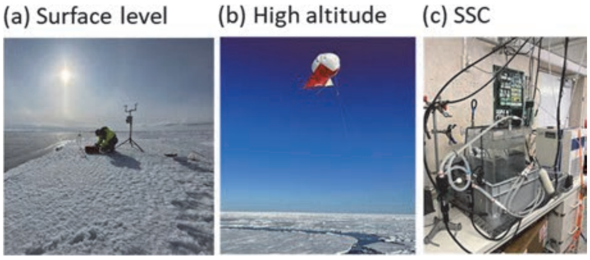

Fig. 1. Ambient aerosol particles collected (a) at the sea ice edge, (b) with a tethered balloon, and (c) from a SSC used to generated sea spray aerosol particles.

The STXM/NEXAFS results reveal that ambient aerosol particles are dominated by ammonium sulfate ($(NH_4)_2SO_4$) and sodium nitrate ($NaNO_3$), while the laboratory-generated sea spray aerosol particles are dominated by sodium chloride (NaCl). The discrepancy between the ambient aerosol particles and those generated using the SSC highlights the potential influence of different sources and formation mechanisms in the ambient environment. Notably, no chloride was detected in ambient particles, suggesting an impact of aging processes on sea spray aerosol compositions, such as dichlorination via acid replacement with nitric acid (HNO_3) and the emission of hydrogen chloride (HCl). [2] Further analysis will be conducted to better understand the different sources and mechanisms at play.

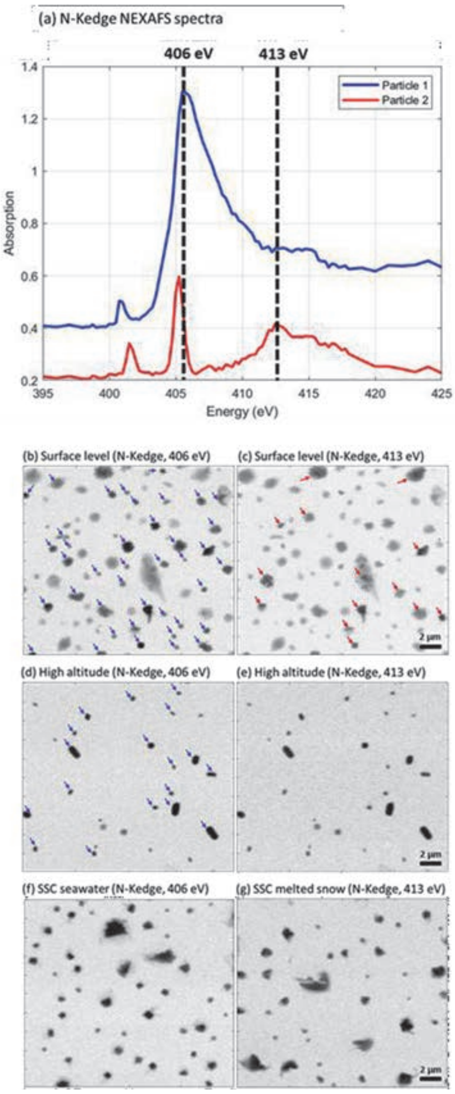

Fig. 2. (a) Nitrogen K-edge NEXAFS spectra with ammonium absorption edge (406 eV) and nitrate absorption edge (413 eV). Overview scans for particles collected (b-c) at surface level close to the sea ice edge, (d-e) at higher altitudes in cloud with a tethered balloon, (f) with the seawater filled SSC and (g) from the SSC filled from melted snow. Blue arrows correspond to particles containing ammonium, red arrows to particles containing nitrate and no arrows to particles with other compositions.

[1] J. Schmale *et al.*, Nat. Clim. Change. **11** (2021) 95.
[2] B. Su *et al.*, Atmos. Environ. **290** (2022) 119365.

BL4U

Investigating Ti-organometallic Complexes Found in Mars-relevant Mineral- microbial Interfaces Exposed Outside the ISS as Potential Biosignatures in the Search for Life on Mars

M.C. Sforna[1] and T. Milojevic[1]

[1]*Center of Molecular Biophysics, CNRS – University of Orleans, Orleans, France*

Searching for traces of life is the core of Mars exploration as conditions were reunited on early Mars for the appearance of Life. Chemolithotrophs (rock-eating microorganisms) may have been predominant on early Mars [1], but the understanding of their putative biosignatures in Martian materials is limited. We investigated *Metallosphaera sedula*, an ancient extremophilic archeon that extracts energy from diverse inorganic electron donors, and which has the particularity to induce specific biomineralization patterns depending of the substrate, which may be preserved for billions of years [2, 3]. *M. sedula* cells were grown on the 4.5 Gyrs-old NWA7034 meteorite [2], and exposed for one year outside of the International Space Station under Martian conditions within the framework of the Japanese Tanpopo-4 orbital project [4, 5]. Preliminary analyses on the retrieved cells showed that despite the abundance of Ti-oxides in NWA7034 [6], there were no traces of Ti- oxides after microbial growth, both in the exposed and in the ground control samples, ruling out photoionization processes. This transformation of Ti- oxides is intriguing, as Ti-oxides are known to be excellent catalyzers for chemical reactions, but, there are no reports of their role on bioprocesses [7]. One question arose from these results: could Ti- organometallic compounds be a suitable signature for the search of life on Mars?

To answer this question, we performed, in May and in October 2024, STXM and XANES spectroscopy at C K-edge, N K-edge, S L-edge and Ti L-edge on the BL4U beamline on exposed and ground control (GC) cells to (1) confirm that Ti accumulation in close proximity with cells is really an organometallic compound, (2) better identify the organometallic complex(es), (3) understand if this complex is preserved under Martian conditions by comparing ground control and ISS-exposed cells, and then to (4) assess Ti-organometallic complexes as potential biosignatures.

In May 2024, we investigated 2 ultra-thin sections of IS cells and ultra-thin section of GC cells, embedded in epoxy resin and deposited on TEM grids. We performed 176 images at the C K-edge and the Ti L- edge, and 25 scans in energy across the C K-edge and the Ti L-edge. In October 2024, we analyzed cells directly dropped on Si3N4 windows (4 windows for ISS, 2 for GC), and were able to better examine the change on the cells resulting from spatial exposure. We performed 141 images at the C K-edge, N K-edge, S L-edge and Ti L-edge, and 47 energy scans, mostly across the C K-edge and the S L-edge.

STXM and XANES at the Ti L-edge did not evidence the presence of Ti-organometallic compounds, but only showed the presence of nanophases of anatase and rutile associated to the cells, suggesting that the transformation of Ti-minerals is not as complete as previously thought.

Our experiment also allowed to investigate the damages on the molecular composition of the cells underwent during ISS exposition. The C K-edge spectra for GC cells show three main bands centered at ~285.1, 287.6 and 288.5 eV, indicating a mixture of biomolecules within *M. sedula*, with prominent lipids, proteins and saccharides features, with a particularly high lipid contribution compared to general composition of cells [8]. Overall, a higher hydroxylation of the functional groups can be observed in the ISS exposed cells compared to GC cells, supported by a globally stronger carboxylic signal, more defined hydroxylated aliphatic peak and carbonyl peaks, and weaker bands for the ketone/phenol/nitrile absorption region. The S L-edge spectra performed on GC and in exposed cells show similar spectra with two main bands, centered at ~173 and ~182 eV spectra, suggesting a +6 redox state for S, most certainly contained in sulphates [9], suggesting a good preservation of the sulfates. The higher hydroxylation is a common features in cells when exposed to UV. Indeed, UV radiation is known to be damageable for cells, increasing the amount of reactive oxygen species in the cells and hydroxylating the functional groups [10, 11]. However, the presence of sulphates not degrading under UV could have limited this damaging action, and allowed their survival under these conditions. These results are included in an article in review.

[1] J.P. Grotzinger *et al*., Science **343** (2014) 12427777.
[2] J.Guo *et al*., Astron. J. **155** (2018) 49.
[3] T. Milojevic *et al*., Commun. Earth Environ. **2** (2021) 39.
[4] D. Kölbl *et al.,* Front. Microbiol. **8** (2017) 1918.
[5] Y. Kawaguchi *et al*., Front. Microbiol. **11** (2020) 2050.
[6] T. Milojevic *et al.,* EGU **23** (2023) 16175.
[7] AR Santos *et al*., Geochim. Cosmochim. Acta **157** (2015) 56.
[8] MR Zierden and AM Valentine. Metallomics **8** (2016) 9.
[9] L.Z. Liu *et al.,* Res. Microbiol. **169** (2018) 590.
[10] G. Sarret *et al*., Geochim. Cosmochim. Acta **63** (1999) 3767.
[11] J. Cadet, J. and J.R. Wagner, J. R. Cold Spring Harbor Perspect. Biol. **5** (2013) a012559.

BL4B

Development of XANES Imaging Method for Visualizing Intracellular Chemical Species

R. Sasaba[1,2] and H. Iwayama[2]
[1]*Graduate School of Frontier Biosciences, The University of Osaka, Suita 565-0871, Japan*
[2]*UVSOR Synchrotron Facility, Institute for Molecular Science, Okazaki 444-8585, Japan*

Detecting the distribution of intracellular molecules or chemical components is very important. Several imaging methods to visualize them, such as Raman microscopy, have been proposed so far. Since the spectral structures of X-ray Absorption Near Edge Structure (XANES) spectroscopy depend on the chemical species, we are developing a XANES imaging method to visualize the distribution of chemical species within a cell using contact-type soft X-ray microscopy [1].

In this method, we measure transmitted X-ray images of biological samples at K- or L-edge energies of elements such as carbon, sulfur, and iron. Biological samples are placed on a Ce:YAG scintillator and covered with a 100 nm-thick Si_3N_4 membrane. The transmitted X-ray image is converted into a visible light image by the scintillator, and then captured by a CMOS camera. By changing photon energies, we can obtain photon-energy dependence of transmitted images Is(X, Y, E), where X and Y represent the positions of the camera and E is a photon energy, respectively. We also measure blank data I_0(X, Y, E) without the sample. From the Lambert-Beer law, we can obtain a three-dimensional XANES image (X, Y, E) from I_0(X, Y, E) and Is(X, Y, E).

The experiment was performed on the beamline BL4B at UVSOR-III. Figure 1 shows the observation result of a human oral epithelial cell using our contact-type soft X-ray microscopy and XANES spectra at four different positions (X,Y) on the sample. Each of the four XANES spectra is different. The No. 1 XANES spectrum corresponds to a cell-free region and consistently shows values close to zero, indicating the background of the spectroscopy. The No. 2 spectrum corresponds to the edge of a cell and exhibits a strong peak around 287 eV. The No. 3 spectrum, taken from the inner region of the cell, shows two peaks at approximately 285 eV and 287 eV. The No. 4 spectrum, acquired from the center of the cell, also exhibits two peaks; however, their intensities are significantly different.

After normalizing all XANES spectra, we extract some feature values from XANES spectra using machine learning techniques. Figure 2 shows the results of these feature calculations. Figure 2(a) displays the peak area around 285 eV, which reflects the amount of aromatic compounds. Figure 2(b) shows the peak area around 287 eV, corresponding to alkyl groups. Figure 2(c) represents the ratio between the peaks at 285 eV and 287 eV, providing contrast related to the relative abundance of aromatic and alkyl compounds. Figure 2(d) shows the spectral difference around 295-320 eV.

These visualized features help us to distinguish different regions within the cell based on their chemical compositions. For example, we could now know how aromatic compounds distribute within a cell.

We are currently working on applying this method to various types of biological samples, such as MDCK cells.

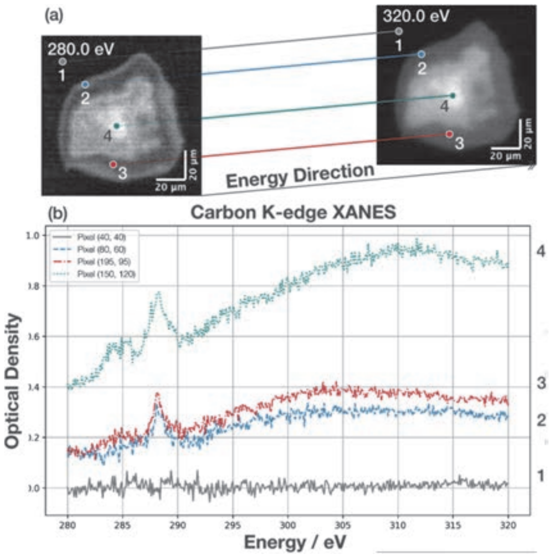

Fig. 1. The imaging result of a human oral epithelial cell using contact-type soft X-ray microscopy and XANES spectra at four different pixels.

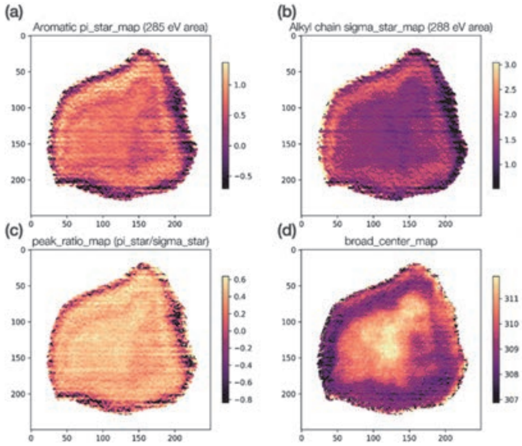

Fig. 2. Maps of spectral features calculated from individual XANES spectra at each pixel position.

[1] T. Ejima *et al.*, J. Phys.: Conf. Ser. **463** (2013) 1.

BL7B

Investigation of Space Weathering Effects on PAHs Using Laboratory Simulations

C. Wu[1], S. Liu[1], K. Yoshioka[1] and I. Yoshikawa[1]
[1]*Department of Complexity Science and Engineering, Graduate School of Frontier Sciences,*
The University of Tokyo, Chiba 277-8561, Japan

Polycyclic aromatic hydrocarbons (PAHs) are widespread cosmic organic molecules. The PAH hypothesis indicates a 217.5 nm absorption bump of the interstellar extinction curve may be attributed to the PAH molecule. This theoretical hypothesis was supported by an experiment of Joblin et al. [1] Additionally, space weathering refers to the physical and chemical changes that occur on the surfaces of airless bodies or objects when exposed to interplanetary environments, resulting in alterations to their spectroscopic features. One significant effect should be noted, this process may cause absorption bands to shift towards longer wavelengths after exposure. There are various approaches to studying space weathering, including the early analysis of Apollo samples and subsequent irradiation experiments conducted on the International Space Station. Among these methods, laboratory simulations of space weathering have become a widely used research technique.

In this study, we employed UV irradiation experiments using 0th-order light on coronene. Subsequently, we utilized beamline BL7B to measure the transmittance spectra of the samples exposed to 0th-order light and unexposed.

In the irradiation experiments, coronene samples were subjected to irradiation for durations of 3 hours, 6 hours and 8 hours, utilizing the 0th-order light from BL7B.

In the transmittance spectra measurement experiment, a photodiode was utilized. The detailed experiment structure can be seen in Fig.1. Additionally, for reducing the effect of higher-order light to obtain more accurate results, various gratings and filters combinations were utilized. Specifically, the setups included the G2 grating plus Quartz and Pyrex filters, as well as G3 grating plus Quartz and Pyrex filters.

In calculating absorption spectrum, due to samples and substrates being too thin, which causes the reflectance to be negligible compared to the transmittance. Therefore, the absorption ratio can be calculated by 100% minus the transmittance ratio. Consequently, the absorption spectrum in Fig.2 can be obtained.

According to the results on Fig. 2, the absorption spectrum has altered after 3-hour and 8-hour of 0th-order light irradiation, compared to the spectrum without irradiation. The detailed performance is peak shift towards shorter wavelengths. The reason for peak shift was considered the hydrogen atom loss.

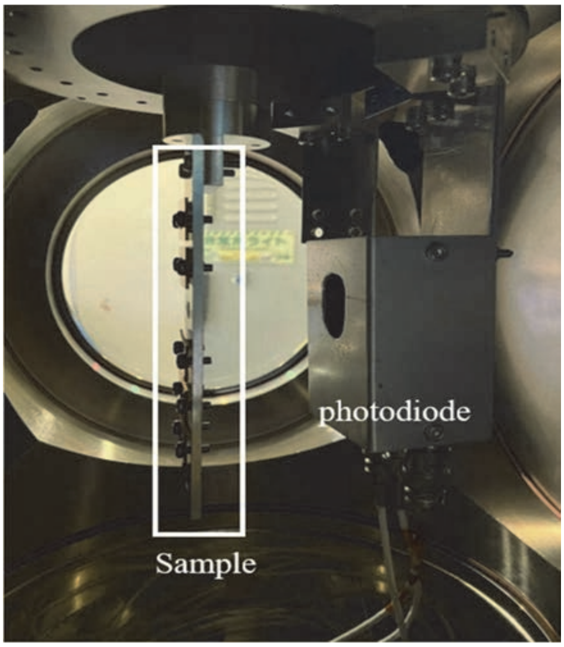

Fig. 1. Spectra measurement experiment.

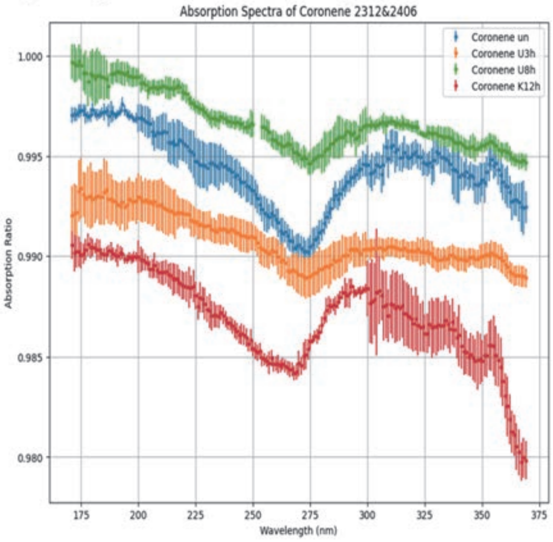

Fig. 2. Absorption spectra of coronene exposed and unexposed.

[1] C. Joblin *et al*., Astrophys. J. **393** (1992) L79.

UVSOR User 14

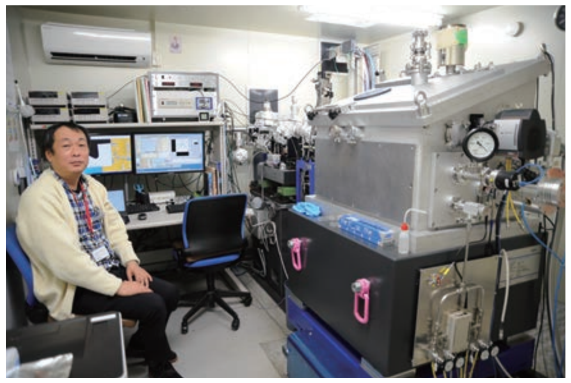

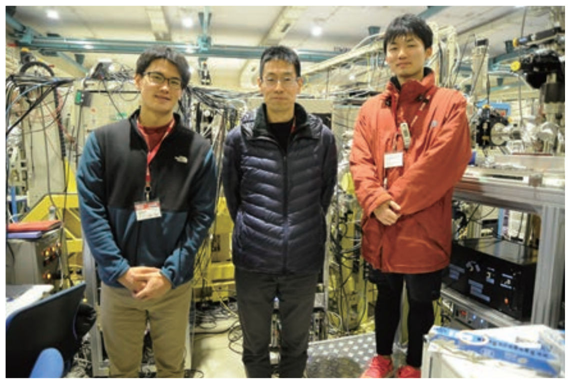

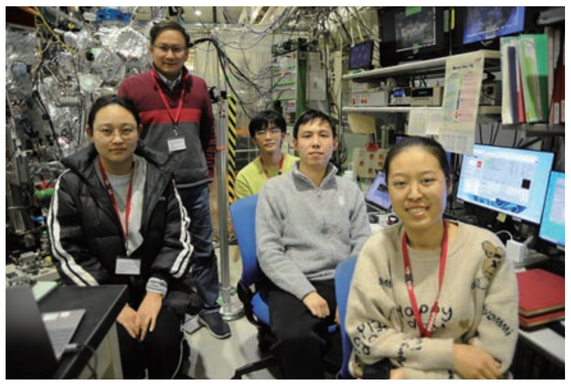

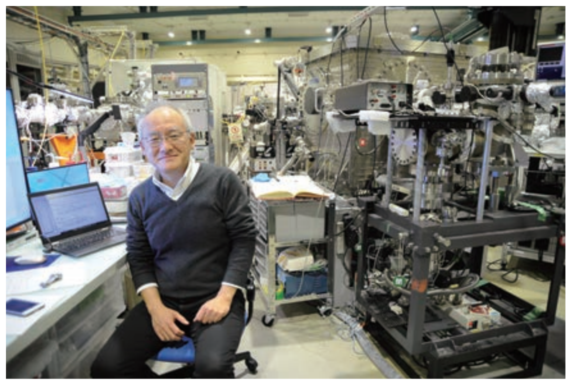

UVSOR User 15

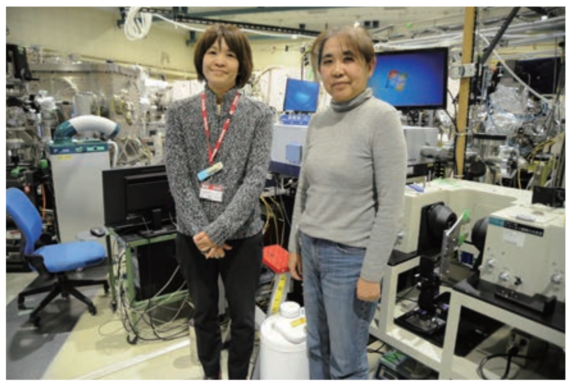

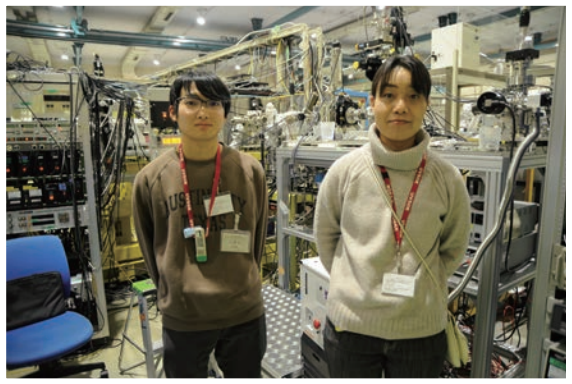

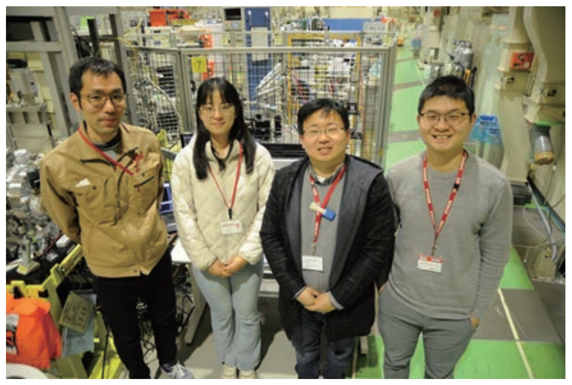

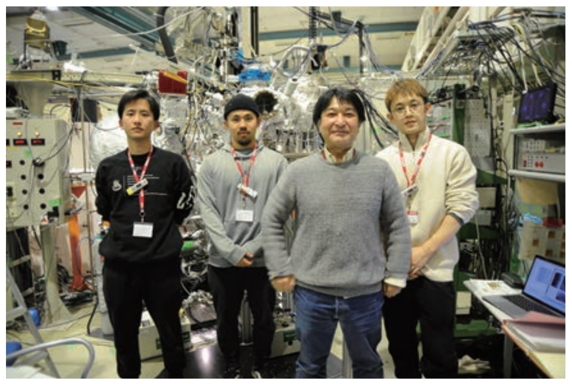

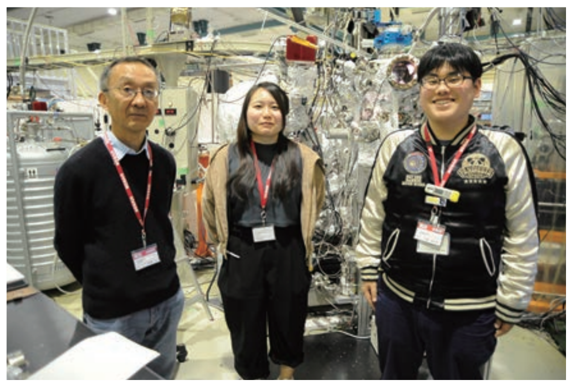

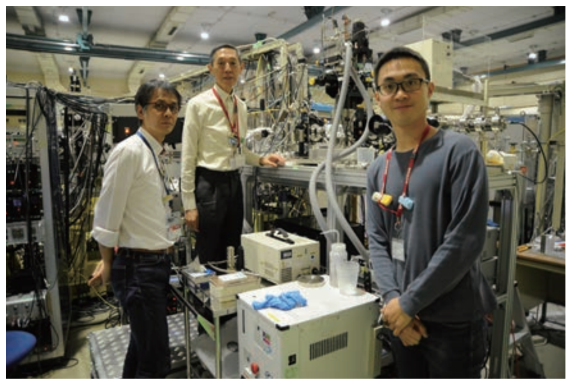

IV

List of Publications

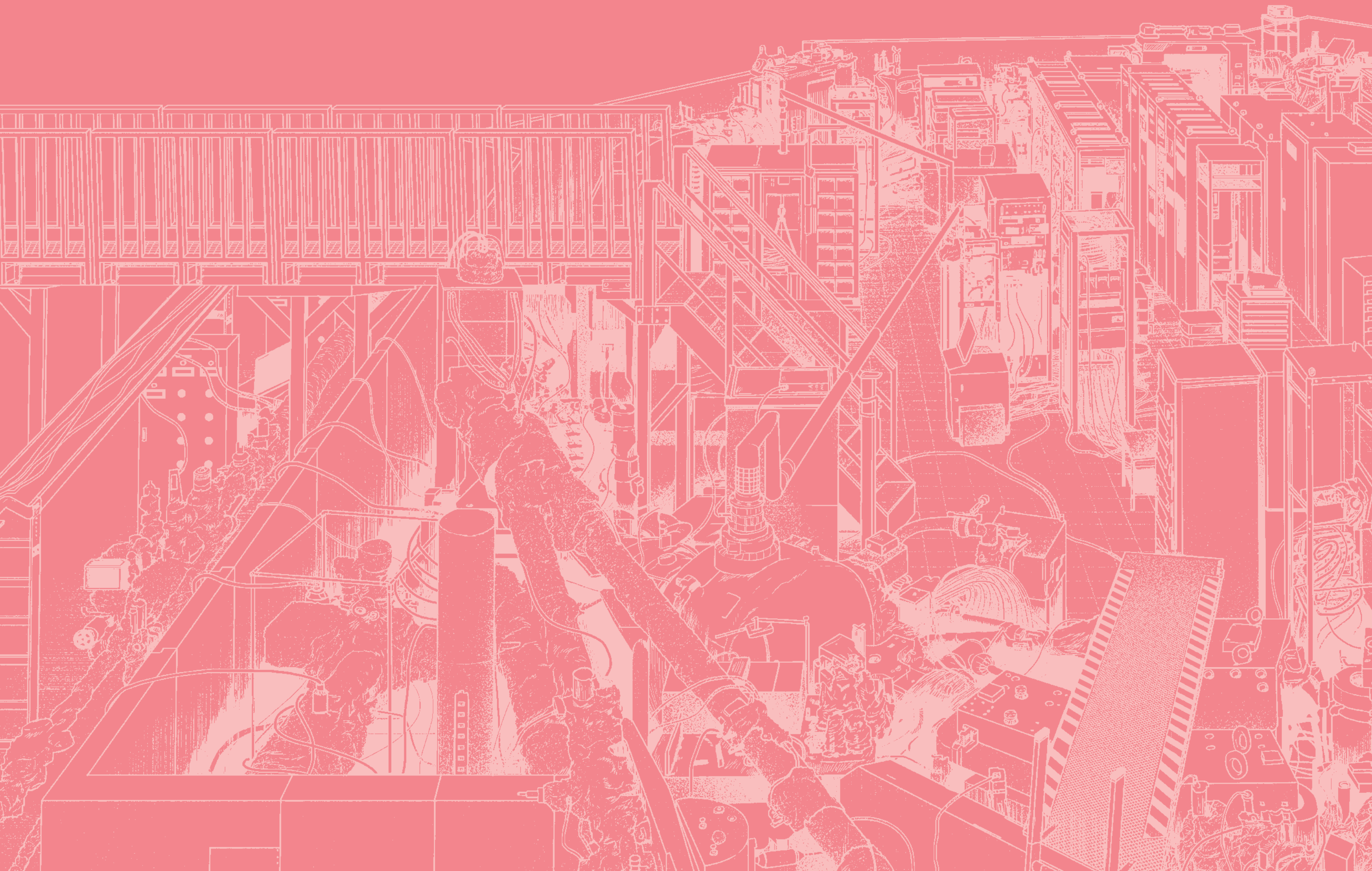

List of Publications (2024)

H. Daimon, T. Matsushita, F. Matsui, K. Hayashi and Y. Wakabayashi
“Recent advances in atomic resolution three-dimensional holography”, Adv. Phys.:X **9** (2024) 2350161.

S. Endo, R. Abe, H. Fujioka, T. Ino, O. Iwamoto, N. Iwamoto, S. Kawamura, A. Kimura, M. Kitaguchi, R. Kobayashi, S. Nakamura, T. Oku, T. Okudaira, M. Okuizumi, M. Omer, G. Rovira, T. Shima, H. M. Shimizu, T. Shizuma, Y. Taira, S. Takada, S. Takahashi, H. Yoshikawa, T. Yoshioka and H. Zen
“Circular Polarization Measurement for Individual Gamma Rays in Capture Reactions with Intense Pulsed Neutrons”, Eur. Phys. J. A, **60** (2024) 166.

M. Fushitani, Y. Hikosaka, M. Tashiro and A. Hishikawa
“State-Selective Dissociative Double Ionization of CH3I and CH2I2 via I 4d Core-Hole States Studied by Multi-Electron–Ion Coincidence Spectroscopy”, J. Chem. Phys. **160** (2024) 174307.

K. Hagiwra, E. Nakamura, S. Makita, S. Suga, S. Tanaka, S. Kera and F. Matsui
“Development of Dual-Beamline Photoelectron Momentum Microscopy for Valence Orbital Analysis”, J. Synchrotron Radiat. **31** (2024) 540.

Y. Hikosaka and S. Fritzsche
“Amplified Collective Auger Decay of Double Inner-Shell Vacancy in Xe”, Phys. Rev. Lett. **134** (2025) 103001.

S. Ichinokura, M. Toyoda, M. Hashizume, K. Horii, S. Kusaka, S. Ideta, K. Tanaka, R. Shimizu, T. Hitosugi, S. Saito and T. Hirahara
“Van Hove Singularity and Lifshitz Transition in Thickness-controlled Li-intercalated Graphene”, Phys. Rev. B **105** (2022) 235307.

S. Ichinokura, A. Hemmi, H. Cun, K. Tanaka, R. Shimizu, T. Hitosugi, T. Greber and T. Hirahara
“Efficiency of Electron Doping to Monolayer Hexagonal Boron Nitride by Alkali Metals”, Appl. Phys. Lett. **122** (2023) 071601.

S. Ichinokura, K. Tokuda, M. Toyoda, K. Tanaka, S. Saito and T. Hirahara
“Van Hove Singularity and Enhanced Superconductivity in Ca-intercalated Bilayer Graphene Induced by Confinement Epitaxy”, ACS Nano **18** (2024) 13738.

T. Inoue, T. Ina, H. Masai, N. Kondo, F. Matsui, T. Kinoshita and A. Nakajima
“Extended X-ray Absorption Fine Structure (EXAFS) Measurements on Alkali Metal Superatoms of Ta-Atom-Encapsulated Si16 Cage”, J. Phys. Chem. Lett. **15** (2024) 5376.

T. Kaneyasu, Y. Hikosaka and M. Katoh
“Attosecond Phase Control of Extreme Ultraviolet Light Pulses and Its Applications to Atomic and Molecular Physics”, Butsuri **79** (2024) 661.

M. Katoh, M. Fujimoto, E. Salehi, M. Hosaka and H. Kawaguchi
“Chirality in Electromagnetic Radiation from Relativistic Electrons”, Chirality **36** (2024) e23677.

M. Kitaura, H. Zen, S. Watanabe, H. Masai, K. Kamada, K.-J. Kim, A. Yoshikawa and J. Ueda
“Relationship between Ce3+ 5d1 level, conduction-band bottom, and shallow electron trap level in Gd3Ga5O12:Ce and Gd3Al1Ga4O12:Ce crystals studied via pump-probe absorption spectroscopy”, Opt. Mater. : X **25** (2025) 100398. Invited Article.

M. kobayashi, S. Yoshimura, H. Iwayama, N. Kondo, J. Takahashi, H. Ota, M. Katoh, K. Kobayashi and H. Nakamura
"First Attempt at Photoionized Plasma Production with VUV Radiation in Synchrotron Light Source UVSOR-III", Plasma Fusion Res. **19** (2024) 1301028.

M. Kobayashi, J. Takahashi, H. Ota, K. Matsuo, M.I.A. Ibrahim, T. Minato, G. Fujimori, M. Katoh, K. Kobayashi, Y. Kebukawa and H. Nakamura
"Emergence of Optical Activity and Surface Morphology Changes in Racemic Amino Acid Films under Circularly Polarized Lyman-α Light Irradiation" Chirality, **36** (2024) e70004.

J. A. Laux, T. Ohigashi, M. R. Bittermann, T. Araki, H. Yuzawa, F. Rancan, A. Vogt and E. Ruehl
"Scanning Transmission Soft X-Ray Microscopy Probes Topical Drug Delivery of Rapamycin Facilitated by Microneedles", ChemPhysChem **26** (2025) e202400819.

T. Mansikkala, S. M. Kangas, I. Miinalainen, P. Angervaniva, N. Darin, M. Blomqvist, R. Hinttala, M. Huttula, J. Uusimaa and M. Patanen
"Soft X-ray spectromicroscopy of human fibroblasts with impaired sialin function", RSC Adv. **14** (2024) 28797.

H. Matsuda, K. Ozawa, Y. Hashimoto, T. Matsushita and F. Matsui
"Use of planar retarding field to improve energy resolution of projection-type electron spectroscopy collimator analyzer", Jpn. J. Appl. Phys. **63** (2024) 046503.

F. Matsui, K. Hagiwara, Y. Sato, E. Nakamura, R. Sagehashi, S. Kera and S. Suga
"Dual-Beamline Photoelectron Momentum Microscopy for Valence Orbital Characterization", Synchrotron Radiat. News **37** (2024) 43.

T. Matsumoto, T. Noguchi, A. Miyake, Y. Igami, M. Matsumoto, T. Yada, M. Uesugi, M. Yasutake, K. Uesugi, A. Takeuchi, H. Yuzawa, T. Ohigashi and T. Araki
"Sodium carbonates on Ryugu as evidence of highly saline water in the outer Solar System", Nat. Astron. **8** (2024) 1536.

T. Mibu, R. Matsuoka, M. Nagasaka and T. Kusamoto
"Emission Enhancement in a Luminescent Polychlorinated Diphenylpyridylmethyl Radical through Coordination to Silver(I)", Dalton Trans. **54** (2025) 2265.

Y. Mondori, Y. Yamauchi, T. Kawakita, S. Ogoshi, Y. Uetake, Y. Takeichi, H. Sakurai and Y. Hoshimoto
"Monodentate σ-Accepting Boron-Based Ligands Bearing Square-Planar Ni(0) Centers", J. Am. Chem. Soc. **147** (2025) 8326.

M. Nagasaka
"Probing Isolated Water Molecules in Aqueous Acetonitrile Solutions Using Oxygen K-Edge X-ray Absorption Spectroscopy", J. Phys. Chem. Lett. **15** (2024) 5165.

M. Nagasaka
"Metal-ligand delocalization of iron and cobalt protoporphyrin complexes in aqueous solutions probed by soft X-ray absorption spectroscopy", Phys. Chem. Chem. Phys. **26** (2024) 23636.

Y. Nakayama, J. Miyamoto, K. Yamauchi, Y. Baba, F. Teshima and K. Tanaka
"Far- and Mid-infrared FT-IR Analysis of Single-crystal Pentacene Using a Linearly Polarized Synchrotron Radiation Light Source", Vib. Spectrosc. **132** (2024) 103601.

Y. Nakayama, K. Yamauchi, Y. Baba, K. Kikuchi, H. Hattori, F. Teshima and K. Tanaka
"Synchrotron Radiation Fourier-transform Infrared Absorption Measurements on the Single-crystal Dinaphtho[2,3-b:2',3'-f]thieno[3,2-b]thiophene", Jpn. J. App. Phys. **63** (2024) 09SP07.

M. Odelius, S. D. Folkestad, T. Saisopa, Y. Rattanachai, W. Sailuam, H. Yuzawa, N. Kosugi, A. Paul, H. Koch and D. Céolin
“Symmetry Breaking around Aqueous Ammonia Revealed in Nitrogen K-edge X-ray Absorption”, J. Phys. Chem. Lett. **16** (2025) 3411.

K. Okazaki, M. Koshimizu, D. Nakauchi, T. Kunikata, T. Kato, N. Kawaguchi and T. Yanagida
“Crystal growth, luminescence, and radiation response characteristics of undoped and Nd-doped langasite-type Ca3TaGa3Si2O14”, J. Alloy Compd. **1008** (2024) 176788.

Y. Taira
“Spatial distribution of gamma rays produced by axially symmetric polarized and optical vortex lasers”, Phys. Rev. A **110** (2024) 043525.

Y. Takebuchi, K. Watanabe, M. Koshimizu, K. Ichiba, T. Kato, D. Nakauchi, N. Kawaguchi and T. Yanagida
“Neutron detection properties of Ti-doped LiGaO2 single crystalline scintillator”, Radiat. Phys. Chem. **223** (2024) 111917.

S. Tsuru and M. Nagasaka
“Solvatochromism Observed in the X-ray Absorption Spectrum of Indole Dissolved in Water”, J. Phys. Chem. A **129** (2025) 3020.

Y. Yao, M. Nagasaka and K. Mochizuki
“Salt-Specific Effect on the Solubility and Aggregation of 1-butanol in Water”, Physica A, **647** (2024) 129917.

S. Yoshioka, K. Yasuda, C. Hsiao, C. Hsu, W. Olovsson, J. Birch, C. Hemmingsson and G. Pozina
“Local Structure of Zn Dopant in b Phase Ga2O3”, J. Phys. Chem. C **128** (2024) 18879.

S. Yoshioka, K. Tsuruta, T. Yamamoto, K. Yasuda, S. Matsumura, N. Ishikawa and E. Kobayashi
“X-ray Absorption Near Edge Structure and First-principles Spectral Investigations of Cationic Disorder in MgAl2O4 Induced by Swift Heavy Ions”, Phys. Chem. Chem. Phys. **20** (2018) 4962.

S. Yoshioka, K. Yasuda, S. Matsumura, T. Sugiyama and E. Kobayashi
“Transition of Cationic Local Structures in Mg1xNixAl2O4”, J. Phys. Chem. C **125** (2021) 5269.

M. Yoshizumi, K. Araki, M. Enomura, H. Murata and A. Nakahira
“Synthesis of Size-Controlled Cerium Oxide Nanoparticles by Forced Thin-Film Type Reactor (in Japanese)”, J. Soc. Mater. Sci., Jpn. **73** (2024) 480.

UVSOR User 16

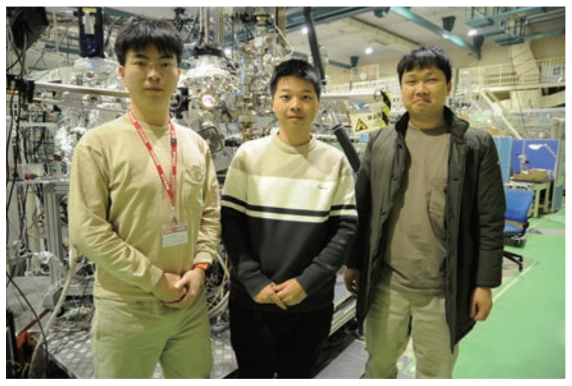

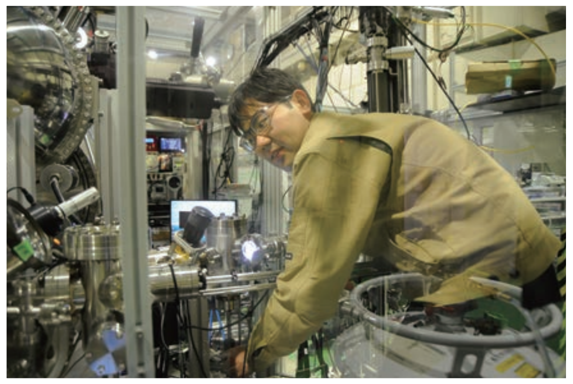

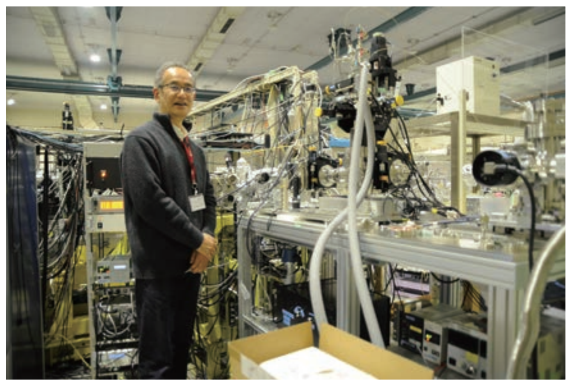

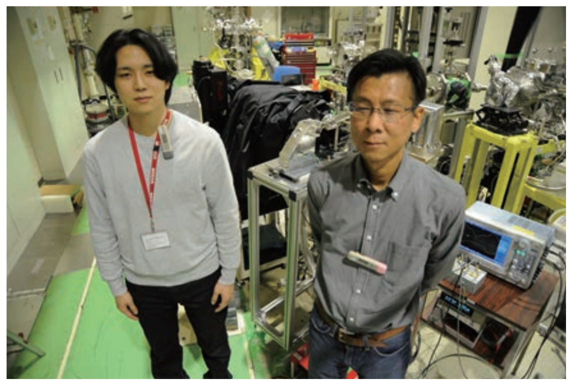

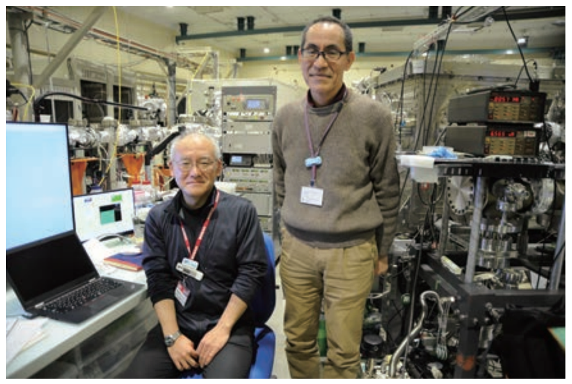

V

Workshops

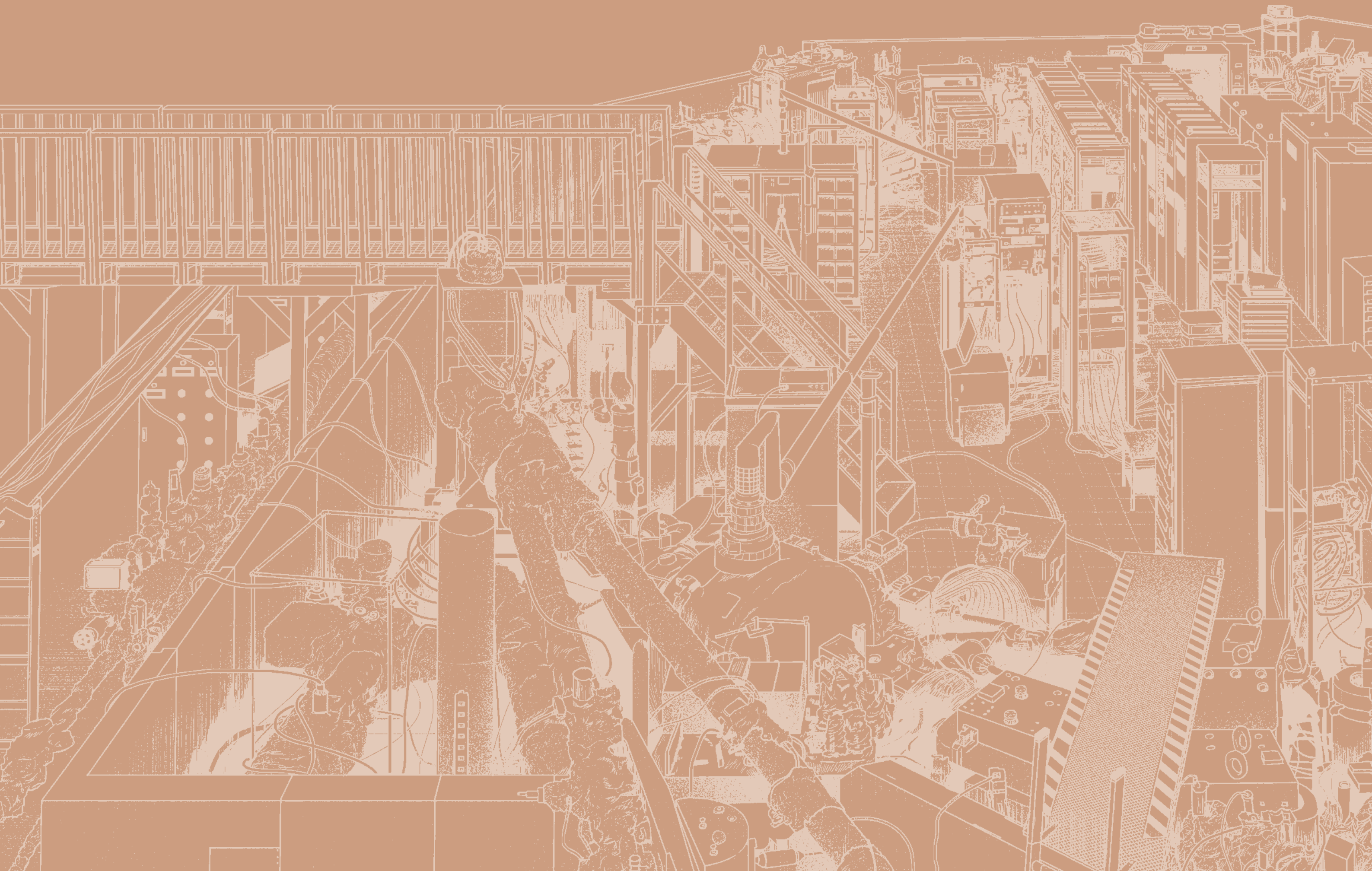

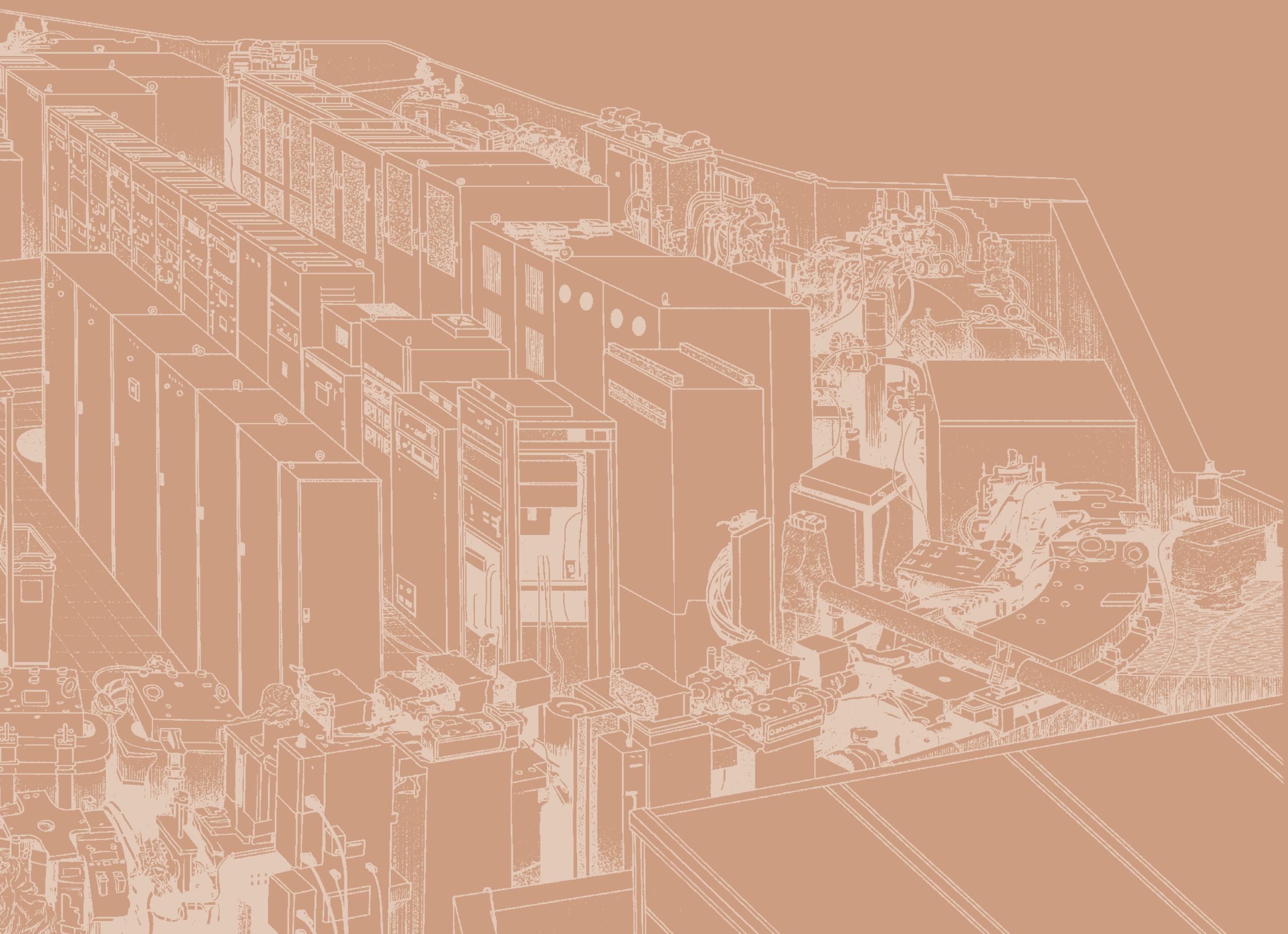

UVSOR Symposium 2024

Date: November 5-6, 2024
Place: Okazaki Conference Center (face-to-face), Zoom (online)

November 5 (Tue.)

13:00 – 13:05	Opening remarks **T. Araki** (UVSOR)
13:05 – 13:25	Facility update **S. Kera** (UVSOR Director)
13:25 – 13:45	*In-situ* analysis of pure iron tensile specimens under stress using gamma-ray-induced positron annihilation lifetime spectroscopy **A. Yabuuchi** (Kyoto University)
13:45 – 14:05	Dual-beamline photoelectron momentum microscopy for valence orbital analysis **K. Hagiwara** (Institute for Molecular Science)
14:05 – 14:35	[Invited Lecture] Observation of electronic states in rare-earth monopnictide using angle-resolved photoemission spectroscopy **K. Kuroda** (Hiroshima University)
14:35 – 15:05	Break Time
15:05 – 15:45	Short Presentation for Poster Session
15:45 – 16:05	Recent results of Photoelectron Momentum Microscopy without and with Spin Resolution **S. Suga** (Osaka University)
16:05 – 16:35	[Special Lecture] Scanning Transmission Soft X-ray Spectro-Microscopy at the PolLux Beamline of the Swiss Light Source **Benjamin Watts** (Paul Scherrer Inst., Swiss Light Source)
16:35 – 17:00	Break Time
17:00 – 18:45	Poster Session
18:45 – 20:15	Opinion exchange meeting

November 6 (Wed.)

09:00 – 09:20	Photoionized plasma production experiments with VUV radiation in UVSOR-III **M. Kobayashi** (National Institute for Fusion Science)
09:20 – 09:50	[Invited Lecture] Development of novel radiation detectors consisting of novel scintillation materials with higher mission efficiency **S. Kurosawa** (Tohoku University)
09:50 – 10:10	Initial results of the world’s first solar flare X-ray focusing imaging-spectroscopic observation performed by the sounding rocket experiment FOXSI-4 **N. Narukage** (National Astronomical Observatory of Japan)
10:10 – 10:25	Break Time

10:25 − 10:55	[Invited Lecture] The Structure Analysis of Soft Matter by Resonant Soft X-ray Scattering
	Y. Takanishi (Kyoto Prefectual University of Medicine)
10:55 − 11:15	Nanoscale surface and interface magnetism investigated at BL4B in UVSOR
	T. Miyamachi (Nagoya University)
11:15 − 12:15	UVSOR USERS' UNION meeting

Poster Session

[P01] Photoionized plasma production experiments with VUV radiation in UVSOR-III
M. Kobayashi (NIFS)

[P02] Status of Single Electron Storage Experiment at UVSOR-III in 2024
Y. Asai (Hiroshima Univ.)

[P03] Unraveling A site order in Bi-modified $SrTiO_3$ based relaxor feroelectrics by probing atomic vacancy
K. Kamoshida (Yamagata Univ.)

[P04] Experimental and theoretical studies of the interaction of ultraviolet optical vortices with biomolecules
K. Matsuo (Hiroshima Univ.)

[P05] Effect of Sb Doping on Mg_2Sn Crystals Studied by Gamma-induced-Positron Annihilation Lifetime Spectroscopy and Photoelectron Holography Experiments
T. Sumi (Yamagata Univ.)

[P06] Measurement of XUV Polarization by Zeeman Quantum Beat of Helium Atom
T. Kaneyasu (SAGA Light Source)

[P07] Electronic Chirality investigated by Photoelectron Circular Dichroism Measurements
H. Kohguchi (Hiroshima Univ.)

[P08] Development of Resonant Soft X-ray Scattering method for soft matter
H. Iwayama (IMS)

[P09] Electronic Structure Measurement of Thin Films of a Rubrene Derivative on Rubrene Single Crystals
T. Yamada (Tokyo Univ. of science)

[P10] Multi-orbital Hybridization in One-Dimensional Monolayer of DPh-BTBT
Y. Ono (Univ. Tsukuba)

[P11] Collective Auger decay of Xe 4d double core-hole states
Y. Hikosaka (Univ. of Toyama)

[P12] Organic-inorganic interfacial magnetic coupling between phenanthroline derivatives and Co nano-islands
K. Fujimoto (Nagoya Univ.)

[P13] Contribution of Co ions in CoPc to the Magnetic Properties of Pcs/γ’-Fe4N Organic-Inorganic Hybrid Thin Films
H. Ono (Nagoya Univ.)

[P14] Structural, electronic and magnetic properties of monatomic layer cobalt nitride grown on Cu(001)
A. Iwai (Nagoya Univ.)

[P15] Thickness dependence of structural, electronic and magnetic properties of Ni thin films on Cu(001)
N. Okamura (Nagoya Univ.)

[P16] Two-dimensional heavy fermion in a monoatomic layer surface alloy CeCux/Cu(111)-(2×2)
H. Yamaguchi (Osaka Univ.)

[P17] Observation of Topological Surface States in Superconducting type-2 Dirac semimetal PdSeTe
Yogendra Kumar (Hiroshima Univ.)

[P18] ARPES investigation of thermoelectric properties in heavy fermion systems
D. Goto (Toyota TI)

[P19] Polarization-dependent angle-resolved photoemission spectroscopy of MoAlB

K. Kawano (Nagoya Univ.)

[P20] Comprehensive Study of electronic States Induced by Quantum Charge Fluctuations in Electron-Doped High-Tc Cuprate Superconductors

H. Yamaguchi (Hiroshima Univ.)

[P21] Enantio-differentiation of chiral crystals by angle-resolved photoemission circular dichroism

K. Fukutani (IMS)

[P22] Electronic state of bulk and monolayer $TiSe_2$ studied by high-resolution ARPES

M. Nishigami (Tohoku Univ.)

[P23] VR equipment for presenting the 3D electronic structure

Shin-ichiro Tanaka (Osaka Univ.)

[P24] Imaging the domain structure of single-crystal Ir(111) thin films by photoelectron momentum microscopy

E. Hashimoto (Aoyama Gakuin Univ.)

[P25] Observation of Rashba splitting and Weyl cones in inversion symmetry broken material $PtBi_2$

Y. Morita (Tohoku Univ.)

[P26] Band structure of electron doped MoS_2

Y. Hasegawa (Univ. of Tsukuba)

[P27] Electronic and magnetic properties of altermagnetic MnTe films and its termination dependence

R. Akiyama (Institute of Science Tokyo)

[P28] Angle-resolved photoemission spectroscopy of garnet-type solid electrolytes $Li_{6.5}La_3Zr_{1.5}Ta_{0.5}O_{12}$ bulk single crystal

K. Masuda (Nagoya Univ.)

[P29] Experimental measurement of valence band dispersion in high-mobility organic semiconductor crystals fabricated by solution process

T. Tasaki (Tokyo Univ. of Science)

[P30] Fabrication and electronic structure observation of a monoatomin-layer material Yb/Si(111)

R. Ichikawa (Osaka Univ.)

[P31] Substrate dependence of the electronic structure of Si(111)($\sqrt{3}\times\sqrt{3}$)-Sn

H. Nishimichi (Institute of Science Tokyo)

[P32] Observation of electronic structures in nodal line semimetal KAlGe by angle-resolved photoemission spectroscopy

T. Nishida (Univ. of Tokyo)

[P33] Uniaxial strain effects on the electronic structure of 1T-TaS_2: micro-ARPES study

S. Suzuki (Tohoku Univ.)

[P34] Infrared absorption spectroscopy for crystals grown by a solution process of pentacene derivative crystals

Y. Baba (Tokyo Univ. of Science)

[P35] Development of Time-Resolved Electron Energy Loss Spectroscopy

K. Nishihara (Osaka Univ.)

[P36] Developement of Atom-Holography Microscope

H. Daimon (IMS)

UVSOR User 17

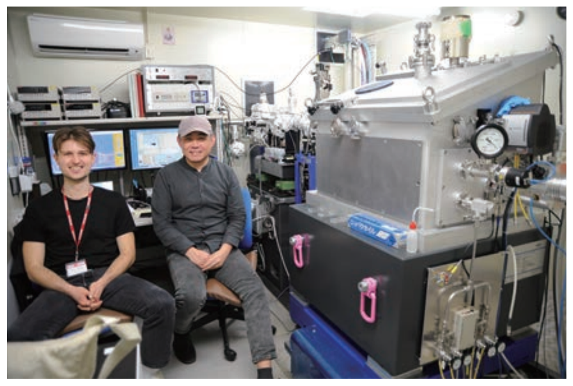

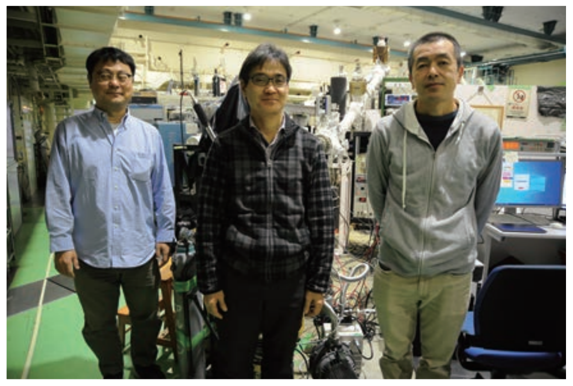

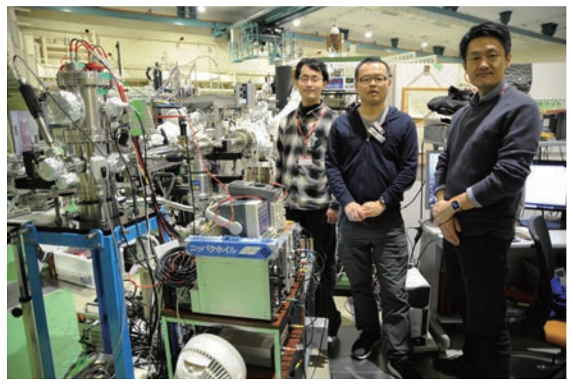

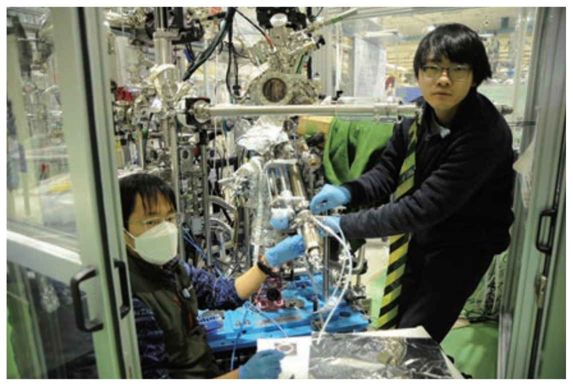

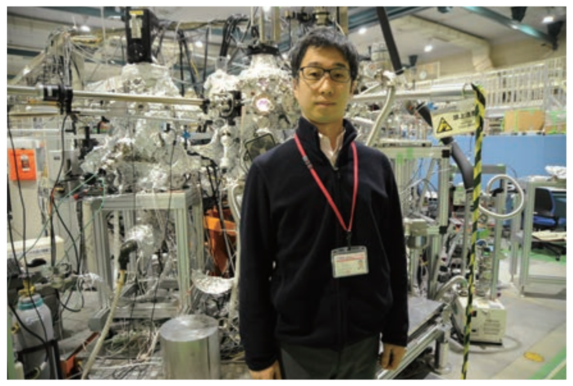

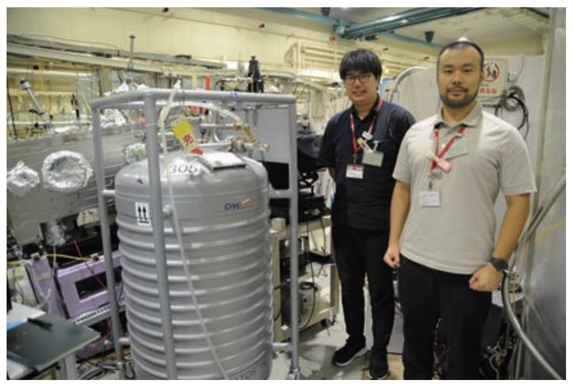

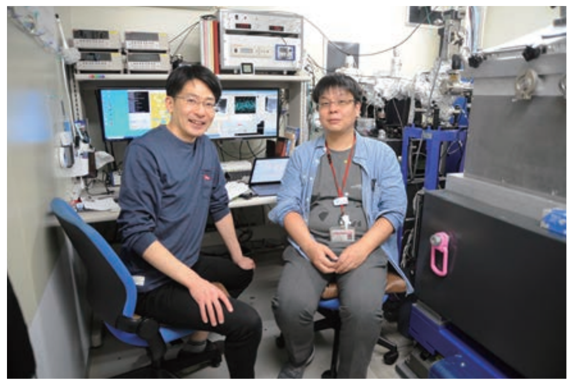

UVSOR User 18

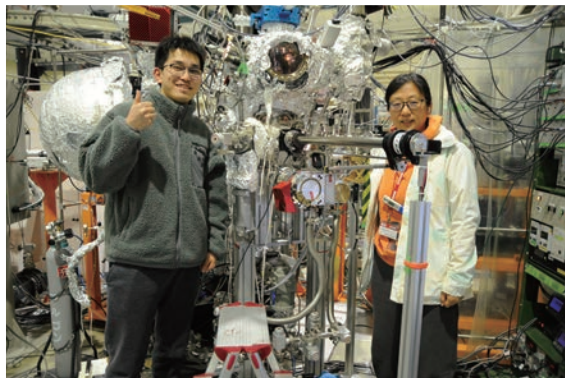

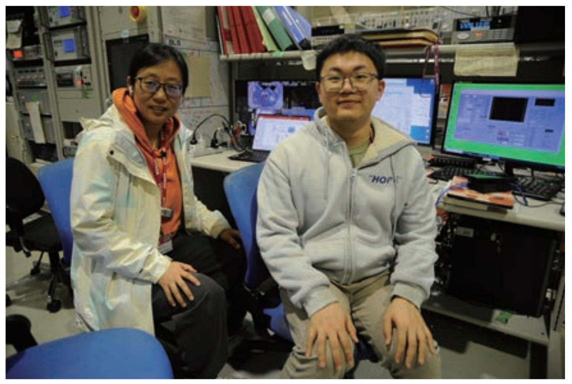

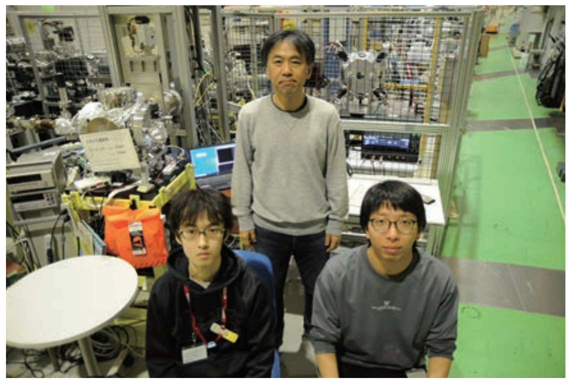

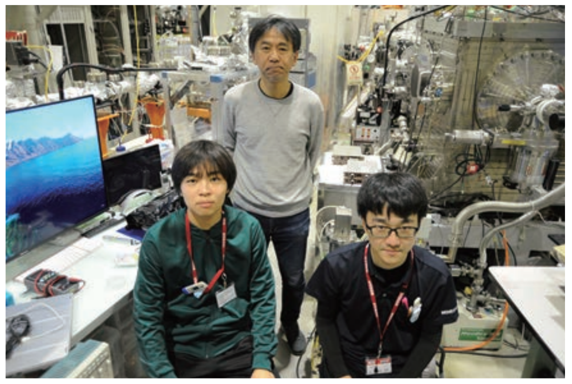

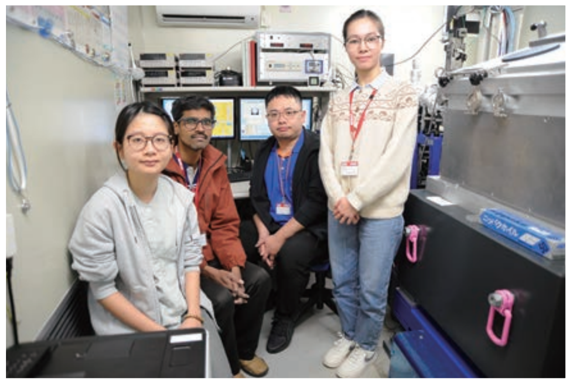

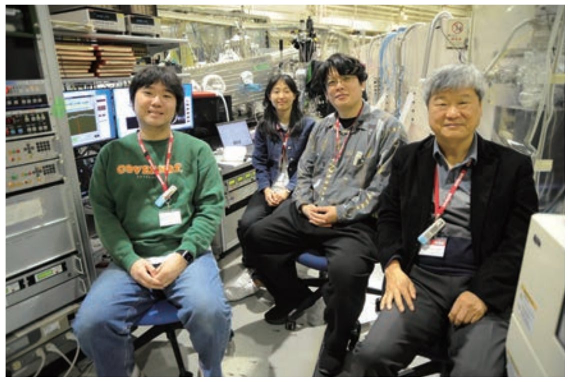

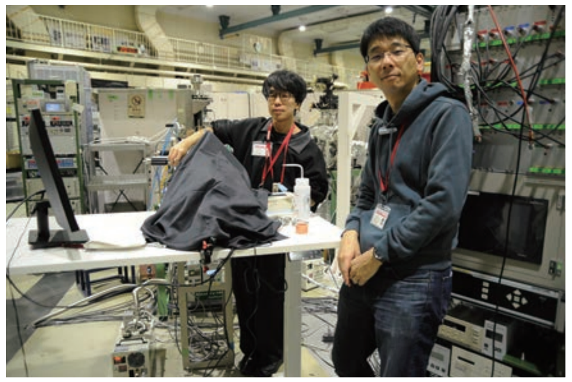

Facts and Figures

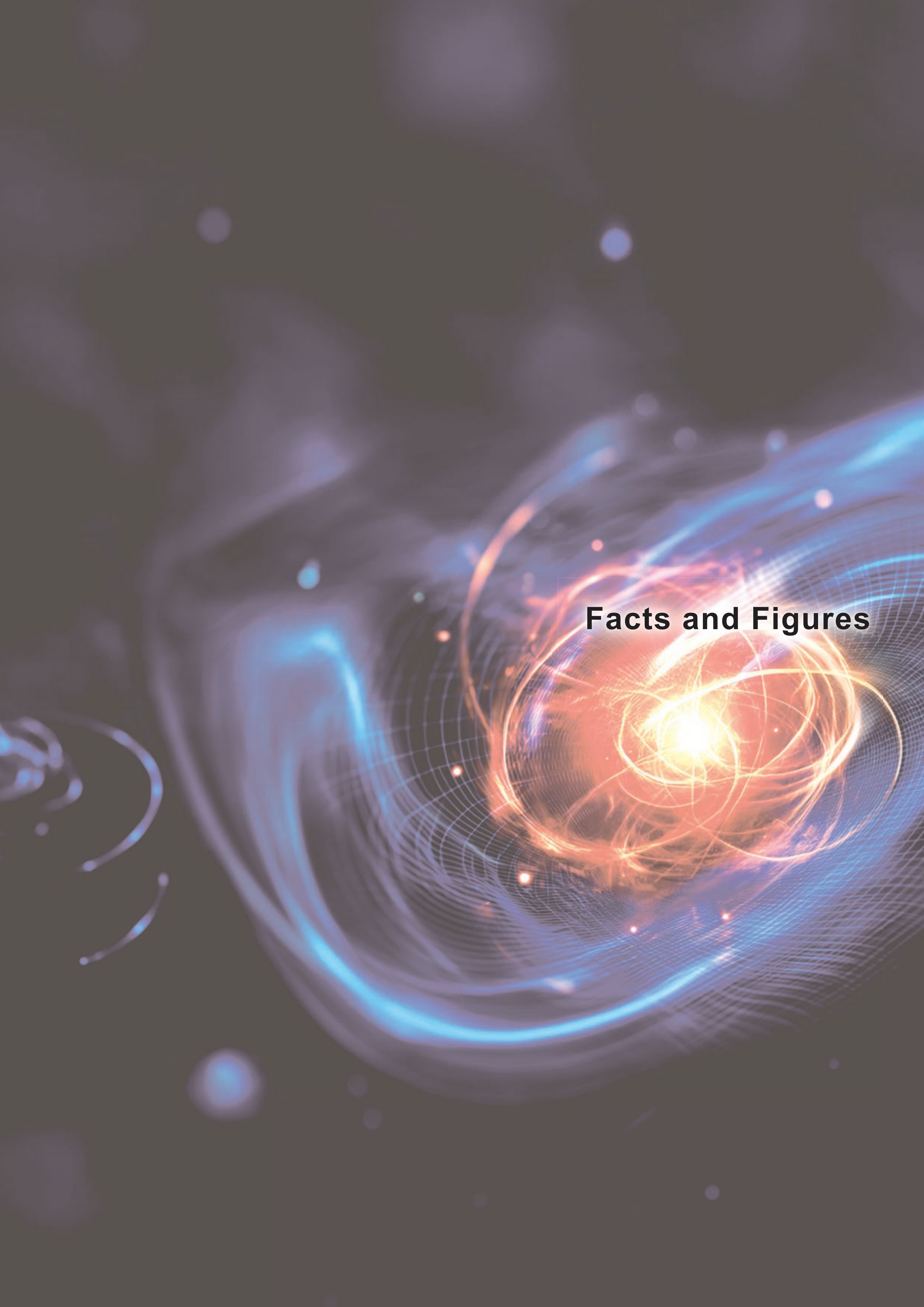

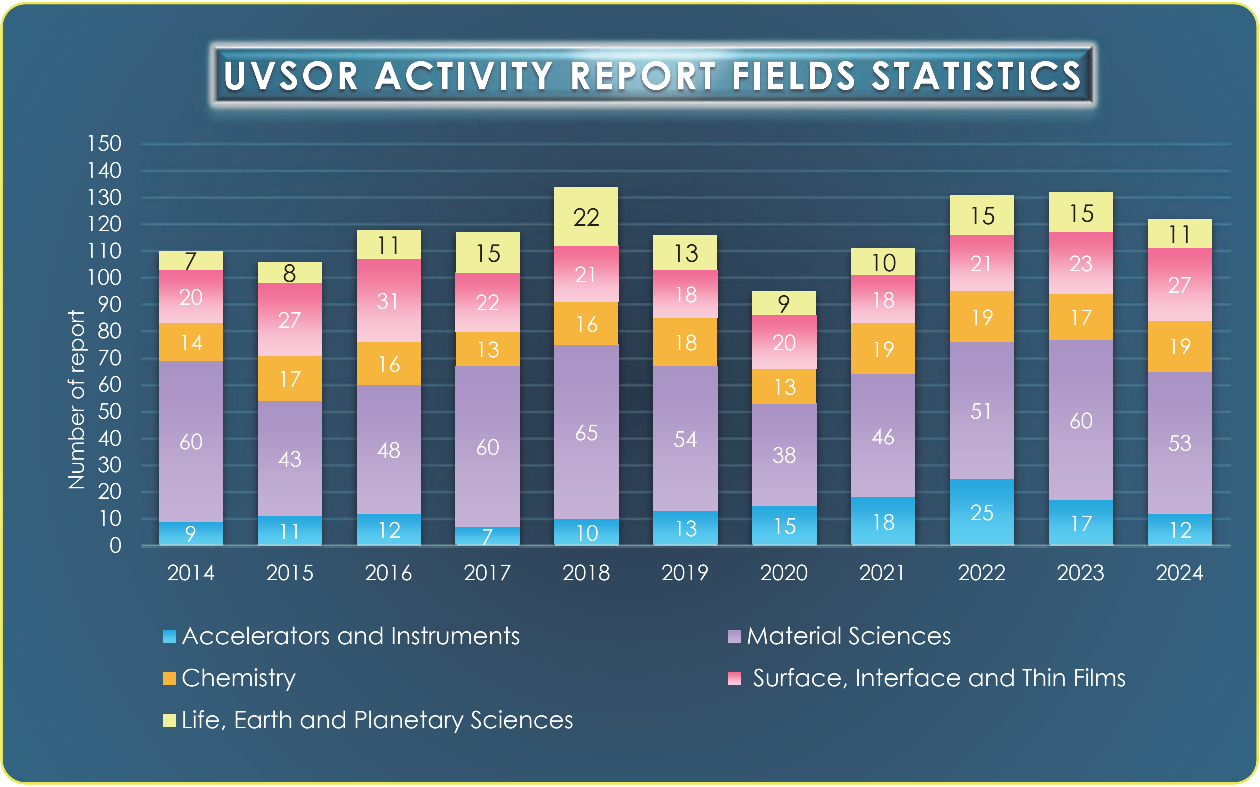
UVSOR ACTIVITY REPORT FIELDS STATISTICS
Number of report
0
10
20
30
40
50
60
70
80
90
100
110
120
130
140
150
2014: 9, 60, 14, 20, 7
2015: 11, 43, 17, 27, 8
2016: 12, 48, 16, 31, 11
2017: 7, 60, 13, 22, 15
2018: 10, 65, 16, 21, 22
2019: 13, 54, 18, 18, 13
2020: 15, 38, 13, 20, 9
2021: 18, 46, 19, 18, 10
2022: 25, 51, 19, 21, 15
2023: 17, 60, 17, 23, 15
2024: 12, 53, 19, 27, 11
Accelerators and Instruments
Material Sciences
Chemistry
Surface, Interface and Thin Films
Life, Earth and Planetary Sciences

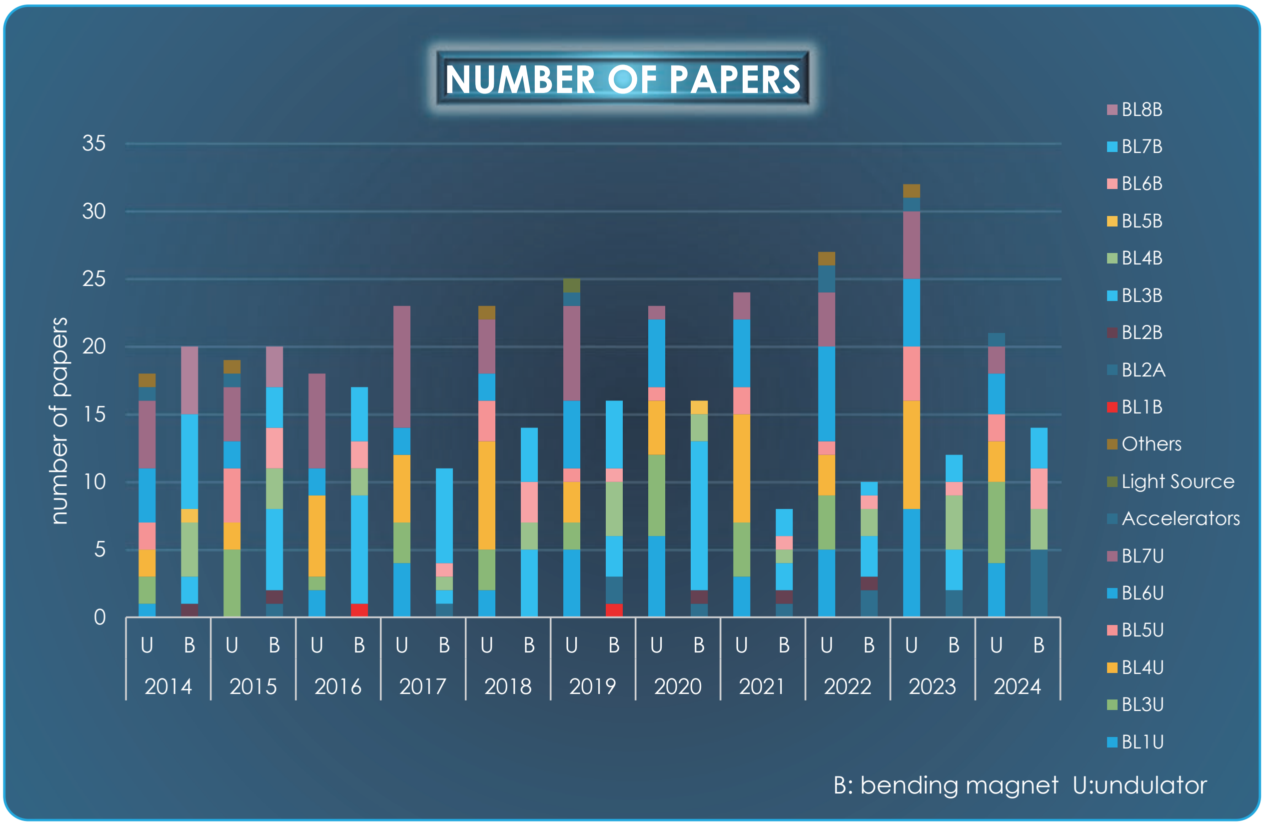
NUMBER OF PAPERS
number of papers
0
5
10
15
20
25
30
35
U
B
2014
2015
2016
2017
2018
2019
2020
2021
2022
2023
2024
BL8B
BL7B
BL6B
BL5B
BL4B
BL3B
BL2B
BL2A
BL1B
Others
Light Source
Accelerators
BL7U
BL6U
BL5U
BL4U
BL3U
BL1U
B: bending magnet U:undulator

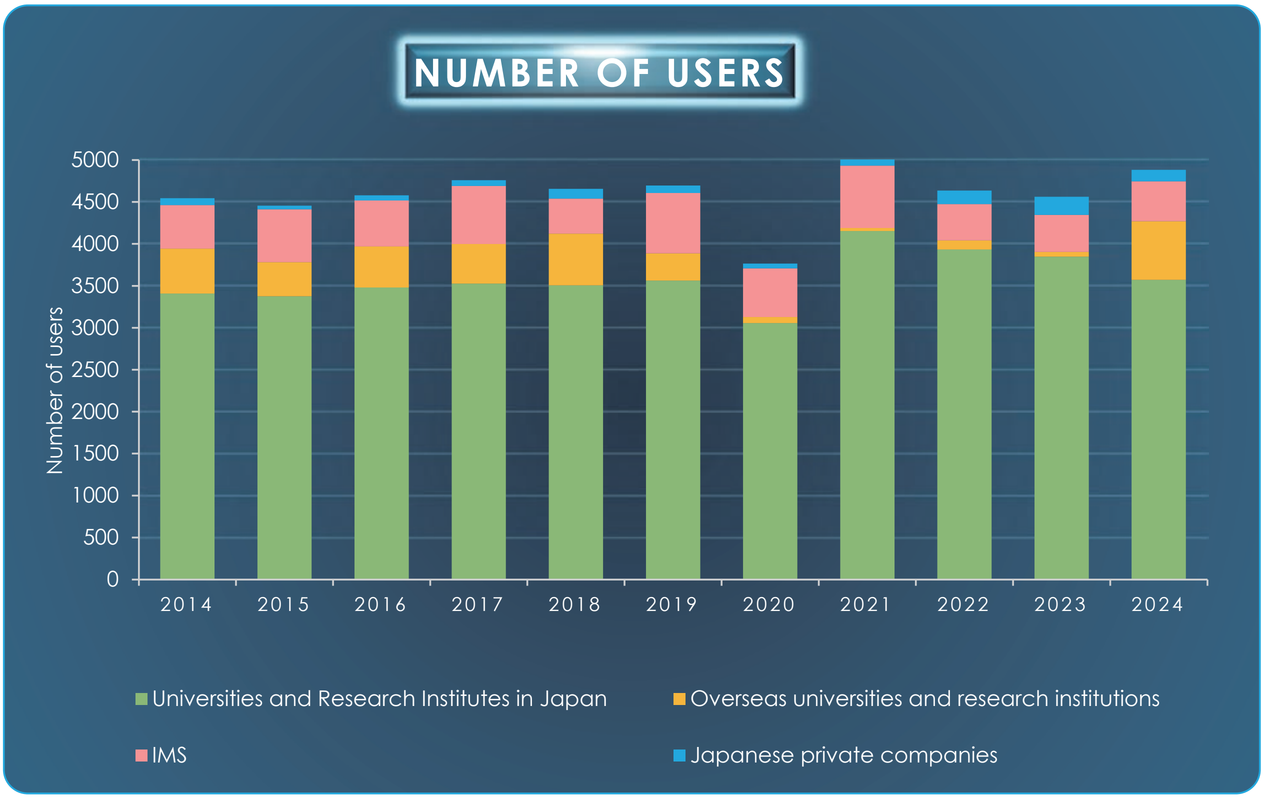
NUMBER OF USERS
Number of users
5000
4500
4000
3500
3000
2500
2000
1500
1000
500
0
2014
2015
2016
2017
2018
2019
2020
2021
2022
2023
2024
Universities and Research Institutes in Japan
Overseas universities and research institutions
IMS
Japanese private companies

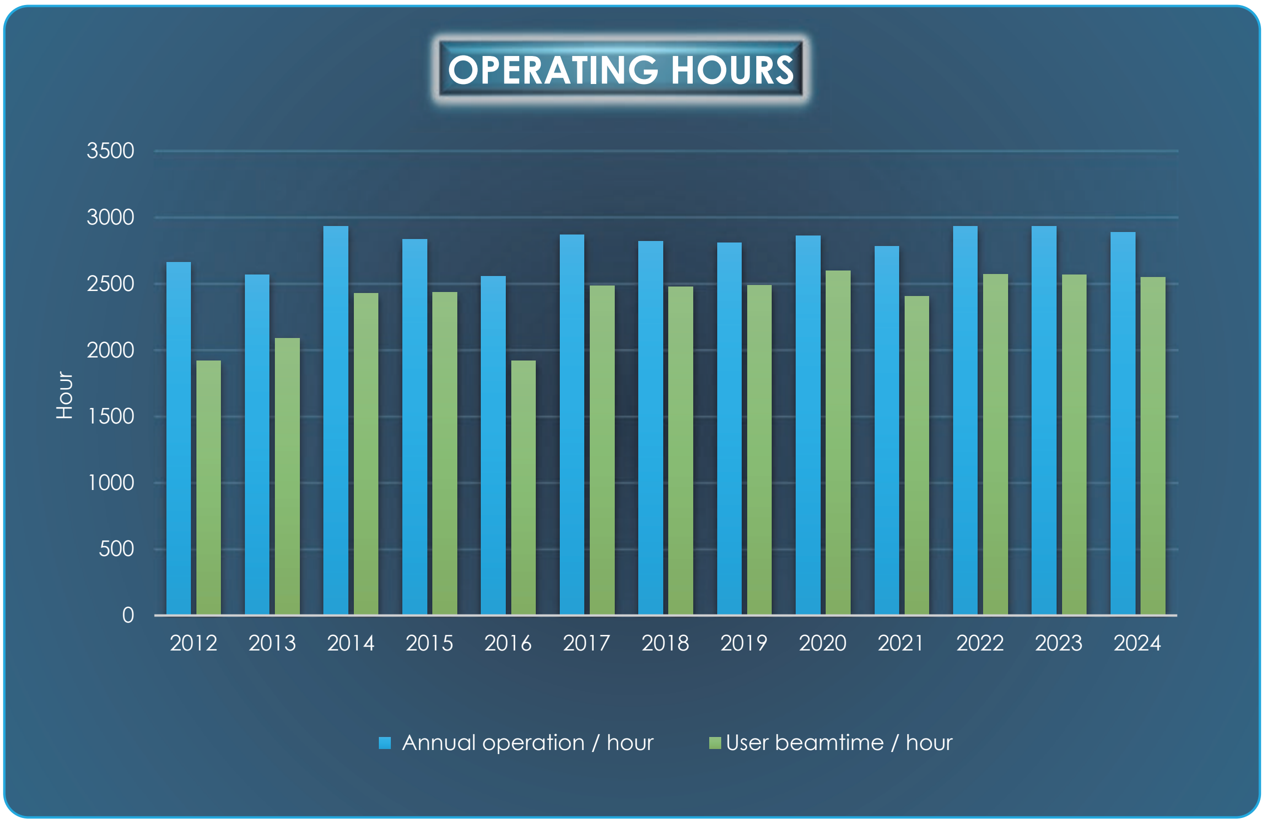
OPERATING HOURS
Hour
3500
3000
2500
2000
1500
1000
500
0
2012
2013
2014
2015
2016
2017
2018
2019
2020
2021
2022
2023
2024
Annual operation / hour
User beamtime / hour

Institute for Molecular Science
National Institutes of Natural Sciences
Okazaki 444-8585, Japan

Tel : +81-564-55-7402
Fax: +81-564-54-7079
http://www.uvsor.ims.ac.jp

Editorial Board: H. Katayanagi, Y. Sato, K. Tanaka

UVSOR III
since 2012